Forced Convection Heat Transfer in a Porous Channel Subjected to Oscillating Flow

Jin Liwen

School of Mechanical & Aerospace Engineering

A thesis submitted to the Nanyang Technological University
in fulfilment of the requirement for the degree of
Doctor of Philosophy

2006

ABSTRACT

The open-cell metal foam is a porous medium which possesses a true metal skeletal structure. The fully inter-connected pore and ligament structures provide the extreme large fluid-to-solid contact surface area and tortuous coolant flow path inside the metal foam, which could increase dramatically the overall heat transfer rate. The high specific surface area, low density and open-celled nature of a metal foam possesses a combination of properties ideally suited for applications in high heat flux thermal management where conventional materials and products are not adequate.

In this research, forced convection in a heated channel filled with open-cell metal foam subjected to oscillating flow has been investigated experimentally and numerically. Aluminium metal foams with different pore densities of 10, 20 and 40 PPI (pores per linear inch) were used as the inserted materials along with air as the fluid phase. The temperature distribution on the substrate surface of the heated wall, velocity of oscillating flow through porous channel and pressure drop across the test section were measured. For oscillating flow, pressure drop and flow velocity increase with the increase of kinetic Reynolds number and dimensionless flow amplitude. The results showed that the hydraulic ligament diameter based kinetic Reynolds number and dimensionless flow amplitude are the critical parameters for the investigation of oscillating flow characteristics in open-cell metal foam. The cycle-averaged temperatures were found to decrease with an increase in the kinetic Reynolds number while the cycle-averaged local Nusselt numbers exhibit the opposite trend. The empirical equation obtained by the experimental study showed that the length-

averaged Nusselt number of oscillating flow through aluminium foam is governed by the kinetic Reynolds number Re, and dimensionless flow amplitude *Ao*.

The experimental results also revealed that for aluminium foams subjected to oscillating flow, the heat transfer rate increases with the increase of the pore density at a constant kinetic Reynolds number i.e. dimensionless oscillatory frequency. However, for a given pumping power, better heat transfer performance can be achieved by low pore density metal foam under the condition of oscillating flow. High pore density metal foams with their extremely large fluid-solid-contact surface areas and tortuous coolant flow paths are suitable to remove extraordinarily high heat fluxes in applications where pumping power is not of concern.

The unsteady macroscopic governing equations of continuity, momentum and energy adopted in the numerical study were obtained based on the volume averaging method. Energy equations were formulated based on the local thermal non-equilibrium model (LTNE) and the properties of the solid (aluminium) and fluid (air) phases were determined. The specific boundary conditions for oscillating flow through aluminium foam channel were formulated and the governing equations were solved by the finite-volume method (FVM) with programmed FORTRAN code. The simulation results for the transient oscillatory velocity and temperature at the different locations along the axial and vertical directions of the porous channel were presented, and the instantaneous characteristics of velocity and temperature for oscillating flow through metal foam were elucidated physically. It was found that the two-dimensional temperature contours in the numerical domain are symmetric about the centre of the channel under different kinetic Reynolds numbers and dimensionless flow amplitudes. The temperature decreases with the increase of the distance along the vertical direction of the channel. The numerical calculations showed that the transient

temperature profile for the dimensionless location near the entrance is lower than that close to the middle of channel in a complete cycle. The cycle-averaged Nusselt number increases with the axial location from the entrance to the centre of the channel.

The numerical results also indicate that the temperature difference between the solid and fluid phases in an aluminium foam channel subjected to oscillating flow cannot be neglected. The temperature difference between the solid and fluid phases at two thermal entrance regions is smaller than that at the middle of the channel, and decreases with the increase of the kinetic Reynolds number. Simulation of the effects of the properties of aluminium foam and kinetic Reynolds number on heat transfer of oscillating flow through porous channel showed agreement with the experimental results.

ACKNOWLEDGMENT

First of all, I would like to express my sincere gratitude to my supervisor, Prof. Leong Kai Choong, for his guidance and encouragement throughout the course of my study. I considered myself very fortunate to be his student. The lengthy discussions with Dr. Leong are always helpful and inspiring. Without his scholarly advice, this work would not have been possible.

I wish to thank Dr. Charles Yang Chun for his encouragement given to this research. I also want to thank technical staff, Mr. Yuan Kee Hock for his assistance in the experiments.

I would also like to acknowledge the financial support received from Nanyang Technological University (NTU). Without the scholarship, this project would not have been feasible.

I am very grateful to my fellow graduate students in the Thermal and Fluids Research Laboratory of the School of Mechanical and Aerospace Engineering of NTU who have rendered much help to me during my stay at NTU.

Finally, special thanks are reserved for my parents and my wife for their faith and encouragement through the years; to them this work is humbly dedicated.

CONTENTS

NOMENCLATURE

Roman Symbols

a	coefficient of the discretisation equation
A,B,C_1,C_2	variables
$\boldsymbol{A}$	surface vector
A_c	cross-sectional area of the channel (m^2)
A_f	surface area of fluid phase (m^2)
a_{fs}	solid-fluid interfacial surface area (m^2/m^3)
A_{heated}	heated area (m^2)
A_m	surface area of solid phase (m^2)
A_p	amplitude of pressure gradient (Pa)
b	half length of fibre (mm)
$\boldsymbol{B}$	total drag force vector
B_x,B_y	additional body force
C	constant
C_d	convection-diffusion coefficient
C_f	form coefficient
c_p	specific heat (J/kg·K)
D	diameter of pipe (m)
d_h	hydraulic diameter of pore (μm)
d_l	ligament diameter of porous media (μm)
d_p	pore diameter (μm)
D_e	hydraulic diameter of the channel (m)
D_f	hydraulic diameter of the fin (m)

D_h	hydraulic ligament diameter of metal foam (m)
D_C	form drag (N)
DI	diffusion rate at control volume face
D_μ	viscous drag (N)
f	oscillatory frequency (Hz)
F	inertia coefficient of porous medium (m^{-1})
F_e,F_w,F_n,F_s	flow rate through control volume faces (kg/s)
F_x,F_y	distributed resistance
F_ω	function of friction factor for oscillating flow
H	height of the channel (m)
H_f	fin height of heat sink (m)
h	heat transfer coefficient ($W/m^2 \cdot K$)
h_{fs}	interfacial heat transfer coefficient ($W/m^2 \cdot K$)
h_x	local heat transfer coefficient ($W/m^2 \cdot K$)
$h_{x,t}$	instantaneous local heat transfer coefficient ($W/m^2 \cdot K$)
J	total fluxes
K_h	hydraulic conductivity (m/s·Pa)
K	permeability of the porous medium (m^2)
k	thermal conductivity (W/m·K)
k_d	thermal dispersion conductivity (W/m·K)
k_{eff}	effective thermal conductivity (W/m·K)
k_{se}	effective thermal conductivity of solid (W/m·K)
k_{fe}	effective thermal conductivity of fluid (W/m·K)
l	half length of fibre in metal foam (μm)
L	length of the test section (m)
M	mass flow rate (kg/s)
P	pressure (Pa)

ΔP	pressure drop (Pa)
q	heat flux (W/m^2)
Q	power input (W)
r	radial coordinate (m)
R_A, R_B, R_c, R_D	simplification quantities for metal foams
r_m	half thickness of fibre in metal foam (μm)
s	fin spacing of heat sink (m)
S	general source term
S_C	constant of the linearised source term
S_P	coefficient of the linearised source term
t	time (s)
T	temperature (^{o}C)
$\overline{T}_m$	space-cycle averaged temperature at the mixing chamber (^{o}C)
T_w	cycle-averaged local surface temperature (^{o}C)
$\overline{T}_w$	space-cycle averaged wall temperature (^{o}C)
T_i	cycle-averaged temperature at the inlet of test section (^{o}C)
$T_{x,t}$	instantaneous local temperature (^{o}C)
u	velocity vector
u	velocity at x-direction (m/s)
v	velocity at y-direction (m/s)
V	volume (m^3)
V_s	volume of solid fraction of the tested metal foam (m^3)
V_t	total volume of the tested metal foam (m^3)
V_x,V_y	additional viscous terms
$\dot{V}$	average maximum volumetric flow rate (m^3/s)
w	channel width (m)
W_p	maximum pumping power (W)

x	axial coordinate (m)
x_{max}	amplitude of flow displacement (m)
y	vertical coordinate (m)

Dimensionless variables

A_0	dimensionless flow displacement
A_{Dh}	hydraulic ligament diameter based dimensionless flow amplitude
d	dimensionless ligament radius of metal foam
f_{max}	maximum friction factor of oscillating flow
f_{osc}	average friction factor of oscillating flow
f_{std}	friction factor of steady flow
Pr	Prandtl number
R	dimensionless radial coordinate
Re	Reynolds number based on the ligament diameter
Re_K	Reynolds number based on the permeability
Re_h	Reynolds number based on the hydraulic diameter of the fin
$Re_{max(Dh)}$	maximum hydraulic ligament diameter based Reynolds number
Re_ω	kinetic Reynolds number
$Re_{\omega(Dh)}$	hydraulic ligament diameter based kinetic Reynolds number
$Nu_{x,t}$	instantaneous local Nusselt number
Nu_x	cycle-averaged local Nusselt number
Nu_{avg}	length-averaged local Nusselt number
$Nu_{s\text{-}avg}$	space-cycle averaged Nusselt number
Pe	Peclet number
Pe^*	effective Peclet number
Pe_x^*	effective local Peclet number
T_{uni}	temperature uniformity index

t^*	dimensionless time
β	Stokes number

Greek Symbols

α^*	effective thermal diffusivity (m^2/s)
ω	angular frequency (rad/s)
ϕ	surface porosity
Φ	any dependent variable
θ	phase lag (deg)
ν	kinematic viscosity (m^2/s)
ζ	maximum residual
δ	uncertainties
δ_t	thickness of thermal boundary layer (m)
ρ	density (kg/m^3)
γ	shape parameter of the porous medium
Γ	dispersion coefficient
ε	porosity of medium
μ	dynamic viscosity ($N \cdot s/m^2$)
μ_e	effective fluid viscosity ($N \cdot s/m^2$)

Subscripts

e, w , n , s	control volume faces
E, W, N, S	grid nodes
f	fluid phase
in	inlet
m	mean
max	maximum
min	minimum
P	central grid point
s	solid phase

LIST OF FIGURES

LIST OF TABLES

PUBLICATIONS ARISING FROM THIS THESIS

Journal Papers

1. Leong, K.C. and Jin, L.W. "Heat transfer of oscillating and steady flows in a channel filled with porous media", *International Communications in Heat and Mass Transfer*, Vol. 31, No. 1, pp. 63 - 72, 2004.

2. Leong, K.C. and Jin, L.W. "An experimental study of heat transfer in oscillating flow through a channel filled with an aluminum foam", *International Journal of Heat and Mass Transfer*, Vol. 48, No. 2, pp. 243-253, 2005.

3. Leong, K.C. and Jin, L.W. "Characteristics of oscillating flow through a channel filled with open-cell metal foam", *International Journal of Heat and Fluid Flow*, Vol. 27, No.1, pp. 144-153, 2006.

4. Leong, K.C. and Jin, L.W. "Effect of oscillatory frequency on heat transfer in metal foam heat sinks of various pore densities", *International Journal of Heat and Mass Transfer*, Vol. 49, Nos. 3-4, pp. 671-681, 2006.

5. Jin, L.W. and Leong, K.C. "Heat transfer performance of metal foam heat sinks subjected to oscillating flow", *IEEE Transactions on Components and Packaging Technologies*, Accepted, 2006.

6. Jin, L.W. and Leong, K.C. "Pressure drop and friction factor of steady and oscillating flows in open-cell porous media", *Transport in Porous Media*, Accepted, 2006.

Conference Papers

1. Jin, L.W. and Leong, K.C. "Effects of displacement and frequency of oscillating flow on heat transfer in a porous channel", *IMECE 2004 ASME International Mechanical Engineering Congress*, November 13 - 19, 2004, Anaheim, California, USA.

2. Leong, K.C. and Jin, L.W. "Heat transfer and fluid flow in metal foam subjected to oscillating flow", *2005 ASME Summer Heat Transfer Conference*, July 17-22, 2005, San Francisco, CA, USA.

3. Jin, L. W. and Leong, K. C. "Numerical study of heat transfer in aluminium foams subjected to oscillating flow", *13th International Heat Transfer Conference*, August 13-18, 2006, Sydney, Australia, Accepted.

CHAPTER 1

INTRODUCTION

1.1 Background

1.1.1 Challenges in Electronics Cooling

The current trend in microprocessor architecture is to increase the level of integration, shrink processor size, and increase clock speeds. The increased requirements for calculation performance resulted in rapid augmentation of the speed and the number of gates on the silicon. Azar and Morabito (2000) reported more than a decade ago that 1.5 μm appeared to be the limit and this caused much enthusiasm about the possibilities for integrated circuits. But today, geometries down to 0.09 ~ 0.13 μm are gaining in popularity and are soon to become a standard. The speed and the number of gates on the components had increased by more than ten times. Table 1-1 presents the details of the transistor count, process size and power dissipation for standard desktop processors manufactured by Intel Co. Ltd. It shows that the reduction in feature size, higher speeds and increased number of parts on the die led to very high heat density on the semiconductor.

Table 1-1 Information for the typical desktop CPU of Intel Corporation

(Source: http://bwrc.eecs.berkeley.edu/cic/summary/)

Year	Transistors (Millions)	Feature size (μm)	Speed (MHz)	Temperature (°C)	Power dissipation (W)
1997	1	0.25	233-333	85	19.05 – 28.3
1999	3	0.18-0.25	350-750	90	25.3 – 34.5
2001	4.2	0.18	933-1600	77	52.8 – 57.1
2002	5.5	0.13	1700-2800	69	70 – 81.8

The need for better performance and an increased level of functional integration as well as die size optimization on the microprocessor leads to preferential clustering of higher power units on the processor. These have resulted in rapid increases in the level of heat fluxes that must be removed for reliable operation of electronic packages. Whether they be microprocessors, RF amplifiers or power chips, advances in semiconductor process technology enable the industry to pack more performance into smaller packages. As reported from Intel Co. Ltd. by Viswanath *et al.* (2000), the general trend is for the maximum processor power consumption to increase by a factor of a little more than two times every four years. For example, the maximum power of Intel's CPU of years 1995 and 1999 were about 9 and 20 W, respectively. Gunther *et al.* (2001) reported that for the latest high performance CPU Pentium 4, the power almost reached 80 W. Figure 1-1 shows the thermal design power in the performance and value desktop processors of Intel's CPU from Pentium to Pentium 4. This presents clearly increasing thermal management issues, as the heat being dissipated from these devices is increasing and the heat fluxes are increasing even faster.

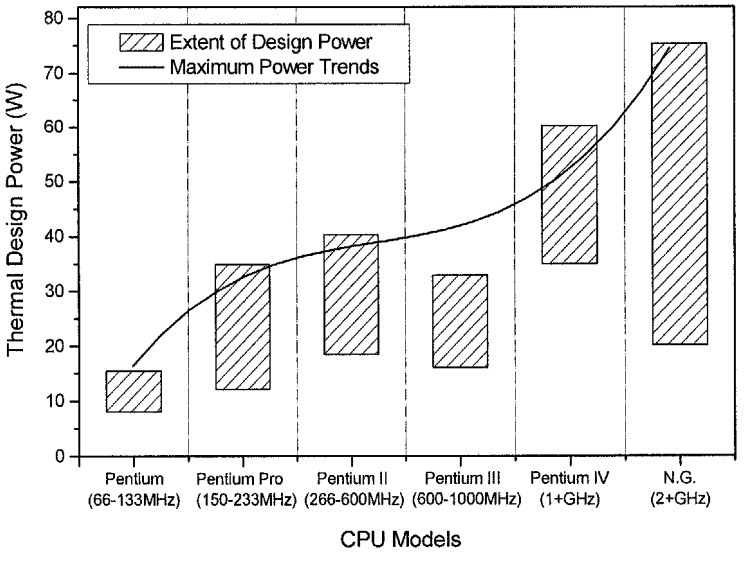

Figure 1-1 Power and heat flux trends in Intel's desktop processors
(Source: Viswanath *et al.*, 2000)

To control the thermal management issues of high-speed microprocessor, many cooling techniques were developed, such as micro-channel, heat pipe or novel types of heat sink. Once the necessary cooling method has been established, the cost for the application of the cooling technique will be the most important. However, the cost of cooling solutions increases even faster than the power dissipation does. Figure 1-2 shows the relative implementation cost of various cooling solutions ranging from a simple extruded aluminium heat sink to the more elaborate heat pipe technology. It is important to observe that as power increases, there is a non-linear relationship between the cooling capabilities and the cost of the solution. With increasing power of electronic packages and the development of cooling techniques, cost will be a significant challenge for all future thermal designs and the speed to accomplish new designs will be a critical factor to their success. This emphasises the importance of finding methods which can effectively and economically dissipate the heat from microprocessors.

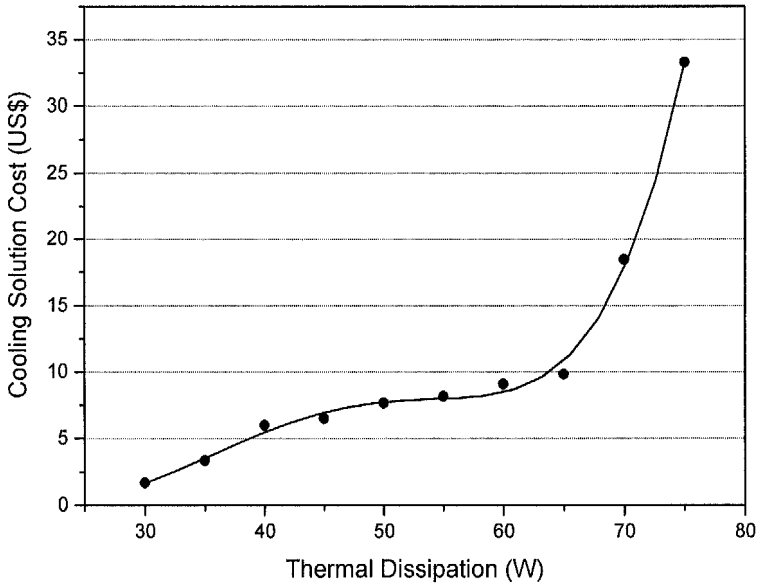

Figure 1-2 Cost of removing heat from a microprocessor
(Source: Gunther *et al.*, 2001)

1.1.2 Development of Heat Removal Techniques

Air cooling is the traditional method of cooling electronic components. The design of a heat sink is based on the Newton's cooling law which states that heat dissipated is equal to the product of the convective heat transfer coefficient, and the temperature rise between the heat sink and cooling air, i.e.

$$Q = h \times A_{\text{heated}} \times (T_{\text{heatsink}} - T_{\text{air}}) \tag{1-1}$$

where Q is the heat rate, h is the convection heat transfer coefficient and A_{heated} is the effective heat transfer area. According to Equation (1-1), there are two ways to improve heat removal capability of heat sink in electronics cooling *viz.* increase the heat transfer coefficient and increase surface area. Hence, many kinds of fins have been designed to increase the exposed air-solid contact surface area. The most common method of increasing the heat transfer coefficient is to increase the flow velocity. However, it also increases the mass flow rate, thus reducing the overall temperature of the exit air. Increasing air velocity beyond 8~10 m/s adds significantly to the backpressure and the acoustic noise. In convective heat transfer, the increase in heat removal is based on available cooling surface area. In many cases, the use of an increased number of flat fins gives better performance although the volume of heat sinks is increased at the same time. From the study of Simons (1983), conventional natural or forced cooling methods are only capable of removing a relatively small amount of heat per unit area per unit temperature difference, about 0.001 W/cm^2·K by natural convection to air, 0.01 W/cm^2·K by forced convection to air, and 0.1 W/cm^2·K by forced convection to liquid. Therefore, conventional natural or forced convection cooling methods are not capable of removing the high heat fluxes for maintaining a proper operational temperature in modern high-speed microprocessors. It is imperative to look for new methods of cooling the modern electronic components.

1.1.3 Porous Media and Oscillating flow

To solve the issue of the thermal management in electronic packages, some new cooling methods were developed such as the micro-channel heat sink, heat pipe and implementation of porous media. The micro-channel is a powerful solution for cooling high-performance electronic components. Tuckerman and Pease (1981) reported that extremely high heat fluxes of up to 790 W/cm^2 can be dissipated by micro-channel heat sinks using water as coolant. On the other hand, the heat pipe still needs a heat sink at the hot end and the cost for fabrication of micro-channel heat sink is very high. For example, the raw substrate material used to manufacture a microchannel range in cost from approximately US$ 500-4000 per m^2. Also, the replication and direct techniques of micro-fabrication still have some problems in mass production (Becker and Gartner, 2000). As compared to heat pipe and micro-channel, the manufacturing of porous media is relatively more developed with very low cost. It can be obtained easily by inserting high conductivity materials or metal foams with different pore densities provided directly by manufacturers.

The porous medium with high thermal conductivity has emerged as an effective method of heat transfer enhancement due to its large surface area to volume ratio and intense mixing of fluid flow. The implementation of a high thermal conductivity porous medium, such as aluminium, copper and other metals into a channel has begun to gain popularity. Many researchers have studied heat transfer in porous media. According to Koh and Colony (1974), the total heat transfer rate will be increased significantly in spite of the lower heat transfer coefficient between the solid-air contact surfaces, and very high heat fluxes can be obtained using single-phase water flow. Chrysler and Simons (1990) suggested the use of packed beds of spherical particles to enhance convective heat transfer from microelectronic chips. Haritonov *et*

al. (1994) experimentally investigated convection heat transfer on flat plates and in channels filled with porous materials such as sintered spherical particles, nets, porous metal, and felts. The above review shows that heat transfer performance can be improved substantially by inserting porous media in channels.

As compared to the porous channel packed with metal particles, spheres or woven-screens, the open-cell metal foam is a novel type of porous medium which has a true metal skeletal structure. It is manufactured by solidification of metal from a super-heated liquidus state in an environment of high pressure and high vacuum. A close-up view of the inside structure for different types of porous media is shown in Figure 1-3. Figures 1-3 (a) and (b) represent the structures for particle inserted bed and woven screen, respectively. It can be seen from Figure 1-3 (c) that the resulting metal foam has a reticulated structure of open, shaped cells connected by continuous solid metal ligaments. The metal foam with fully inter-connected structure, low thermal inertia, high surface area to volume and permeability opens itself to many applications, especially in heat transfer enhancement. Lu *et al.* (1998) investigated analytically the heat transfer efficiency of using an aluminium foam as a heat sink and concluded that the advantage of designing heat sinks with honeycombs is that high heat transfer performance can be achieved with relatively small pressure drop. Kim *et al.* (2001) studied forced convection from an aluminium foam in an asymmetrically heated channel and noted that the inertia coefficient of the metal foam is a function of friction factor for steady flow through the channel. Driven by the applications of open-cell metal foam, some investigators have performed research into the fluid flow in metal foam. Boomsma and Poulikakos (2002) investigated the characteristics of steady water flow through aluminium foams with different compression and pore sizes. Their results revealed that permeability and form coefficient accurately described the

pressure drop versus flow velocity behaviour in porous media. Boomsma *et al.* (2003b) experimentally studied the metal foam as a compact heat exchanger and compared its performance with a traditional heat exchanger subjected to uni-directional flow. They pointed out that the open-cell aluminium foam generated thermal resistances that were two to three times lower than the best commercially available heat exchangers tested and with lower pressure drop. This indicates that open-cell metal foams with high thermal conductivity can be used to design novel heat sinks with better heat transfer performance and less pumping power.

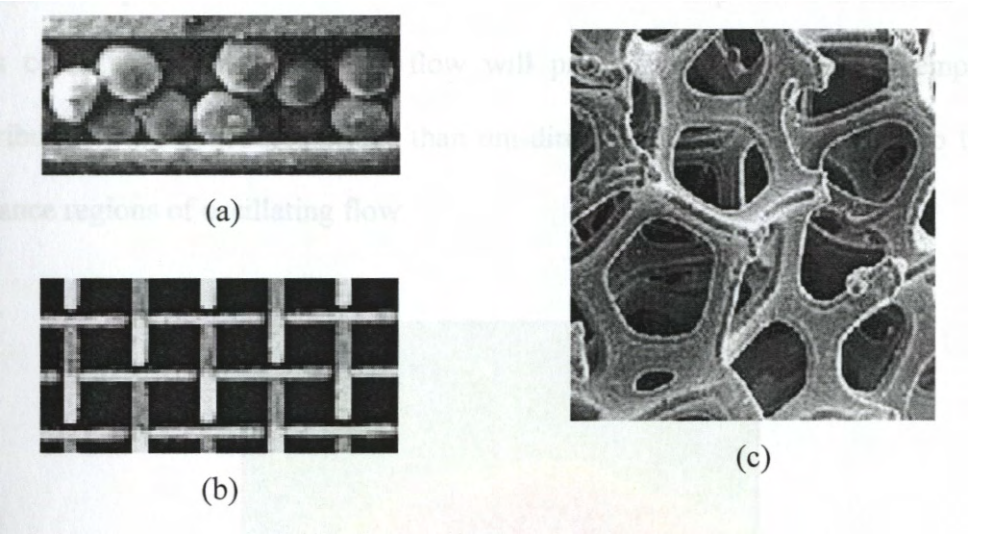

Figure 1-3 Typical structures of (a) particles inserted bed (b) wire-screen (c) metal foam
[Source: (a) Jiang *et al.*, 2001; (b) Xu and Wirtz, 2002; (c) http://www.ergaerospace.com/duocel/]

However, one-directional flow through the porous channel yields a relatively high surface temperature difference along the flow direction. Hwang and Chao (1994) studied the heat transfer of sintered bronze bead channels with uniform heat fluxes of up to 3.2 W/cm^2. They observed a local surface temperature difference of more than 50°C between the most upstream and the most downstream locations in the case of q = 3.2 W/cm^2 in their experiments. For modern high-speed microprocessors, the reliability of transistors and operating speed are not only influenced by the average

temperature but also by temperature uniformity on the substrate surface. An illustration of non-uniform temperature distribution on the substrate level of Pentium 4 processor is shown in Figure 1-4. It is clear that a large temperature difference exists between high and low power density areas. With increased chip performance, the non-uniformity of on-die power distribution increases, and there are regions of the die with high heat flux densities. The temperature of the hot spot can often affect calculated performance due to prolonged gate delay, and will always govern the overall reliability of the silicon (Mahajan *et al.*, 2002). Therefore, maintaining the uniformity of on-die temperature distribution below certain limits is imperative in thermal design. It is conceivable that oscillating flow will produce a more uniform temperature distribution on a substrate surface than uni-directional flow due to the two thermal entrance regions of oscillating flow.

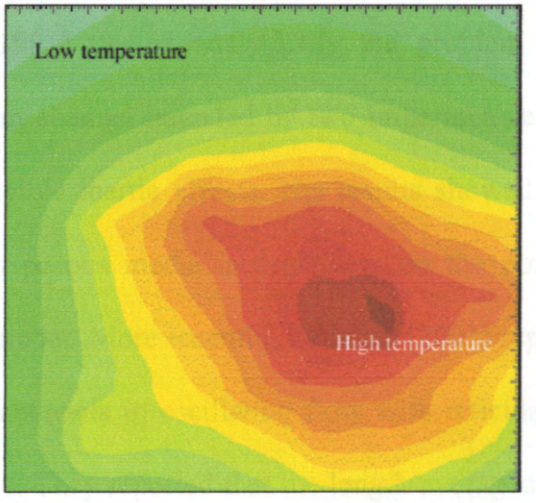

Figure 1-4 Illustration of the non-uniformity temperature distribution in a typical Pentium 4 processor
(Source: Gunther *et al.*, 2001)

Research into the heat transfer enhancement of oscillating flow through an empty channel tube have been conducted widely through analytical and experimental methods. Walsh *et al.* (1993) experimentally investigated forced convection cooling

in micro-electronic cabinets by oscillatory flow techniques. Their results show that electronic component operating temperatures can be reduced by as much as 40% when an oscillatory flow device is employed. Zhao and Cheng (1995) presented both experimental and numerical results for laminar forced convection of an incompressible periodically reversing flow in a pipe of finite length at constant heat flux. The average heat transfer rate was found to increase with both the kinetic Reynolds number and the dimensionless oscillation amplitude but decrease with the length-to-diameter ratio.

Compared to the foregoing research efforts on oscillating flow through empty channels, published investigations on oscillating flow heat transfer through porous channels are really scarce. Sozen and Vafai (1990) conducted a numerical study of compressible flow through a packed bed. The effect of oscillating boundary conditions on the transport phenomena was investigated with the packed wall insulated. Khodadadi (1991) treated analytically the problem of oscillating flow through a porous medium channel bounded by two impermeable parallel plates with the assumption of negligible inertia effects. His results showed that the oscillatory fully developed flow in porous media is dependent on the porous medium shape parameter and Stokes number. More recently, Fu *et al.* (2001) reported the results for heat transfer in porous channels in oscillating flow with reticulated vitreous carbon and metal foam materials. They reported that the length-averaged Nusselt number for oscillating flow is higher than that for steady flow. The effects of thermal conductivity and permeability of different metal foam materials on heat transfer were analysed. However, the effects of the kinetic Reynolds number and the dimensionless amplitude of flow displacement on heat transfer of oscillating flow in porous channel were not discussed.

The previous works revealed that higher heat transfer rate and more uniform temperature distribution can be obtained by a channel filled with porous media subjected to oscillating flow. However, the above investigations showed that studies of heat transfer in oscillating flow were restricted to channels filled with particles or wire-screens, and investigations of fluid flow behaviour in metal foams were limited to the uni-directional flow condition. As mentioned previously, the structure of the open-cell metal foam is completely different from that of the traditional porous media, which have been investigated widely. This leads to some unknowns of heat transfer and fluid flow of oscillating flow in metal foam porous medium. For the design of novel heat sinks using open-cell metal foams subjected to oscillating flow, the heat transfer characteristics and fluid behaviour in metal foams under oscillating flow condition need to be investigated further.

1.2 Objective and Scope

The objective of this study is to achieve fundamental understanding of fluid flow and heat transfer in a channel filled with metal foam subjected to oscillating flow. The cycle averaged and transient heat transfer characteristics of oscillating flow through metal foam will be investigated experimentally and numerically. The scope of this study includes the following:

(1) A series of experiments will be conducted on the investigation of oscillating flow through a channel filled with various open-cell metal foams. The proposed study involves experiments with different oscillatory frequencies and flow displacements. The surface temperature distribution on the substrate surface of the heated wall, velocity of oscillating flow through porous channel and pressure drop across the test section will be measured.

(2) The effects of the different dimensionless oscillatory frequencies, flow

displacements and materials properties on the fluid behaviour and heat transfer characteristics in open-cell metal foam will be analysed. The heat transfer performance between oscillating flow and steady flow through metal foam will be compared. The heat transfer rate versus pumping power of the cooling system subjected to oscillating flow will be considered for application in electronics cooling.

(3) Theoretical formulation of the heat transfer process and numerical computation of oscillating flow through open-cell metal foam channel will be performed. A series of FORTRAN programmes will be written to implement the numerical simulation for heat transfer in a two-dimensional domain. The local thermal non-equilibrium model (LTNE) will be employed to investigate the temperature difference between the solid and fluid phases in metal foam channel subjected to oscillating flow.

(4) The simulation results for the transient oscillatory velocity and temperature at the different locations along the axial and vertical directions of the porous channel will be presented. The instantaneous characteristics of local temperature and Nusselt number for oscillating flow through metal foam will be elucidated physically. The effects of the kinetic Reynolds number and dimensionless flow amplitude on the cycle-averaged and the length-averaged Nusselt numbers will be also analysed.

(5) The cycle-averaged temperature distribution on the substrate surface, the axial velocity and the total heat transfer rate of oscillating flow in metal foam channel obtained by the experimental study will be compared to those obtained by the numerical simulation. The deviation between experimental and numerical results will be discussed.

1.3 Outline of Thesis

The preceding section of this chapter introduces the increased trend of power clustering on the modern electronics device due to the improved calculation speed.

The motivation of this research is to investigate the potential heat transfer performance of forced convection in metal foam subjected to oscillating flow which possesses two thermal entrance regions. The objective and scope of this research are presented.

An extensive literature review of fluid flow and heat transfer in porous medium is presented in Chapter 2. The fluid flow and heat transfer of both steady and oscillating flows through porous medium are reviewed.

Chapter 3 describes the experiments of oscillating flow through metal foam channel. The experimental facility, measuring system and physical properties of the tested aluminium foams are described in detail. The error of the measurements and the uncertainty of the calculated parameters are analysed in this chapter.

The experimental results for fluid flow and heat transfer of oscillating flow through aluminium foams 10, 20 and 40 PPI are discussed in Chapters 4 and 5, respectively. The pressure drop and flow velocity through aluminium foams with various pore densities are compared under different flow amplitudes and oscillation frequencies. A correlation equation for the maximum friction factor for oscillating flow through metal foam is obtained based on the similarity analysis presented in Chapter 4. Chapter 5 deals with the cycle-averaged heat transfer characteristics of oscillating flow through metal foams. An empirical equation for the length-average Nusselt number is obtained in terms of the kinetic Reynolds number and dimensionless flow amplitude. The temperature uniformity and heat transfer performance of steady and oscillating flows through the tested materials are compared by a dimensionless grouping parameter which is obtained by theoretical analyses. For cooling electronic packages, the heat removal capability of metal foam is assessed together with the driven force required to operate the oscillatory system i.e. the pumping power.

Chapter 6 presents a mathematical model for forced convection in porous medium and the numerical simulation scheme. The specific boundary conditions of oscillating flow through simulated domain and the properties of metal foams are formulated. The problems of the iteration step and convergence criteria of the programmed FORTRAN codes which are based on the finite-volume method are discussed. The derivation of the energy equations of fluid and solid phases based on the local thermal non-equilibrium model using volume averaging method is shown in Appendix D.

In Chapter 7, the simulation results of the instantaneous oscillatory velocity, temperature and Nusselt number at the different locations along the both axial and vertical directions of the porous channel are presented. The two-dimensional temperature distributions of the fluid phase are simulated in the controlled domain with different oscillatory frequencies and flow displacements. The effects of the kinetic Reynolds number and dimensionless flow amplitude on the heat transfer of oscillating flow through porous channel with different properties are analysed and elucidated physically. Numerical and experimental results are compared and the deviations between the experimental and the simulated results are analysed.

The thesis ends with conclusions derived in this research and suggestions for future research in Chapter 8.

CHAPTER 2

LITERATURE REVIEW

2.1 Momentum Transport in Porous Media

2.1.1 Laminar Flow

The fundamental theory of fluid flow through permeable media was firstly proposed by Henry Darcy in 1856. He measured the flow rate by collecting a certain volume of water during a certain time at the outlet of the column until the measured volume was equal to the afflux volume, thus establishing a steady flow. His experimental results were presented by Equation (2-1) in terms of volumetric flow rate $\dot{V}$ and pressure difference across the sand.

$$\dot{V} = \frac{K_h A_c}{H}(P + H - P_0) \tag{2-1}$$

where K_h is the hydraulic conductivity, and A_c and H are the column cross-sectional area and the height of the sand, respectively. P-P_0 is the pressure difference converted from atmospheric pressure between upper and lower sand layers. From the results reported by Darcy, Equation (2-1) can be rewritten as

$$K_h = u\frac{H}{\Delta P} \tag{2-2}$$

where u is the axial fluid velocity and ΔP is the total pressure drop. Equation (2-2) is for incompressible and isothermal creeping flow of Newtonian fluid through a relatively long, uniform and isotropic porous medium with low hydraulic conductivity. However, the effect of fluid viscosity was not considered in Darcy's work.

Following Darcy's equation, Hazen observed the fluid viscosity effect in

connection to the original flow equation published by Darcy. Hazen's experiments were performed under isothermal conditions, i.e., invariant fluid temperature from inlet to outlet of the filter. The Hazen-Darcy equation is described as

$$u = \left(\frac{K}{\mu_f} \right) \frac{\Delta P}{H} \tag{2-3}$$

where K is the specific permeability and μ_f is the fluid dynamic viscosity. It is the first time that the viscosity effect was included in the original fluid flow equation. The specific permeability K is a hydraulic parameter supposedly independent of fluid properties. Furthermore, some research were conducted to study the effect of form structure of porous media on flow behaviour, which was not included in the Hazen-Darcy equation. Based on the Hazen-Darcy equation, Dupuit developed Darcy's equation in 1863 by considering more parameters:

$$0 = \frac{\Delta P}{\Delta x} - \frac{\mu_f}{K} u - C_f \rho_f u^2 \tag{2-4}$$

where ρ_f and C_f are the fluid density and form coefficient for porous media, respectively. Equation (2-4) provides a global balance of forces acting on a finite fully saturated permeable volume with uni-directional steady flow of an incompressible fluid. The last two terms of Equation (2-4) represent the lumped viscous and the lumped form effects within the permeable medium, respectively.

Brinkman (1947) studied the limitation of Hazen-Darcy equation regarding the viscous shear stresses caused by the surface of a permeable medium on an adjacent volume element of fluid. He noticed that the fluid viscous shear stress effect should become negligible as compared to the viscous drag when the permeability is small, and pointed out that in a porous medium, the fluid viscous shear stress caused by one surface can affect, by increasing or decreasing, the fluid shear stress caused by a neighbouring surface. He obtained the following equation to describe the flow

through the porous media:

$$0 = -\nabla(\phi P) + \mu_e \nabla^2 \mathbf{u} - \frac{\mu_f}{K}\phi \mathbf{u} + C_f \rho_f \phi^2 |\mathbf{u}|\mathbf{u} \tag{2-5}$$

where $\mathbf{u}$ and μ_e are the velocity vector and the effective fluid viscosity, respectively. $\phi = A_f / A_m$ is the surface porosity, A_f and A_m are the areas occupied by the fluid and solid, respectively. In the last two decades, some efforts were made to achieve a general equation for describing flow characteristics in porous media. Vafai and Tien (1981) presented the following general equation for fluid flow through an isotropic, rigid and homogeneous porous medium.

$$\rho_f \left[\frac{\partial \mathbf{u}}{\partial t} + (\mathbf{u}\nabla)\mathbf{u} \right] = -\nabla(\varepsilon P) + \mu_e \nabla^2 \mathbf{u} - \frac{\mu_f}{K}\varepsilon \mathbf{u} + C_f \rho_f \varepsilon^2 |\mathbf{u}|\mathbf{u} \tag{2-6}$$

where ρ_f is the fluid density, μ_f is the fluid dynamic viscosity and ε is the porosity of porous medium. Equation (2-6) is an extension of Equation (2-4) with the inertia term included. To obtain Equation (2-6), the volume averaging technique was employed to achieve a closure problem, i.e. some of the forces acting on a representative permeable volume need to be modelled. Cheng and Zhu (1987), Cheng (1987) and Vortmeyer and Schuster (1988) analysed the phenomena of steep temperature gradients in forced convection in a packed column by taking into consideration the effects of thermal dispersion, variable porosity and non-uniform velocity distribution. In addition, the use of the Forchheimer's approach to account for the non-linear particle drag was conducted by Lauriat and Prasad (1989). Hsu and Cheng (1990) obtained a generalised equation of flow through porous media by applying the effective viscosity term into Equation (2-4), i.e. they lumped the forces acting on the fluid phase of the permeable medium into effective viscous and form forces. Ling and Dybbs (1992) presented a numerical-theoretical investigation of the influence of temperature-dependent fluid viscosity on the steady forced convection over an

isothermal flat plate bounding an infinite porous medium. The results indicate a deviation of up to forty percent in Nusselt number when compared with results obtained assuming uniform fluid viscosity. Liu *et al.* (1993) indicated a decrease in the form coefficient as the flow velocity increases. The rate of increase of the ratio of pressure-drop to fluid-speed was found to decrease as the particle diameter-based Reynolds number increases beyond 100.

Givler and Altobelli (1994) estimated the effective viscosity following the determination of the permeability and the form coefficient from global measurements. Knupp and Lage (1995) extended the Hazen-Dupuit-Darcy model, i.e. Equation (2-4), to the tensor permeability case by building a convex variational principle that minimises the flow work. Nield and Lage (1998) proposed a theoretical model to account for the fluid temperature variation along the direction transverse to the flow direction, and the effect of this temperature variation on the fluid viscosity, velocity, and total pressure drop. Nield *et al.* (1999) demonstrated the validity of Equation (2-3) for the case of forced convection of a liquid with temperature-dependent viscosity between uniformly heated parallel flat plates. Their experimental apparatus was designed to minimise the fluid temperature variation in the direction transverse to the flow, simplifying the theoretical analysis. Teng and Zhao (2000) presented a momentum equation for Newtonian-fluid flow in homogeneous and isotropic porous media based on the momentum conservation over a representative elementary volume. Their result can be considered as a generalised form of Darcy's law which applies to both Stokes and non-Stokes flows in porous media.

2.1.2 Turbulence

Another area of fluid in porous media is the theory of turbulent flow passing the porous media. It is also known that particles size, shape and density are the important

factors to the turbulent flow in porous media. Tsuji *et al.* (1984) reported that particle size and density can enhance or suppress turbulence in porous media. Small particles with small density tend to laminarise a turbulent flow through porous media. Schreck and Kleis (1993) showed that the turbulence intensity decreases with the increase of particle concentration for the case of disperse solid particles in porous medium, and observed that particles increase the isotropy of the flow.

It is obvious that increasing the fluid flow velocity can lead to turbulence in a porous media. MacDonald *et al.* (1979) and Dybbs and Edwards (1984) observed turbulent characteristics for flow in a porous medium i.e. highly unsteady chaotic flow within the pores and constant friction coefficient with the increase of Reynolds number. Rudraiah *et al.* (1985) and Rudraiah (1988) studied turbulent natural convection in porous media using the Hazen-Darcy equation which was extended by the inclusion of the convective acceleration term. Lee and Howell (1987) derived a model by including turbulence eddy diffusivity in the viscous diffusion term of the general momentum equation. They did not time-average the general momentum equation and neglected an additional contribution of the Reynolds stress in their model. Gratton *et al.* (1994) presented a randomly varying morphology-based turbulence model obtained by the hierarchical modelling methodology. Prescott and Incropera (1995) proposed a κ-ε model for simulating the momentum transport within the porous zone by adding a sink term in the κ-equation of turbulent clear flow. Travkin and Catton (1995) introduced a two-temperature heat and momentum transport model in which the morphology of the medium played a fundamental role. Their momentum model considered the elementary volume morphology as that of straight channels and did not include the convective inertia term. Wang and Takle (1995) presented a turbulence model for the boundary-layer flow near porous

obstacles. Lage *et al.* (1997) observed the transition from one quadratic regime to another quadratic regime, with different form coefficients, when increasing the speed of a fluid flow through a porous medium. Antohe and Lage (1997) derived a macroscopic turbulence κ-ε model for incompressible flow in porous media. The turbulent model was derived by time-averaging the general equation for porous media with all terms: time acceleration, convective inertia, pressure gradient, fluid viscous shear, viscous drag and from drag. Analyses of the κ-ε equations proved that for a small permeability medium, small enough to minimise the form drag, the effect of a porous matrix is to damp turbulence. For the large permeability case, the analyses is inconclusive as the form drag contribution can either enhance or damp on the turbulence. The model demonstrates that the only possible solution for steady unidirectional flow is zero macroscopic turbulence kinetic energy.

2.2 Heat Transfer in Porous Media

Heat transfer enhancement technique of using porous media plays a very important role in thermal management issues. It is congruously recognised that heat transfer can be intensified substantially by increasing the surface area of using porous materials in contact with the coolant. Heat transfer performance in porous medium has been successfully applied in the cooling of micro-electronic chips, powerful laser mirrors, aerospace craft, and even in thermal nuclear fusion. Haritonov *et al.* (1994) and Subbojin and Haritonov (1996) reported applications of using porous media in systems to cool mirrors used in laser equipments. Sherman *et al.* (1990) reported that structured cellular foam could be applied widely for heat removal in a variety of aerospace and industrial applications.

2.2.1 Forced Convection

Early research on forced convective heat transfer through a porous channel were performed by Koh and Colony (1974), Vafai and Tien (1981), Kaviany (1985) and other investigators. Koh and Colony (1974) theoretically studied the enhancement of heat transfer for forced-convection in a channel filled with high thermal conductivity porous medium. Their results showed that the heat transfer rate can be increased by three times for the fixed wall temperature condition. The work of Vafai and Tien (1981) was one of the early studies to account for the boundary and inertia effects on the flow and heat transfer in porous media. They found that the momentum boundary layer thickness is of the order of $\sqrt{K/\varepsilon}$, where K and ε are the permeability and porosity of porous media, respectively. Kaviany (1985) investigated laminar heat convection in porous channel bounded by parallel plates maintained at equal and constant temperatures. The velocity profile and Nusselt number were determined for flow through a porous channel for a simplified case where the axial conduction in the energy equation and velocity square term in the momentum equation were assumed to be negligible in his study. His results showed that Nusselt number for fully-developed fields increases with an increase in the porous media shape parameter, i.e., $\gamma = (w^2\varepsilon/K)^{1/2}$, where w is channel width. The results also showed that excess pressure drop, associated with the entrance region, decreases as γ increases. Analyses of traditional convection heat transfer in porous media were performed by Vafai and Tien (1982), and Tien and Hunt (1987). In their studies, the Darcian or slug flow models were used which neglected the non-Darcian effects such as the viscous shear force along the solid boundaries, the inertial convective force and thermal dispersion.

Towards the end of the last century, convection heat transfer in porous media has been extensively investigated due to its many important engineering applications.

Cheng *et al.* (1988) studied forced convection in a packed channel with asymmetric heating. The energy equation for the thermally developing flow, which took into consideration transverse thermal dispersion and variable thermal conductivity, was solved numerically. It was found that a wall function must be introduced to model the transverse thermal dispersion process in order to account for the wall effect on the lateral mixing of fluid. Hunt and Tien (1988) studied the effect of thermal dispersion on forced convection in fibrous media. The results showed that the porous medium enhances heat transfer from a surface as compared to predicted results for slug or for laminar flow in a channel due to dispersion, a non-Darcian phenomenon describing the intra-pore mixing that develops as the fluid moves past the solid particles. The dispersive transport increases with flow rate and permeability, and at large Reynolds numbers, overwhelms transport from solid conduction within the fibrous medium. Zebib and Wo (1989) studied two-dimensional forced convection air cooling of a single heated block mounted on the wall of a horizontal channel. Afrid and Zebib (1989, 1991) investigated numerically a two-dimensional conjugate conduction natural convection cooling of mounted blocks on an insulated vertical plate, and a three-dimensional laminar and turbulent natural convection cooling of heated blocks. They concluded in the first paper that increasing the spacing between the heated blocks led to a better cooling. In the second paper, they showed that there exists a qualitative similarity of the flow and thermal fields of the laminar and turbulent models. Lower temperatures were obtained with a turbulent model which are in good agreement with experimental results.

Research on heat transfer enhancement by forced convection at the vertical walls of heat generating blocks evenly mounted on the lower plate of a channel through the insertion of porous materials between the blocks was performed by Amer *et al.* (1998).

A control volume method was utilised to solve the conservation equations using a pressure velocity formulation. A staggered grid was considered such that the velocity components were located at the control volume faces whereas the pressures and temperatures were located at the centres of control volumes as suggested by Patankar (1980). The sudden change in the diffusion coefficients (viscosity or thermal conductivity) was handled by use of the harmonic mean to ensure conservation and uniqueness of mass and heat fluxes at each control volume face. Their results showed that the insertion of a porous material between the blocks may enhance the heat transfer rate on the vertical sides of the blocks. Although the porous matrix reduces the heat transfer coefficient on the horizontal face, significant increases in the mean Nusselt number (up to 50%) were predicted and the maximum temperatures within the heated blocks were reduced in comparison with the pure fluid case.

Convective heat transfer in porous media was also studied without the assumption of incompressible flow. For compressible flow, the majority of the investigations concentrated on ideal-gas behaviour, and employed the assumption of local thermal equilibrium between the solid and fluid phases. Analytical solutions for simplified cases were reported by Kidder (1957) for isothermal flow of an ideal gas through a porous medium and by Morrison (1972) for isothermal and adiabatic flows of an ideal gas through a porous medium. Goldstein and Siegel (1971) performed an analytical investigation on steady, non-isothermal ideal gas flow in a porous medium and utilised the local thermal equilibrium assumption and the Darcy formulation. Vafai and Sozen (1990a) conducted an analysis of energy and momentum transport in porous bed numerically. A model with compressibility and transient inlet temperature was employed.

It is generally known that heat transfer can be enhanced by using saturated porous

media in a forced convective fluid flow system. Previous researchers focused on many aspects and various conditions of a channel filled with porous media. Forced convection in a composite system, in which a fluid - saturated porous material occupies only a part of the passage has been investigated by Poulikakos and Kazmierczak (1987). The intention of their study was to avoid the significant pressure drop when a full porous media system fills a confined passageway. Huang and Vafai (1994) considered a forced convection problem in an isothermal parallel plate channel with porous blocks (partially inserted with porous media) using a vorticity stream function formulation. They showed that significant heat transfer augmentation can be achieved through the use of multiple emplaced porous blocks. Furthermore, for highly permeable and conducting porous media, it may not be necessary to fill the gap completely to attain the maximum heat transfer. Following this idea, enhanced heat transfer in an annular duct partially filled with a porous medium with high permeability and conductivity was observed by Chikh *et al.* (1995 a, b). The effects of permeability, thermal conductivity and the thickness of the porous material were investigated using a Brinkman-extended Darcy model. Their results showed that there exists a critical thickness of the porous layer at which heat transfer is minimum in the case of low thermal conductivity materials, while this does not show up for highly conducting materials. Their results showed that heat transfer is enhanced by increasing either permeability or thermal conductivity. Sung *et al.* (1995) simulated numerically the forced convection from an isolated heat source in a channel in which the loss of pressure drop was reduced by employing a partially-porous channel. A numerical study of pulsating flow and heat transfer characteristics in a circular pipe partially filled with a porous medium was presented by Guo *et al.* (1997). The Brinkman-Forchheimer-extended Darcy model was adopted for the porous matrix

region, which was attached to a pipe wall. The impacts of Darcy number, thickness of porous layer, ratio of effective thermal conductivity of porous material to fluid, as well as pulsating frequency, and amplitude were investigated. Enhanced longitudinal heat conduction due to pulsating flow and the enhanced convective heat transfer from high conducting porous material were examined. Their results showed that the maximum effective thermal diffusivity was occurred at a critical thickness of porous layer. Zhao and Liao (2000) experimentally and theoretically investigated phase-change heat transfer in porous structure heated with a permeable heating source. The heat transfer coefficient of the problem was modelled and the prediction showed agreement with the experimental data.

In addition, heat transfer in porous media for various applications was also studied. Ortega and Moffat (1985) and Moffat and Ortega (1986) studied free convection with and without shrouding wall in an array of simulated electronic components. Chrysler and Simons (1990) suggested the use of packed beds of spherical particles to enhance convective heat transfer from microelectronic chips while Kuo and Tien (1988) suggested the use of foam metal for the same application. A review of theoretical and experimental research on the thermal control of electronic equipment has been made by Peterson and Ortega (1990).

2.2.2 LTE and LTNE Models

Most of the above investigations for heat transfer in porous media were performed under the assumption that the temperatures of solid and fluid phases are equal. From the point of view of the energy equation, there are two different models in theoretical and numerical research: local thermal equilibrium (LTE) model and local thermal non-equilibrium (LTNE) model. The LTE model assumes that the solid-phase temperature is equal to the fluid temperature, i.e. local thermal equilibrium between

the fluid and the solid-phases at any location in the porous media. This model simplifies theoretical and numerical research, although the assumption of local thermal equilibrium between the fluid and the solid-phases is inadequate. The LTNE model builds two energy equations for solid and fluid phases, respectively, which shows the temperature difference between porous medium and fluid flow.

As the use of LTNE model leads to in-depth understanding of the convection heat transfer processes in porous media, more attention has been paid to the local thermal non-equilibrium model in theoretical and numerical investigations. Representative works include those of Vafai and Sozen (1990), Quintard and Whitaker (1993) and Amiri and Vafai (1994). The work of Vafai and Sozen (1990) was one of the early attempts to account for the temperature difference between solid and fluid phases in porous media. They employed two energy equations for the solid and fluid phases separately, i.e. LTNE model:

$$\varepsilon\langle\rho_f\rangle c_{pf}\frac{\partial\langle T_f\rangle}{\partial t}+c_{pf}\langle p_f\rangle\langle u_f\rangle\nabla\langle T_f\rangle=\nabla\left(k_{fe}\nabla\langle T_f\rangle\right)+h_{fs}a_{fs}\left(\langle T_s\rangle-\langle T_f\rangle\right) \tag{2-7}$$

$$(1-\varepsilon)\rho_s c_{ps}\frac{\partial\langle T_s\rangle}{\partial t}=\nabla\left(k_{se}\nabla\langle T_s\rangle\right)-h_{fs}a_{fs}\left(\langle T_s\rangle-\langle T_f\rangle\right) \tag{2-8}$$

where "< >" is the local volume averaged quantity, and k_{se}, k_{fe}, T_s and T_f are the effective thermal conductivities and temperatures for solid and fluid phases, respectively. h_{fs} and a_{fs} are the fluid-to-solid heat transfer coefficient and the specific fluid and solid contact surface area, respectively. Their results showed significant discrepancies between the fluid and solid phase temperature distributions. They allowed a simple characterisation scheme for interpreting the applicability of LTE condition and the one-dimensional approach for various compressible flow conditions and porous bed configurations. Quintard and Whitaker (1993) discussed one- and two-equation models for transient diffusion processes in two-phase systems. Amiri

and Vafai (1994) employed a general fluid flow model and a two-phase energy equation (LTNE) to investigate the forced convective heat transfer within a channel with constant wall temperature. They included the effects of variable porosity and thermal dispersion in their analysis and error maps for assessing the importance of various simplifying assumptions that are commonly used were established in their work.

Jiang *et al.* (1996) investigated the effects of viscous dissipation, appropriate boundary conditions, thermal dispersion, particle diameters and the variable properties of oil on the convection heat transfer in porous media using numerical model including local thermal non-equilibrium. Their numerical results were compared with experimental data and showed that the convection heat transfer in porous transfer in porous media can be predicted numerically using the local thermal non-equilibrium model with the ideal constant wall heat flux boundary condition. Kuznetsov (1998) obtained an analytical solution for the temperature difference between the solid and liquid phases for the problem of local thermal non-equilibrium in a parallel plate channel with constant heat flux using a perturbation approach. Quintard and Whitaker (1998) pointed out that when using two-equation models, several questions need to be asked, and the results showed that the two-equation model cannot handle high-frequency heat waves. Quintard (1998) presented a general two-temperature model dealing with local thermal non-equilibrium heat transfer in porous media by including the effect of interfacial thermal barriers. The heat exchange flux in the macroscopic equations was approximated as a time convolution integral involving the temperature at the boundary. However, the two-temperature model presented in his report is not easily implemented. Moreover, under some conditions (e.g. if the frequency of the fluid-phase temperature variations is small enough so that a single heat wave enters

the solid-phase) the time convolution integral for the heat exchange flux can be approximated by the volumetric heat transfer coefficient multiplied by the temperature difference between the solid-phase and fluid-phase, which is the usual expression for the two-equation model. Most cases consider steady-state heat transfer processes, so that the usual two-equation model is used widely.

Recently, Lee and Vafai (2000) employed the non-local thermal equilibrium model to investigate the forced convective flow through channel filled with a porous medium subjected to a constant heat flux. They obtained analytical solutions for the fluid and solid phase temperature distributions. Marafie and Vafai (2001) analysed the non-Darcian effects on temperature differentials in porous media by LTNE model. The temperature differences between solid and fluid phases were presented, and error maps for the validity of LTE model were established for various physical conditions. Their results showed that the Darcy number and the inertial parameter have a lesser influence in establishing the validity of the assumption for LTE model.

2.2.3 Effects of Material Properties

2.2.3.1 Generalised Porous Media

The physical properties of porous media are effective for heat transfer augmentation as they intensify the mixing of the flowing fluid and enhance convection heat transfer. Knowledge of the thermal properties and physical parameters of a porous medium is important for studying heat transfer of flow through the porous media. Thermal conductivity, heat transfer coefficient, Darcy number, permeability and porosity are the effective parameters of heat transfer of porous media.

Koh and Stevens (1975) conducted experiments on heat transfer in porous media with different permeabilities. In their study, uniform velocity across the channel was

assumed. For relatively high porosities and permeabilities (which are desirable for pressure drop consideration), a non-uniform velocity distribution is expected near the wall. As an extension of Koh and Stevens' work, the influences of such effects as non-Darcian effects, variable porosity, variable thermal physical properties, and thermal dispersion in the porous medium on the fluid flow and heat transfer were studied by Choi and Kulacki (1990) and David *et al.* (1991). The problem of using porous inserts to enhance heat transfer in a rectangular channel with constant wall temperatures were considered by Tong *et al.* (1993). The flow was considered to be hydrodynamically and thermally fully developed. A flow model that includes inertia and viscous effects was used to determine the velocity profile inside the porous region. The velocity profiles showed that porous inserts with a thickness not too close to the channel height had the effect of forcing more fluid to flow next to the walls. Jeigarnik *et al.* (1991) experimentally investigated convection heat transfer on flat plates and in channels filled with porous material such as sintered spherical particles, nets, porous metal, and felts. The working fluid entered or exited the test section through several channels which were perpendicular to the test section. Most of their experimental data were for convection heat transfer in sintered bronze porous layers with different thickness (0.86 ± 3.9 mm) and particle diameters (0.1 - 0.6 mm). They found that the porous media increased the heat transfer coefficient by 5 - 10 times although the hydraulic resistance was also increased. Huang and Vafai (1994) presented a detailed investigation of forced convection augmentation in a channel using multiple emplaced porous blocks. The effects of Reynolds numbers, Darcy numbers, inertial parameters and geometric parameters on forced convection enhancement in a channel using multiple emplaced porous blocks have been analysed. Their results showed that some parametric values such as the Reynolds number, Darcy number and Prandtl number

have significant effects on the heat transfer characteristics.

Recently, Lage *et al.* (1997) studied a low permeability microprobe heat sink for cooling phased-array radar systems. Their results suggested an increased overall heat transfer coefficient could be obtained that would reduce the operational temperature of the electronics for the same waste heat generation rate. Jiang *et al.* (1999) performed an experimental investigation to study the fluid flow and forced convection heat transfer in a plate channel filled with metallic or nonmetallic spherical particles. The effects of particle diameter, particle thermal conductivity and flow velocity on the convection heat transfer in glass, stainless steel and bronze spherical particles were examined. The results show that the porous media greatly increased the heat transfer coefficient although the hydraulic resistance was increased even more. For glass, stainless steel and bronze packed bed, the heat transfer coefficient was enhanced 5-6, 6-8 and 7-12 times, respectively. The effects of particle diameter, particle thermal conductivity and fluid velocity were examined for a wide range of thermal conductivities (from 75.3 W/m·K for bronze to 0.744 W/m·K for glass) and for three nominal particle sizes (0.278, 0.428 and 0.7 mm). The coolant water flow rate in the porous plate channel ranged from 0.01568 to 0.1992 kg/s. The Nusselt number and the heat transfer coefficient increased with decreasing bronze particle diameter, but decreased with decreasing glass particle diameter.

More recently, Rachedi and Chikh (2001) carried out a numerical investigation of electronic cooling enhancement. The one-energy equation model was adopted to analyse the thermal field and the control volume method based on finite differences with appropriate averaging for diffusion coefficients was used to solve the coupling between solid, fluid and porous regions. The effect of parameters such as Reynolds number, Darcy number and thermal conductivity ratio were considered in order to

obtain the most appropriate properties of the porous substrate that allow optimal cooling. Their results showed that for high thermal conductivity of the porous substrate, substantial enhancement was obtained compared to the fluid case even if the permeability is low. In the mixed convection case, the insertion of the foam between the blocks led to a temperature reduction of 50%. Jiang and Ren (2001) conducted a numerical investigation of forced convection heat transfer in porous media using a thermal non-equilibrium model. The effects of viscous dissipation, thermal dispersion, particle diameters and the variable properties of oil on convection heat transfer were analysed using a numerical model including the thermal non-equilibrium assumption. Their results showed that for a channel filled with glass beads with water as the working fluid, the convection heat transfer coefficient increases as the particle diameter increases; whereas for the bronze particles porous channel with water as the working fluid, the convection heat transfer coefficient increases as the particle diameter decreases. Yang and Hwang (2003) presented numerical predictions on the turbulent fluid flow and heat transfer characteristics for rectangular channel with porous baffles which were arranged on the bottom and top channel walls in a periodically staggered way. The parameters studied including the entrance Reynolds number, the baffle height and type of baffles (solid and porous). Their results indicated that the transport phenomena can be greatly improved by using a porous-type baffle instead of solid-type baffles on the channel wall.

2.2.3.2 Open-Cell Metal Foam

Studies on the effect of material properties showed that heat transfer characteristics were influenced significantly by porous media with different geometrical and thermal specifications. The open-cell metal foam has the desirable qualities for heat transfer enhancement, i.e. a high specific solid-fluid interface surface area and a tortuous fluid

path to promote mixing. The effective thermal conductivity and heat transfer coefficient of open-cell metal foam with high porosity and permeability have attracted much attention due to the local thermal dispersion caused by the eddies inside the metal foam.

Lu *et al.* (1998) investigated analytically the heat transfer efficiency of using aluminium foams as heat sinks. The overall heat transfer coefficient and pressure drop through the metal foam were analysed. They concluded that the advantage of designing heat sinks using honeycombs is that high heat transfer performance can be achieved with relatively small pressure drop. Calmidi and Mahajan (1999) studied the effective thermal conductivity of high porosity fibrous metal foams. Their results showed that the overall effective thermal conductivity of the fluid system could be dramatically increased by metal foams made of aluminium and copper. An analytical model of Equation (2-9) for obtaining the effective thermal conductivity of metal foams was derived in their work. The equation for calculating the effective thermal conductivity was validated by the experimental data.

$$k_{eff} = \left(\frac{2}{\sqrt{3}} \left(\frac{r\frac{b}{l}}{k_f + \left(1+\frac{b}{l}\right)\frac{k_s - k_f}{3}} + \frac{(1-r)\frac{b}{l}}{k_f + \frac{2b}{3l}(k_s - k_f)} + \frac{\frac{\sqrt{3}}{2} - \frac{b}{l}}{k_f + \frac{4r}{3\sqrt{3}}\left(\frac{b}{l}\right)(k_s - k_f)} \right) \right) \tag{2-9}$$

Lu (1999) numerically studied the heat transfer efficiency of metal honeycombs. He demonstrated that heat transfer performance would be further improved if a honeycomb heat sink were to be designed for turbulent flow, although flow-induced noise may become significant. His results were of relevance to thermal management applications in high power electronics where compact and highly efficient heat dissipation media were required.

Noting the influence of the structure on the thermal conductivity of the metal foam matrix based on the work of Calmidi and Mahajan (1999), Boomsma and Poulikakos (2001) developed a geometrical effective thermal conductivity model of a saturated porous metal foam based on the idealised three-dimensional basic cell geometry of a foam with a tetrakaidecahedron structure. It was shown that changing the fluid conductivity has a relatively small effect on increasing the effective thermal conductivity. For an aluminium foam (k_s = 218 W/m·K) with 95% porosity in vacuum, the three-dimensional model predicted k_{eff} to be 3.82 W/m·K. Using air as the saturated fluid increased the thermal conductivity to 3.85 W/m·K, and water (k_f = 0.613 W/m·K) increased the thermal conductivity to 4.69 W/m·K. It showed that despite the high porosity of the foam, the thermal conductivity of the solid phase controls the overall effective thermal conductivity to a large extent, a fact that must be dealt with in the foam manufacturing process if specific ranges of the foam effective conductivity were desired. To obtain the equation for the effective thermal conductivity of open-cell metal foam, Bhattacharya *et al.* (2001) presented comprehensive analytical and experimental investigations on the determination of the effective thermal conductivity for high porosity metal foam. A series of equations were developed to represent the thermal conductivities in different layers. For the case of very large geometric parameter, i.e. the half thickness of the fibre is much larger than the radius of circular intersection of metal foam, the effective thermal conductivity k_{eff} can be expressed as

$$k_{eff} = \left(\frac{2}{\sqrt{3}} \left(\frac{\frac{r_m}{l}}{k_f + \frac{(k_s - k_f)}{3}} + \frac{\frac{\sqrt{3}}{2} - \frac{r_m}{l}}{k_f} \right) \right)^{-1} \tag{2-10}$$

where L is the half length of fibre, k_f and k_s are the thermal conductivities for solid and

fluid phases, respectively.

Due to the enhanced heat transfer in metal foam, some applications of using metal foams as heat sinks and heat exchangers were investigated. Bhattacharya and Mahajan (2002) designed a finned metal foam heat sink with 5 PPI and 20 PPI pore density for electronics cooling in forced convection. Their results indicated that the 5 PPI samples resulted in higher heat transfer coefficients compared to the 20 PPI samples for a given pressure drop or fan power. Based on the experimental data, an empirical correlation for Nusselt number in terms of Peclet number and dimensionless ratio of hydraulic diameter to pore diameter was obtained as

$$\mathrm{Nu} = 6.43\mathrm{Pe}_K^{3/5}\left(\frac{d_h}{d_p}\right)^{-2/3} \tag{2-11}$$

where Pe_K is the effective permeability based Peclet number, d_h and d_p are the hydraulic diameter and diameter of pore, respectively. The correlation equation showed that when d_h increases or equivalently the number of fins decreases, the heat transfer coefficient decreases. The thermal enhancement effects due to conduction and extended surface area of the fins are small. On the other hand, when d_p increases or equivalently, PPI decreases, the heat transfer coefficient decreases. A generalised Nusselt number formulation for the finned metal foam was also proposed which incorporated the effects of thermal dispersion and interfacial heat transfer between the solid and fluid phases. Boomsma *et al.* (2003b) experimentally studied the metal foam as a compact heat exchanger and compared its performance with a traditional heat exchanger. Their results showed that the compressed open-cell aluminium foam heat exchangers generated thermal resistances that were two to three times lower than the best commercially available heat exchanger tested. Zhao *et al.* (2004) studied the thermal radiation in ultralight metal foam with open cells for the high temperature

applications, such as such as the porous radiant burner and acoustic liner in combustors. They measured the effective thermal conductivity of one type of high temperature metal foam, FeCrAlY (Fe 73%, Cr 20%, Al 5%, Y 2%) foams, as a function of temperature in the range of 300–800 K under both atmospheric and vacuum conditions. The overall effect of thermal radiation on the whole thermal transport process (conduction, radiation and natural convection) for FeCrAlY foams having different cell sizes and porosities was quantified. Their results showed that the contribution of radiative transfer increases significantly with increasing temperature, accounting for up to 50% of the effective foam conductivity. Hsieh *et al.* (2004) performed an experimental investigation of heat transfer characteristics of aluminium-foam heat sinks. In their work, the effects of porosity, pore density and flow velocity on the heat transfer characteristics were studied, and the phenomenon of LTNE was also observed and reported. The deduced temperature difference between the solid and fluid phases clearly indicated the existence of non-local thermal equilibrium conditions within the heat sink. The increase of the porosity and the pore density enhances the LTNE phenomenon.

2.3 Oscillating Flow in Porous Media

Oscillating flow has been studied by many investigators due to the two thermal entrance regions and reversed flow direction characteristics. The velocity distribution, frictional loss of oscillatory boundary layer and the associated heat transfer characteristics were investigated diffusely.

2.3.1 Flow Behaviour

Early studies of oscillating flow behaviour were conducted by Womersley (1955) and Uchida (1956) for an empty channel or tube. The features of pressure drop for

oscillating flow are of crucial importance for designing cryocoolers or regenerators with inserted porous media (woven-screens). Some research were performed on oscillating flow through a channel inserted with particles and woven-screens by both analytical and experimental methods. Rix (1984) found that the pressure drop in Stirling machine subjected to oscillating flow could be predicted accurately if the friction coefficient provided by Tong and London (1957) was adjusted to be a constant value of 3.5. Roach and Bell (1988) performed experiments to obtain the pressure drop in a packed column under rapidly reversing flow conditions, and noted that higher friction factor was obtained by oscillatory flow. Tanaka *et al.* (1990) experimentally investigated the fluid flow in wire-screens and sponge metals under the condition of an oscillating flow. They obtained an empirical equation for the friction factor in terms of the hydraulic wire diameter based Reynolds number. However, their results were obtained by a single flow displacement, and the effects of oscillatory frequency were not counted. Khodadadi (1991) treated analytically the problem of oscillating flow through a porous medium channel bounded by two impermeable parallel plates with the assumption of negligible inertia effects. His results showed that the oscillatory flow in porous media was dependent on the porous medium shape parameter and Stokes number. When a highly viscous fluid undergoes slow pulsation in a porous medium with high porosity, the phase lag vanishes and similar velocity profiles in the same phase with that of the pressure gradient wave were observed.

To obtain the appropriate governing parameters for the oscillatory pressure drop through a packed channel, Zhao and Cheng (1996b) experimentally investigated pressure drop characteristics in a packed column which consisted of three different sizes of woven-screens subjected to a periodically reversing flow of air. They showed

that the oscillatory pressure drop factor increases with the maximum fluid displacement and the oscillation frequency. The correlation equation obtained by Zhao and Cheng (1996b) indicated that the friction factor of oscillating flow in woven-screens is governed by the kinetic Reynolds number and the dimensionless flow amplitude. In addition, Zhao and Cheng (1996c) investigated experimentally the transition to turbulence of an oscillatory air flow in a pipe and a correlation equation was obtained for the prediction of the onset of turbulence. Ju *et al.* (1998) studied the oscillating pressure drops and phase shift characteristics for regenerators filled with wire-screens under high frequency oscillation. They obtained values for the cycle-averaged pressure drop in the oscillating flow across the regenerator which were two to three times higher than these of steady flow at the same Reynolds numbers. Wakeland and Keolian (2003) reported the pressure losses across single screens subjected to low-frequency oscillating flow for $0.002 < Re < 400$, where Re is the Reynolds number based on wire diameter and peak approach velocity. The friction factor was found to depend on Reynolds number, but not on the oscillatory amplitude, over the range of conditions measured.

As a novel type of porous media, the metal foam opens itself to many applications as mentioned in Chapter One due to the shaped open cells, fully inter-connected and reticulated structures. However, existing investigations of flow characteristics in open-cell metal foam were confined to conditions of steady or uni-directional flows. Kim *et al.* (2001) studied forced convection through an aluminium foam and noted that the inertia coefficient of the metal foam is a function of friction factor for steady flow through the channel. Boomsma and Poulikakos (2002) investigated the characteristics of water flow through aluminium foams with different compression and pore sizes. Their results revealed that the permeability and the form coefficient

accurately described the pressure drop versus flow velocity behaviour in porous media. Ko and Anand (2003) investigated forced convection in a rectangular channel inserted with metal foam baffles. Their results showed that the friction factor decreased slightly with an increase in the Reynolds number and increased with baffle thickness and pore density. Boomsma *et al.* (2003a) numerically studied the steady flow through open-cell metal foams using a new approach based on a fundamental periodic unit of eight cells. Their results of pressure drop for the flow through the cellular unit were compared on a length-normalised basis against experimental data. They postulated that the discrepancy between the two sets of data may be caused by the lack of pressure drop-increasing wall effects in their simulations.

The above investigations of fluid flow in metal foam were limited to the condition of steady flow. Due to the particular structure for open-cell metal foam, the results obtained for oscillating flow in woven-screens may not apply to metal foams. To the best of the author's knowledge, there is no published work which studied oscillating flow characteristics in metal foam. The problem of flow behaviour in open-cell metal foam subjected to oscillating flow remains open.

2.3.2 Heat Transfer Characteristics

For modern high-speed microprocessors, the reliability of transistors and operating speed are not only influenced by the average temperature but also by temperature uniformity on the substrate surface. As reported by Hwang and Chao (1994), over 50°C temperature difference between the inlet and the hottest location of a porous channel was reached for the case of q = 3.2 W/cm^2 in their experiments. This indicates that steady flow through a porous channel heat sink still yield a relatively high local substrate temperature. Heat transfer in oscillating flow can be considered as an effective method to obtain uniform temperature with two thermal entrance region

due to the reversed flow direction of oscillating flow.

Heat transfer characteristics of oscillating flow were initially studied for in an empty channel or tube. Numerous studies have been devoted to pulsating and reciprocating flows and their associated heat transfer problems during the past few decades (Kurzweg, 1985; Gedeon, 1986; Siegel, 1987; Walsh *et al.*, 1993; Cooper *et al.*, 1994; Zhao and Cheng, 1995, 1998a, 1998b). Kurzweg (1985) and Gedeon (1986) analysed the enhancement of axial heat transfer in an oscillatory flow between two parallel plates. Siegel (1987) obtained an analytical solution for heat transfer of a pulsating flow in a channel with uniform heat flux. Walsh *et al.* (1993) experimentally investigated forced convection cooling in micro-electronic cabinets by oscillatory flow techniques. Cooper *et al.* (1994) experimentally investigated convective heat transfer from a heated floor section of a rectangular duct to a low frequency and large tidal displacement oscillatory flow. Phase correlated oscillatory flow velocity and temperature profiles were presented. A non-dimensional correlation based on a new correlation parameter was obtained for the oscillatory-flow Nusselt number. Zhao and Cheng (1995, 1998a) presented a numerical solution for laminar forced convection of an incompressible periodically reversing flow in a pipe of finite length at constant wall temperature. They found that the four parameters that govern the heat transfer characteristics for the problem under consideration are the kinetic Reynolds number Re_ω the dimensionless oscillation amplitude A_0, the length to diameter ratio L/D, and the Prandtl number of the fluid. A thorough review of heat transfer in oscillating flow through an empty channel was presented by Zhao and Cheng (1998b).

In addition, Tong and Sirignano (1987, 1989) studied the effect of oscillating gas pressure and velocity on the droplet vaporisation rate based on a complex droplet vaporisation model. Oscillation in the rates of vaporisation of an array of repetitively

injected droplet in the combustor was obtained from the summation of individual droplet histories. The nonlinear in-phase frequency response of the entire vaporisation process to pressure oscillations was calculated and the results indicated that spray vaporisation can provide the driving force in combustion instability.

Driven by the heat transfer enhancement of using oscillating flow, heat transfer performance of porous media under the condition of oscillating flow had gained more attention. Vafai and Sozen (1990b) conducted a numerical study of compressible flow through a packed bed. The effect of oscillating boundary conditions on the transport phenomena was investigated with the packed wall insulated. Tanaka *et al.* (1990) determined the heat transfer coefficient between solid and fluid phases using the concept of number of heat transfer units. The heat transfer coefficient was found to be lower than that in uni-directional flow through porous media. Sozen and Vafai (1990) numerically analysed the forced convection flow through a packed bed under oscillating compressible flow. Oscillating gas phase temperature, pressure and inlet boundary conditions were considered. The effect of oscillating boundary conditions on the transport phenomena in the packed bed was investigated and comparisons were made under constant-temperature and constant-pressure boundary conditions. The average energy storage characteristics were found to be very close in both oscillating and constant inlet boundary conditions. Yuan and Dybbs (1992) reported higher heat transfer coefficient of oscillating flow than that of steady flow. The significant influence of frequency effect on the heat transfer coefficient was also reported. Kim *et al.* (1994) numerically studied the heat transfer between the channel wall and the fluid of a porous channel subjected to pulsating flow. In their computation, local thermal equilibrium was assumed which led to the one-energy-equation model. Their results showed that when the Darcy number is large, velocity profiles at low frequency are

akin to quasi-steady flows in a non-porous channel, and for high frequency, only a narrow portion very close to the wall is affected. Fedorov and Viskanta (1997) studied numerically heat transfer in an electronic package formed by embedded discrete sources in contact with a porous heat sink. They pointed out that the local thermal equilibrium assumption is questionable due to the obvious temperature difference between the solid and the fluid phases.

An investigation by Paek *et al.* (1999) on the transient cool-down of a porous medium in pulsating flow portrayed the heat transfer characteristics of a pulsating flow which is different from an oscillating flow through a porous material. Temperature histories inside the porous medium indicated that the global heat transfer characteristics are affected negligibly by the introduction of flow pulsation for small amplitudes, i.e. non-reversed flow. Jue (2000) presented an investigation of oscillating flow in a rectangular cavity filled with porous medium. The thermal convection in a fluid-saturated porous medium was analysed to explore the difference of flow field and heat transfer characteristics for a series of fluid parameters including Grashof number, Reynolds number, porosity and Darcy number. The numerical data provided a systematic understanding of unsteady, oscillatory cavity flow and heat transfer phenomena in a porous medium. The physical domain considered in this study was a two-dimensional rectangular cavity with aspect ratio of the fluid was Newtonian and the flow was laminar and incompressible. The results provided the effect of different porous medium properties on fluid flow and heat transfer. The porous medium was found to diminish the flow heat flux variation. In addition, the flow restriction retarded the stable stratification effect caused by the temperature gradient from the top surface and resulted in a convex temperature distribution in porous medium. Fu *et al.* (2000b, 2001) investigated the heat transfer of a channel filled with materials of

aluminium and RVC foam materials of different pore densities (PPI) and reticulated vitreous carbon of 45 PPI subjected to oscillating flow. Leong (2003) experimentally studied the forced convection in metal foams subjected to oscillating flow. His results showed that the length-averaged Nusselt number for oscillating flow is higher than that for steady flow, and that the temperature distribution for oscillating flow is more uniform than that for steady flow. He concluded that the metal foam heat sink in oscillating flow can be considered as an effective method for electronics cooling.

2.4 Summary

As a summary of the literature review, fluid flow and heat transfer problems were investigated extensively in various kinds of porous media. It is generally recognised that heat transfer can be enhanced substantially by implementation of a highly conductive porous medium. Oscillating flow through porous media can be applied as an effective heat removal method which can provide a uniform temperature distribution on the substrate surface for electronic package. However, published results for open-cell metal foam, which possesses a totally different structure from other porous media subjected to oscillating flow are rather scarce. The above review shows that studies of heat transfer in oscillating flow were focused mainly on channels filled with particles or wire-screens. Published research of fluid flow behaviour in metal foams were limited to the conditions of steady and uni-directional flows. Driven by the motivation of applying oscillating flow forced through metal foam to cool high power electronic devices, forced convection of oscillating flow behaviour and heat transfer characteristics in open-cell metal foams are investigated in this study.

CHAPTER 3

EXPERIMENTAL SETUP AND PROCEDURES

3.1 Experimental Facility

3.1.1 Test Setup

To study the fluid flow behaviour and heat transfer characteristics of oscillating flow through an open-cell metal foam channel, the experimental facility has to possess the capability for providing oscillating flow with various flow displacements and frequencies. Figure 3-1 is the schematic diagram of the experimental facility. The present setup was modified from an existing experimental facility which was designed by a former research fellow (Fu, 2000a), as part of a research programme funded by the then National Science and Technology Board, Singapore. The original experimental setup was modified to perform experiments of oscillating flow with suitable ranges of flow displacement and frequency. As shown in Figure 3-1, the facility consists of four major parts: (1) oscillating flow generator, (2) test section, (3) velocity measurement section and (4) coolers. Aluminium foams 10, 20 and 40 PPI are inserted into the test section as porous media and air is used as coolant. It can be seen that the oscillatory flow provided by the oscillating flow generator is forced periodically through the metal foam test section, and the heat generated by the film heater is carried by the oscillating flow and removed by the water coolers at the two ends of the test section.

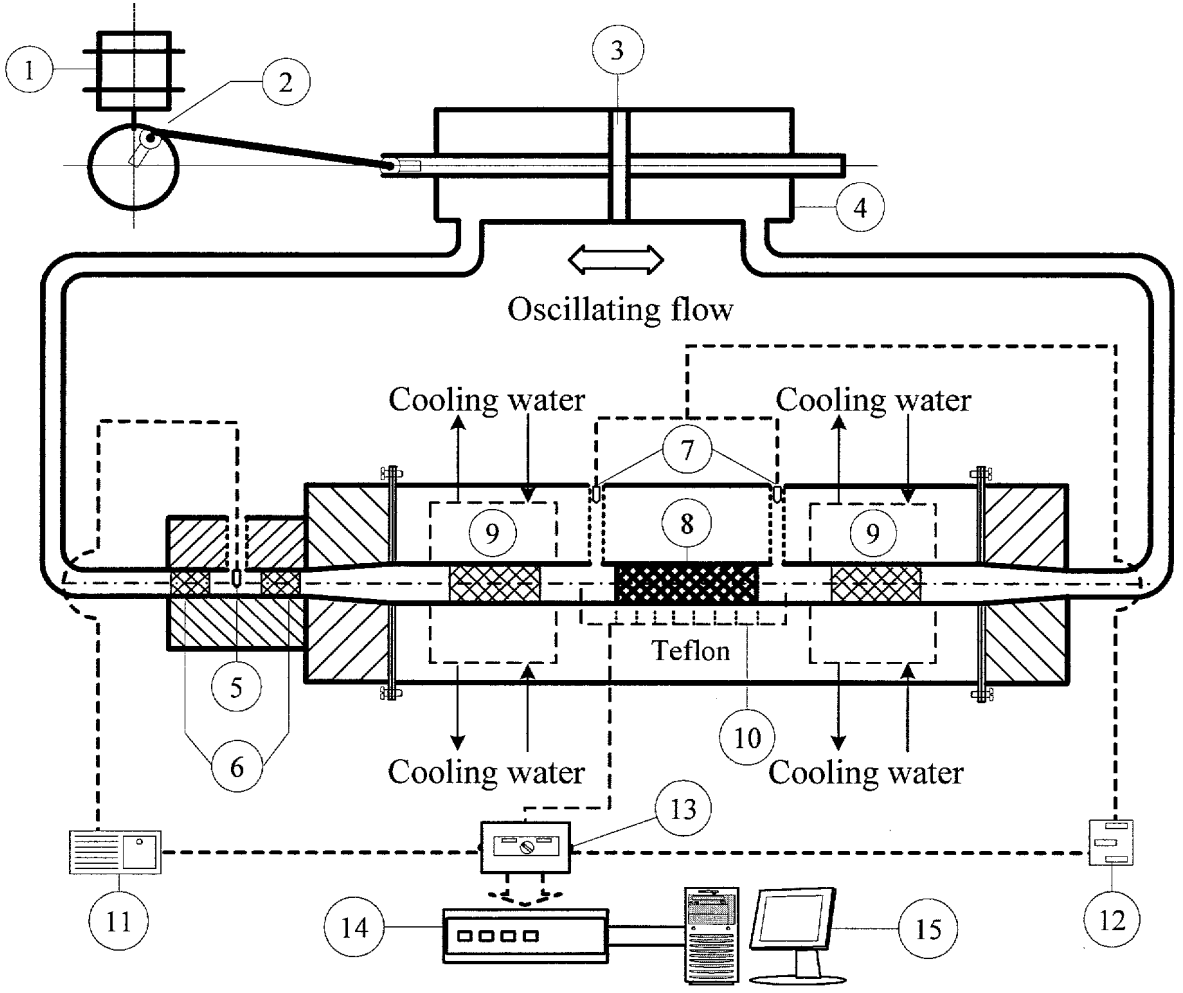

1. Motor
2. Crank shaft
3. Piston
4. Cylinder
5. Hot-wire
6. Mesh
7. Pressure sensor
8. Aluminium foam
9. Coolers
10. Thermocouples
11. Constant temperature anemometer
12. Pressure transducer
13. Voltage amplifier
14. Data acquisition card
15. Personal computer

Figure 3-1 Schematic diagram of experimental setup

3.1.1.1 Oscillating Flow Generator

The oscillating flow generator is a mechanism that generates a sinusoidal oscillatory flow. The mechanism consists of a compression cylinder, a piston and a crankshaft with adjustable stroke lengths. These are firmly fixed at the base onto a solid board by screw bolts to withstand vibrations caused by the oscillating motion of the generator. The supporting shafts are two ball bearings elevated to the height of the piston axis to ensure smooth oscillatory movement. The piston is connected to the crankshaft. The crankshaft is driven by a DC electric motor (LEESON 0.75kW) with variable speed capabilities. Figure 3-2 shows the main structure of moving components in the oscillating flow generator. By adjusting the motor speed and the stroke length, oscillating flows of different amplitudes and frequencies can be generated.

It was noted from preliminary experiments, a temperature-lift of the inlet flow (1 ~ 2^{o}C) was observed for high oscillatory frequency (> 10 Hz) due to the friction between the piston and cylinder. In this study, oscillating frequencies ranging approximately from 1 to 10 Hz were selected. A machined plate of 100-mm diameter with a narrow slot across the surface was attached to the motor shaft. Different oscillating amplitudes could be obtained by varying the distance of the crank from the plate centre along the slot. Different locations from the centre of the plate were selected and oscillating flows with maximum displacements of 52, 60 and 68 mm were provided.

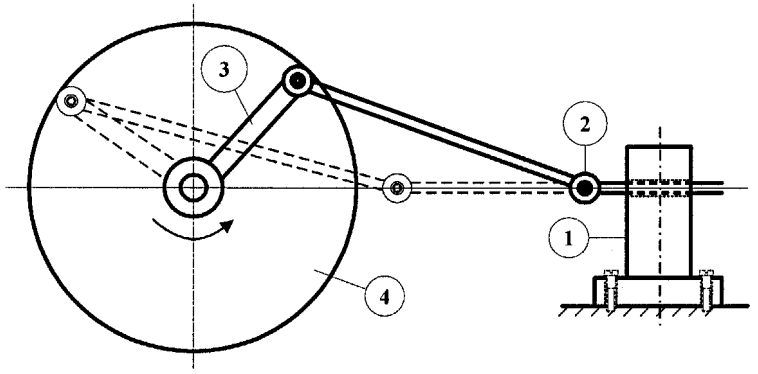

1. Bracket 2. Crankshaft 3. Narrow slot 4. Machined plate disc

Figure 3-2 Movement mechanism of the oscillating flow generator

3.1.1.2 Test Section

The test section is a well-shaped block of aluminium metal foam with dimensions of 50 × 50 × 10 mm. Figure 3-3 shows the cross sectional view of the test section. A film heater (60 mm × 60 mm × 10 mm) was firmly mounted on the bottom of channel to supply a constant heat flux, and a 1-mm height copper plate with eight narrow slots perpendicular to the flow direction was attached on the surface of film heater. The metal foam and copper plate were clamped tightly onto the surface of film heater by screws which secured the upper and bottom channels. In addition, highly conductive thermal grease (OMEGA OT-201) of thermal conductivity of 2.3 W/m·K was applied on the two sides of the copper plate as a filling material to distribute the heat evenly and to reduce the thermal contact resistances. This arrangement allows the thermal contact resistances to be neglected and the heat flux can be considered as uniform at the bottom section of the channel. A small hole in the Teflon material allowed the insertion of 10 thermocouples into the heated section. The copper plate was cleaned and eight thermocouples (24 a.w.g. K-type with wire diameter of 45 μm) were fixed into eight narrow slots. The response sensitivity of these thermocouples is up to 500 Hz which satisfied the requirements of the experiments. The dimensionless

locations of these thermocouples in terms of x/D_e (where $D_e = 5H / 3$ is the hydraulic diameter of the channel) are 0, 0.4284, 0.8568, 1.2858, 1.7142, 2.1456, 2.5716 and 3. The other two thermocouples were placed at the inlet and outlet to measure the bulk temperatures. The two taps of the pressure transducer (VALIDYNE DP15) are located before and after the test section for pressure drop measurements. By adjusting the supply voltage to the heater, which could be monitored through the display from a digital voltmeter and an ammeter, the desired input heat flux could be obtained. In the present experimental study, input power ranged from 20 to 60 W. The whole test section was made of Teflon material and the channel was well insulated.

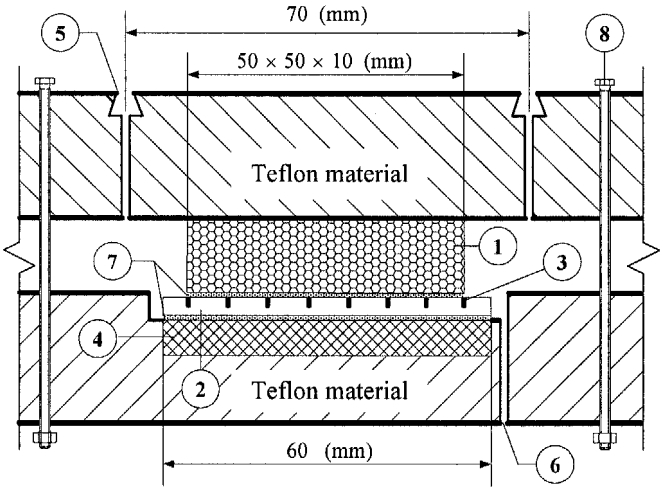

1. Aluminium foam 2. Copper plate 3. Thermocouples
4. Film heater 5. Pressure measuring tap 6. Thermocouples hole
7. Thermal grease 8. Screw

Figure 3-3 Cross sectional view of the test section

3.1.1.3 Velocity Measurement Section

As shown in Figure 3-4, the velocity measurement section consists of a column (made of aluminium) of 16 mm diameter. A hot wire sensor (TSI 1210-20w) was mounted at the centre of two parts that are packed with 40 mesh woven screen discs. The packed screen provides a uniform velocity profile. The velocity measured by this arrangement is approximately the same as the cross section averaged velocity through

the column due to the extremely thin velocity boundary layer of flow through the porous media. A constant temperature hot wire anemometer (TSI IFA-100) was used to measure the velocity at the velocity measurement section which was then converted to that through the test section. It is noted that the measured velocities will always be positive even though the velocity direction is reversed on every other half-cycle. This is because of the fact that the single hot-wire sensor cannot distinguish the flow direction. To reflect a correct velocity direction, the measured values of velocity were processed by reversing its sign on every other half-cycle.

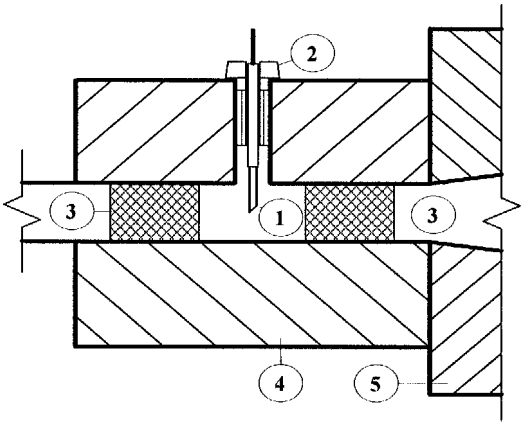

1. Single hot-wire 2. Retainer 3. Mesh
4. Aluminium block 5. Teflon material

Figure 3-4 Cross sectional view of the velocity measurement section

3.1.1.4 Coolers

The two unheated sections comprise the same porous material as the test section with the same dimensions. They were installed adjacent (but separated) to the two ends of the test section. Two pairs of the coolers were installed at the upper and bottom sections of the two unheated sections. As shown in Figure 3-5, the coolers are parts of the channel filled with 10 PPI aluminium foams. Cooling water was forced through the two coolers to remove the heat generated by the film heater. The heat carried by the flow was transferred to the surface of coolers through the unheated

porous material. The two unheated sections inserted with metal foam porous media at the two ends of the test section also build up a uniform velocity profile for flow through the test section.

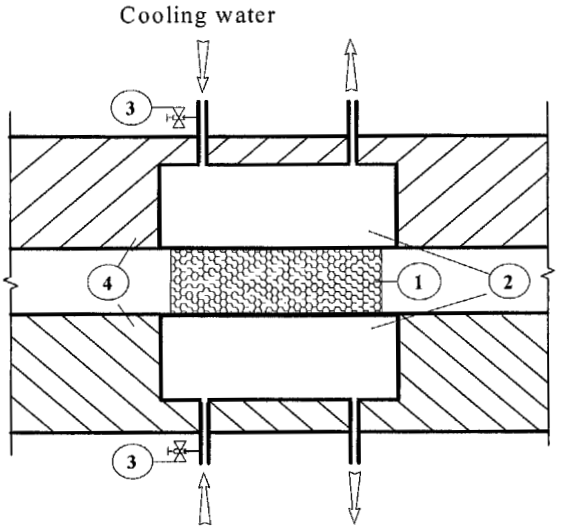

1. 10 PPI Metal foam 2. Mini water tank
3. Valve 4. Teflon material

Figure 3-5 Schematic diagram of the water cooling system

3.1.2 Measuring System

3.1.2.1 Measuring Sensors

Three types of measuring sensors, namely, thermocouple, pressure sensor and single hot-wire were used to measure temperature, pressure drop and flow velocity in the metal foam channel subjected to oscillating flow, respectively.

The local substrate surface temperatures at different locations along the axial directions in the test section, the air temperature at the inlet and outlet bulks of the test section as well as the ambient temperature, were measured in the present experiment. Eight thermocouples were arranged perpendicular to the airflow direction to measure temperature distribution. Attention was given to the placement of the thermocouples onto the copper plate. By clamping the channel tightly and filling the interface with

thermal grease, the temperatures of metal foam and fluid flow at the bottom of the channel are assumed to be same in the measurements. Two thermocouples were fixed between the test section and the unheated section to measure the inlet and outlet bulk temperatures. For temperature measurement, the response of the temperature sensor is critical. In the present experiments, K-type thermocouples which possess fast response capability with the error of ±0.4% for the full range were used. The ten thermocouples were calibrated together before use to measure wall surface temperature along the test section.

The pressure drop across the test section was measured by a differential pressure transducer VALIDYNE DP15. The DP15 is a differential pressure transducer that features field-replaceable sensing diaphragms so that the full scale may be changed anywhere between $\pm 5.5 \times 10^{-2}$ kPa and 2.2×10^{3} kPa. The rugged construction of the DP15 makes it highly resistant to shock and vibration. Because the diaphragm is the only moving part, the frequency response of the DP15 to pressure pulsations is exceptionally high. To obtain the standard analogue signal output, the DP15 pressure sensor was connected to the VALIDYNE CD15 by a four-conductor shielded cable. The CD15 is a carrier demodulator which supplies a 5 kHz excitation to the transducer and provides zero balance and span adjustments. The analogue output signal is available from the front panel on two binding posts. The standard output signal options of the CD15 include 4-20 mA and ±1 VDC with the accuracy of ±0.25% of full-scale.

In the present experiments, both steady and oscillating flow velocities need to be measured. For oscillating flow with relatively high frequency, a sensor with fast response to the transient velocity is needed. The velocity measuring system consists of a single hot-wire sensor (TSI 1213-20W) and a constant-temperature anemometer

(TSI IFA 100). The TSI 1213-20W hot-wire permits measurement of up to three mean velocity components with a single sensor by rotating the probe about its axis in the maximum ambient temperature of 150 °C. TSI IFA 100 is a high-performance, low-noise, constant-temperature anemometer. It can be used for measuring velocities in liquids or gases in applications with high-frequency response and high accuracy. Under the incompressible flow assumption made in this experimental study, the velocity through the test section can be obtained by measuring the velocity at the velocity measurement section. Detailed information of the measuring equipment and the photograph of the experimental facility can be found in Appendix A.

3.1.2.2 Data Acquisition System

The data measured by thermocouple, pressure transducer and hot-wire were monitored and acquired by a data acquisition system. The data acquisition system consists of a volt amplifier (KEITHLEY MB01), high-performance analogue and digital I/O boards (KEITHLEY DAS-1402) and an operating software (TESTPOINT 3.3) within a personal computer. The illumination diagram of the data acquisition system is shown in Figure 3-6. It is noted that the analogue signals of pressure drop and velocity were modulated to the acceptable input range of amplifier by the pressure carrier demodulator and the constant-temperature anemometer before transferring to the volt amplifier board into different channels. The amplified standard signals were input into the data acquisition card installed in a Pentium 3 personal computer by a 16 channel-cable.

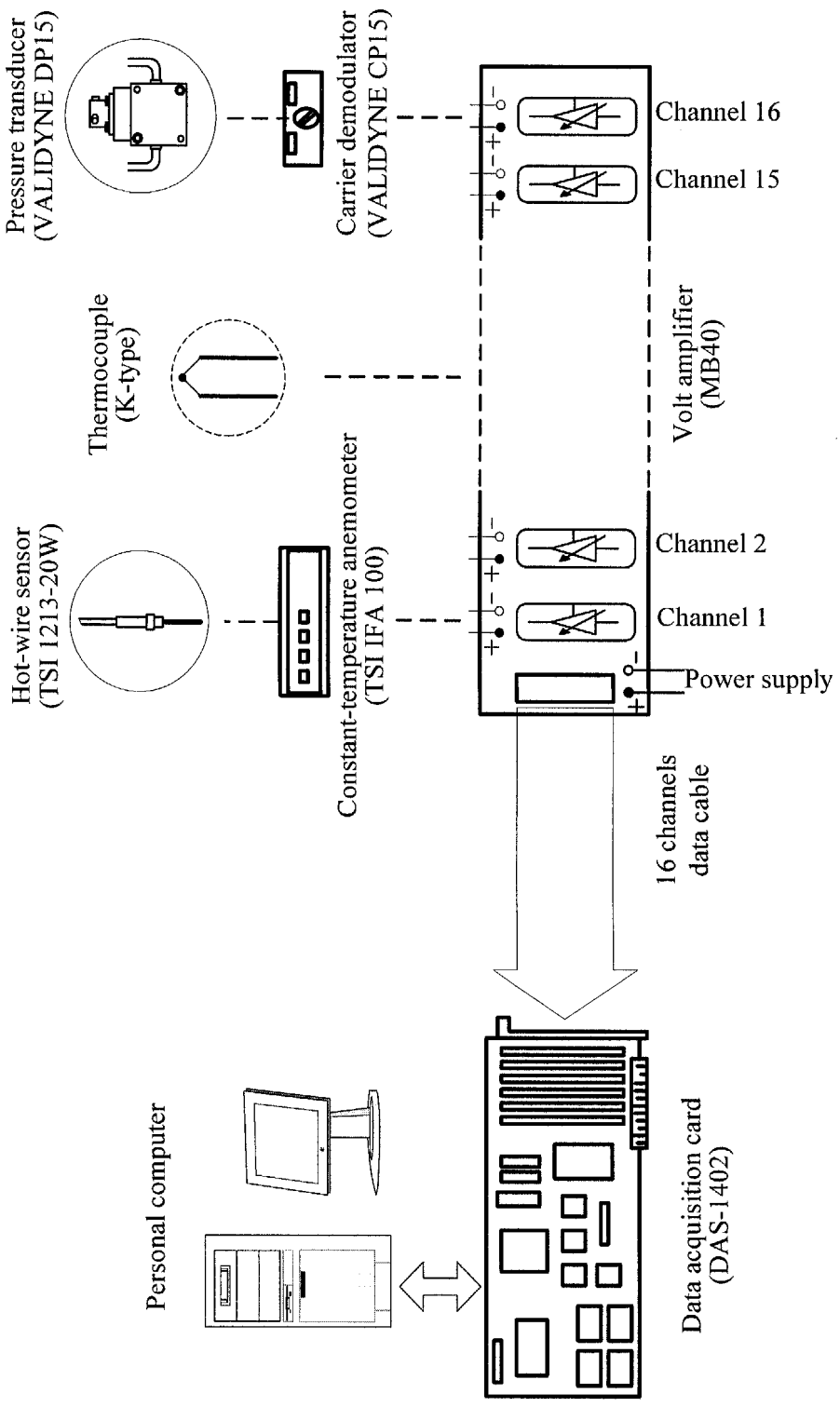

Figure 3-6 Data acquisition system for the temperature, velocity and pressure drop measurements.

The volt amplifier MB01 consists of sixteen MB40 wide bandwidth millivolt input modules, which accept ±5 mV to ±100 mV input signals and provide either a –5 V to +5 V or 0 to +5 V output. Each module features a 10 kHz bandwidth for every channel. A protection circuit assures safe operation even if a 240 V_{rms} power line is connected to the input. A one-pole anti-aliasing filter is located at the module's input, while a three-pole low-pass filter in the output stage sets the bandwidth and yields optimum noise performance. This amplifier operates on the input signal after subtraction of a stable, laser-trimmed voltage, which sets the zero-scale input value. Therefore, it is possible to suppress a zero-scale input that is many times the total span to provide precise expanded scale measurements. Signal isolation is provided by transformer coupling using a proprietary modulation technique for linear, stable performance. A demodulator on the output side of the signal transformer recovers the original signal, which is then filtered and buffered to provide a clean, low-impedance output. A single +5 V supply powers a clock oscillator that drives power transformers for the input and output circuits. It ensures that signals from the ten thermocouples, pressure transducer and constant temperature anemometer can be amplified accurately and acquired orderly by the data acquisition card.

The KEITHLEY DAS-1402 data acquisition board is switch-configurable for 16 single-ended analogue input channels. Analogue inputs are individually programmed for gain and are switch-configurable for either unipolar (0-10 V) or bipolar (±10 V) signals for every channel, which match exactly the output from the volt amplifier MB01. A three-channel counter/timer provides timing for analogue input operations or generation of output pulses at any rate from to 1 pulse/hour to 100 kHz. The option of acquisition rate covers sufficiently the range of the oscillatory frequency tested in the experiments (1-10 Hz). The frequency of the oscillating flow and the period of

pressure drop can be measured by this function under the control of software TESTPOINT. The interface of operating program for controlling data acquisition and output were shown in Figure 3-7. TESTPOINT provides high-speed control of D/A cards for control systems and generation and editing of arbitrary waveforms. It provides high-level A/D functions to simplify data acquisition. The properties of VBX (Visual Basic Extension) and OCX (OLE Control Extension) objects added to TESTPOINT are programmable. Any number of objects can be used in any order, individually or combined with other objects to create user defined objects. In the present experiments, the data monitoring and operating functions were programmed by VBX and OCX objects integrated in the TESTPOINT, and the data acquisition rates were set to match the different oscillating flow frequencies.

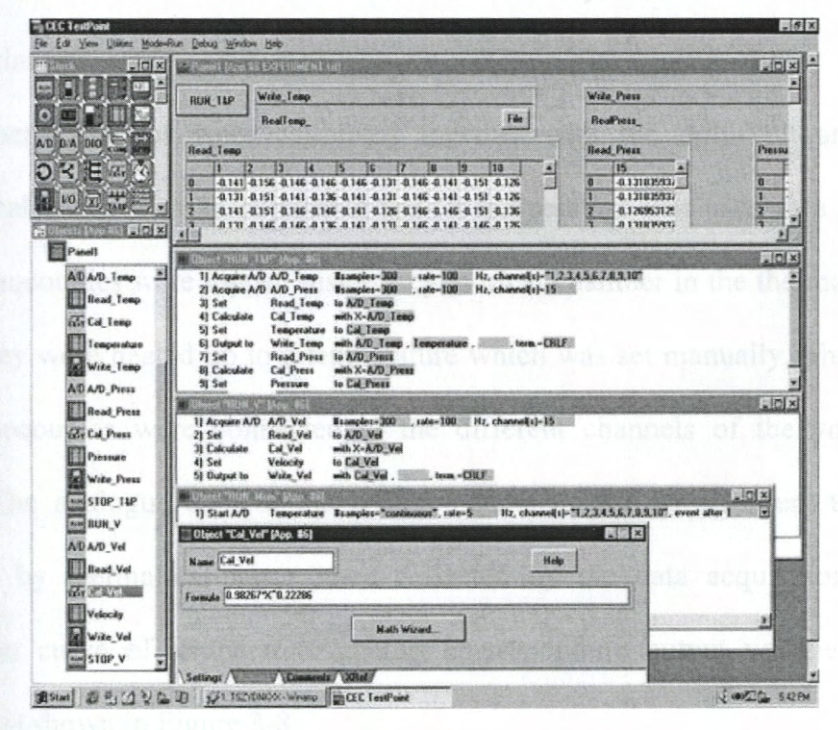

Figure 3-7 Interface of control programme TESTPOINT

3.2 Procedures and Data Reduction

Various procedures were employed to study the oscillating flow behaviour and heat transfer characteristics in a channel filled with open-cell metal foams. The experimental data for temperature, pressure drop and velocity were reduced based on the cycle-time averaging methods due to the appearance of periodicity factor in oscillating flow. The uncertainties of the measured and calculated quantities were analysed using the method introduced by Taylor (1997).

3.2.1 Experimental Procedures

3.2.1.1 Calibration of Sensors

To obtain accurate data of the temperature, pressure drop and velocity for oscillating flow through the channel filled with metal foam, the thermocouples, pressure sensor and hot-wire were calibrated carefully before the commencement of the experiments.

Ten thermocouples were calibrated together with the mini-volt amplifiers. A thermal-calibrator with an adjustable pre-set temperature was used as a heat source. All thermocouples were dipped inside a cylindrical chamber in the thermal-calibrator, where they were heated up to a temperature which was set manually. The other ends of thermocouples were connected to the different channels of the volt amplifier MB01. The analogue data of the enlarged voltages for the different temperatures provided by thermal-calibrator were collected by the data acquisition card. The calibration curve of temperature against corresponding output voltage and fitting equation is shown in Figure 3-8.

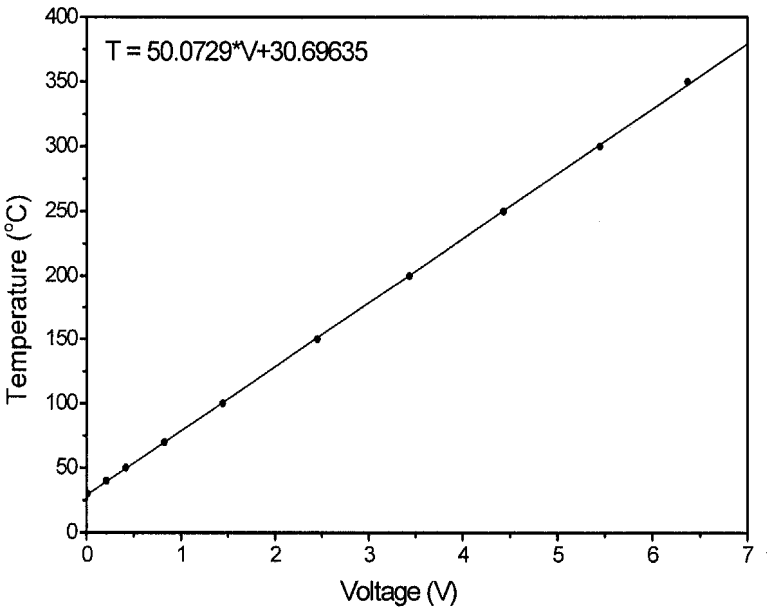

Figure 3-8 Calibration curve of thermocouple

The pressure transducer was calibrated with an inclined manometer. During calibration, the manometer was set at the "Top Inclined" position, with a scale multiplier of 0.2. The liquid level was adjusted to 0 kN/m^2 to eliminate any offset under the condition that the tube was in the horizontal position. Initial pressure readings were obtained based on the pressure difference across the test section. A pressure source (supplied by a compressor) with an adjustable pressure valve was used to obtain stable and accurate data. The transducer was connected to the main line of the pressure source for the bleeding process to take place. The output voltage was displayed on the virtual control panel created using TESTPOINT previously. By slowly turning the valve (to allow for different air flow rates, and thus pressure) and adjusting the Zero & Span Control, a full scale pressure of 500 Pa was applied for a 5 VDC output from the demodulator which corresponded to the maximum sensitivity available from the connected transducer. The input pressure was gradually reduced to zero and the zero setting of the demodulator was rechecked and locked. Voltage from

the Demodulator and the corrected manometer's pressure reading were carefully recorded to facilitate the plotting of the calibration curve. A calibration curve of pressure against corresponding output voltage and the fitting equation is shown in Figure 3-9.

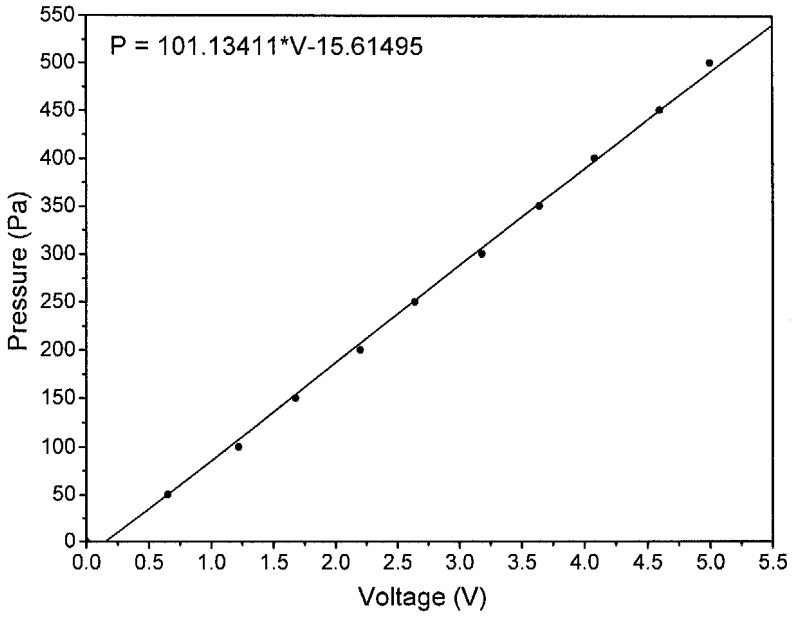

Figure 3-9 Calibration curve of pressure sensor

The velocity calibration equipment consists of three parts: the Hot Wire Sensor, TSI 1126 Air Velocity Calibrator and TSI 100 Anemometer. The TSI 1126 is manually operated and is able to generate a wide range of turbulent air velocity values. These velocities can be determined by measuring differential pressures across nozzles in the calibrator. To assemble the calibrator, the filter/regulator assembly, which includes a pressure regulator, valve, filter, hose and fittings, was attached to the main line of air supply. The rubber hose was connected to the inlet of the calibrator to generate air of various velocities, and the hot-wire probe was attached to the top of the flow-settling chamber and was carefully oriented. The voltage output of the anemometer and the pressure drop across the nozzle were measured first. Figure 3-10 shows the curve of the voltage output with the pressure drop of the nozzle.

The relationship between the corrected velocity and pressure drop can be calculated by

$$u = \sqrt{\frac{2(P_1 - P_S)}{\rho_f}} \tag{3-1}$$

where u is the corrected velocity, ρ_f is the density of the air and $\Delta P = P_1 - P_S$ is the pressure drop between exit nozzle and atmosphere. As shown in Figure 3-11, the calibrating curve of relationship between the corrected velocity and the voltage output can be obtained by using Equation (3-1).

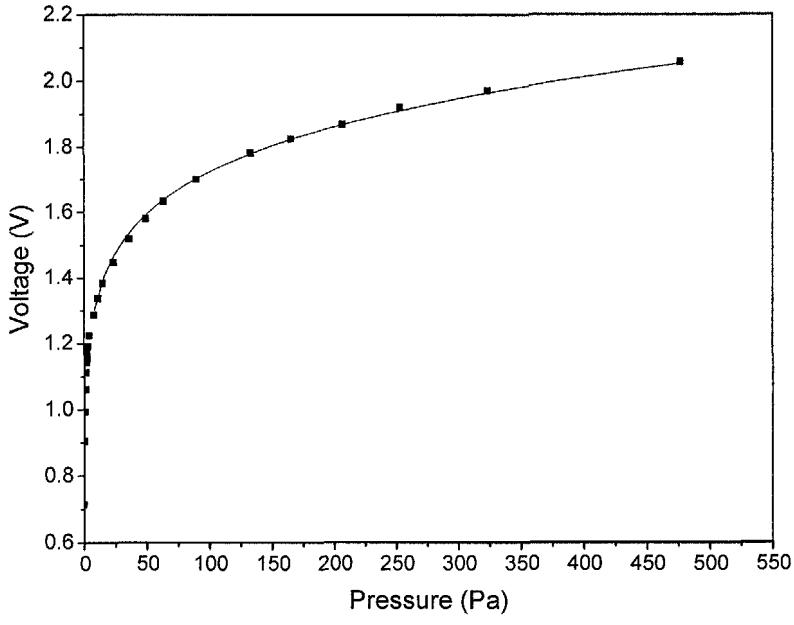

Figure 3-10 Output voltages versus pressure drop across nozzle

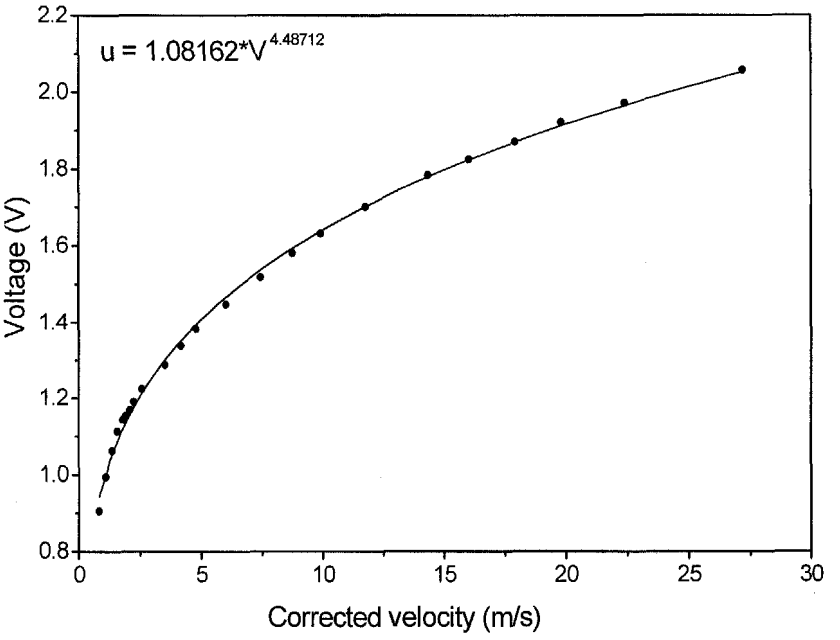

Figure 3-11 Output voltage versus corrected velocity

3.2.1.2 Procedures

To investigate the flow behaviour and heat transfer characteristics in metal foam channel subjected to oscillating flow, a series of the experiments were conducted using different procedures. For every experimental procedure, the DAS 1402 data acquisition board and operating software TESTPOINT were used to collect data for temperatures, velocity and pressure drop in test section.

To study the oscillating flow behaviour in a channel filled with metal foam, the velocity and pressure drop across the test section were measured under the unheated condition. The oscillatory frequencies were adjusted by changing the motor speed and frequencies from 1 to 10 Hz were tested. The experiments were performed by increasing the oscillatory frequency while keeping the maximum flow displacement unchanged. After a set of readings had been recorded, the distance of the crank from the plate centre along the slot was changed to commence another experiment of oscillating flow through porous channel with a different flow amplitude. Different

oscillating flow amplitudes were obtained by varying the distance of the crank from the plate centre along the slot and the maximum flow displacements of 52, 60 and 68 mm were selected.

The oscillating flow facility is also capable of performing steady flow experiments. By leaving one end of the test section open to the atmosphere, experiments of steady flow through metal foam channel can be conducted through an auto-balance compressor with the same test section configuration and sensors. In the steady flow experiments, compressed air from a mains supply was connected to the facility and a flow regulator and a valve were installed to adjust the flow velocity through the test section. The experiments of steady flow were controlled by adjusting the valve installed on the main line of the compressed air supply. The data for both oscillating and steady flows were monitored and recorded by the same data acquisition system.

The experiments of heat transfer in metal foam under the oscillating flow condition were proceeded by increasing the power input while keeping the oscillating frequency unchanged for a fixed flow amplitude. To obtain a cyclic steady state, the temperatures on the substrate surface were monitored by the data acquisition system. 100 cycles of data were obtained under different sampling rates by adjusting the acquired A/D rate for different oscillating frequency. When a set of reading had been recorded, the test apparatus had to be cooled down to temperature of ambient about 25°C before the next set of experiments can be started. In the present experiments, the flow velocity through the test section, the pressure drop across the test section and the temperature distribution along the axial direction on the substrate surface were measured.

3.2.2 Uncertainty

For electronic cooling applications, time-averaged characteristics are of practical

interest instead of instantaneous quantities. As mentioned earlier, instantaneous higher power dissipation may not damage the electronic components, but a long-lasting higher temperature will decrease their performance or even damage them. Therefore, to minimise the data reduction uncertainty, the cycle-averaged method was employed to reduce the present experimental data over 100 complete cycles. The heat losses through the insulation were determined for different surface temperatures under the condition of no air flow through the test section. The net heat inputs were obtained by subtracting the heat losses from gross heat inputs at the corresponding temperature. By calculating the air enthalpy rise along the test section, the error of energy balance was found to be within 6 percent.

The uncertainties of the measured data can be classified into two groups: random uncertainties, which can be treated statistically; and systematic uncertainties, which cannot be treated in the same way. With careful experimentation, systematic uncertainty was minimised. The accuracies of the thermocouple temperature and pressure transducer readings are within ±0.1°C and ±0.25% of full-scale, respectively. The accuracy of the velocity measured by the hot-wire anemometer is ±0.01 m/s. After the cycle-averaging process, uncertainties of temperature, velocity and pressure are 3.0 percent, 2.0 percent and 2.0 percent, respectively. The uncertainties of the measured quantities are estimated based on the measurement accuracy. Based on the assumption that the uncertainties of the measured data are independent and random with normal distribution, the uncertainties of the calculated parameters are determined by the method described by Taylor (1997). The uncertainties of the important parameters such as f_{max}, Nu_x and Nu_{avg} are calculated to be 9.7%, 5.7% and 8.9%, respectively. Details of the uncertainty calculation are given in Appendix B.

3.3 Duocel Open-cell Aluminium Foam

3.3.1 Solid Skeleton Processing

The tested porous media in the present experiments are called Duocel metal foams. Duocel is the descriptive name given to a wide range of open-celled foam materials produced by ERG Materials and Aerospace Corporation. Duocel open-cell aluminium foam has true metal skeletal structure. Its purity is typically that of the parent alloy metal with no voids, inclusions or entrapments. The skeletal structure of open-cell metal foam is manufactured by directional solidification of metal from a super-heated liquidus state in an environment of overpressures and high vacuum (Banhart, 2001). The metallic melts are formed by a casting technique and a wide range of sizes of great uniformity can be obtained. This method is called infiltration, where some sort of solid mould of pore shapes is made and then molten metal is poured followed by removal of the mould. An open cell polymer template with the desired cell size and relative density is used. This is then coated with a mould-casting slurry (ceramic powder, plaster or plastics foam), which is then dried and embedded in sand. The mould is then baked to harden the casting material and to decompose the polymer template. Subsequently, the mould is filled with a metal alloy and allowed to cool. After cooling, the mould materials are removed leaving the metal foam equivalent to the original polymer foam. As compared to other metal porous media, open-cell aluminium foam is a rigid, highly porous and permeable structure and has a controlled density of metal per unit volume. The solid-metal ligaments routinely test to 99 percent purity of the parent alloy, are not porous, and approximate single-strand drawn wire.

The Duocel aluminium foam can be cut, turned, ground, drilled, rolled and finished with normal tolerances. Through forming, a metal foam can easily conform to

complex shapes. Any bonding technique that can be used for the parent metal can be used for Duocel metal foam. It can be vacuum- or dip-brazed, epoxied, or adhesion bonded. Unlike other similar porous materials, open-cell metal foam can be brazed to metals, forming an integral metal-to-metal bond. This property allows open-cell metal foams to have good performance in the application of heat sink due to the flexible processing, which can provide the required shape and high thermal conductivity by brazing different metal.

The specific physical characteristics and structures of open-cell metal foam open itself to many applications, such as heat sinks for electronic components, cryogenic heat exchanger, heat shielding for aircraft exhaust, containment matrix and burn rate enhancer for solid propellants, compact heat exchangers, gas diffusers for semiconductor etch and deposition equipment, energy absorber for blast shock wave, regenerator for thermal engines, flow straightener in wind tunnels and air cooled condenser-cooling towers.

Density and cell size of metal foam are expressed as pores per linear inch (PPI) and can be varied independently to match the properties of the material to meet specific design requirements. Density is continuously variable from 3 percent to 12 percent and cell size can be 5, 10, 20, or 40 PPI. In the present study, the middle density of 8% and the pore size of 10, 20 and 40 PPI were used as the tested materials to study the fluid flow and heat transfer in a porous channel subjected to the oscillating flow.

3.3.2 Polyhedron Pore Structure

Using the infiltration casting technique, the resulting porous material has a reticulated structure of open, duo-decahedron-shaped cells connected by continuous, solid metal ligaments. The matrix of cells and ligaments is completely repeatable, regular, and uniform throughout the entirety of the material. Figure 3-12 shows the

open-cell aluminium foam with the pore density of 10, 20 and 40 PPI which were tested in the present experiments. It can be seen that the pore size and the ligament diameter decrease with the increase of the pore density. However, there is no general relationship between the pore density and the porosity due to the complex structure in the open-cell metal foam (Boomsma *et al.*, 2003a).

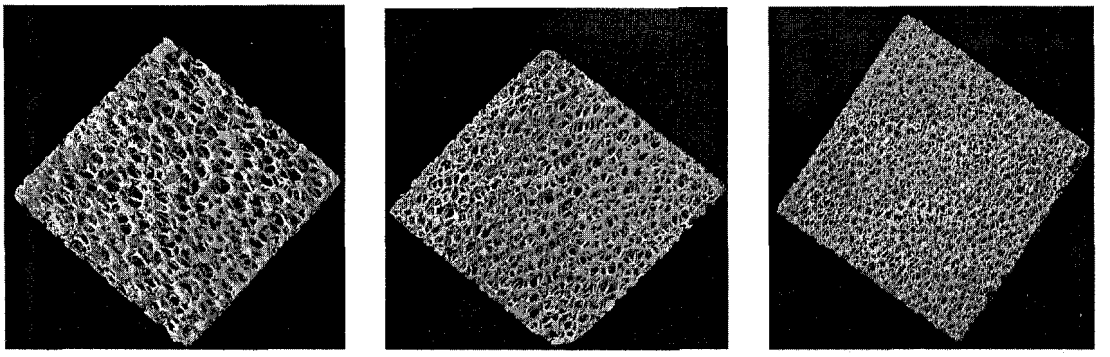

Figure 3-12 Open-cell aluminium foams of 10, 20 and 40 PPI

Figure 3-13 shows a closed-up view of the pore structure of the open-cell aluminium foam. The foam has a reticulated structure of open, shaped cells connected by continuous solid metal ligaments. A closer view at a typical single cell of open-cell metal foam shows that the cell has the approximate shape of a tetrakaidecahedron. The cells inside the metal foam are generally 12 to 14 sided polyhedral whose pentagonal or hexagonal faces are open to one another and there is a lumping of material at joints where the ligaments meet. The fully inter-connected pore and ligament structures provide the extreme large fluid-to-solid contact surface area, and intervein the tortuous coolant flow path inside the metal foam, which could increase dramatically the overall heat transfer rate of fluid flowing through metal foam.

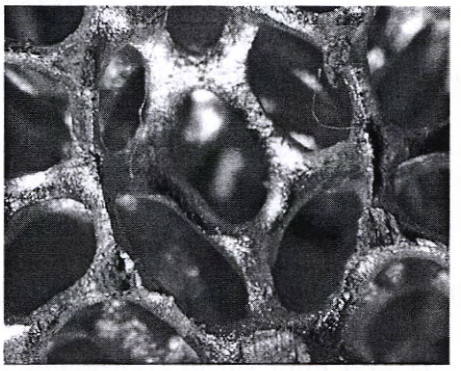

Figure 3-13 Closed-up view inside the open-cell metal foam

Since the structure is considerably complex, an idealised configuration was used to represent the framework inside of metal foam as shown in Figure 3-14 (a). The interfaces of the conterminous pores are quadrangle or pentagon, and the solid trabeculas form the border of the every interface. It is noted that a lumping of material is located at joints where the ligaments meet at the corner of the polygon. The flow restriction and pressure drop in the metal foam will be influenced significantly by the ligament's shape and structure. The schematic graphics of the solid ligament with partial lumping was shown in Figure 3-14 (b). The main part of the ligament is approximately a column with the diameter of d_l, which was used as a hydraulic parameter of metal foam to define the critical dimensionless variables in the results and discussion.

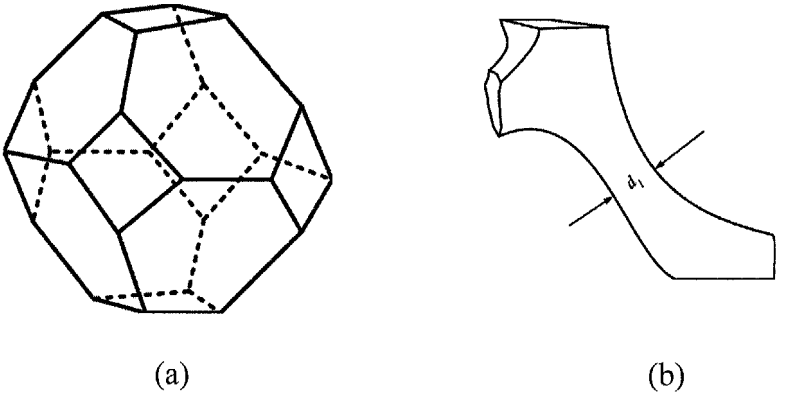

(a) (b)

Figure 3-14 (a) Ideal pore structure and (b) the definition of ligament diameter of open-cell metal foam

3.3.3 Physical Properties of the Tested Foams

The various physical properties of open-cell foam are important to the different applications of metal foam. For example, in the application of energy absorption such as in Solid Rocket-Booster (SRB) and Blast Container (BC), the effective compressive strength and the stress-strain characteristics of metal foam are of most concerns. However, in the application of the fluid flow control devices (gas diffuser and mixer) of using metal foam, the large surface area to volume ratio and the compression capability are the basic parameters which improve the performance of the system.

In heat transfer applications using open-cell metal foam, the properties of metal foam of the solid surface, ligament diameter and effective thermal conductivity are critical for heat transfer performance. The total heat transfer rate of flow through metal foam could be increased significantly by increasing the solid-air contact surface area and effective thermal conductivity. Figure 3-15 (a) presents the relation between the solid surface area and density of the metal foam. It can be seen that the contact surface area of metal foam increases with the increase of both mass and pore densities. The ligament diameter is an important parameter to study the flow behaviour in metal foam since the ligaments compose the tortuous lacuna path of metal foam and influence the restriction for flow through the open-cell foam. Figure 3-15 (b) shows the trend of the ligament diameter to the mass and pore densities of metal foam. It indicates that the ligament diameter decreases with the increase of the pore density, or with the decrease of the mass density. The above physical properties show that the mass density is a function of the solid surface area and ligament diameter of open-cell metal foam. To investigate the fluid flow and heat transfer in metal foam, the materials tested in the present experiments possess moderate mass density of about

8%. The detailed information of Duocel aluminium foam is given in Appendix C.

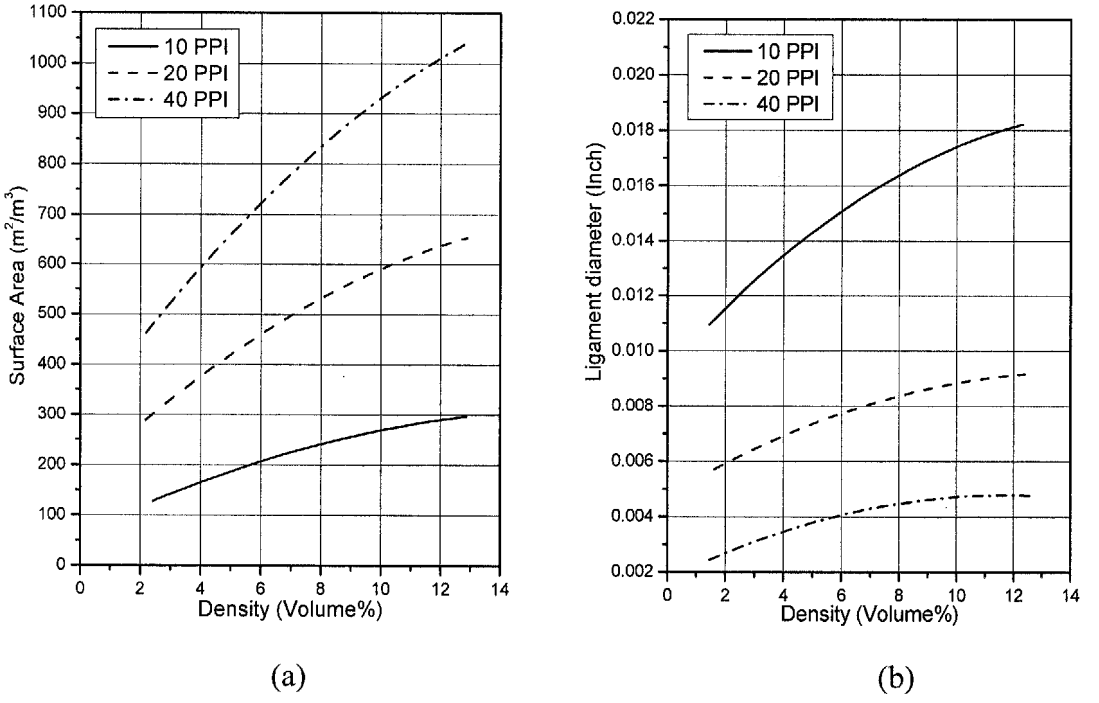

(a) (b)

Figure 3-15 (a) Various solid surface areas and (b) various ligament diameters for metal foams with the different mass and pore densities
(Source: DUOCEL aluminium foam data sheet, 2002)

3.4 Summary

A detailed description of the experiments is presented in this chapter. The experimental study of the fluid flow and heat transfer of oscillating flow through metal foams channel can be conducted using the experimental setup with various maximum flow displacements and oscillatory frequencies. The flow velocity, pressure drop across the test section and the temperature at the substrate surface can be measured by the calibrated hot-wire, pressure transducer and thermocouple, respectively. The experimental procedures are elucidated and the uncertainties of the calculated parameters are analysed. In addition, the form structure characteristics of the tested aluminium foams are illustrated.

CHAPTER 4

FLUID CHARACTERISTICS OF OSCILLATORY FLOW THROUGH METAL FOAMS

4.1 Analysis of Similarity Parameters

For fully developed oscillating flow through a circular pipe, the transient friction factor $f(\omega t)$ can be expressed as:

$$f(\omega t) = \frac{\mu_f \left(\frac{\partial u}{\partial r}\right)_{r=D/2}}{\frac{1}{2}\rho_f u_{\max}^2} \tag{4-1}$$

where ω is the angular frequency of the imposed pressure gradient. D and r are the diameter of the pipe and the radial coordinates, respectively. Thus, the average friction factor f_{osc} in a complete oscillatory cycle can be given by

$$f_{osc} = \frac{1}{2\pi}\int_0^{2\pi} |f(\omega t)| d\omega t \tag{4-2}$$

For fully developed oscillating flow through a pipe, the mass and momentum governing equations for incompressible flow are

$$\frac{\partial u}{\partial x} = 0 \tag{4-3}$$

$$\frac{\partial u}{\partial t} = -\frac{1}{\rho_f}\frac{\partial P}{\partial x} + \nu_f\left(\frac{\partial^2 u}{\partial r^2} + \frac{1}{r}\frac{\partial u}{\partial r}\right) \tag{4-4}$$

where u is the axial velocity and ν_f is the kinematic viscosity of fluid. The pressure gradient for a sinusoidal motion flow can be expressed as

$$\frac{1}{\rho_f}\frac{\partial P}{\partial x} = A_p \cos \omega t \tag{4-5}$$

where A_p is the oscillation amplitude for the imposed pressure gradient. A modified solution which is based on the result obtained by Uchida (1956) for the axial velocity profile of a fully developed oscillating flow gives

$$u = \frac{A_p D^2}{\mathrm{Re}_\omega \nu_f}[(1-A)\sin \omega t + B\cos \omega t] \tag{4-6}$$

where A and B are the variables given by

$$A = \frac{ber\left(\frac{1}{2}\sqrt{\mathrm{Re}_\omega}\right)bei\left(\sqrt{\mathrm{Re}_\omega}\right)R + bei\left(\frac{1}{2}\sqrt{\mathrm{Re}_\omega}\right)ber\left(\sqrt{\mathrm{Re}_\omega}\right)R}{ber^2\left(\frac{1}{2}\sqrt{\mathrm{Re}_\omega}\right) + bei^2\left(\frac{1}{2}\sqrt{\mathrm{Re}_\omega}\right)} \tag{4-7a}$$

$$B = \frac{ber\left(\frac{1}{2}\sqrt{\mathrm{Re}_\omega}\right)ber\left(\sqrt{\mathrm{Re}_\omega}\right)R + ber\left(\frac{1}{2}\sqrt{\mathrm{Re}_\omega}\right)ber\left(\sqrt{\mathrm{Re}_\omega}\right)R}{ber^2\left(\frac{1}{2}\sqrt{\mathrm{Re}_\omega}\right) + bei^2\left(\frac{1}{2}\sqrt{\mathrm{Re}_\omega}\right)} \tag{4-7b}$$

where $\mathrm{Re}_\omega = \omega D^2/\nu_f$ is the kinetic Reynolds number and $R = r/D$ is the dimensionless radial coordinate. *ber* and *bei* are the Kelvin functions. By differentiating Equation (4-6) and substituting into Equation (4-2), an exact expression of the average friction factor for oscillating flow in a pipe is given by (Zhao and Cheng, 1996a)

$$f_{osc} = \frac{64}{\pi}\frac{F_\omega}{A_0} \tag{4-8}$$

where $A_0 = x_{max}/D$ is the dimensionless flow amplitude and x_{max} is the maximum flow displacement. The function F_ω can be expressed as

$$F_\omega = \frac{\sqrt{C_1^2 + C_2^2}}{16\sqrt{(\frac{1}{2}\sqrt{\mathrm{Re}_\omega} - 2C_1)^2 + 4C_2^2}} \tag{4-9}$$

where C_1 and C_2 are variables given by

$$C_1 = \frac{ber\left(\frac{1}{2}\sqrt{\mathrm{Re}_\omega}\right)bei'\left(\frac{1}{2}\sqrt{\mathrm{Re}_\omega}\right) - bei\left(\frac{1}{2}\sqrt{\mathrm{Re}_\omega}\right)ber'\left(\frac{1}{2}\sqrt{\mathrm{Re}_\omega}\right)}{ber^2\left(\frac{1}{2}\sqrt{\mathrm{Re}_\omega}\right) + bei^2\left(\frac{1}{2}\sqrt{\mathrm{Re}_\omega}\right)} \tag{4-10a}$$

$$C_2 = \frac{ber\left(\frac{1}{2}\sqrt{\mathrm{Re}_\omega}\right)ber'\left(\frac{1}{2}\sqrt{\mathrm{Re}_\omega}\right) + bei\left(\frac{1}{2}\sqrt{\mathrm{Re}_\omega}\right)bei'\left(\frac{1}{2}\sqrt{\mathrm{Re}_\omega}\right)}{ber^2\left(\frac{1}{2}\sqrt{\mathrm{Re}_\omega}\right) + bei^2\left(\frac{1}{2}\sqrt{\mathrm{Re}_\omega}\right)} \tag{4-10b}$$

Equations (4-9) and (4-10) show that F_ω is only governed by the parameter of the kinetic Reynolds number Re_ω. By considering Equation (4-8), it can be deduced that the average friction factor of oscillating flow through a pipe with constant L and D is governed by the parameters of the kinetic Reynolds number and dimensionless flow amplitude, i.e.

$$f_{osc} = f(A_0, \mathrm{Re}_\omega) \tag{4-11}$$

Zhao and Cheng (1996b) studied oscillating flow in wire-screens with various flow displacements. A correlation equation for the friction factor in terms of the hydraulic wire diameter based kinetic Reynolds number and the dimensionless fluid displacement amplitude was presented. Their results validated that the dimensionless fluid displacement and the kinetic Reynolds number are also the terms of the friction factor for oscillating flow through porous channel.

4.2 Determination of Critical Properties of Metal Foams

The critical physical properties of the open-cell metal materials with pore densities of 10, 20 and 40 PPI were determined experimentally. The porosity and the ligament diameter of the metal foams were measured directly while the inertial coefficient and permeability were obtained by employing a second-order polynomial fitting method to the data of velocity and pressure drop.

4.2.1 Porosity and Ligament Diameter

As mentioned previously, the Duocel aluminium foam supplied by ERG Materials and Aerospace Corporation was fabricated by the infiltration casting technique in which a solid mould of pore shapes was made before molten metal was poured into the mould. Therefore, the ligament structure can be controlled properly and the diameters of ligaments inside of metal foam can be considered to be of equal lengths. In the present study, the ligament diameter of the tested aluminium foam was measured by a Scanning Electron Microscope (SEM). To reduce the random effect of the ligament diameter on the study of flow characteristics, the average diameter of ten ligaments measured randomly by the SEM was used as the ligament diameter in the present study.

Porosity is commonly defined as the total void volume divided by the total volume occupied by the solid matrix and void volume. Each void may be connected to more than one other pore (interconnected), connected only to one other pore (dead end), or not connected to any other pore (isolated). The volume fraction of the interconnected pores is called the effective porosity. Fluid flows through the interconnected pores only. For Duocel open-cell foam, the porosity is equal to the effective porosity due to the metal foam with the uncompressed fully-opened cell structure. The porosity ε of the metal foam can be obtained by measuring the total volume of the metal foam from its external dimensions and the volume of the solid fractions. The porosity of porous material is calculated by

$$\varepsilon = \frac{V_t - V_s}{V_t} \tag{4-12}$$

where V_t and V_s are the total volume and the volume of solid fraction of porous material, respectively.

4.2.2 Inertial Coefficient and Permeability

The term, inertial coefficient describes the effects of the local aspects of the pore space morphology on momentum transport in the porous media. Permeability is a measure of the flow conductance of the porous matrix, which relates to the average flow velocity through the pores with pressure drop in porous media. The critical properties of permeability K and inertia coefficient F of the tested metal foams were obtained by applying the quadratic curve fitting method to pressure drop versus fluid velocity data obtained under steady flow conditions. The following relation between measured pressure drop and flow velocity is derived:

$$\frac{\Delta P}{L} = Au + Bu^2 \tag{4-13}$$

where ΔP is the pressure drop across the media, L is the length of the media, and u is average flow velocity in the metal foam channel. The two coefficients, A and B are defined as

$$A = \frac{\mu_f}{K},\ B = \rho_f \frac{F}{\sqrt{K}} \tag{4-14}$$

where μ_f and ρ_f are the dynamic viscosity and density of the fluid, respectively. It can be observed from Equations (4-13) and (4-14) that the permeability and inertia coefficient of metal foam are also dependent on the dynamic viscosity μ_f and density ρ_f of the fluid. Figure 4-1 presents the data of pressure drop per unit length versus velocity for steady flow through the aluminium 10, 20 and 40 PPI foams. By fitting the second-order polynomial of Equation (4-13) through the data points, coefficients A and B can be determined. By substituting the values of A and B into Equation (4-14), the corresponding values for permeability K and inertia coefficient F can be obtained. The measured values of physical properties for the tested metal foams are listed in Table 4-1.

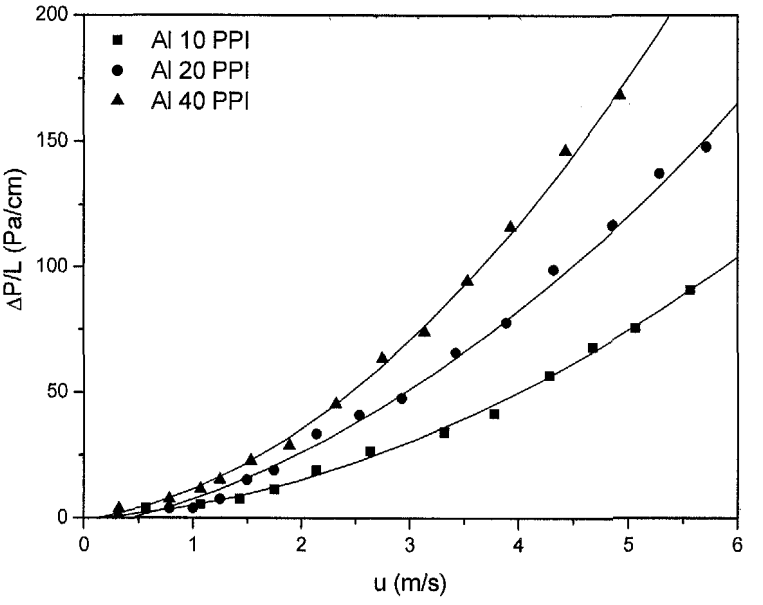

Figure 4-1 Pressure drop versus flow velocity in open-cell aluminium foam with pore densities of 10, 20 and 40 PPI

Table 4-1 Physical properties of aluminium foam

Physical properties	Al 10 PPI	Al 20 PPI	Al 40 PPI
Ligament diameter, d_l (μm)	427.2	221.3	112.6
Porosity, ε	0.91	0.90	0.90
Density, Volume %	8-10	8-10	8-10
Inertia coefficient, F	0.042	0.05	0.087
Permeability, K (10^{-8} m^2)	4.2	3.1	2.8

4.3 Oscillatory Flow in Metal Foam Channel

4.3.1 Hydraulic Ligament Diameter Based Parameters

Based on the above analyses, the kinetic Reynolds number and dimensionless fluid displacement are the critical parameters for oscillating flow through porous channel. Considering the wire-screen and metal foam, the wires and the ligaments are the solid struts inside the woven-screen and metal foam, respectively. The flow restrictions and pressure drops in metal foam will be influenced significantly by the ligament's shape and structure. To study the characteristics of oscillating flow through open-cell metal foam, and to explore the difference of flow behaviour in open-cell foam with other types of porous media, the hydraulic ligament diameter is employed as the geometry characteristic parameter of open-cell metal foam. The effect of the aluminium foam on oscillating flow behaviour is accounted for by defining the hydraulic ligament diameter of metal foam D_h as

$$D_h = \frac{\varepsilon d_l}{1-\varepsilon} \tag{4-15}$$

where d_l and ε are the ligament diameter and porosity of the aluminium foam, respectively.

The kinetic Reynolds number was used for presenting the fluid status of oscillating flow in metal foam, which could represent the periodic characteristic of oscillating flow, i.e. dimensionless oscillatory frequency. The similarity parameters of the hydraulic ligament diameter based kinetic Reynolds number $\mathrm{Re}_{\omega(Dh)}$ and the dimensionless fluid amplitude A_{Dh} are defined as

$$\mathrm{Re}_{\omega(Dh)} = \frac{\omega D_h^{\,2}}{\nu_f} \tag{4-16}$$

$$A_{Dh} = \frac{x_{\max}}{D_h} \tag{4-17}$$

where x_{max}, ω and ν_f are the maximum flow displacement, angular frequency and kinematic viscosity of fluid, respectively. According to Equations (4-15) ~ (4-17), the effect of the average ligament diameter is included in the calculations. To compare the characteristics between the oscillating flow characteristics in open-cell metal foams and wire-screens, the maximum friction factor defined by Tanaka *et al.* (1990) for oscillating flow through porous channel is employed as follows:

$$f_{max} = \frac{\Delta P_{max} D_h}{\frac{1}{2} \rho_f L (u_{max})^2} \tag{4-18}$$

where ΔP_{max} is the maximum pressure drop in porous channel and u_{max} is the maximum flow velocity. ρ_f and L are the flow density and the length of the tested aluminium foam, respectively.

4.3.2 Pressure Drop and Velocity

4.3.2.1. Effects of Kinetic Reynolds Number and Dimensionless Flow Amplitude

The oscillating flow in metal foam channel is driven by the piston with sinusoidal motion. Figures 4-2 (a) and (b) show the temporal variations of the pressure drop across the channel filled with aluminium 20 PPI and 40 PPI respectively. The pressure drop profiles were obtained by the dimensionless flow amplitude A_{Dh} = 26.1, 30.2 and 34.2 for aluminium 20 PPI at a kinetic Reynolds number $Re_{\omega(Dh)}$ = 6.1 and A_{Dh} = 51.6, 59.5 and 67.5 for aluminium 40 PPI at a kinetic Reynolds number $Re_{\omega(Dh)}$ = 2.4, respectively. It appears that the temporal variations of pressure drop are almost in the same cycle with the ideal sinusoidal waveforms, which describes the piston's movement for different maximum displacements at a fixed frequency. It can be seen that the pressure drop increases with the increase in the dimensionless flow displacement amplitude at a fixed value of the kinetic Reynolds number, i.e.

dimensionless frequency. It is noted that no significant effect of the dimensionless flow amplitude on the flow velocity was observed in the present experiments.

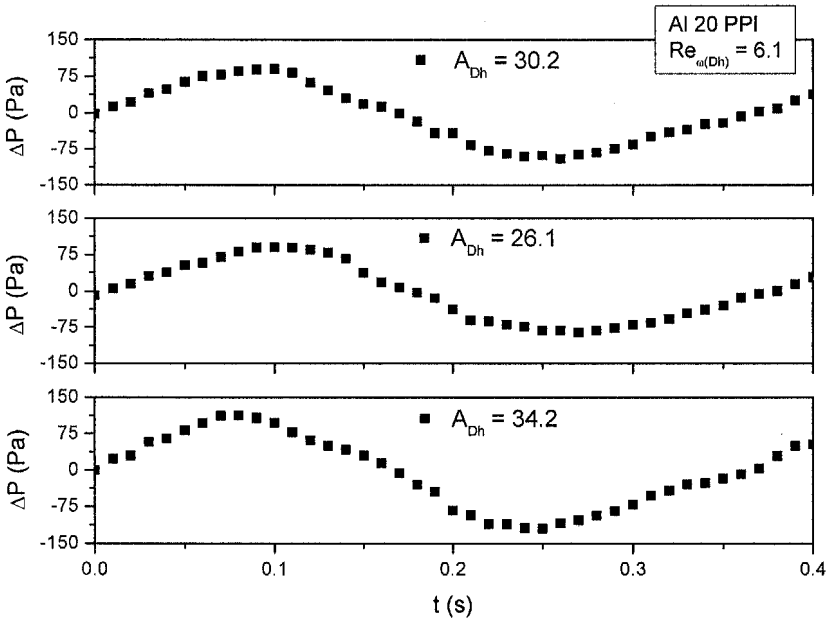

(a)

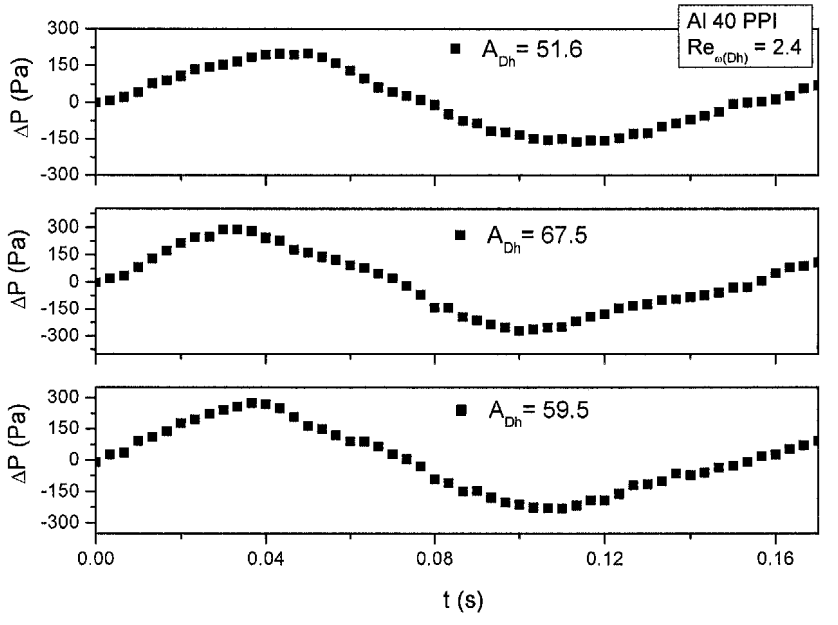

(b)

Figure 4-2 Temporal variations of the pressure drop for oscillating flow in (a) aluminium 20 PPI (b) aluminium 40 PPI with different A_{Dh}

Figures 4-3 (a) and (b) present the typical variations of flow velocity and pressure drop through aluminium 10 and 20 PPI along the cycles of oscillating flow. Figure 4-3 (a) was obtained for aluminium 10 PPI with kinetic Reynolds number $Re_{\omega(Dh)}$ = 24.0, 31.1 and 40.9 at the maximum flow displacement A_{Dh} = 16.6, and Figure 4-4 (b) was obtained for aluminium 20 PPI with kinetic Reynolds number $Re_{\omega(Dh)}$ = 5.3, 6.8 and 9.1 at the maximum flow displacement A_{Dh} = 34.2. It can be seen that the profiles of flow velocity increase with the increase of kinetic Reynolds number and vary almost sinusoidally due to the reversing flow direction. High pressure drop corresponds to high flow velocity which shows that the phase difference between the velocity and pressure drop is very small. To focus the investigation on the similarity parameters of kinetic Reynolds number and dimensionless flow amplitude, the phase difference between the piston motion and oscillating flow is neglected. Khodadadi (1991) showed that the phase lag θ_n between the velocity component and the pressure gradient in a porous channel subjected to oscillating fluid flow can be predicted by

$$\theta_n = \tan^{-1}\left(\frac{n\beta^2}{\gamma^2}\right) \tag{4-19}$$

where $\beta = \left(w^2\omega/\nu_f\right)^{1/2}$ is the Stokes number, w is the channel width and $\gamma = \left(w^2\varepsilon/K\right)^{1/2}$ is the shape parameter of the porous medium. For the present experiments, the kinematic viscosity ν_f of the air is taken to be 15.7 × 10^{-6} m^2/s and permeability K of aluminium 10 and 20 PPI are 4.2 × 10^{-8} m^2 and 3.1 × 10^{-8} m^2, respectively. The phase lag θ_n is calculated to be 3.5 and 2.7 degrees for oscillating flow through 10 and 20 PPI at the angular frequency ω = 21.4 (i.e. $Re_{\omega(Dh)}$ = 24.0 for 10 PPI and $Re_{\omega(Dh)}$ = 5.3 for 20 PPI) and cycle number n = 1, respectively. This indicates that the phase difference between velocity and pressure drop is very small

for open-cell aluminium foams and agrees with the trends observed in the present experiments.

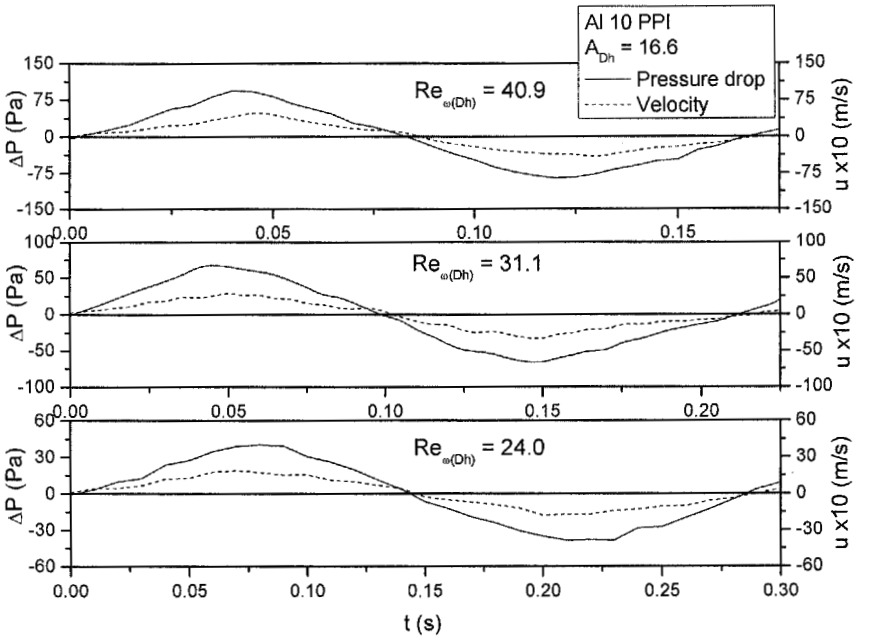

(a)

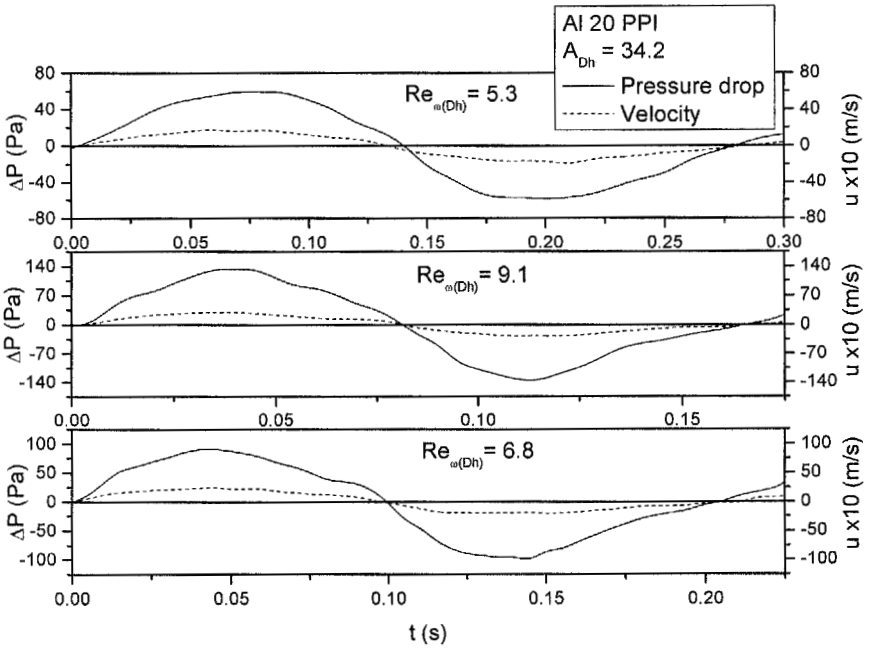

(b)

Figure 4-3 Typical variations of velocity and pressure drop of oscillating flow through (a) aluminium 10 PPI at A_{Dh} = 16.6 and $Re_{\omega(Dh)}$ = 24.0, 31.1 and 40.9 (b) aluminium 20 PPI at A_{Dh} = 34.2 and $Re_{\omega(Dh)}$ = 5.3, 6.8 and 9.1

To evaluate the effects of flow displacement and oscillatory frequency on the pressure drop of oscillating flow in metal foam, the pressure drop in aluminium 20 PPI for different dimensionless flow amplitudes and in aluminium 40 PPI for different kinetic Reynolds numbers are plotted in Figures 4-4 and 4-5, respectively. Figure 4-4 shows the typical temporal variations of the pressure drop across the channel filled with aluminium 20 PPI for dimensionless flow amplitudes A_{Dh} = 26.1, 30.2 and 34.2 at the kinetic Reynolds number $Re_{\omega(Dh)}$ = 6.8. It can be seen that the pressure drop differences are only about 8 ~ 15 Pa for various flow displacements. It presents that the pressure drop increases slightly with the increase of the dimensionless flow amplitude at a fixed value of the kinetic Reynolds number. Once again, it is observed that the temporal variations of pressure drop vary in phase for different maximum displacements. This indicates that the displacement of flow has a negligible effect on the moving cycle of oscillating flow in open-cell foam. The effects of the different kinetic Reynolds numbers on the variations of pressure drop across the aluminium 40 PPI foam are illustrated in Figure 4-5 for a complete cycle at A_{Dh} = 67.5 for $Re_{\omega(Dh)}$ = 1.0, 1.7 and 2.4. A difference in pressure drop of about 130 Pa was observed between the kinetic Reynolds number of 2.4 and 1.7. It shows that the pressure drop for high oscillatory frequency is much higher than that for low oscillatory frequency at a fixed flow displacement. These two figures indicate that the pressure drop always depends on the kinetic Reynolds number and dimensionless flow amplitude for oscillating flow through a porous channel with constant properties.

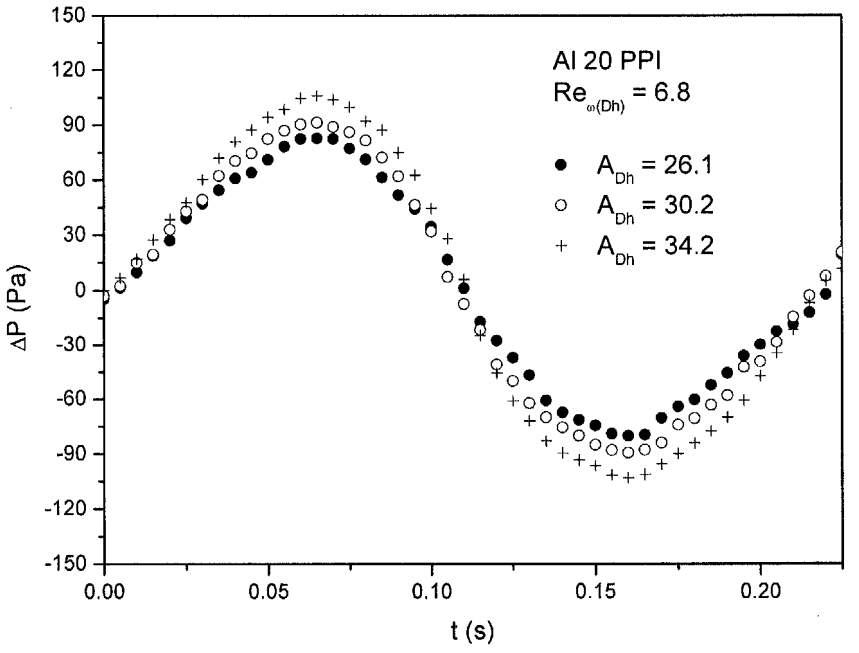

Figure 4-4 Effect of the maximum flow displacement on pressure drop in aluminium foam 20 PPI at $Re_{\omega(Dh)} = 6.8$

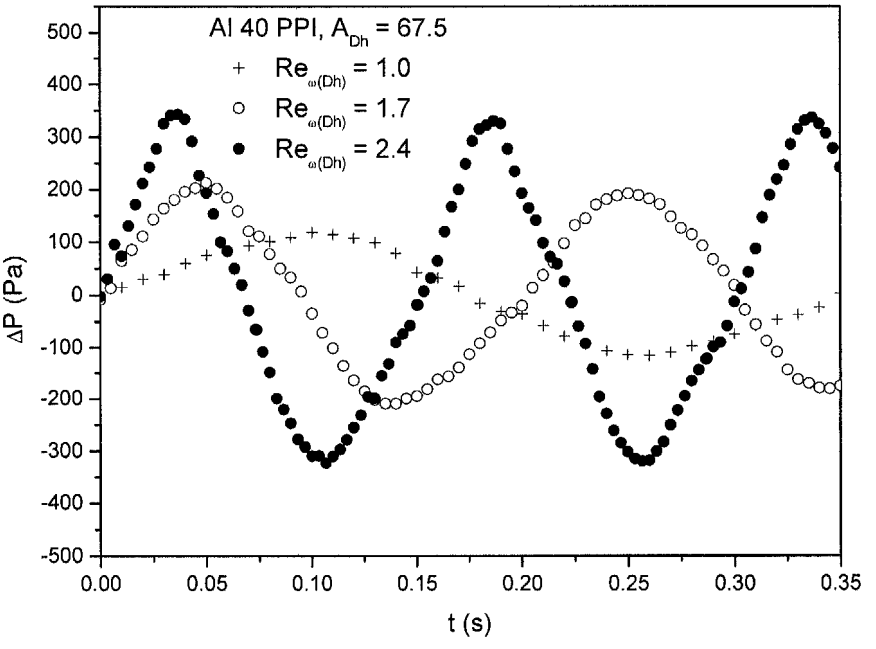

Figure 4-5 Effect of kinetic Reynolds number on pressure drop of oscillating flow through aluminium 40 PPI at $A_{Dh} = 67.5$

4.3.2.2 Various Pore Densities

Figure 4-6 shows the variations of pressure drop in aluminium foams of 10, 20 and 40 PPI at a given maximum flow displacement x_{max} = 68 mm, i.e. the dimensionless flow oscillation amplitude A_{Dh} = 14.6, 30.2 and 59.5 for aluminium 10, 20 and 40 PPI, respectively. The oscillatory frequency was set to 3.9 Hz, i.e. the kinetic Reynolds number $Re_{\omega(Dh)}$ = 27.6, 6.1 and 1.5 for aluminium 10, 20 and 40 PPI, respectively. It is observed that the amplitudes of pressure drop increase markedly with the increase of the foam's pore density. From the results presented in Figures 4-4, 4-5 and 4-6, it can be concluded that the pressure drop of oscillating flow in metal foam depends on its density, maximum flow displacement and oscillatory frequency. Moreover, the close-up views of Figures 4-4 and 4-5 indicate that the pressure drop in metal foam channel is dominated by the kinetic Reynolds number $Re_{\omega(Dh)}$ rather than by the dimensionless flow amplitude A_{Dh}. In fact, the pressure drop of oscillating flow in aluminium foam channel is relatively independent of the dimensionless flow amplitude A_{Dh}.

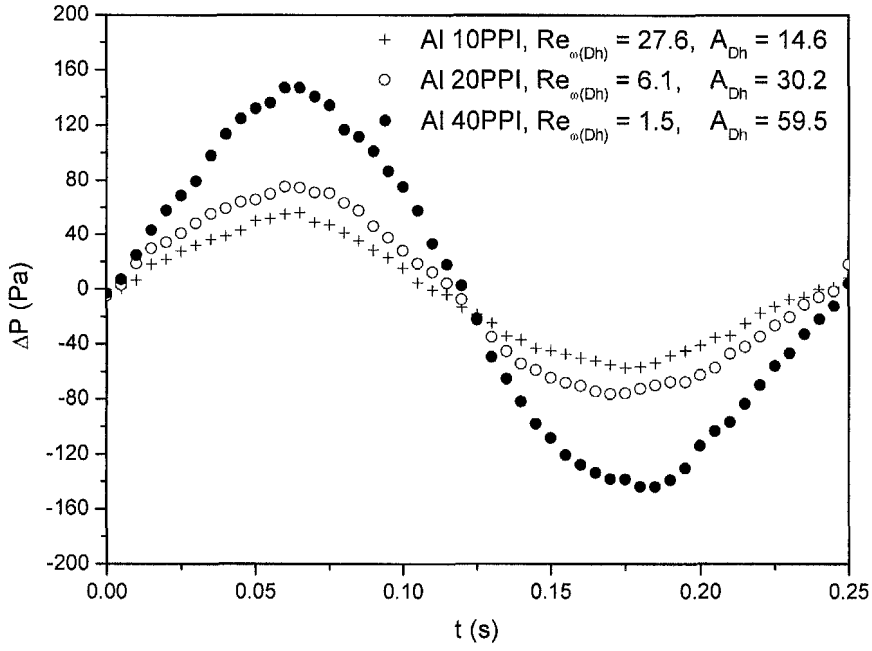

Figure 4-6 Effect of different pore densities of aluminium foam on pressure drop of oscillating flow

4.3.3 Maximum Friction Factor

Oscillating flow behaviour has been studied amply in Stirling engine and heat exchangers, where the inserted porous media are woven-screens. To the best of the author's knowledge, there is no published result of friction factor which represents the fluid characteristics in metal foam subject to oscillating flow. To study the maximum friction factor of oscillating flow through the metal foam channel, the measured maximum pressure drop versus hydraulic ligament diameter based Reynolds number is plotted in Figure 4-7. The maximum Reynolds number based on the hydraulic ligament diameter is defined as

$$\mathrm{Re}_{\max(Dh)} = \frac{u_{\max} D_h}{v_f} \tag{4-20}$$

where $u_{\max}$ is the average maximum velocity through the cross-section of porous channel. For oscillating flow through a porous channel, the maximum cross-sectional velocity $u_{\max}$ is related to the maximum flow displacement $x_{\max}$ by

$$u_{\max} = \frac{x_{\max}\omega}{2} \tag{4-21}$$

By comparing Equations (4-20) and (4-16), the Reynolds number in Equation (4-20) can be expressed in terms of A_{Dh} and $\mathrm{Re}_{\omega(Dh)}$ as

$$\mathrm{Re}_{\max(Dh)} = \frac{A_{Dh}\mathrm{Re}_{\omega(Dh)}}{2} \tag{4-22}$$

Figure 4-7 illustrates the maximum pressure drop of oscillating flow through aluminium foams of 10, 20 and 40 PPI for the range of hydraulic ligament diameter based Reynolds number $\mathrm{Re}_{\max(Dh)}$ = 46 ~ 790 and dimensionless flow displacement amplitude A_{Dh} = 12.7 ~ 67.5. It can be seen that for aluminium foams of different pore densities, the maximum pressure drops of oscillating flow increase with the increase of the dimensionless flow amplitude and the maximum hydraulic ligament diameter

based Reynolds number. The maximum pressure drop increases substantially with an increase in the pore density for aluminium 40 PPI with the highest value of pressure drop being achieved at A_{Dh} = 51.6 and $\mathrm{Re}_{\max(Dh)}$ = 244.3. When compared with the pressure drop of oscillating flow through woven screens obtained by Zhao and Cheng (1996b) and Ju and Zhou (1998), it is noted that maximum pressure drop in a channel filled with aluminium foams is much lower than that in a channel packed with wire-screens.

In order to obtain an empirical equation for the maximum friction factor of oscillating flow through the open-cell metal foam, the kinetic Reynolds numbers $\mathrm{Re}_{\omega(Dh)}$ versus the computed data of maximum friction factor $f_{\max}$ times the dimensionless flow displacement amplitude A_{Dh} are plotted in Figure 4-8. The data ranges of hydraulic ligament diameter based kinetic Reynolds number and dimensionless flow amplitude are $0.46 < \mathrm{Re}_{\omega(Dh)} < 57.9$ and $12.7 < A_{Dh} < 67.5$, respectively. The following correlation for the maximum friction factor for oscillating flow in open-cell aluminium foam is derived based on the experimental data obtained from this study:

$$f_{\max} = \frac{1}{A_{Dh}}\left(\frac{86.7}{\mathrm{Re}_{\omega(Dh)}^{0.19}} + 0.61\right) \tag{4-23}$$

Equation (4-23) is obtained by using a least-squares method with an error of ±14.8%. The error range of the empirical equation plotted on Figure 4-8 shows that the friction factor of oscillating flow in metal foam is fitted well by Equation (4-23). The correlation equation indicates that oscillating flow behaviour in an open-cell metal foam is governed by the dimensionless flow displacement amplitude A_{Dh} and the kinetic Reynolds number $\mathrm{Re}_{\omega(Dh)}$ based on the hydraulic ligament diameter of open-cell foam.

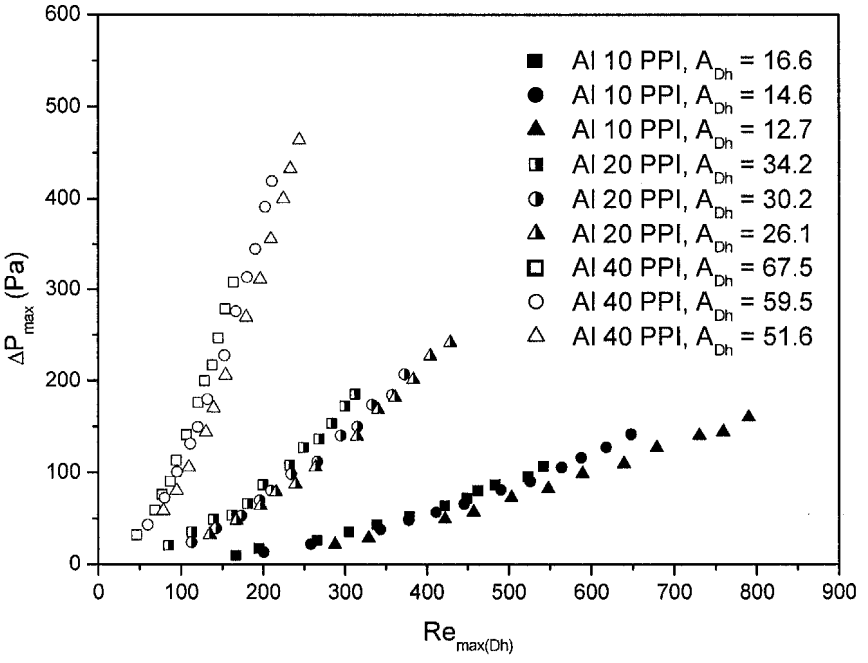

Figure 4-7 Maximum pressure drop of oscillating flow versus Reynolds number based on the hydraulic ligament diameter for aluminium foams of 10, 20 and 40 PPI

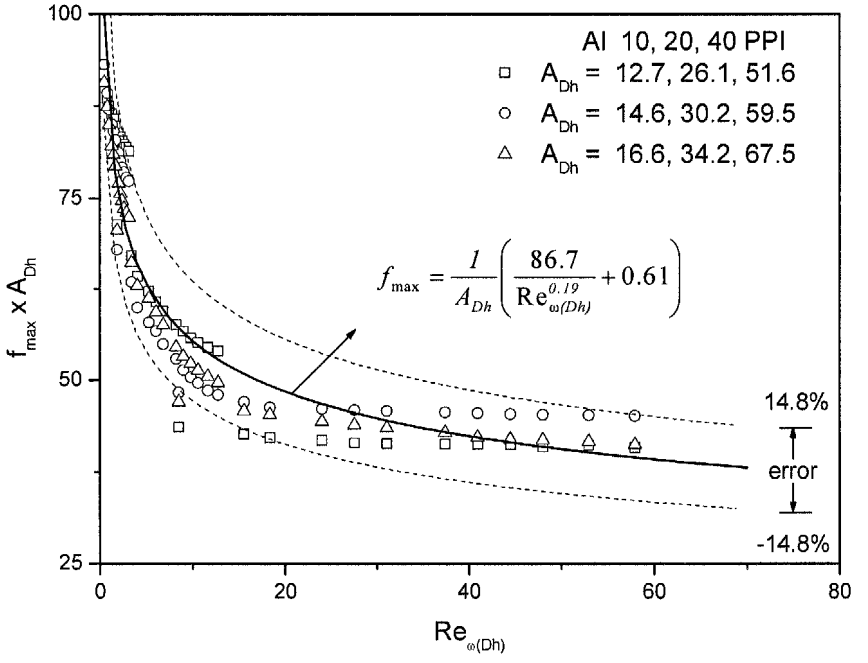

Figure 4-8 Maximum friction factor for oscillating flow in open-cell aluminium foam in terms of the kinetic Reynolds number and the dimensionless flow displacement amplitude

Steady flow through metal foam has been investigated widely because of its numerous applications in heat transfer enhancement. To explore the difference of the friction factors of oscillating and steady flow through the open-cell metal foam, the maximum friction factors obtained by the present experiments are compared to the results obtained by Kim *et al.* (2000), which experimentally studied fluid behaviour in the same materials under the steady flow condition. As shown in Figure 4-9 (a), the maximum friction factors of oscillating flow through porous channel were calculated using Equation (4-18) for dimensionless flow amplitudes A_{Dh} = 12.7 ~ 67.5 and the hydraulic ligament diameter based maximum Reynolds number $Re_{max(Dh)}$ from 46.1 to 790.2. Figure 4-9 (b) presents the friction factor versus Reynolds number based on the channel height for steady flow through aluminium foams with pore densities of 10, 20 and 40 PPI. It can be seen that for both steady and oscillating flows through metal foam porous channel, the friction factor for high pore density foam is smaller than that for low pore density foam. For oscillating flow, the maximum friction factor in 10 PPI aluminium foam decreases with an increase in the dimensionless flow displacement amplitude. The same trends are observed for the other two foams tested in the experiments over different ranges of maximum Reynolds number $Re_{max(Dh)}$. The value of the friction factor for oscillating flow calculated by Equation (4-18) depends on the three parameters of maximum pressure drop, velocity and hydraulic ligament diameter of metal foam. Comparing the data of f_{max} and f_{std} plotted in Figures 4-9 (a) and (b), it is obvious that the maximum friction factor of oscillating flow is higher than the friction factor of steady flow in metal foams with different pore densities. Zhao and Cheng (1996b) obtained a similar result which showed that the friction factor of oscillating flow is higher than that of steady flow in a channel filled with wire-screens.

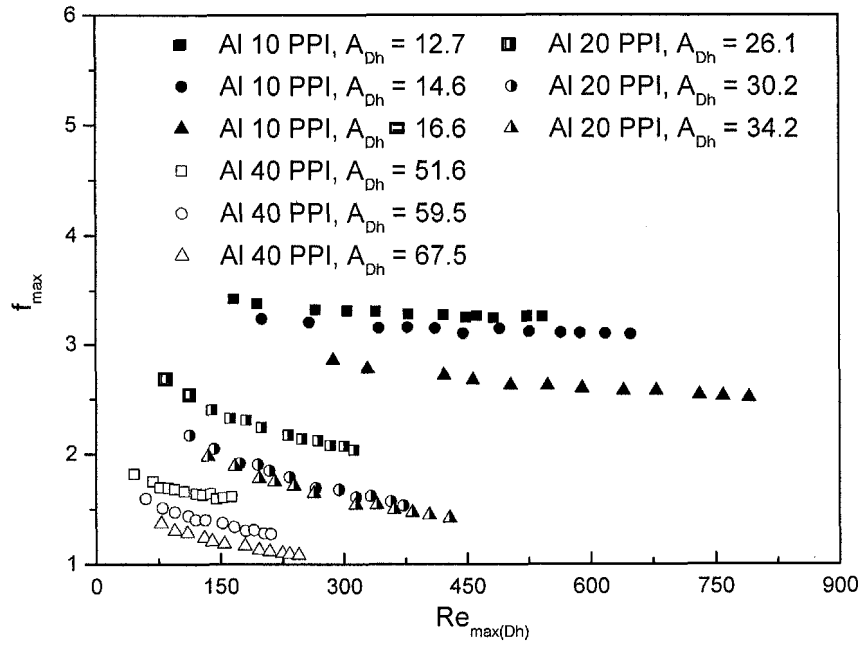

(a)

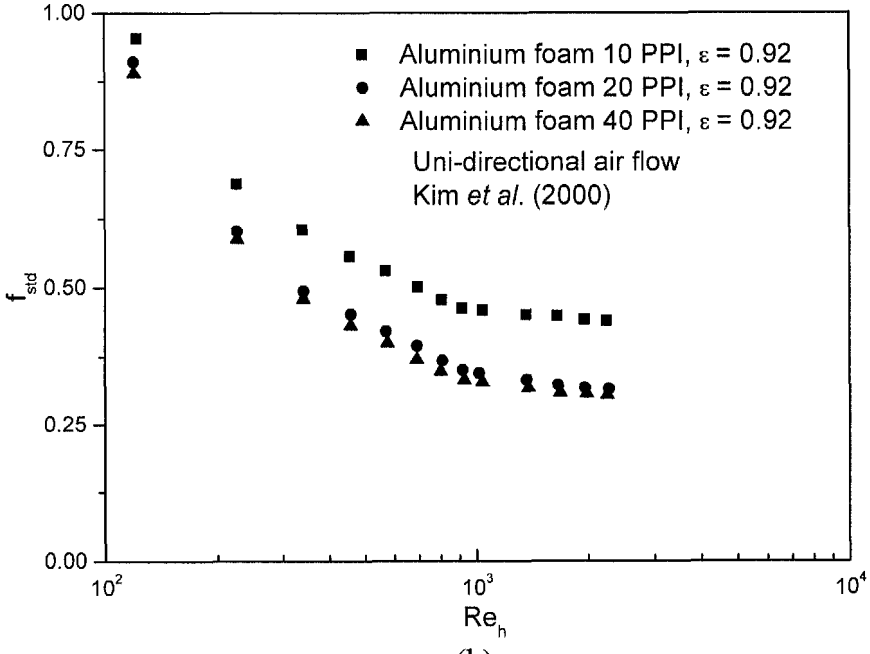

(b)

Figure 4-9 (a) Maximum friction factor of oscillating flow in aluminium foam 10, 20 and 40 PPI (b) Friction factor of steady flow in aluminium foam 10, 20 and 40 PPI (Kim *et al.*, 2000)

The woven-screen is used to enhance the heat exchange subjected to oscillating flow in Stirling engines and cryocoolers. To compare the oscillating flow characteristics in open-cell metal foam with other type of porous media, the maximum friction factor versus the maximum Reynolds number for both open-cell metal foams and woven-screens are presented in Figure 4-10. The solid line in Figure 4-10 (a) is plotted based on Equation (4-24) obtained by Tanaka *et al.* (1990) given by

$$f_{max} = \frac{198}{Re_{max(Dh)}} + 1.737 \tag{4-24}$$

The other three curves are plotted using Equation (4-23) for dimensionless flow displacement amplitudes A_{Dh} = 15, 30 and 70, which cover the range of flow amplitudes performed in the present experiments. It is obvious that the maximum friction factor for oscillating flow in open-cell metal foam is smaller than that for oscillating flow in wire-screens, especially for low Reynolds numbers and large dimensionless flow displacement amplitudes. It is noted that the maximum friction factor obtained by Tanaka *et al.* (1990) was for oscillating flow under the condition of a fixed flow displacement. Furthermore, Figure 4-10 (b) compares the maximum friction factors to the results obtained by Zhao and Cheng (1996b), which include the effects of the flow displacement on the maximum friction factor. The data of maximum friction factors for woven-screens were plotted by the following equation obtained by Zhao and Cheng (1996b):-

$$f_{max} = \frac{1}{A_{Dh}}\left(\frac{403.2}{Re_{\omega(Dh)}} + 1789.1\right) \tag{4-25}$$

It is noted that in Equation (4-25), A_{Dh} and $Re_{\omega(Dh)}$ are based on the hydraulic diameter of the screens which is defined as $D_h = \varepsilon d_w/(1-\varepsilon)$, where d_w is the diameter of the wire of woven-screens. The maximum friction factors were calculated at

dimensionless flow amplitudes A_{Dh} = 614.7 and 829.4 by Equations (4-23) and (4-25) for oscillating flow through metal foam and woven-screen channels, respectively. Once again, a large difference of maximum friction factor between oscillating flow in metal foam and woven-screens is observed. The difference in the maximum friction factor between metal foams and woven-screens decreases as the kinetic Reynolds number increases. For both types of porous channels, the maximum friction factor increases with the decrease of the dimensionless flow amplitude A_{Dh} subjected to oscillating flow condition. The large difference of the maximum friction factor between oscillating flow in open-cell foam and wire-screen is due to the difference in the material structures. The cells of aluminium foam are generally 12 to 14 sided polyhedral whose pentagonal or hexagonal faces are open to one another. The fully inter-connected pore structure without dead end pores allows a fluid to flow through the metal foam more readily when compared to a channel filled with wire-screens.

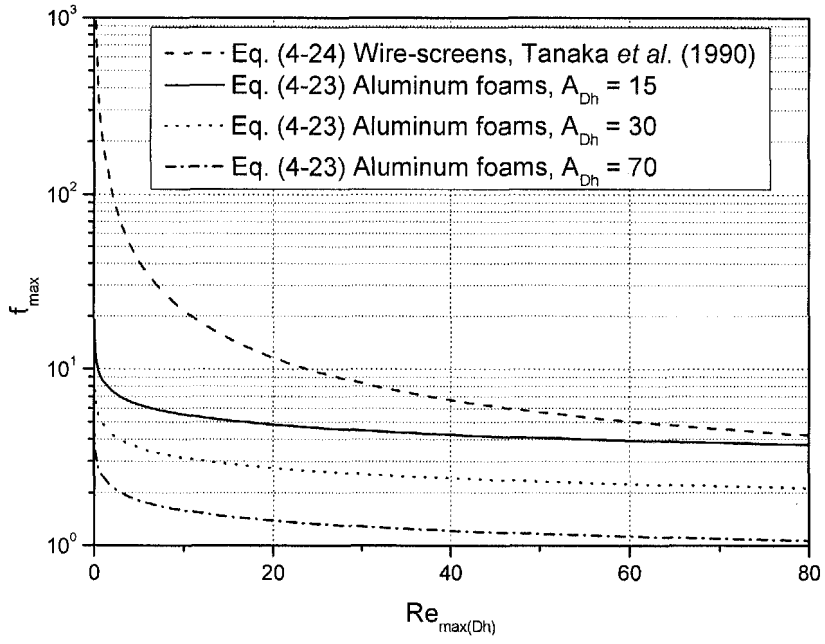

(a)

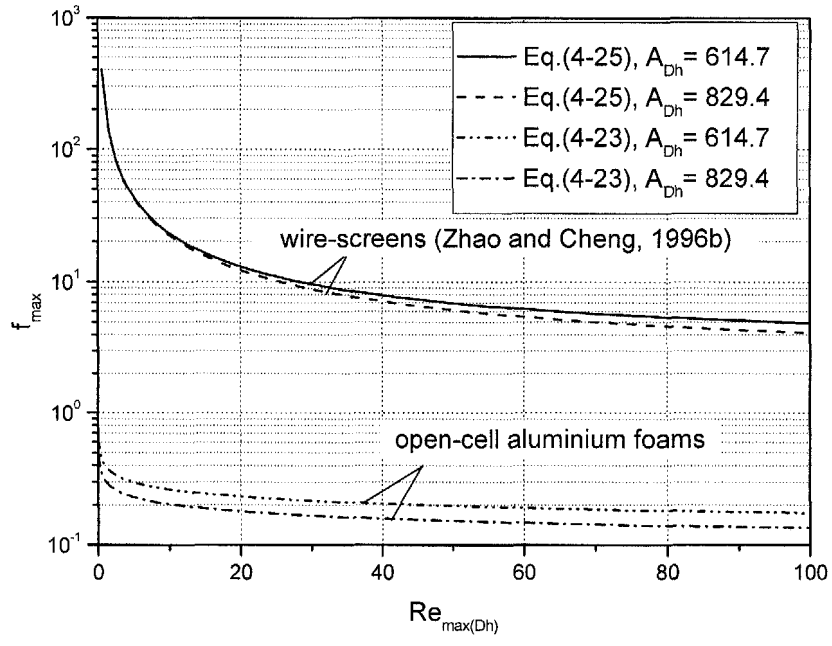

(b)

Figure 4-10 (a) Comparison of maximum friction factors for open-cell aluminium foams and wire-screens with A_{Dh} = 15, 30 and 70, (b) comparison of maximum friction factors for open-cell aluminium foams and wire-screens with A_{Dh} = 614.7 and 829.4

4.4 Summary

Experimental results of fluid characteristics of oscillating flow through aluminium foams 10, 20 and 40 PPI were discussed in this chapter. The properties of tested foams such as permeability K, inertia coefficient F and ligament diameter d_l were determined experimentally. The results showed that flow velocity and pressure drop in aluminium foams increase with the increased kinetic Reynolds and dimensionless flow amplitude. The pressure drop of oscillating flow in high pore density metal foam is higher than that in low pore density metal foam, due to the low permeability and high inertia coefficient. The experimental data showed that the oscillatory frequency and maximum flow displacement are the critical factors for pressure drop of oscillating flow through porous channel. Based on the analyses of the similarity parameters, a correlation equation of the maximum friction factor of oscillating flow through aluminium foams were obtained in terms of the hydraulic ligament diameter based kinetic Reynolds number and dimensionless flow amplitude, i.e. Equation (4-23). It indicates that the fluid characteristics for oscillating flow through aluminium foam is governed by the hydraulic ligament diameter based kinetic Reynolds number $Re_{\omega(Dh)}$ and dimensionless flow amplitude A_{Dh}.

CHAPTER 5

HEAT TRANSFER CHARACTERISTICS OF OSCILLATORY FLOW IN METAL FOAMS

5.1 Theoretical Analysis

One of the primary reasons for studying forced convection in metal foams is their possible application in electronics cooling. Transport phenomena in porous media have been studied extensively in the past two decades. However, most comprehensive studies have been conducted on low porosity media such as packed beds and channels filled with granular substances, since they have direct applications in heat transfer enhancement. A limited number of studies dealt with high porosity media like metal foam material, especially for oscillating flow cooling manner in metal foams. To investigate forced convection heat transfer in metal foams subjected to oscillating flow, a theoretical analysis is performed to obtain a dimensionless grouping parameter which can be used to evaluate the total heat transfer rates in metal foam channel subjected to oscillating and steady flows.

5.1.1 Governing Equations

For the local thermal non-equilibrium model, two energy equations are used to take into account the temperature difference between solid and fluid phases of porous media. Under the assumptions of two-dimensional incompressible flow and uniform porosity of porous media, the generalised macroscopic governing equations of forced convection in porous medium can be expressed as (Vafai and Sozen, 1990)

Fluid phase continuity equation:

$$\nabla \cdot (\rho_f \mathbf{u}) = 0 \tag{5-1}$$

Fluid phase momentum equation:

$$\frac{1}{\varepsilon}\frac{\partial \mathbf{u}}{\partial t} = -\frac{1}{\rho_f}\nabla P_f + \frac{\nu_f}{\varepsilon}\nabla^2 \mathbf{u} - \frac{\nu_f}{K}\mathbf{u} - \frac{F}{\sqrt{K}}|\mathbf{u}|\mathbf{u} \tag{5-2}$$

Fluid phase energy equation:

$$\varepsilon \rho_f c_{pf} \frac{\partial T_f}{\partial t} + \rho_f c_{pf} \mathbf{u} \cdot (\nabla T_f) = \nabla \cdot (k_{fe} \nabla T_f) + h_{fs} a_{fs} (T_s - T_f) \tag{5-3}$$

Solid phase energy equation:

$$(1-\varepsilon)\rho_s c_{ps} \frac{\partial T_s}{\partial t} = \nabla \cdot (k_{se} \nabla T_s) - h_{fs} a_{fs} (T_s - T_f) \tag{5-4}$$

where T_s and T_f are the temperature of fluid and solid phases, respectively. $\mathbf{u}$ is the velocity vector. k_{se} and k_{fe} are the effective thermal conductivities of solid and fluid phases, respectively.

To concentrate on the analysis of forced convection heat transfer in a channel filled with porous media, one-dimensional incompressible and fully developed flow is assumed. In addition, the properties of porous medium are assumed to be uniform. The effective thermal conductivities of fluid and solid phases are approximately by

$$k_{fe} = \varepsilon k_f + k_d \tag{5-5}$$

$$k_{se} = (1-\varepsilon) k_s \tag{5-6}$$

where k_d, k_f and k_s are the thermal dispersion conductivity of porous medium and the thermal conductivities of fluid and solid phases, respectively. Substituting Equations (5-5) and (5-6) into Equations (5-3) and (5-4), respectively, the energy governing equations can be rewritten as

Fluid phase energy equation:

$$\varepsilon\rho_f c_{pf}\frac{\partial T_f}{\partial t}+\rho_f c_{pf}u\frac{\partial T_f}{\partial x}=(\varepsilon k_f+k_d)\frac{\partial^2 T_f}{\partial y^2}+h_{fs}a_{fs}(T_s-T_f) \tag{5-7}$$

Solid phase energy equation:

$$(1-\varepsilon)\rho_s c_{ps}\frac{\partial T_s}{\partial t}=(1-\varepsilon)k_s(\frac{\partial^2 T_s}{\partial x^2}+\frac{\partial^2 T_s}{\partial y^2})-h_{fs}a_{fs}(T_s-T_f) \tag{5-8}$$

5.1.2 Scale Analysis

In electronic cooling applications, time-averaged characteristics are of interest rather than those at a certain instant of time. Therefore, the following equations are defined as time-averaged components:

$$T_f=\overline{T}_f+\Delta T_f \tag{5-9a}$$

$$T_s=\overline{T}_s+\Delta T_s \tag{5-9b}$$

$$h_{fs}=\overline{h}_{fs}+\Delta h_{fs} \tag{5-9c}$$

$$u=\overline{u}+\Delta u \tag{5-9d}$$

where the quantity with bar "–" is the time-averaged component of that quantity while the quantity with "Δ" is the fluctuation component of the quantity. Applying the time-averaged components of Equations (5-9a) ~ (5-9d) into Equations (5-7) and (5-8), the energy equations of fluid and solid phases are

Fluid phase energy equation:

$$\rho_f c_{pf}\left(\overline{u}\frac{\partial\overline{T}_f}{\partial x}+\overline{\Delta u\frac{\partial(\Delta T_f)}{\partial x}}\right)=$$
$$(\varepsilon k_f+k_d)\frac{\partial^2\overline{T}_f}{\partial y^2}+\overline{h}_{fs}a_{fs}(\overline{T}_s-\overline{T}_f)+\overline{\Delta h_{fs}a_{fs}(T_s-\Delta T_f)} \tag{5-10}$$

Solid phase energy equation:

$$0=(1-\varepsilon)k_s(\frac{\partial^2\overline{T}_s}{\partial x^2}+\frac{\partial^2\overline{T}_s}{\partial y^2})-\overline{h}_{fs}a_{fs}(\overline{T}_s-\overline{T}_f)-\overline{\Delta h_{fs}a_{fs}(T_s-\Delta T_f)} \tag{5-11}$$

Substituting Equation (5-12) into Equation (5-10),

$$\left[\overline{h}_{fs}a_{fs}(\overline{T}_s-\overline{T}_f)+\overline{\Delta h_{fs}a_{fs}(T_s-\Delta T_f)}\right]=(1-\varepsilon)k_s(\frac{\partial^2\overline{T}_s}{\partial x^2}+\frac{\partial^2\overline{T}_s}{\partial y^2}) \tag{5-12}$$

The fluid phase energy Equation can be re-written as

$$\begin{aligned}&\rho_f c_{pf}\left(-\overline{u}\frac{\partial\overline{T}_f}{\partial x}+\overline{\Delta u\frac{\partial(\Delta T_f)}{\partial x}}\right)=\\&(\varepsilon k_f+k_d)\frac{\partial^2\overline{T}_f}{\partial y^2}+(1-\varepsilon)k_s(\frac{\partial^2\overline{T}_s}{\partial x^2}+\frac{\partial^2\overline{T}_s}{\partial y^2})\end{aligned} \tag{5-13}$$

The term $\overline{\Delta u\frac{\partial(\Delta T_f)}{\partial x}}$ can be neglected because it is small compared to the averaged convection term $-\overline{u}\frac{\partial\overline{T}_f}{\partial x}$. Equation (5-13) can now be rewritten as follows:

$$\rho_f c_{pf}\left(-\overline{u}\frac{\partial\overline{T}_f}{\partial x}\right)=(\varepsilon k_f+k_d)\frac{\partial^2\overline{T}_f}{\partial y^2}+(1-\varepsilon)k_s(\frac{\partial^2\overline{T}_s}{\partial x^2}+\frac{\partial^2\overline{T}_s}{\partial y^2}) \tag{5-14}$$

Based on the condition of constant heat flux at the bottom wall along the x axial direction, Equation (5-14) can be reduced to

$$\rho_f c_{pf}\left(-\overline{u}\frac{\partial\overline{T}_f}{\partial x}\right)=(\varepsilon k_f+k_d)\frac{\partial^2\overline{T}_f}{\partial y^2}+(1-\varepsilon)k_s\frac{\partial^2\overline{T}_s}{\partial y^2} \tag{5-15}$$

For the scale analyses of the heat transfer in a porous channel, the symbol " ¯ " in Equation (5-15) is dropped for simplicity. The scale analysis can be expressed as:

$$\rho_f c_{pf}u\frac{\Delta T}{x}\sim(\varepsilon k_f+k_d)\frac{\Delta T}{\delta_t^{\,2}}+(1-\varepsilon)k_s\frac{\Delta T}{\delta_t^{\,2}} \tag{5-16}$$

where ΔT is the temperature difference of the hot wall surface and the bulk temperature of the fluid. δ_t is the thickness of the thermal boundary layer. It is noted

that the temperature scales for solid and fluid phases are assumed to be the same. Equation (5-16) can be rearranged as

$$\frac{\delta_t^2}{x^2} \sim \frac{[\varepsilon k_f + k_d + (1-\varepsilon)k_s]}{\rho_f c_{pf} u x} \tag{5-17}$$

Definitions of the effective thermal conductively k_{eff}, effective thermal diffusivity α^* of porous media and the effective local Peclet number Pe_x^* are shown as:

$$k_{eff} = \varepsilon k_f + k_d + (1-\varepsilon)k_s \tag{5-18}$$

$$k_d = 0.025 \rho_f c_f u \sqrt{K} \tag{5-19}$$

$$\alpha^* = \frac{k_{eff}}{\rho_f c_{pf}} \tag{5-20}$$

$$\mathrm{Pe}_x^* = \frac{ux}{\alpha^*} \tag{5-21}$$

Note that Pe_x^* is a function of x. Substituting Equations (5-18) ~ (5-21) into Equation (5-17):

$$\frac{\delta_t}{x} \sim \left(\frac{ux}{\alpha^*}\right)^{-\frac{1}{2}} = \mathrm{Pe}_x^{*-\frac{1}{2}} \tag{5-22}$$

The local Nusselt number Nu_x can be expressed as

$$\mathrm{Nu}_x = h_x \frac{D_e}{k_f} \sim \frac{k_{eff}}{\delta_t} \frac{D_e}{k_f} = \left(\frac{k_{eff}}{k_f}\right)\left(\frac{D_e}{x}\right)\left(\mathrm{Pe}_x^*\right)^{\frac{1}{2}} \tag{5-23}$$

where D_e is the hydraulic diameter of channel. The length-averaged Nusselt number is given by (Zhao and Cheng, 1995)

$$\mathrm{Nu}_{avg} = \frac{1}{L}\int_0^L \mathrm{Nu}_x dx = \frac{1}{L}\int_0^L \left(\frac{k_{eff}}{k_f}\right)\left(\frac{D_e}{x}\right)\left(\frac{ux}{\alpha^*}\right)^{\frac{1}{2}} dx \tag{5-24}$$

Performing the integration of the local Nusselt number over the entire length of the porous channel along the flow direction, the scale analysis of the length-averaged

Nusselt number can be expressed as:

$$\mathrm{Nu}_{avg} \sim \left(\frac{k_{eff}}{k_f}\right)\left(\frac{D_e}{L}\right)^{\frac{1}{2}}\left(\mathrm{Pe}^*\right)^{\frac{1}{2}} \tag{5-25}$$

where $\mathrm{Pe}^* = \frac{uD_e}{\alpha^*}$ is the Peclet number based on the hydraulic diameter of the channel.

5.2 Oscillatory Heat Transfer in Metal Foam Channel

5.2.1 Cycle-averaged Heat Transfer Characteristics

As described previously, the current experimental facility was designed to test oscillating flow in metal foam channel which possesses the reversed flow direction in every half-cycle. The test section was heated uniformly at the bottom of the channel by a film heater, and two identical coolers are located at the two ends of the test sections. The reciprocating motion of air flow in the test section was created by a sinusoidal movement generator which was designed such that the fluid displacement and frequency can be adjusted. In the first half-cycle, the fluid passes through the test section and carries the heat generated by film heater into the unheated section where the coolers located. The fluid temperature drops quickly because the cooling water is forced through the coolers to remove the heat carried by oscillating flow. In the next half-cycle as the fluid reverses its direction, the cooler fluid enters the channel and cool down the test section again. In order to evaluate the heat transfer performance of oscillating flow in metal foam channel, the cycle-averaged local temperature and Nusselt number are introduced in the present study. The cycle-averaged local surface temperature is defined as the average temperature of local wall temperatures measured by thermocouple during a certain number of the reciprocating cycles. The cycle-averaged local Nusselt number is calculated based on the cycle-averaged surface temperature as follows:

$$\mathrm{Nu}_x = \frac{h_x D_e}{k_f} \tag{5-26}$$

where k_f is the thermal conductivity of the fluid. D_e and h_x are the hydraulic diameter of the channel and the local heat transfer coefficient, respectively.

$$D_e = \frac{5H}{3} \tag{5-27}$$

$$h_x = \frac{Q}{A_{\text{heated}}(T_w - T_i)} \tag{5-28}$$

where T_w and T_i are the cycle-averaged local surface and the bulk air inlet temperatures, respectively. H is the height of the channel, and Q and A_{heated} are the power input and the heated area on the bottom of the channel, respectively. In the calculation, k_f is evaluated from the text by Holman (1990) based on measured local air temperatures at atmospheric pressure.

To focus on investigating the heat transfer characteristics of oscillating flow in open-cell metal foam, the aluminium foam 40 PPI was selected as the tested material to conduct experiments with various power inputs. The effects of oscillatory frequency and flow displacement on the heat transfer in porous channel are studied through the dimensionless flow amplitude A_0 and the kinetic Reynolds number Re_ω, which were defined based on the hydraulic diameter of channel.

$$A_0 = \frac{x_{\max}}{D_e} \tag{5-29}$$

$$\mathrm{Re}_\omega = \frac{2\pi f D_e^{\,2}}{\nu_f} \tag{5-30}$$

where $x_{\max}$ is the maximum flow displacement and f is the oscillatory frequency. The oscillatory frequency was obtained by measuring the number of times the flow reverses its direction in a specified period of time, and the maximum flow

displacement was determined by the length of the stroke movement. For various power inputs, the heat transfer experiments were performed by changing the oscillatory frequency, i.e. kinetic Reynolds number at each flow displacement of 52, 60 and 68 mm.

5.2.2 Local Temperature and Nusselt Number Distributions

Figure 5-1 shows the cycle-averaged local surface temperature distribution along the axial direction with the different oscillatory frequencies and the maximum flow displacements for the power inputs of 20 and 60 W. To reflect the actual temperature distribution of oscillating flow and to compare with that of steady flow, the dimensional temperature is used in the calculations. Figure 5-1 (a) presents the local surface temperature of oscillating flow through metal foam 40 PPI with the kinetic Reynolds number ranged from 198 ~ 793 and with the maximum flow displacement of 52 mm. It can be observed that the cycle-averaged temperature distribution decreases with the increase of Reynolds number but increases with the increase of the input heat flux. Due to the flowing characteristic of oscillating flow - the flow direction reverses its direction during each cycle which yields two thermal entrances in the test section. To express the trend clearly, a quadratic polynomial was employed to fit the experimental data. The distribution fitting curves of the local surface temperature are convex and approximately symmetric about the centre of the test section where the temperature is the highest. The measured highest temperatures are located at positions x/D_e =1.2858 and 1.7142 around the centre of the test section. The local surface temperatures near both entrances (x/D_e = 0 and 3) are lower than that at the centre of the test section. For example, at power input Q = 60 W and Re_ω = 793, the local surface temperatures at x/D_e = 1.2858 and 1.7142 are 171.5 and 171.9 °C, respectively. The surface temperatures of the two entrances positions x/D_e = 0 and 3

are 165.4 and 166.3 °C, respectively. The same trends can be found in Figure 5-1 (b) for oscillating flow through Aluminium 40 PPI with various frequencies at a fixed flow displacement of 68 mm. It is also observed that the inlet and outlet bulk temperatures (isolated points plotted on Figure 5-1) are much lower than the temperatures in the test section due to the cooling effect of the coolers located at the two ends of the test section. The temperatures at the inlet bulk are almost equal to that at the outlet bulk. This is because of the presence of two entrances in the test section which serve as heat sinks for each entrance.

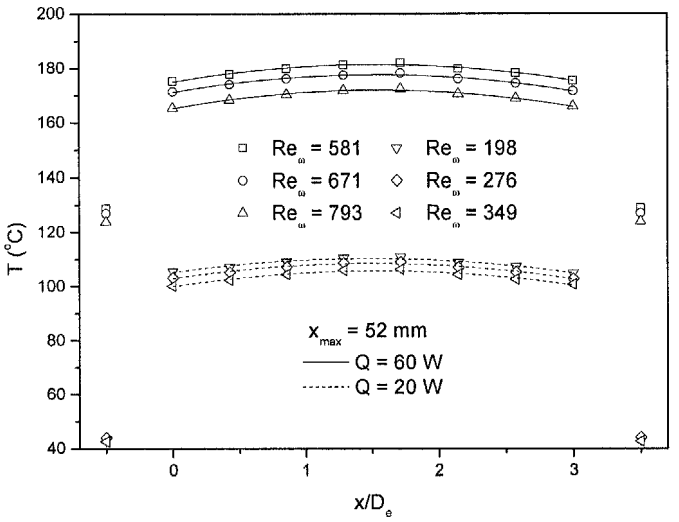

(a)

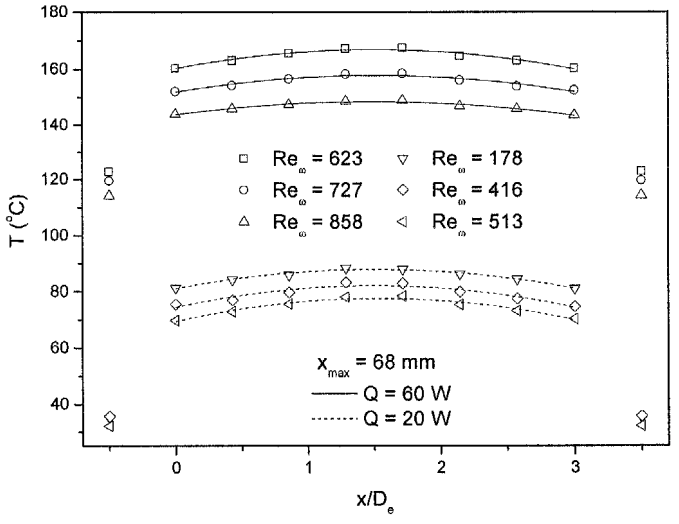

(b)

Figure 5-1 Cycle-averaged local temperature distributions for (a) the maximum flow displacement of 52 mm, (b) the maximum flow displacement of 68 mm for power inputs of 20 and 60 W

Figure 5-2 shows the cycle-averaged local Nusselt number versus the dimensionless axial distance for the cases presented in Figure 5-1. The data of the local Nusselt number shown in Figure 5-2 are calculated by Equation (5-26) based on the cycle-averaged local surface temperature. The choice of the inlet bulk temperature to calculate the local Nusselt number takes into consideration the thermal potential for heat transfer from the heated surface to the cold fluid (air flow). Figure 5-2 (a) shows the cycle-averaged local Nusselt number distribution for oscillating flow through aluminium 40 PPI with different kinetic Reynolds number at the maximum flow displacement of 52 mm. It can be seen that the cycle-averaged local Nusselt number in the thermal entrance region is higher than that in the location around the centre of the test section. As shown in Figure 5-2 (a) for the power input Q = 20 W and Re_{ω} = 793, the cycle-averaged local Nusselt number reaches higher values of 238 and 235 at the two thermal entrances. The lower values of the averaged Nusselt number of 205 and 203 are obtained at the dimensionless locations x/D_e = 1.2858 and 1.7142 around the centre of the test section, respectively. As a consequence, the distribution curves of the cycle-averaged local Nusselt number for oscillating flow are concave. Figure 5-2 (b) presents the same trend of local Nusselt number distribution of oscillating flow through metal foam channel with different kinetic Reynolds number at the maximum flow displacement of 68 mm. It is also observed that the cycle-averaged Nusselt number increases with the increase of kinetic Reynolds number at the fixed flow displacement for different power inputs. A similar trend was reported by Zhao and Cheng (1995) through a numerical study of heat transfer in an empty tube subjected to oscillating flow.

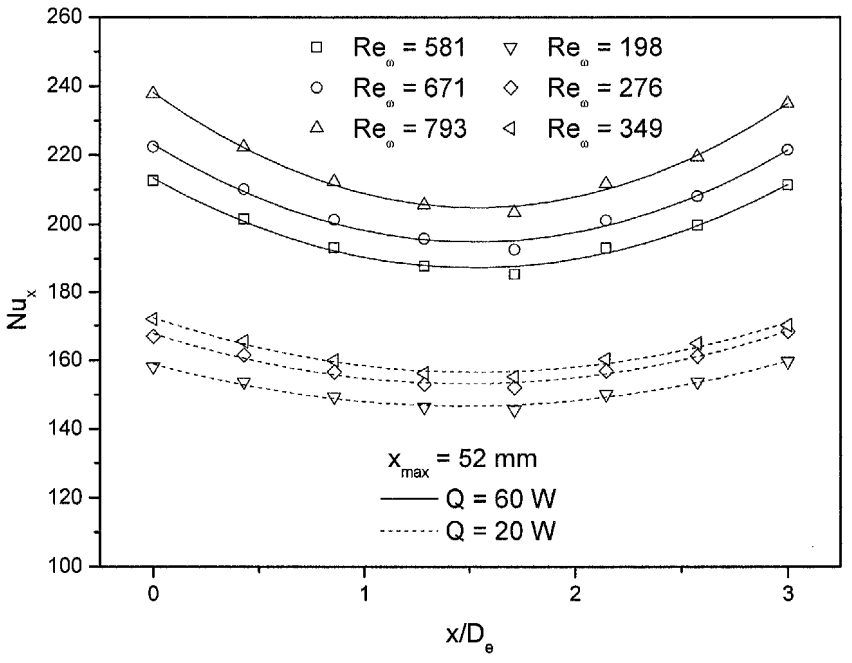

(a)

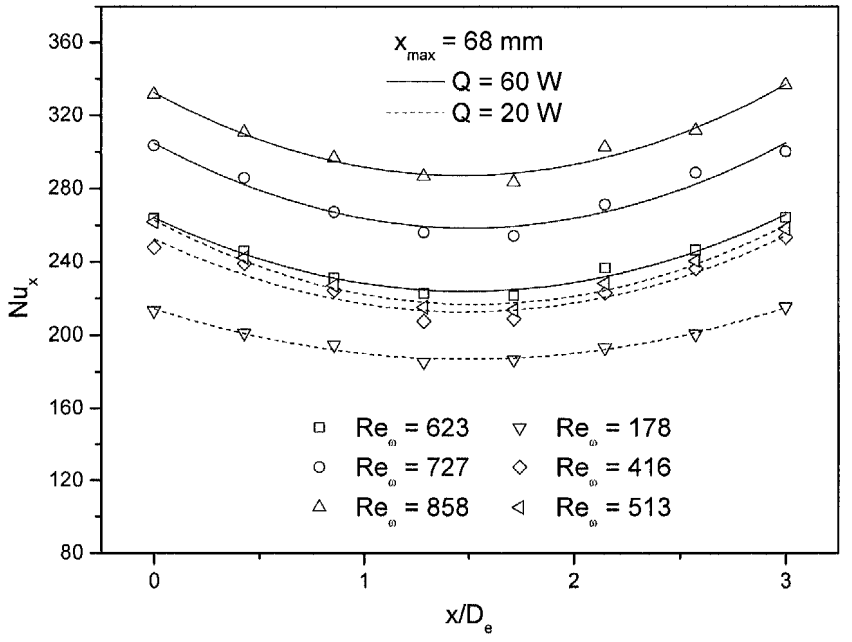

(b)

Figure 5-2 Cycle-averaged local Nusselt number distributions for (a) the maximum flow displacement of 52 mm, (b) the maximum flow displacement of 68 mm for power inputs of 20 and 60 W

Figure 5-3 (a) presents the cycle-averaged local surface temperature distribution on the substrate surface along the axial direction in oscillating flow with oscillatory frequency f = 3.1 ~ 3.8 Hz and power inputs Q = 20, 40 and 60 W for both empty and porous channels. For both empty and porous channels, there are two thermal entrance regions in the test section due to the reversing flow direction. The surface temperatures located at the two entrances are lower than that at the centre of the test section. The local surface temperature distribution curves are convex with the maximum point at the centre of the test section. It is obvious that for different input power, the surface temperature profile in the empty channel is much higher than that in channel filled with metal foam. The advantages of large surface-area-to-volume ratio and intense mixing of flowing flow of metal foam resulted in a much lower surface temperature distribution in a porous channel subjected to oscillating flow.

Figure 5-3 (b) shows the cycle-averaged local Nusselt number in both empty and porous channels along the dimensionless axial distance with the range of oscillation frequency from 3.1 to 3.8 Hz for power inputs Q = 20, 40 and 60 W. From Figure 5-3 (b), it can be seen that the cycle-averaged local Nusselt number decreases as dimensionless location x/D_e approaches the centre of the test section. The Nusselt number distribution curves are concave with the minimum value around the centre of the test section as the symmetric point. The results obtained by Fu *et al.* (2001) show the same trends of Nusselt number distribution for oscillating flow in a porous channel. It is obvious that the cycle-averaged Nusselt number for oscillating flow in porous channel is much higher than that in an empty channel. Calculating the mean value of the cycle-average local Nusselt numbers shown in Figure 5-3 (b), the result shows that the average Nusselt number in aluminium foam 40 PPI is about 3 times larger than that in empty channel. It is noted that the difference of cycle-averaged

local Nusselt number between the two ends of the test section and centre locations in porous channel is larger than that in empty channel. This indicates that heat transfer performance can be significantly enhanced at the thermal entrance region in oscillating flow through a channel filled with metal foam. The higher heat transfer rate in porous channel is because that the effective thermal conductivity of oscillating flow will be increased by the inserted aluminium foam.

Based on the stagnant effective thermal conductivity model, Calmidi and Mahajan (1999) obtained a correlation of effective thermal conductivity k_{eff} for metal foam, which can be expressed as

$$k_{eff} = \varepsilon k_f + 0.181(1-\varepsilon)^{0.762} k_s \tag{5-31}$$

where k_f and k_s are thermal conductivities of the fluid and solid phases. Using Equation (5-31), the variation of effective thermal conductivity of oscillating flow through the channel filled with aluminium foam 40 PPI is shown in Figure 5-4. It should be noted that for $\varepsilon = 1$, i.e. empty channel, the effective thermal conductivity is equal to the fluid thermal conductivity. It can be seen that the effective thermal conductivity decreases with the increase of the porosity of metal foam. Comparing the tested porous channel ($\varepsilon = 0.9$) and empty channel ($\varepsilon = 1$), it can be seen that the effective thermal conductivity in metal foam is much higher than that in empty channel. The large difference in the effective thermal conductivity results in high heat transfer rate achieved by oscillating flow through metal foam as compared to that through empty channel.

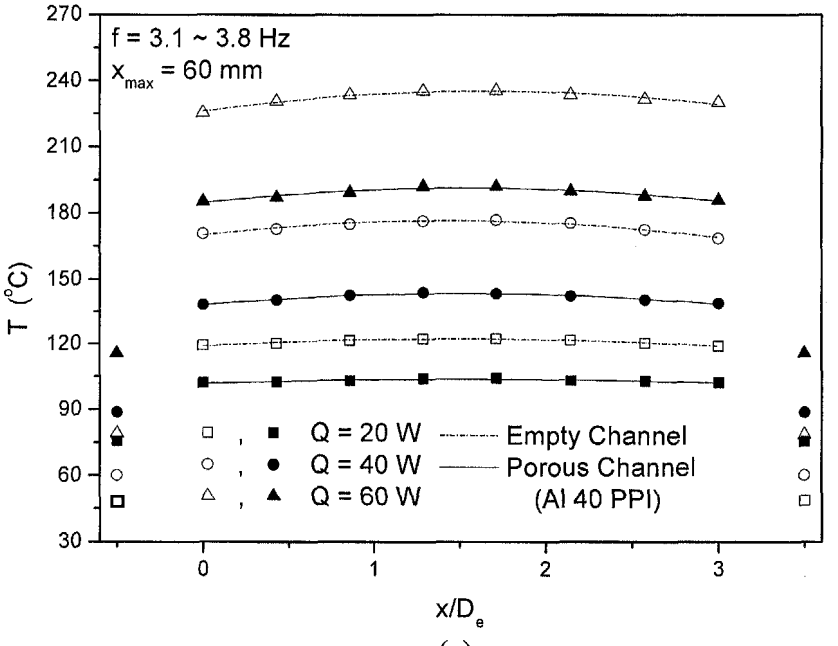

(a)

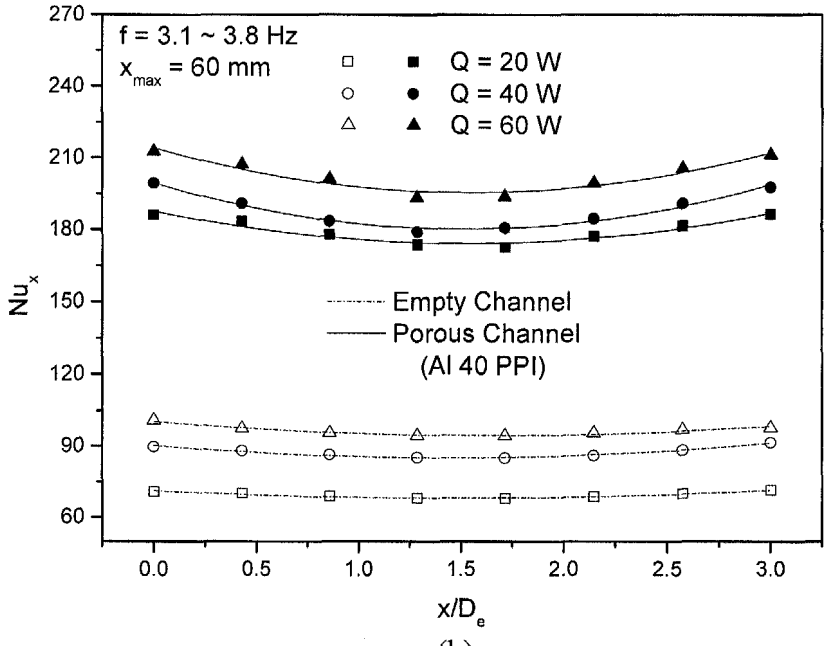

(b)

Figure 5-3 Comparison of heat transfer in oscillating flow through porous and empty channel: (a) cycle-averaged surface temperature distribution; (b) cycle-averaged local Nusselt number distribution

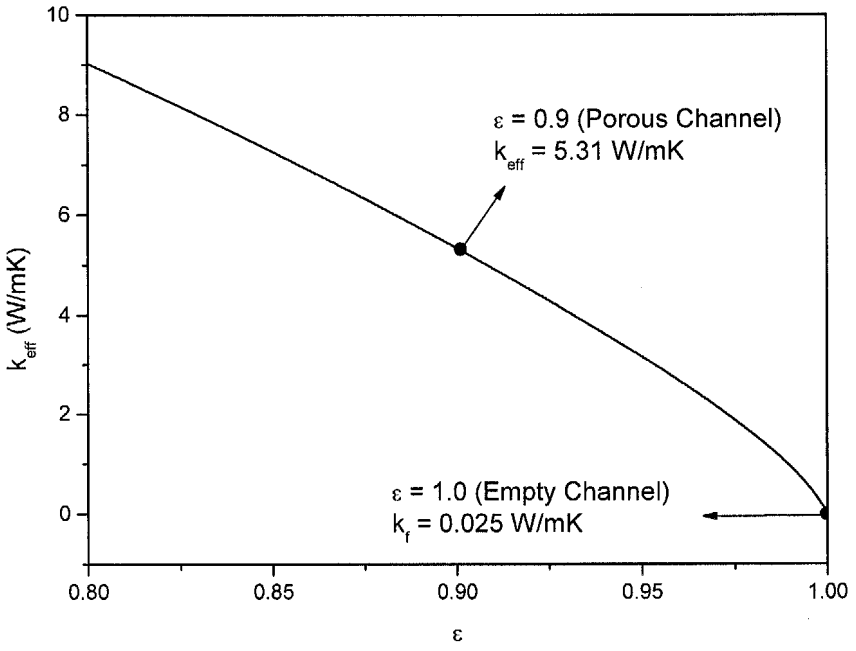

Figure 5-4 Variation of the effective thermal conductivities with the porosities of the channel

5.2.3 Effects of Oscillatory Frequency and Flow Amplitude

The discussion of the fluid behaviour in open-cell metal foam shows that the oscillatory frequency and the flow amplitude are the critical factors in oscillating flow through a porous channel. To reveal the effects of the oscillatory frequency and the maximum flow displacement on the heat transfer of oscillating flow through open-cell metal foam, the dimensionless flow amplitude defined in Equation (5-29) and the kinetic Reynolds number defined in Equation (5-30) are employed to study the heat transfer characteristics of oscillating flow through metal foam channel.

The effect of kinetic Reynolds number on the cycle-averaged local surface temperature of aluminium foam 40 PPI for amplitudes of flow displacement A_0 = 3.1, 3.6 and 4.1 at the power input Q = 40 W is presented in Figures 5-5, 5-6 and 5-7, respectively. Figure 5-5 shows the temperature distribution on the substrate surface for oscillating flow with the kinetic Reynolds number ranging from 198 to 883 at the

dimensionless flow amplitude of 3.1, i.e. the maximum flow displacement of 52 mm. It can be observed that the cycle-averaged local surface temperature profile decreases with the increase of the kinetic Reynolds number for different flow displacement. For a close-up view of temperature profiles shown in Figure 5-5, the temperatures for Re_ω = 459 is about 10°C lower than that for Re_ω = 272 for different locations of the test section. It implies that high oscillatory frequency corresponds to low cycle-averaged local surface temperature. Figures 5-6 and 5-7 show the same trend of temperature profiles for different flow amplitudes. As shown in these figures, a temperature difference of approximately 30 ~ 40°C can be achieved between the maximum and minimum kinetic Reynolds numbers for the dimensionless flow amplitude from 3.1 ~ 4.1. Once again, it can be seen that the temperature distribution curves are of convex shape with the maximum point located around the centre of the test section.

Figures 5-8, 5-9 and 5-10 present the distributions of the calculated local Nusselt numbers for oscillating flow with various kinetic Reynolds numbers at the dimensionless flow amplitude A_0 = 3.1, 3.6 and 4.1, respectively. Figure 5-8 shows the effect of kinetic Reynolds number on the cycle-averaged local Nusselt number of oscillating flow in porous channel for Re_ω = 198 ~ 883 and x_{max} = 52 mm i.e. A_0 = 3.1. It is shown that the cycle-averaged local Nusselt number increases with the increase of kinetic Reynolds number, i.e. oscillatory frequency. Physically, higher oscillatory frequency means shorter cycle time for oscillating flow reverses its direction. It implies that for a certain cooling period, high frequency results in more cooler fluid entering the porous channel alternately from the two inlets and then the heat transfer performance is enhanced. It is also seen that for varying oscillatory frequency, the distribution curves of cycle-averaged local Nusselt number are concave about the centre of the test section as the symmetric point. The same distribution of cycle-

averaged local Nusselt number can be found in Figures 5-9 and 5-10 for oscillating flow through porous channel with the various flow amplitudes.

From a more close-up view of these figures, it is observed that the trend of the increase of cycle-averaged local Nusselt number is subdued with the increase of the kinetic Reynolds numbers at a fixed flow displacement. For example, as shown in Figure 5-9, the local Nusselt number increases by approximately 20 ~ 30 at different locations of the test section when the kinetic Reynolds number increased from 178 ~ 336. However, it only increases by 5 ~ 8 for kinetic Reynolds numbers from 582 ~ 727 along the test section. This implies that at very high kinetic Reynolds number, the increase in heat transfer of oscillating flow through open-cell foam channel is marginal.

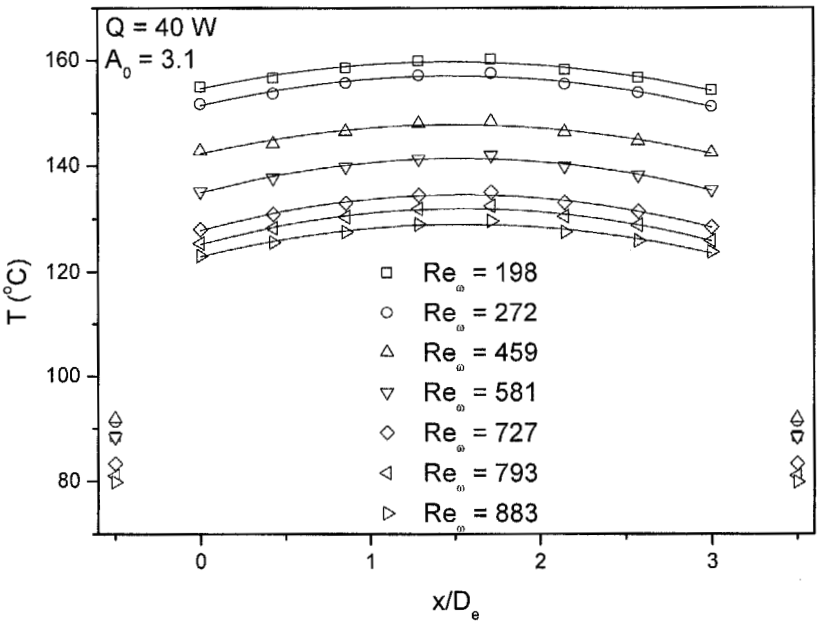

Figure 5-5 Effect of kinetic Reynolds number Re_ω on the distribution of cycle-averaged local surface temperature at $A_0 = 3.1$

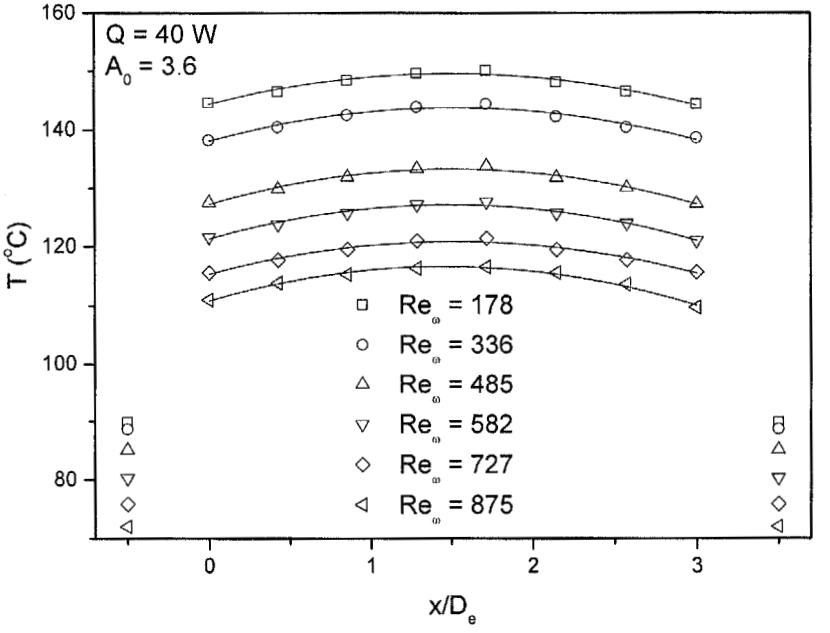

Figure 5-6 Effect of kinetic Reynolds number Re_ω on the distribution of cycle-averaged local surface temperature at $A_0 = 3.6$

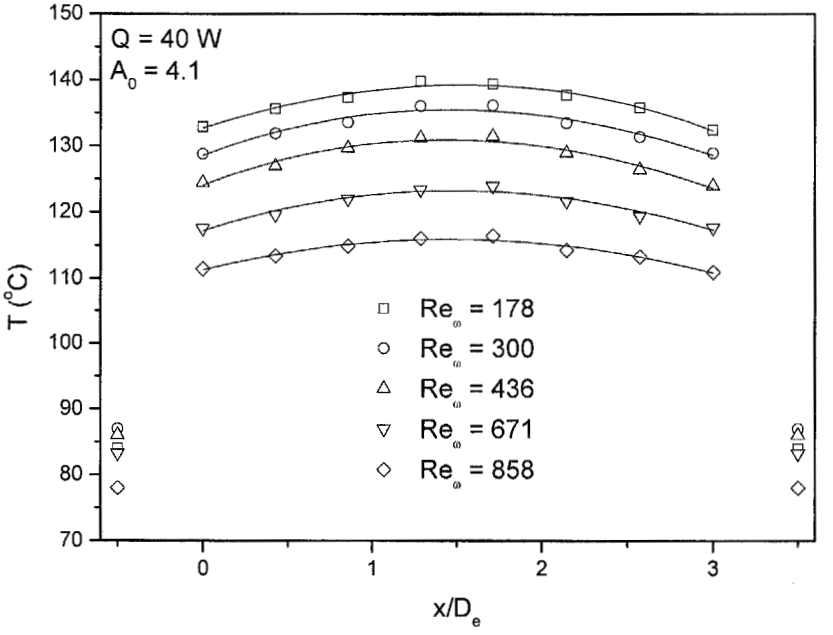

Figure 5-7 Effect of kinetic Reynolds number Re_ω on the distribution of cycle-averaged local surface temperature at $A_0 = 4.1$

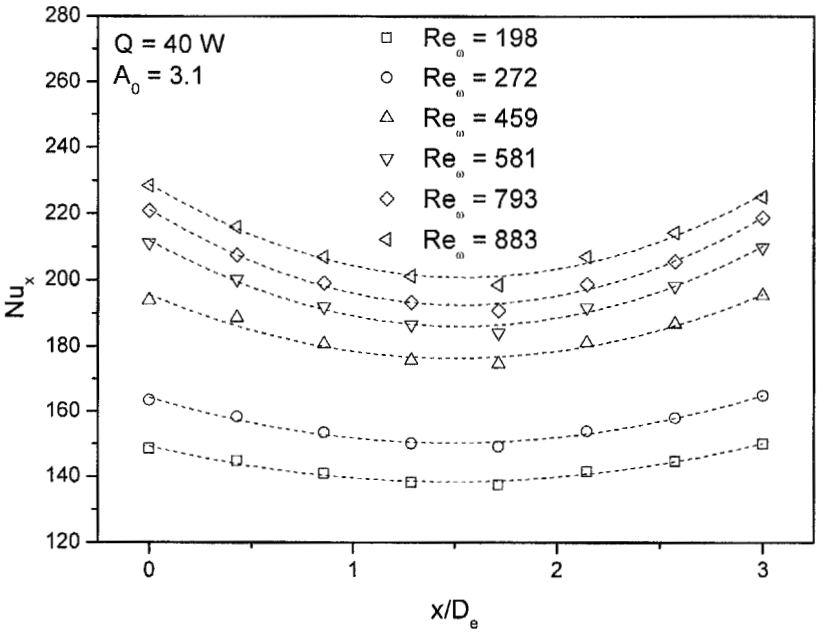

Figure 5-8 Effect of kinetic Reynolds number Re_ω on the distribution of cycle-averaged Nusselt Number at $A_0 = 3.1$

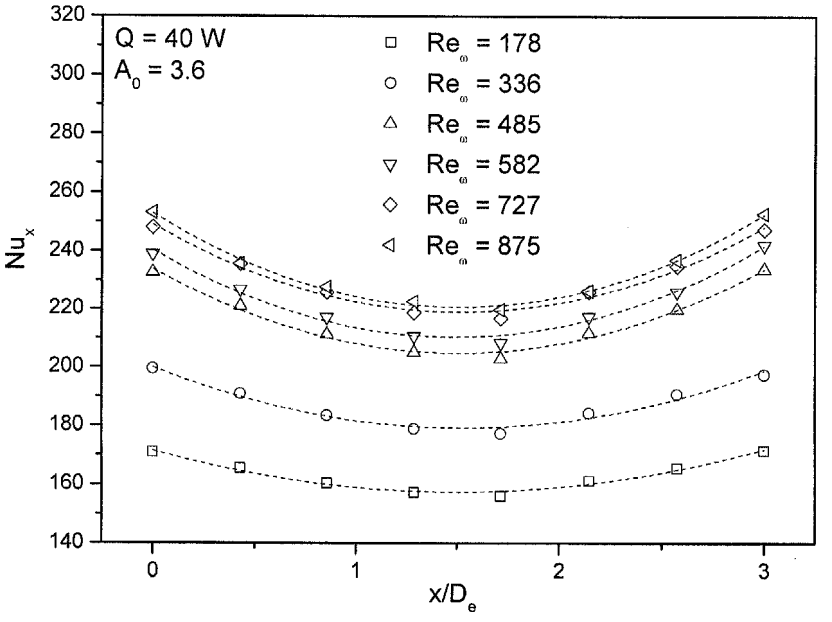

Figure 5-9 Effect of kinetic Reynolds number Re_ω on the distribution of cycle-averaged Nusselt Number at $A_0 = 3.6$

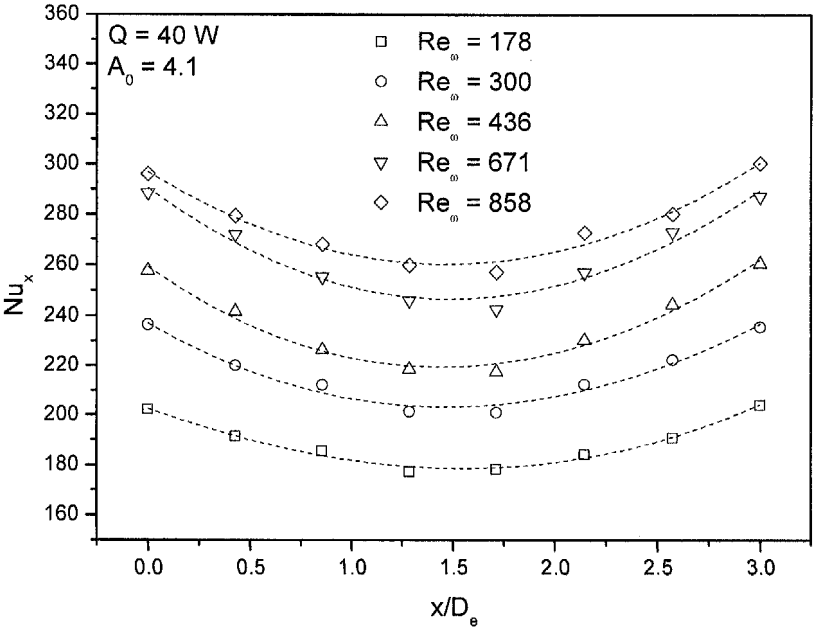

Figure 5-10 Effect of kinetic Reynolds number Re_ω on the distribution of cycle-averaged Nusselt Number at $A_0 = 4.1$

Figure 5-11 shows the effect of dimensionless amplitude of flow displacement A_0 on heat transfer of oscillating flow in a porous channel with different kinetic Reynolds numbers. It can be seen from Figure 5-11 that the temperature profile decreases with an increase in the dimensionless amplitude of flow displacement for various kinetic Reynolds numbers. For various flow amplitudes and kinetic Reynolds numbers, the cycle-averaged local surface temperature distributions are of concave shape with the lowest temperatures at the two thermal entrance regions. The same profile of temperature distribution curve for different flow amplitudes at Re_ω = 727 and 858 to 884 is obtained as shown in Figure 5-12.

Figures 5-13 and 5-14 present the effect of dimensionless flow amplitude A_0 on the distribution of cycle-averaged Nusselt number at different Reynolds numbers. It is clear that the profile of cycle-averaged local Nusselt number for large A_0 is higher than that for small A_0. A closer observation shows that the curvature of Nusselt number distribution curves for large displacements is larger than those for small displacements. This implies that length of the thermal entrance region for oscillating flow with large amplitude of displacement is longer than that for oscillating flow with small amplitude of displacement. It can be deduced that higher heat transfer rates can be obtained by larger displacement oscillating flows with high kinetic Reynolds number in a porous channel. From a close-up view of Figures 5-13 and 5-14, it can be observed that the increase of cycle-averaged local Nusselt number is almost well-proportioned with the increase of the dimensionless flow amplitude. For example, as shown in Figure 5-13, the increase of the cycle-averaged local Nusselt number profile for Re_ω = 178 ~198 is about 10 and 12 when the dimensionless flow amplitude is increased from 3.1 to 3.6 and from 3.6 to 4.1, respectively. This indicates that higher maximum flow displacement provides significant enhancement in heat transfer for

oscillating flow through the open-cell metal foam.

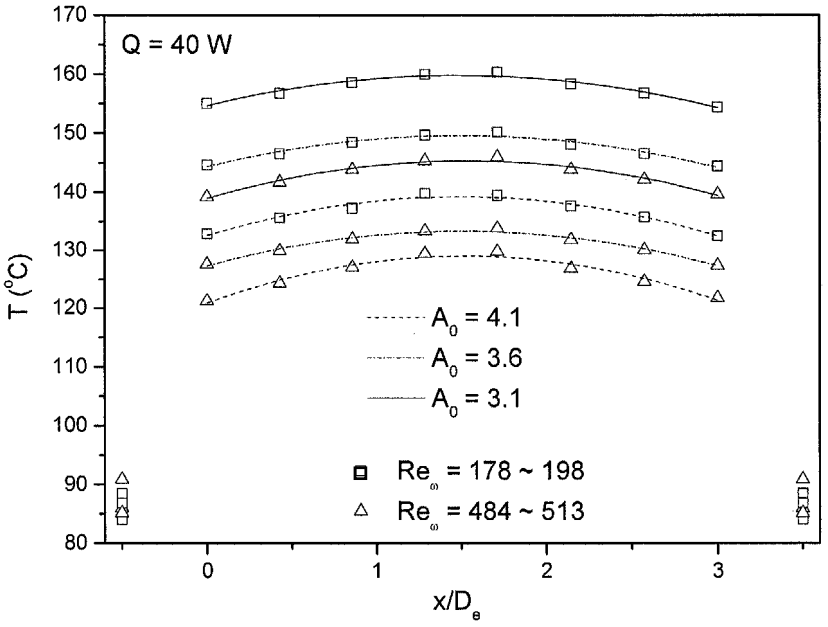

Figure 5-11 Effect of dimensionless flow amplitude on the distribution of cycle-averaged surface temperature at Re_ω = 178 ~ 513

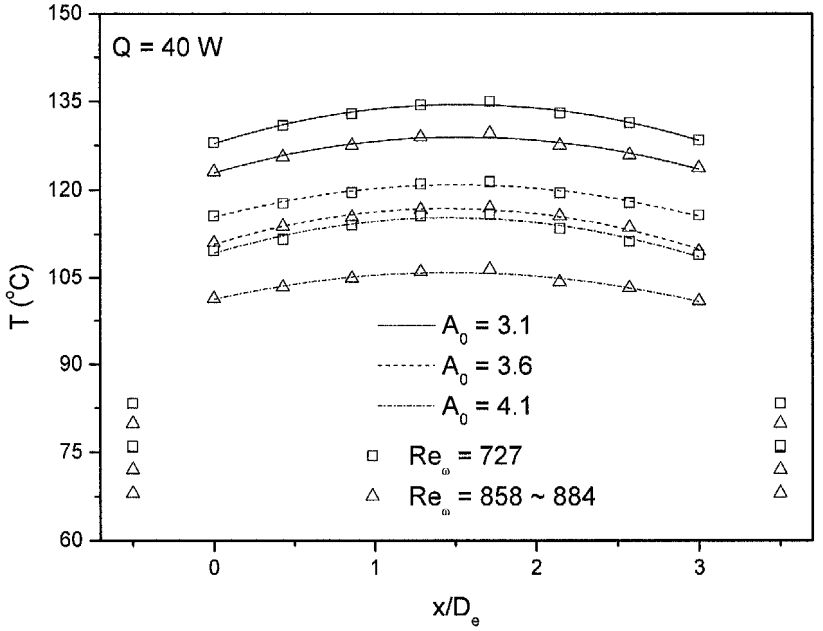

Figure 5-12 Effect of dimensionless flow amplitude on the distribution of cycle-averaged surface temperature at Re_ω = 727 ~ 884

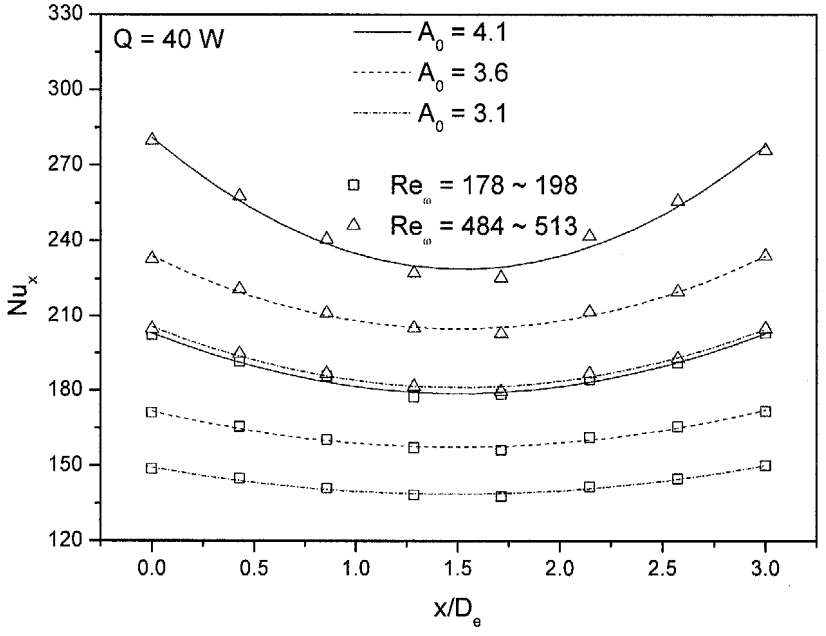

(b)

Figure 5-13 Effect of dimensionless flow amplitude on the distribution of cycle-averaged Nusselt number at Re_ω = 178 ~ 513

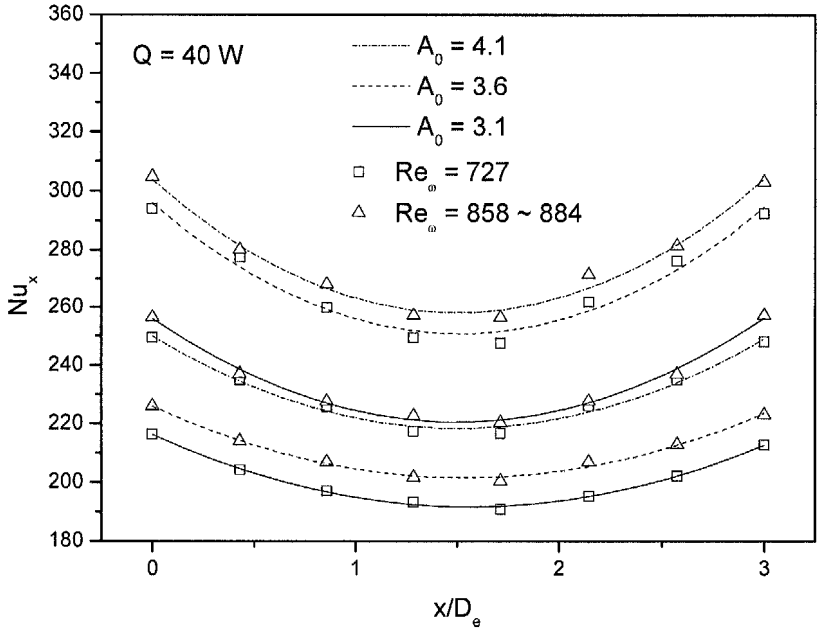

Figure 5-14 Effect of dimensionless flow amplitude on the distribution of cycle-averaged surface temperature at Re_ω = 727 ~ 884

5.2.4 Total Heat Transfer Rate

In order to evaluate the effects of dimensionless amplitude of flow displacement A_0 and kinetic Reynolds number Re_ω on the total heat dissipation rate in a porous channel subjected to oscillating flow, the length-averaged Nusselt number was used to calculate the averaged Nusselt number of the whole length of the section. Figure 5-15 presents the length-averaged Nusselt number versus kinetic Reynolds number with different dimensionless amplitude of flow displacement for a porous channel with L/D_e = 3. Generally, the length-averaged Nusselt number Nu_{avg} increases with both dimensionless parameters of A_0 and Re_ω. An interesting finding in this figure is that for a fixed dimensionless amplitude of flow displacement A_0, the length-averaged Nusselt number approaches a constant value for a kinetic Reynolds number Re_ω of about 874. This implies that very high oscillatory frequency has very little contribution to an increase in heat transfer rate in oscillating flow through a porous channel. This suggests that oscillating flow at relatively low frequency and high amplitude of displacement has a substantial effect on the heat transfer behaviour in a porous channel since the temperature fluctuation on the wall surface cannot follow the oscillatory velocity at a very high frequency. The length-averaged Nusselt number is effectively increased by increasing the kinetic Reynolds number in a suitable range from 178 to 874 for L/D_e = 3 and A_0 = 3.1 ~ 4.1.

The response speed of the temperature variation under oscillatory condition related to the delay time which represents the time when the temperature at a position in porous channel fluctuates from the initial temperature to the mean temperature. In general, the delay time decreases with the enhanced heat transfer due to the increased thermal diffusivity, which is a measure of how quickly a temperature disturbance can propagate through a material.

However, it is rather difficult to determine the practical delay time of the temperature variation at one position in the porous channel with the oscillation frequency. Therefore, a dimensionless delay time t^* introduced by Chatwin (1975) is used to evaluate the fluctuation speed of temperature response to the flow oscillatory speed. The dimensionless delay time t^* can be obtained from the effective thermal diffusivity α^* which can be expressed as

$$t^* = \frac{\alpha^*}{\omega x_{\max}^2} = \frac{k_{eff}}{\rho_f c_{pf} \omega x_{\max}^2} \tag{5-32}$$

where k_{eff}, ω, $x_{\max}$ are the effective thermal conductivity, angular frequency and maximum flow displacement, respectively. The dimensionless delay times against the kinetic Reynolds numbers for oscillating flow through metal foam with different maximum flow displacements are plotted in Figure 5-16. It can be seen that the dimensionless delay time decreases first with increase of the flow amplitude and kinetic Reynolds number, and then approaches a constant value while the kinetic Reynolds number increases consecutively. It is also observed that the dimensionless delay time of oscillating flow with large flow amplitude is lower than that with small flow amplitude before the delay time approaches the constant value. This indicates that the temperature fluctuation speed cannot respond to the oscillation frequency if the kinetic Reynolds number is very high.

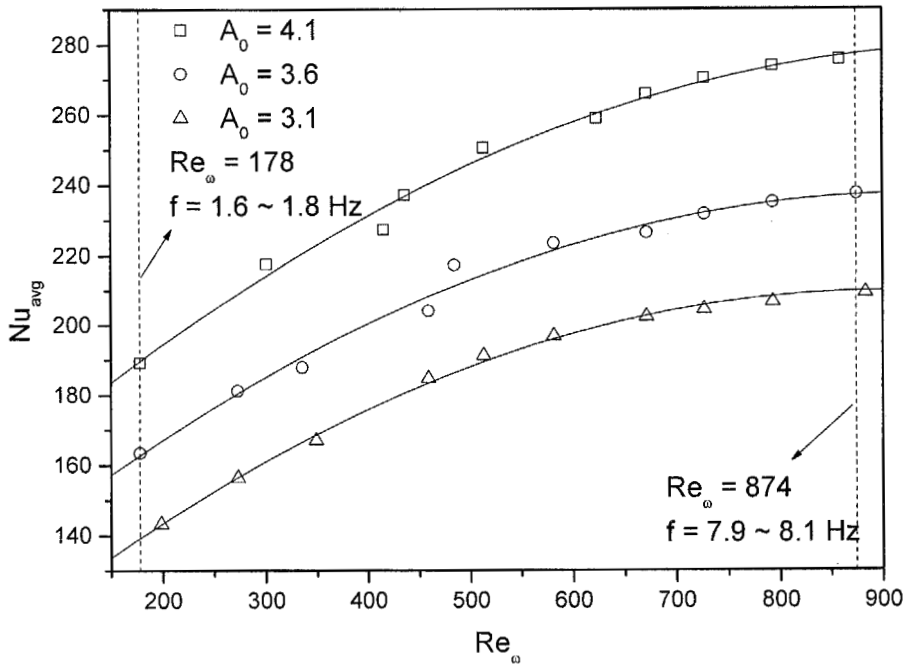

Figure 5-15 Effects of A_0 and Re_ω on the length-averaged local Nusselt number for a porous channel with $L/D_e = 3$

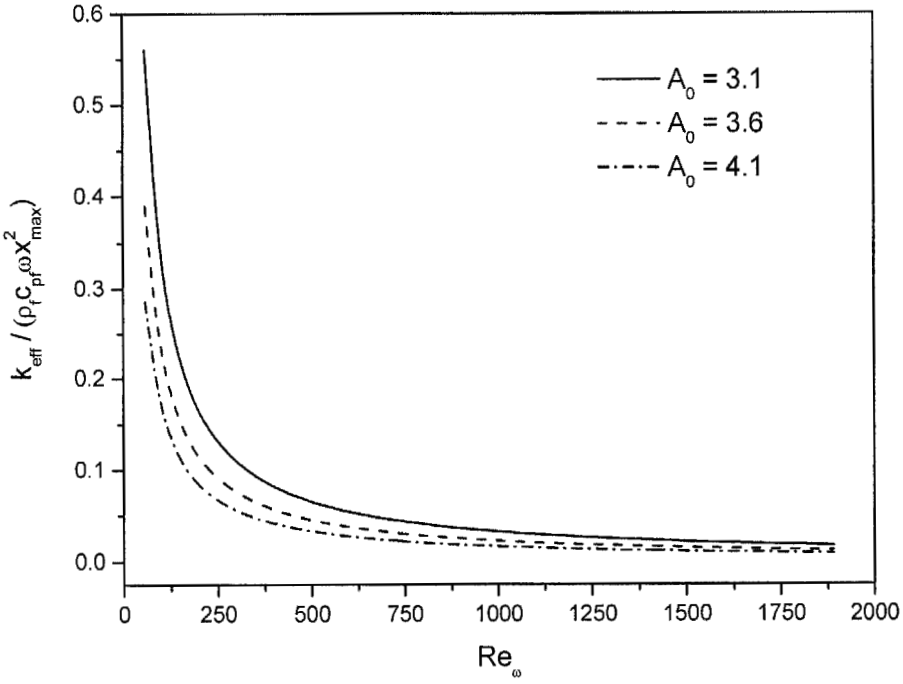

Figure 5-16 Dimensionless delay time $k_{eff}/\rho_f c_{pf}\omega x_{max}{}^2$ as a function of kinetic Reynolds number Re_ω

Using the least squares method, the data in Figure 5-15 can be collapsed onto a fitting line as shown in Figure 5-17. The resulting correlation equation of the length-averaged Nusselt number with the dimensionless amplitude of flow displacement and kinetic Reynolds number for oscillating flow with Re_ω = 150 to 900 and A_0 = 3.1 to 4.1 in a porous channel of L/D_e = 3 is

$$\mathrm{Nu}_{avg} = 12.38 A_0^{0.95}\, \mathrm{Re}_\omega^{0.31} \tag{5-33}$$

Equation (5-33) indicates that the effect of A_0 on the heat transfer behaviour in oscillating flow is more dominant than that of Re_ω due to the larger exponent of A_0. It implies that higher heat transfer performance can be obtained by oscillating flow through a porous channel with relatively low frequency and high displacement. A similar correlation equation obtained by Zhao and Cheng (1995) is given by

$$\mathrm{Nu}_{s\text{-}avg} = 0.02 A_0^{0.85}\, \mathrm{Re}_\omega^{0.583} \tag{5-34}$$

where $\mathrm{Nu}_{s\text{-}avg}$ is the space-cycle averaged Nusselt number defined as

$$\mathrm{Nu}_{s\text{-}avg} = \frac{qD}{k_f\left(\overline{T}_w - \overline{T}_m\right)} \tag{5-35}$$

where $\overline{T}_w$, $\overline{T}_{\mathrm{m}}$ and D are the space-cycle averaged wall temperature, space-cycle averaged temperature at the mixing chamber and the diameter of the pipe, respectively. Equation (5-34) gives the space-cycle Nusselt number in terms of Re_ω and A_0 in a long empty tube with constant heat flux subjected to oscillatory flow. Equations (5-33) and (5-34) indicate that the oscillatory frequency and flow amplitude have similar effect on the heat transfer for oscillating flow through empty and porous channels. The high heat transfer rate of oscillating flow through porous media obtained by the present study result in the large difference in the constants of Equations (5-33) and (5-34).

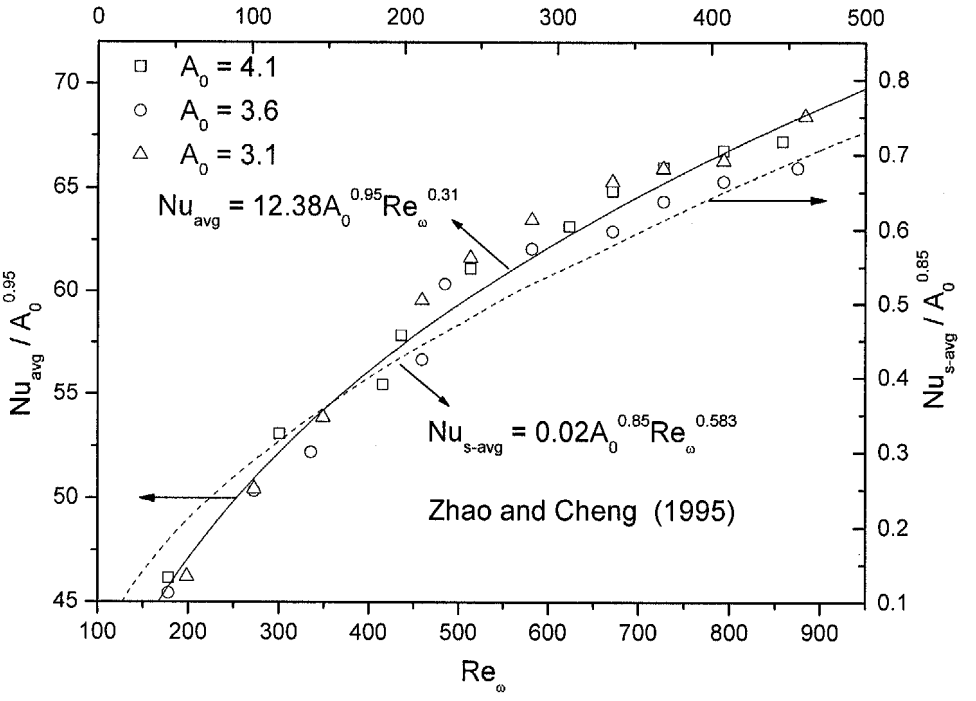

Figure 5-17 Correlation equation of the length-averaged local Nusselt number with A_0 and Re_ω for a porous channel with $L/D_e = 3$

5.3 Thermal Management Using Metal Foams

One of the primary reasons for studying forced convection in metal foams is their possible application in electronics cooling. The fibres of the metal foam with high thermal conductivity can be thought of as a complex network of extended surfaces emanating from the substrate of the heated surface. Furthermore, when a fluid flows through the metal foam matrix, it follows tortuous paths and undergoes considerable mixing. As a result, the efficiency of heat transfer from the fibres to the fluid is very high. For electronics cooling application, both temperature profile and temperature uniformity on the substrate need to be considered. To explore the advantage of using oscillating flow, it is necessary to compare heat transfer performance and temperature uniformity for oscillating and steady flows through a metal foam channel.

5.3.1 Comparison of Steady and Oscillating Flows

5.3.1.1 Heat Transfer Performance

To compare the total heat transfer rates in metal foams subjected to steady and oscillating flows, the temperature and Nusselt number distributions in metal foams with different pore densities were examined. The dimensionless grouping parameter (Equation 5-25) derived Section 5.1.2 will be used to evaluate the thermal management performance for steady and oscillating flows through metal foams. As mentioned in Chapter 3, the oscillating flow facility is also capable of performing steady flow experiments. By leaving one end of the test section open to the atmosphere, experiments of steady flow through metal foam channel can be conducted through an auto-balance compressor with the same test section configuration and sensors. Air flow velocity was adjusted by a flow regulator and a valve installed on the mains supply.

For electronics cooling, the chip devices are susceptible to excessively high local temperatures. Therefore, the temperature distribution along the flow direction of the test section is of practical interest in design. Figures 5-18 (a), (b) and (c) present the local temperature distributions along the axial direction for steady flow through Aluminium foam 10, 20 and 40 PPI, respectively. Reynolds number $\mathrm{Re} = ud_l / \nu_f$ is defined based on the ligament diameter which takes into consideration the physical properties of the metal foam. From these figures, general features of steady flow through porous channel can be observed. The local surface temperature increases with the increase of the dimensionless axial position x/D_e and the decrease of the Reynolds number. Compared to the magnitudes of the temperature distribution of oscillating flow through the aluminium foam channel, the temperature difference between the locations of x/D_e = 0 and x/D_e =3 for steady flow can be considered to be significant.

For power input Q = 20 W, the temperature profile of steady flow through aluminium foam 40 PPI rises from 49°C to 64°C with dimensionless x/D_e from 0.4284 to 2.5741 at Reynolds number Re = 32. When Reynolds number drops to 11, the temperatures at positions x/D_e = 0.4284 and 2.5741 rise to 75°C and 96°C, respectively.

Figures 5-19 (a), (b) and (c) plot the local Nusselt number distribution along the axial direction for Aluminium foam 10 PPI, 20 PPI and 40 PPI under the conditions described in Figure (5-18). It can be seen that the local Nusselt number increases with the increase of the Reynolds number. The local Nusselt numbers reach the maximum at the thermal entrance region, decreases with the increase of the axial distance for fixed Reynolds number and approaches a minimum. For example, in Figure 5-19 (a), the local Nusselt number reaches the highest value of 267 at the first test point (x/D_e = 0) for Aluminium 10 PPI, where Reynolds number is 91, and then drops to the minimum around 142 quickly at the last test point (x/D_e = 3) along the axial direction. The variation of local Nusselt number for a lower Reynolds number along the axial direction is less significant than that for a larger Reynolds number. For Aluminium 20 PPI, the difference in the local Nusselt number between two ends of test section is 153 when power input Q = 20 W and Reynolds number is 59, whereas the difference in the Nusselt number is only 82.1 with a reduced Reynolds number of 36. It can also be observed from Figure 5-19 that the profile of Nusselt number for high PPI aluminium foam is higher than that for low PPI foam under the same Reynolds number. The Nusselt number of steady flow through aluminium foam 40 PPI varies from 330 to 172 at Re = 24, however, the Nusselt number varies from 209 to 128 for steady flow through aluminium 20 PPI with Re = 23.

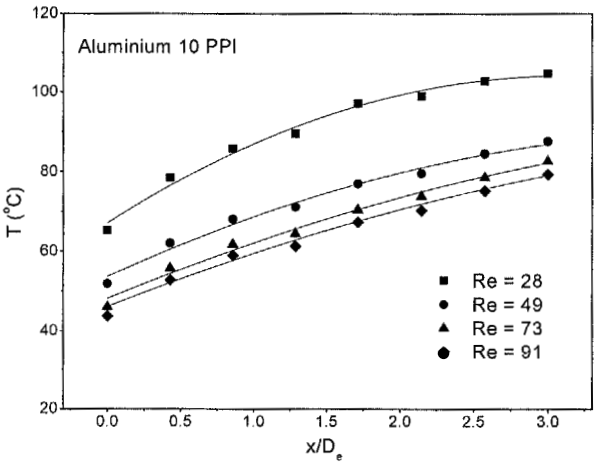

(a)

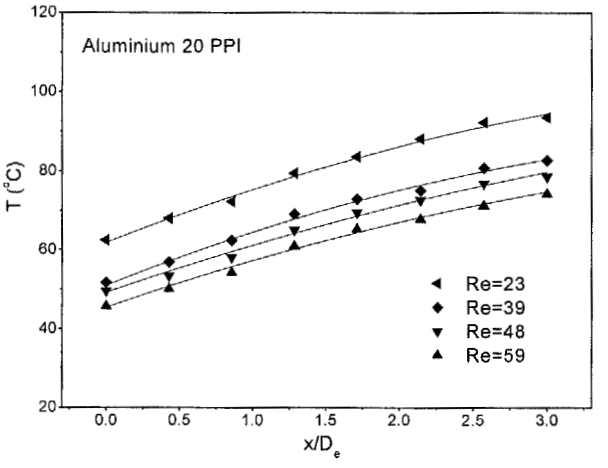

(b)

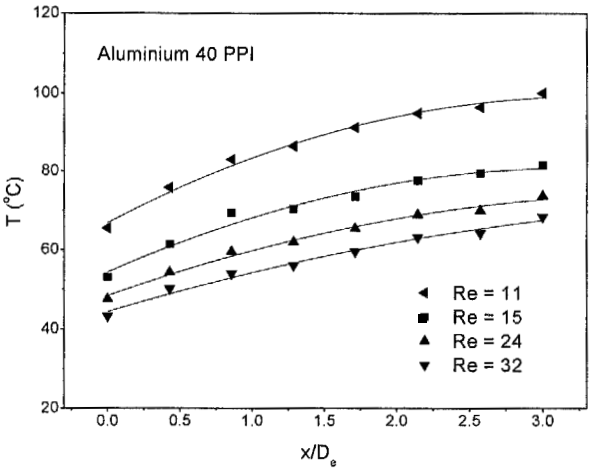

(c)

Figure 5-18 Local temperature distributions for steady flow through aluminium foams (a) 10 PPI (b) 20 PPI (c) 40 PPI with various Reynolds numbers

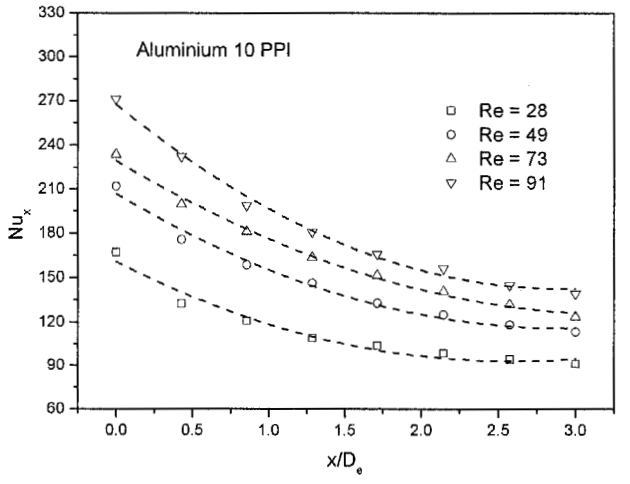

(a)

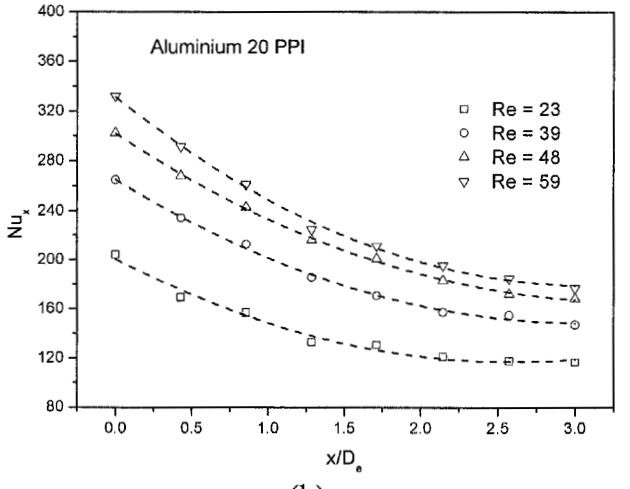

(b)

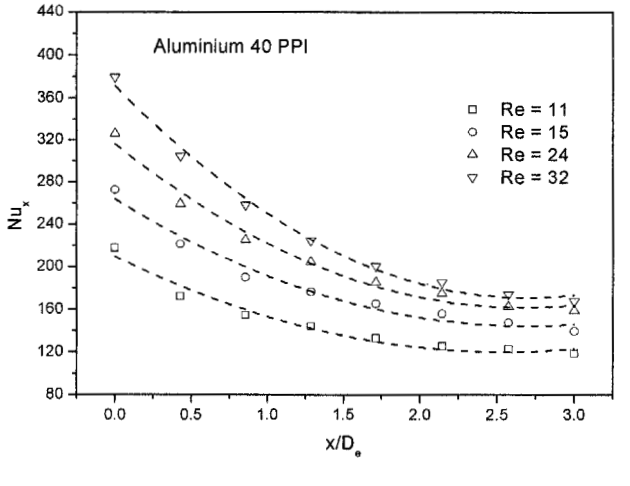

(c)

Figure 5-19 Local Nusselt number distributions for steady flow through aluminium foams (a) 10 PPI (b) 20 PPI (c) 40 PPI with various Reynolds numbers

Figure 5-20 presents the cycle-averaged local surface temperature of oscillating flow through metal foam 10, 20 and 40 PPI with different kinetic Reynolds numbers at A_0 = 4.1. It can be observed that the cycle-averaged temperature distribution in the tested foams decrease with an increase in Reynolds number. Comparing the temperature distributions in different aluminium foams at approximately same kinetic Reynolds number, it is found that the temperature profile for high pore density foam is lower than that for low pore density foam. At Re_ω = 643, the maximum temperature at the centre and minimum temperature at two ends of the channel for aluminium foam 20 PPI are 83°C and 76°C, respectively. However, the temperatures at the above locations for aluminium foam 40 PPI at Re_ω = 623 are 72°C and 66°C, respectively. It is also observed that the inlet and outlet bulk temperatures (isolated points plotted on Figure 5-20) are much lower than the temperatures in the test section due to heat removal at the coolers located at the two ends of the test section.

Figure 5-21 displays the cycle-averaged local Nusselt numbers versus the dimensionless axial distance for the cases presented in Figure 5-20. The data of the local Nusselt number shown in Figure 5-20 were calculated by Equation (5-26) based on the cycle-averaged local surface temperature. It can be seen that the cycle-averaged local Nusselt number in the thermal entrance region is higher than that in the location around the centre of the test section. As shown in Figure 5-21 (c) for the power input Q = 20 W and Re_ω = 858, the cycle-averaged local Nusselt number reaches higher values of 315 and 320 at the two thermal entrances. The lower values of the averaged Nusselt number of 271 and 274 are obtained at the dimensionless lengths x/D_e = 1.2858 and 1.7142 around the centre of the test section, respectively. It can also be observed that the higher Nusselt number distribution was obtained by high PPI foam as compared to that of low PPI foam at the same kinetic Reynolds number.

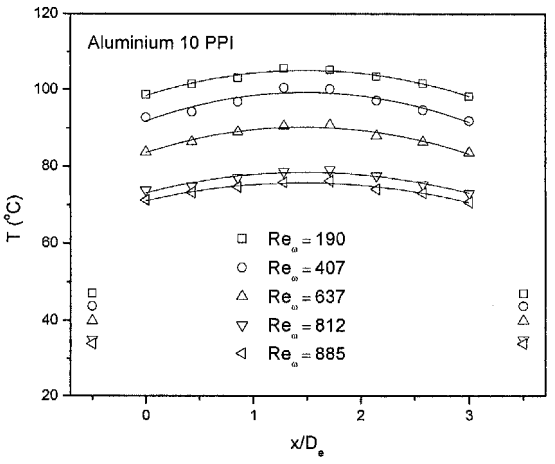

(a)

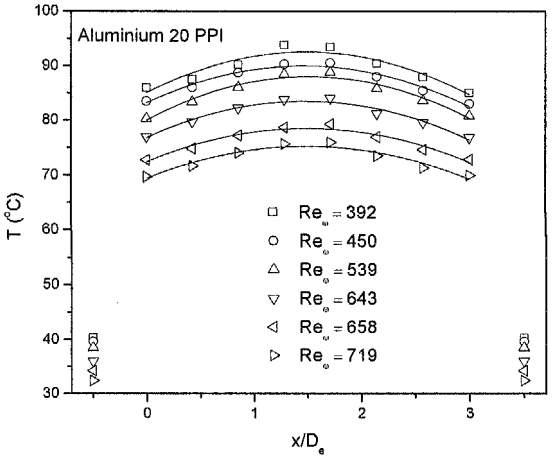

(b)

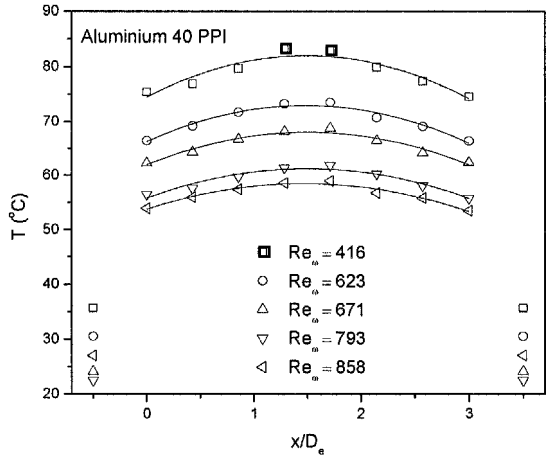

(c)

Figure 5-20 Cycle-averaged temperature distributions on the substrate surface of the test section for (a) Al 10 PPI (b) Al 20 PPI (c) Al 40 PPI at different kinetic Reynolds numbers

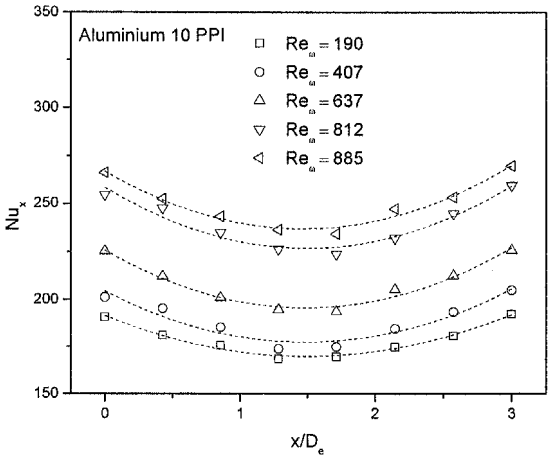

(a)

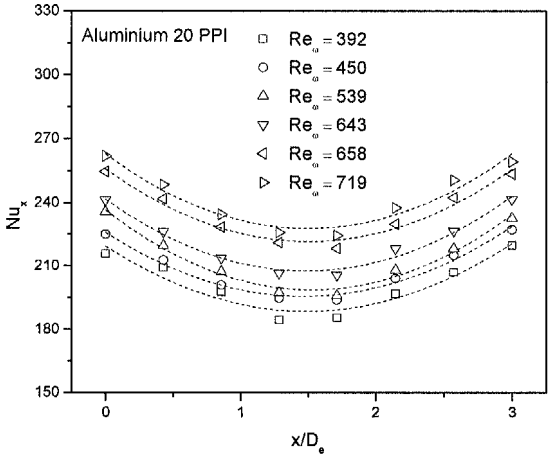

(b)

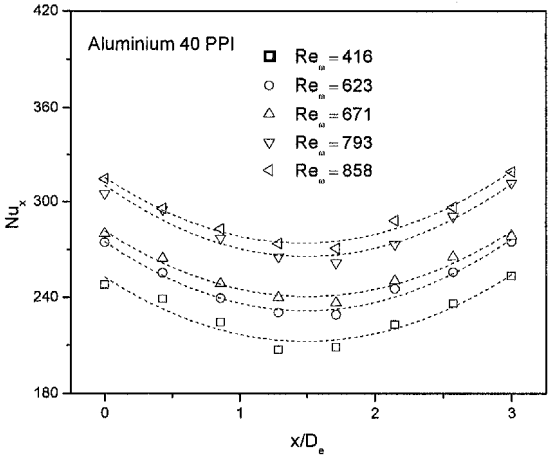

(c)

Figure 5-21 Cycle-averaged local Nusselt numbers of oscillating flow through (a) Al 10 PPI (b) Al 20 PPI (c) Al 40 PPI with different kinetic Reynolds numbers

To compare the heat transfer performance between the steady and oscillating flows through metal foam channel, the length-averaged Nusselt number is used to calculate the average local Nusselt number over the whole length of the test section. Based on the derivation of Equation (5-25), the dimensionless grouping parameter $\left(\frac{k_{eff}}{k_f}\right)\left(\frac{D_e}{L}\right)^{\frac{1}{2}}\left(\mathrm{Pe}^*\right)^{\frac{1}{2}}$ can be used to compare the heat transfer rates of steady and oscillating flows through the metal foam. The length-averaged Nusselt number can be expressed as

$$\mathrm{Nu}_{avg} = C\left(\frac{k_{eff}}{k_f}\right)\left(\frac{D_e}{L}\right)^{\frac{1}{2}}\left(\mathrm{Pe}^*\right)^{\frac{1}{2}} \tag{5-36}$$

where C is a constant and Pe^* is the effective Peclet number. The velocity used in the calculation of the effective Peclet number is the mean velocity of the fluid flow through the porous channel. For oscillating flow though porous channel, the mean velocity is the time-averaged value of the absolute velocity in a complete cycle at the cycle-steady state since the flow direction is reversed at every half-cycle. As shown in Figure 5-22, the length-averaged Nusselt numbers for steady and oscillating flows can be collapsed into two straight lines by employing the grouping parameter. It can be seen that the length-averaged Nusselt numbers for both oscillating and steady flows increase with the grouping parameter. The slope of the line for oscillating flow is larger than that for steady flow. The constant C obtained by the present study for steady and oscillating flows are 0.34 and 0.51, respectively. The larger value of constant C for oscillating flow shows that better heat transfer performance of oscillating flow through the metal foam channel can be obtained compared to steady flow. The ratio $\frac{\mathrm{Nu}_{avg}(osc)}{\mathrm{Nu}_{avg}(std)}$ shows that heat transfer rate for oscillating flow can be

1.5 times than that for steady flow through aluminium foams. The presence of two thermal entrance regions at the test section with higher cycle-averaged local Nusselt number results in a higher length-averaged Nusselt number for oscillating flow.

The heat transfer dissipation rates for metal foam and traditional finned heat sinks are also compared in Figure 5-22. Lau and Mahajan (1989) studied heat transfer of a finned heat sink in a ducted arrangement. Their results showed that the heat transfer rates for finned heat sinks can be expressed as

$$\mathrm{Nu}_{avg} = C(0.023\mathrm{Re}_h^{0.8}\mathrm{Pr}^{0.4}) \tag{5-37}$$

where Pr is the Prandtl number and C is a constant. $\mathrm{Re}_h = uD_f / \nu_f$ is the Reynolds number based on the hydraulic diameter of the fin $D_f = 4sH_f / (s+2H_f)$, where H_f and s are the height and the fin spacing of the heat sink, respectively.

The average Nusselt numbers for a finned heat sink with flow velocities ranging from 1 - 5 m/s subjected to uni-directional flow are plotted as a dash-dot line in Figure 5-22. It can be seen that the average Nusselt numbers of oscillating and steady flows through metal foams are higher than that of uni-directional flow through finned heat sinks, especially for aluminium foam heat sinks subjected to oscillating flow condition. It is also observed that the increase of average Nusselt number with flow velocity for finned heat sinks is not as significant as that for aluminium foam heat sinks. These results demonstrate that significant heat transfer enhancement can be achieved by replacing traditional fin heat sinks with metal foams.

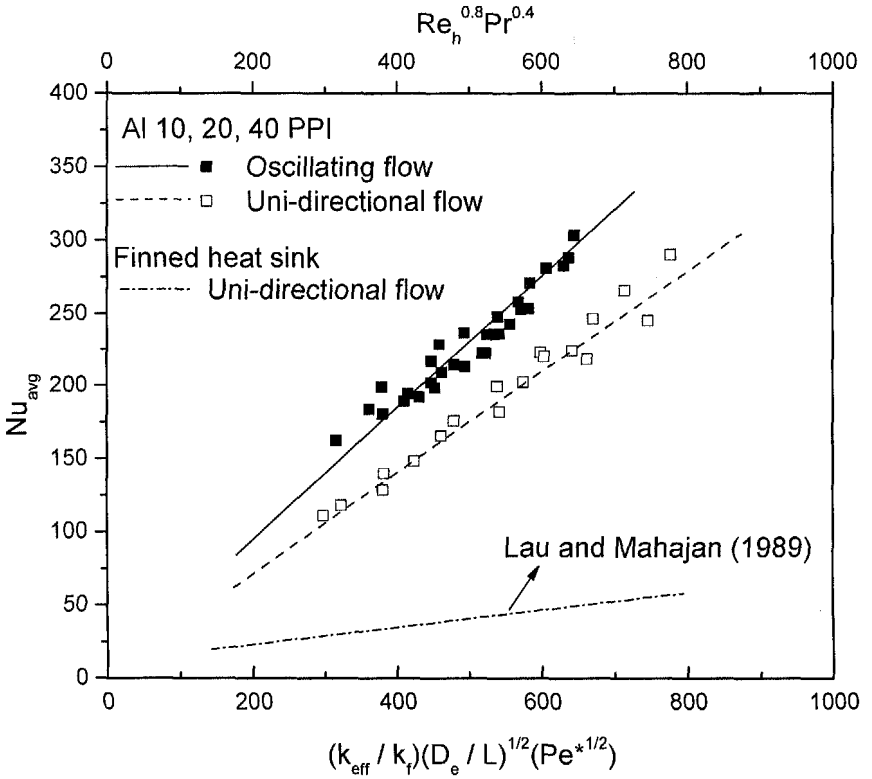

Figure 5-22 Grouping parameter $(k_{eff}/k_f)(D_e/L)^{1/2}Pe^{*1/2}$ as a function of length-averaged Nusselt number for oscillating and steady flows through aluminium foam and comparison between metal foams and finned heat sinks

5.3.1.2 Temperature Uniformity

Based on the above observations, it is shown that the temperature-lifts are different for steady and oscillating flows. For steady flow, the surface temperature increases along the flow direction and reaches the maximum temperature at x/D_e = 3. For oscillating flow, the surface temperature distribution curves are convex with the maximum value around the centre of the test section. The results indicate different temperature distribution uniformity for various Reynolds number. To quantify the temperature distribution uniformity, an index I_{uni} is defined as

$$I_{uni} = \frac{T_{max} - T_{min}}{T_{max}} \tag{5-38}$$

where T_{max} and T_{min} are the maximum and minimum temperatures on the surface of the test section, respectively. In the calculation, the maximum and minimum temperatures on the substrate surface for steady flow are obtained at the outlet and inlet of the test section, respectively due to the gradually increased temperature profile of steady flow along the porous channel. For oscillating flow, however, the maximum temperature is obtained at the location around the centre of the test section due to the convex temperature distribution. The minimum temperature is obtained at the left or right ends of the test section, which depends on the location of the minimum temperature. This index represents the ratio of the maximum temperature difference to the maximum local temperature on the surface. From Equation (5-38), a smaller value of index I_{uni} means better uniformity of surface temperature distribution. When the surface temperature distribution is uniform, the index I_{uni} will approach zero.

Figure 5-23 shows the comparison of temperature distribution uniformity for steady and oscillating flows through Aluminium foams 10 PPI, 20 PPI and 40 PPI. It is obvious that the ratio of the maximum temperature difference to the maximum local temperature on the surface for oscillating flow is much smaller than that for steady flow. According to data shown in Figure (5-23), the average temperature uniformity index of oscillating flow is more than 6 times lower than that for steady flow. This indicates that the surface temperature distribution for oscillating flow is more uniform than that for steady flow. Two thermal entrance regions of oscillating flow result in low temperature-lifts along the porous channel. For high-speed microprocessors, the reliability of transistors and operating speed are not only influenced by the average temperature but also by temperature uniformity on the substrate surface. The temperature of the hot spot can often affect calculated performance due to prolonged gate delay, and will always govern the overall reliability of the silicon. Therefore,

oscillating flow through porous media is a potential cooling method to maintain a uniform on-die temperature distribution below certain limits.

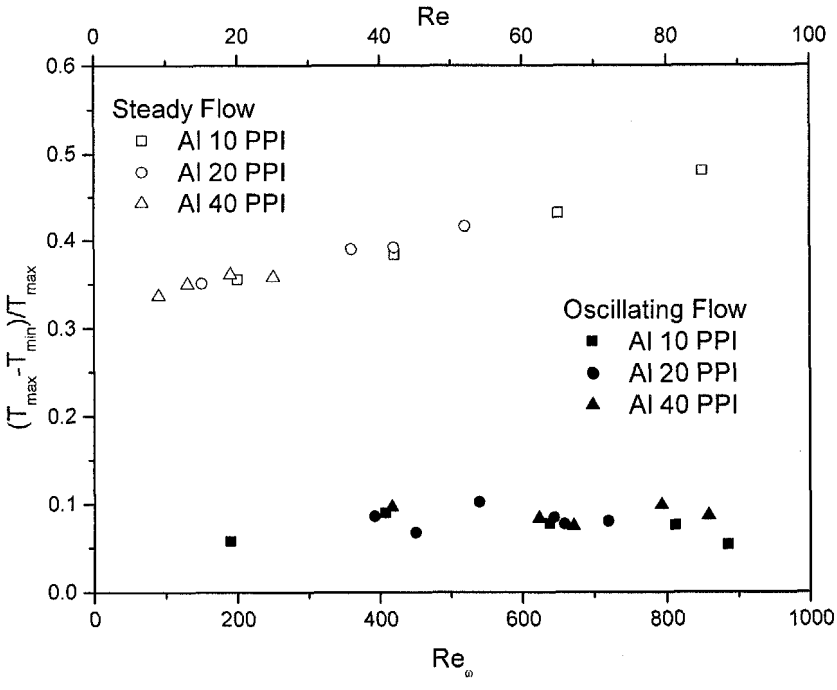

Figure 5-23 Temperature uniformity for steady and oscillating flows in 10 PPI, 20 PPI and 40 PPI Aluminium foams

5.3.2 Pumping Power of Oscillatory Cooling System

For electronics cooling application, the required power for driving coolant through heat sink is one of the critical concerns in the thermal design. To evaluate the driven force in metal foam with different pore densities subjected to oscillating flow, the pumping power of oscillatory cooling system need to be analysed with the heat transfer performance. Figure 5-24 shows the variations of the measured maximum pressure drop and velocity with kinetic Reynolds number for oscillating flow through aluminium 10, 20 and 40 PPI foams. The data show that the maximum pressure drops and velocities increase with increasing kinetic Reynolds number i.e. dimensionless oscillatory frequency. It can be seen that the maximum pressure drop for aluminium

foam with high pore density is much higher than that for aluminium foam with low pore density. However, the data for the maximum flow velocity plotted on Figure 5-24 show that the increase of velocity with the kinetic Reynolds number is not as significant as that of pressure drop. This implies that the appropriate velocity for cooling electronic components can be obtained at a relative low pressure drop by using oscillating flow through an aluminium foam heat sink. For a closer view, the large difference of the maximum pressure drop between oscillating flow through aluminium 10 and 40 PPI foam can be observed at approximately the same flow velocity.

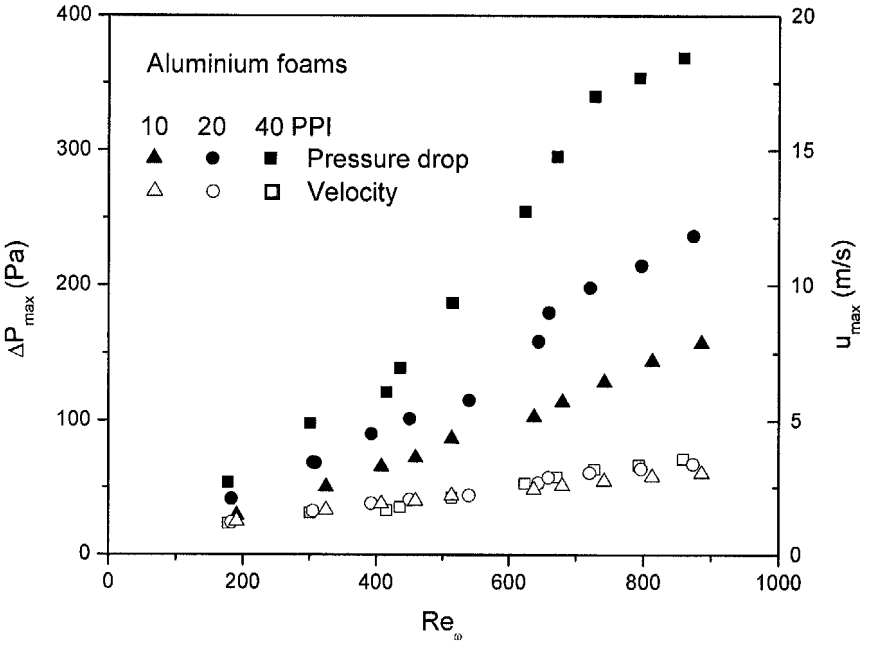

Figure 5-24 Maximum pressure drop and velocity of oscillating flow through aluminium foam 10, 20 and 40 PPI with different kinetic Reynolds numbers

It was noted in Figure 5-24 that the differences in flow velocity for oscillating flow in aluminium 10, 20 and 40 PPI are very small for constant kinetic Reynolds number. However, a large difference in pressure drop was observed at the same time. This implies that a higher driven force is required in oscillating flow through high pore density foam in order to obtain the same flow velocity as compared to that required in low pore density foam due to the conservation of energy principle. In the design of heat sinks for cooling electronic packages, the heat removal capability of the heat sink must be assessed together with the driven force required to operate the system i.e. the pumping power. The required maximum pumping power for oscillating flow through metal foam heat sink can be calculated by

$$W_p = \Delta P_{\max} \dot{V} \tag{5-39}$$

where W_p and $\dot{V}$ are the average maximum pumping power and volumetric flow rate, respectively. $\dot{V}$ was determined by the average maximum flow velocity through the cross-sectional area of the tested channel.

The data for the maximum pumping power versus the length-averaged Nusselt number for oscillating flow through aluminium 10, 20 and 40 PPI foams are plotted in Figure 5-25. It can be seen that the relationship between the maximum pumping power and length-averaged Nusselt number is nonlinear. The pumping power increases with the length-averaged Nusselt number of oscillating flow in aluminium foam with various pore densities. The data on Figure 5-25 show clearly that the high length-averaged Nusselt numbers of Figure 5-21 for oscillating flow in aluminium 40 PPI are achieved at the expense of larger pumping power. The trend of fitting curves shows that the same length-averaged Nusselt number under small pumping power can be obtained by oscillating flow through aluminium foam with low pore density. It can

also be observed that the increase of length-averaged Nusselt number at large pumping power is not significant, especially for high pore density aluminium foam. For example, with an increase in the average Nusselt number from 270 ~ 290 in aluminium 40 PPI, the pumping power is increased sharply from 3.1 to 6.3 W. At the same time, there is only 1.3 times increase in pumping power when the average Nusselt number is increased from 250 ~ 270. This indicates that relatively high heat transfer performance can be obtained in low pore density metal foam subject to oscillating flow by an appropriate pumping power. The present results suggest that in designing a novel heat sink, metal foams of low pore density can be used to enhance heat transfer with low pumping power. High pore density metal foams with their extremely large fluid-solid-contact surface areas and tortuous coolant flow paths are suitable to remove high heat fluxes in applications where pumping power is not of concern.

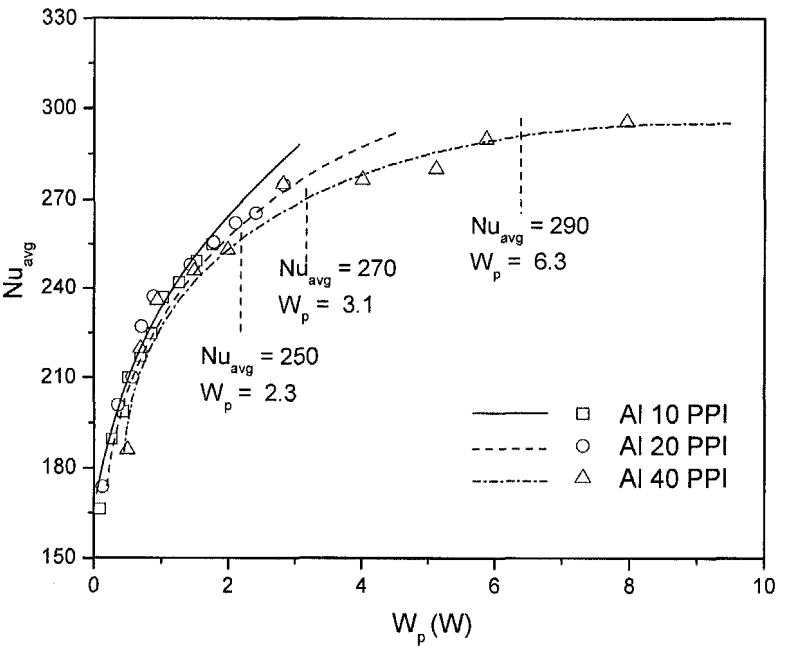

Figure 5-25 Pumping power versus length-averaged Nusselt number for oscillating flow through aluminium foam 10, 20 and 40 PPI

5.4 Summary

Chapter 5 presents the theoretical analyses of forced convection in porous medium and experimental data of the heat transfer for oscillating flow through metal foam channel. The results show that the cycle-averaged temperature decreases with an increase in the oscillatory frequency and flow displacement while the cycle-averaged local Nusselt numbers exhibit the opposite trend. The empirical equation obtained by the experimental study showed that the length-averaged Nusselt number of oscillating flow through aluminium foam is governed by the kinetic Reynolds number and dimensionless flow amplitude. Heat transfer enhancement for oscillating flow through metal foam depends more sensitively on flow displacement than on oscillatory frequency.

Based on the local thermal non-equilibrium model, the scale analysis shows that the dimensionless grouping parameter $\left(\frac{k_{eff}}{k_f}\right)\left(\frac{D_e}{L}\right)^{\frac{1}{2}}\mathrm{Pe}^{*\frac{1}{2}}$ is a function of the length-averaged Nusselt number. The comparison of heat transfer between steady and oscillating flows through metal foam shows that the length-averaged Nusselt number of oscillating flow can be 1.5 times larger than that of steady flow through metal foam channel. The average Nusselt numbers for metal foam subjected to oscillating and steady flows are higher than that for uni-directional flow through finned heat sink. The average temperature uniformity index of oscillating flow in aluminium foam 10, 20 and 40 PPI is more than 6 times lower than that of steady flow. The discussion of removal capability versus the required driven force suggests that metal foams of low pore density can be used to enhance heat transfer with an appropriate pumping power and high pore density metal foams are suitable to remove extraordinarily high heat fluxes in applications where pumping power is not of concern.

CHAPTER 6

MATHEMATICAL MODELLING AND NUMERICAL SIMULATION

6.1 Mathematical Formulation

Through the experimental study, heat transfer of oscillating flow through metal foam channel was discussed mainly based on the cycle- and length-averaged characteristics. To achieve good understanding of heat transfer of oscillating flow through metal foam channel, a numerical study was carried out to investigate the characteristics of transient heat transfer in metal foam subjected to oscillating flow.

6.1.1 Statement of the Problem

The problem analysed in this investigation is the forced convection in a channel filled with metal foam material subjected to oscillating flow. The schematic diagram of the problem is shown in Figure 6-1. The bottom wall of the channel is subjected to a constant heat flux while the other three walls are adiabatic. The width of the plate channel is assumed to be sufficiently long and the heat flux at the bottom of the channel is supposed to be uniform so that the problem can be considered essentially as two-dimensional. The effect of property variation of metal foam is neglected in the present study due to the high thermal and physical stability of the tested metal foams. Air flow is driven forward and backward sinusoidally through the porous channel. The porous medium in the channel is assumed to have uniform porosity and to be isotropic.

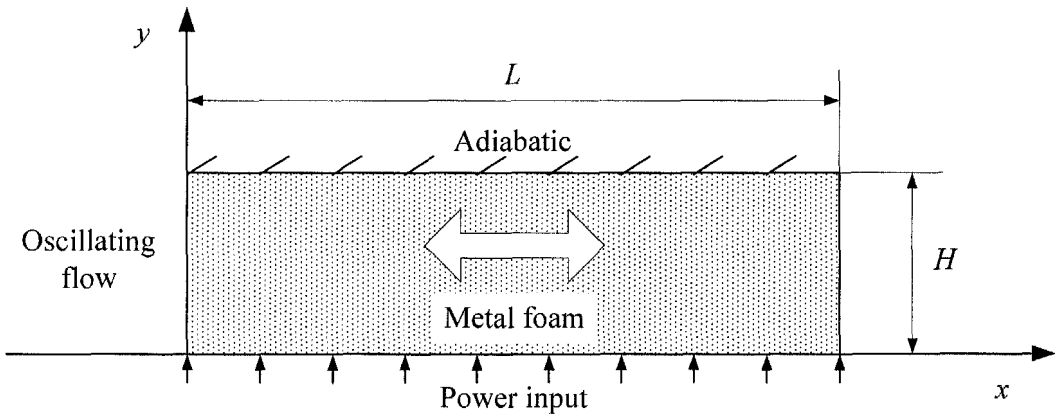

Figure 6-1 Schematic diagram of the problem

6.1.2 Governing Equations

6.1.2.1 Local Volume Averaging

In order to formulate the governing equations of forced convection in metal foam channel, it is necessary to use the general Navier-Stokes equations with the appropriate thermophysical properties of the solid and fluid phases. The macroscopic conservation equations of forced convection in metal foam can be obtained by a local volume averaging of the microscopic conservation equations over a representative elementary volume (REV) (Whitaker, 1967). Central to the concept of volume averaging is the REV as shown in Figure 6-2 and the main advantage of this technique is that the porous medium can be treated as a continuum. The field quantities are defined as averages over sufficiently large REVs, and the size of the REV is the smallest volume that leads to statistically meaningful local averaging quantities.

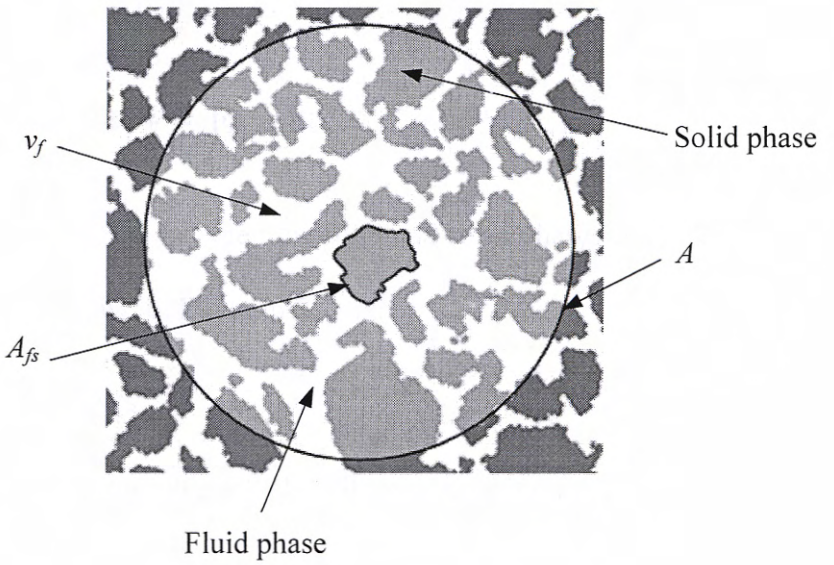

Figure 6-2 Demonstrative delineation for a REV

Local volume averaging involves averaging the microscopic equations over REVs. In order to do this, consider a REV in porous medium consisting of solid phase and a fluid. If Φ is the quantity being averaged, then its local volume average is defined as

$$\langle \Phi \rangle = \frac{1}{V} \int_V \Phi dV \tag{6-1}$$

where the symbol < > refers to the volume average. For a quantity associated with the fluid alone, the volume averaged value is

$$\langle \Phi \rangle = \varepsilon \frac{1}{V_f} \int_{V_f} \Phi dV \tag{6-2}$$

where V is the local elementary volume, V_f is the volume occupied by fluid phase in REV and ε is the porosity of the media. To obtain the macroscopic equations from the microscopic equations, the following averaging theorems similar to those obtained by Whitaker (1967) and Slattery (1967) relating the volume average of a spatial derivative to the spatial derivative of the volume average are needed:

$$\langle \nabla \Phi \rangle = \nabla \langle \Phi \rangle + \frac{1}{V} \int_{A_{fs}} \Phi d\mathbf{A} \tag{6-3}$$

$$\langle \nabla \cdot \Phi \rangle = \nabla \cdot \langle \Phi \rangle + \frac{1}{V} \int_{A_{fs}} \Phi \cdot d\mathbf{A} \tag{6-4}$$

where A_{fs} is the interface between the fluid and solid phases in the REV and $d\boldsymbol{A}$ is the surface vector as shown in Figure 6-2.

6.1.2.2 Continuity Equation

The microscopic continuity equation for steady incompressible flow is given by

$$\nabla \cdot \mathbf{u}_f = 0 \tag{6-5}$$

where $\mathbf{u}_f$ is the microscopic velocity vector. Using Equations (6-2) and (6-4), the volume average of Equation (6-5) is

$$\nabla \cdot \left(\varepsilon \langle \mathbf{u}_f \rangle \right) = 0 \tag{6-6}$$

where $\varepsilon \langle \mathbf{u}_f \rangle = \mathbf{u}$ is the Darcy velocity vector. Thus, the macroscopic steady continuity equation can be written as

$$\nabla \cdot \langle \mathbf{u} \rangle = 0 \tag{6-7}$$

6.1.2.3 Momentum Equation

The microscopic momentum equation for an incompressible flow in a porous medium is given by the Navier-Stokes equation

$$\rho_f \left(\frac{\partial \langle \mathbf{u}_f \rangle}{\partial t} + \nabla \cdot \left(\langle \mathbf{u}_f \mathbf{u}_f \rangle \right) \right) = -\nabla (\langle P_f \rangle) + \mu_f \nabla^2 \langle \mathbf{u}_f \rangle \tag{6-8}$$

where ρ_f and μ_f are the density and viscosity of the fluid, and P_f is the pressure of the fluid phase. Integrating the above equation with respect to a REV and with the aid of Equations (6-3) and (6-4) gives

$$\rho_f\left(\frac{\partial\langle\mathbf{u}\rangle}{\partial t}+\nabla\cdot\left\langle\frac{\mathbf{uu}}{\varepsilon}\right\rangle\right)=-\nabla\langle\varepsilon P_f\rangle+\mu_f\nabla^2\langle\mathbf{u}\rangle+\mathbf{B} \tag{6-9}$$

where

$$\mathbf{B}=-\frac{1}{V}\int_{A_{fs}}P_f d\mathbf{A}+\frac{\mu_f}{V}\int_{A_{fs}}(\nabla\mathbf{u}_f)\cdot d\mathbf{A} \tag{6-10}$$

is the total drag force per unit volume due to the presence of the solid materials in porous media. Vafai and Tien (1981) studied the two-dimensional flow through porous media and pointed out that the flow resistances caused by the inertial forces in porous media must be considered for high permeability medium. The inertia effects increase with the higher permeability and velocity and lower fluid viscosity. Hsu and Cheng (1990) analysed the total drag force for both high and low Reynolds number flows in a porous medium, and derived a composite expression for the drag force as

$$\mathbf{B}=-\left(\frac{\varepsilon\mu_f\langle\mathbf{u}\rangle}{K}+\rho_f\frac{\varepsilon F\langle\mathbf{u}\rangle|\langle\mathbf{u}\rangle|}{\sqrt{K}}\right) \tag{6-11}$$

where K and F are the permeability and inertia coefficient of the porous medium. The above expression for **B** indicates that the drag force is composed of two terms. The first term is the Darcy term which accounts for the linear dependence of pressure drop on flow velocity at low Reynolds number. The second term expresses that at higher velocities, inertia effects become significant and a quadratic dependence of pressure drop on velocity is expected. Based on the above analyses, it is noted that the inertia effects of metal foam on fluid through porous channel cannot be neglected due to the high porosity and permeability of the metal foam medium. In addition, the flow velocity investigated in the present study is not low enough to account for the body forces only by the linear dependence of pressure drop on flow velocity due to the application of metal foam in electronics cooling. Therefore, the drag force per unit

volume in metal foam is a quadratic function of the flow velocity, which includes the effect of inertial coefficient on fluid flow at a relative high Reynolds number through metal foam channel. Thus, the suitable equation to describe momentum transport in a metal foam porous medium in Cartesian coordinates is

$$\rho_f\left(\frac{\partial\langle\mathbf{u}\rangle}{\partial t}+\frac{1}{\varepsilon}\nabla\cdot\langle\mathbf{u}\rangle\langle\mathbf{u}\rangle\right)= \\ -\varepsilon\nabla\langle P_f\rangle+\mu_f\nabla^2\langle\mathbf{u}\rangle-\frac{\varepsilon\mu_f}{K}\langle\mathbf{u}\rangle-\frac{\varepsilon\rho_f F}{\sqrt{K}}|\langle\mathbf{u}\rangle|\langle\mathbf{u}\rangle \tag{6-12}$$

In addition, an order of magnitude analysis on the momentum equation shows that the momentum boundary layer is of the order of $(K/\varepsilon)^{1/2}$ and that the convective term $\langle(\mathbf{u}\cdot\nabla)\mathbf{u}\rangle$ responsible for boundary layer growth is significant only over a length of δ_t (Vafai and Thiyagaraja, 1987), which can be estimated by

$$\delta_t=\frac{Ku}{\nu_f} \tag{6-13}$$

Using typical values of $K = 0.5\times10^{-7}$ m^2, $u = 2$ m/s and $\nu_f = 1.56\times10^{-5}$ m^2/s, δ_t is estimated to be smaller than 7 mm. This indicates that a fully developed momentum boundary layer is in force beyond a very short developing length. Therefore, fluid flow in the metal foam channel is considered to be fully developed in the present study.

6.1.2.4 Energy Equation

From the point of view of the energy equation, there are two different models in theoretical and numerical research: local thermal equilibrium (LTE) model and local thermal non-equilibrium (LTNE) model. The LTE model assumes that the solid-phase temperature is equal to the fluid temperature, i.e. local thermal equilibrium between the fluid and the solid-phases at any location in the porous media. The LTNE model builds two energy equations for solid and fluid phases, respectively, which shows the

temperature difference between the porous medium and fluid flow.

Energy transport in porous media has generally been studied with the assumption of local thermal equilibrium between the two phases. A single homogeneous equation is used to describe the transport in LTE model. Under this condition, the steady volume-averaged energy equation can be expressed as

$$\rho_f c_{pf}\left(\nabla\cdot\left(\mathbf{u}T\right)\right)=\nabla\cdot\left(\left(k_{eff}+k_d\right)\nabla T\right) \tag{6-14}$$

where T and u refer to the volume averaged temperature and velocity. K_{eff} is the effective thermal conductivity and is used to account for the molecular diffusion through the solid and fluid phases. k_d is the dispersion thermal conductivity used to account for the effect of pore-level hydrodynamics on the macroscopic transport.

The single-equation of Equation (6-14) treats the energy conservation for solid and fluid phases in thermal equilibrium condition. However, for forced air convection in metal foam, it is noted that the large difference in thermal conductivity between the solid (aluminium) and fluid (air) phases cannot be ignored. At least, it needs further confirmation. Hence, the two-equation model, i.e. LNTE model, is the ideal governing equation for the present problem. For unsteady flow, the microscopic energy equations of the solid and fluid phases are as follows:

Solid phase

$$\rho_s c_{ps}\frac{\partial T_s}{\partial t}=\nabla\cdot\left(k_s\nabla T_s\right) \tag{6-15}$$

Fluid phase

$$\rho_f c_{pf}\left(\frac{\partial T_f}{\partial t}+\nabla\cdot\left(\mathbf{u}T_f\right)\right)=\nabla\cdot\left(k_f\nabla T_f\right) \tag{6-16}$$

where the temperature and heat flux are continuous at the fluid-solid interface, and T_s, k_s, T_f and k_f are the temperatures and thermal conductivities for fluid and solid phases respectively. Similar to the derivation of Equation (6-12) based on the REV, the

macroscopic energy equations for solid and fluid phases in porous media under the condition of forced convection can be derived as

Solid phase

$$(1-\varepsilon)\rho_s c_{ps}\frac{\partial\langle T_s\rangle}{\partial t}=\nabla\left(k_{se}\nabla\langle T_s\rangle\right)-h_{fs}a_{fs}\left(\langle T_s\rangle-\langle T_f\rangle\right) \tag{6-17}$$

Fluid phase

$$\varepsilon\rho_f c_{Pf}\frac{\partial\langle T_f\rangle}{\partial t}+\rho_f c_{pf}\langle\mathbf{u}\rangle\nabla\langle T_f\rangle=\nabla\left(k_{fe}\nabla\langle T_f\rangle\right)-h_{fs}a_{fs}\left(\langle T_s\rangle-\langle T_f\rangle\right) \tag{6-18}$$

where k_{se} and k_{fe} are the effective thermal conductivities and temperatures for solid and fluid phases, and h_{fs} and a_{fs} are the fluid-to-solid heat transfer coefficient and the specific fluid and solid contact surface area, respectively. The term, $h_{fs}a_{fs}\left(\langle T_s\rangle-\langle T_f\rangle\right)$, is used to achieve coupling between the two energy equations and represents the energy transferred between the two phases due to the temperature difference.

According to the above analysis of the forced convection in metal foam porous media, the assumptions upon which the numerical model is based are stated as follows:

1. The porosity of porous medium is uniform and isotropic.

2. The fluid flow in porous channel is assumed to be incompressible and fully developed.

3. Natural convection effects are negligible. This assumption is based on the fact that the porous channel is dominated by forced convection.

4. Radiation heat transfer is neglected due to the relatively low temperature (< 200 °C) in the porous channel.

To concentrate on the investigation of the fluid flow and heat transfer in a channel filled with metal foam subject to oscillating flow, the following macroscopic governing equations of the present problem (with the volume averaging symbol < >

dropped) are summarised based on the above assumptions as

Continuity equation

$$\frac{\partial(\varepsilon\rho_f)}{\partial t}+\nabla\cdot\left(\rho_f\mathbf{u}\right)=0 \tag{6-19}$$

Momentum equation

$$\frac{1}{\varepsilon}\frac{\partial\mathbf{u}}{\partial t}+\frac{1}{\varepsilon^2}\nabla\cdot\mathbf{uu}=-\frac{1}{\rho_f}\nabla P_f+\frac{\nu_f}{\varepsilon}\nabla^2\mathbf{u}-\frac{\nu_f}{K}\mathbf{u}-\frac{F}{\sqrt{K}}|\mathbf{u}|\mathbf{u} \tag{6-20}$$

Fluid phase energy equation

$$\begin{aligned}&\varepsilon\rho_f c_{pf}\frac{\partial T_f}{\partial t}+\rho_f c_{pf}\mathbf{u}\frac{\partial T_f}{\partial x}=\\&\frac{\partial}{\partial x}\left(\left(k_{fe}+k_d\right)\frac{\partial T_f}{\partial x}\right)+\frac{\partial}{\partial y}\left(\left(k_{fe}+k_d\right)\frac{\partial T_f}{\partial y}\right)+h_{fs}a_{fs}(T_s-T_f)\end{aligned} \tag{6-21}$$

Solid phase energy equation

$$(1-\varepsilon)\rho_s c_{ps}\frac{\partial T_s}{\partial t}=\frac{\partial}{\partial x}\left(k_{se}\frac{\partial T_s}{\partial x}\right)+\frac{\partial}{\partial y}\left(k_{se}\frac{\partial T_s}{\partial y}\right)-h_{fs}a_{fs}(T_s-T_f) \tag{6-22}$$

where ρ_f, ν_f, c_{pf} and T_f represent the density, kinematic viscosity, specific heat, temperature of the flow fluid, and ρ_s, c_{ps} and T_s are the density, specific heat, and temperature of porous media, respectively.

6.1.3 Modelling Heat Transfer in Open-cell Metal Foam

To solve the problem of heat transfer in metal foam channel, the permeability K and inertial coefficient F in the Equation (6-20), and the effective conductivities k_{se}, k_{fe} and the dispersion conductivity k_d in Equations (6-21) and (6-22), need to be determined to close the equations.

The permeability K and inertial coefficient F were determined previously in the experimental study by fitting the second-order polynomial of Equation (4-13) to the measured data of pressure drop and velocity under the steady flow condition. This

method is used extensively to obtain K and F for porous media due to the consideration of the quadratic relation between the total drag force and flow velocity.

For open-cell metal foam, a geometrical effective thermal conductivity model of a saturated porous metal foam was developed by Boomsma and Poulikakos (2001) based on the idealised three-dimensional basic cell geometry of a foam with tetrakaidecahedron shape, which is also observed by the present study as shown in Figure 3-11. The effective conductivity k_{eff} can be determined by

$$k_{eff} = \frac{\sqrt{2}}{2(R_A + R_B + R_C + R_D)} \tag{6-23}$$

where $R_A \sim R_D$ are the simplification quantities of the unit cell subsection for metal foam, which can be formulated as

$$R_A = \frac{4d}{(2e^2 + \pi d(1-e))k_s + (4 - 2e^2 - \pi d(1-e))k_f} \tag{6-24a}$$

$$R_B = \frac{(e-2d)^2}{(e-2d)e^2 k_s + (2e - 4d - (e-2d)e^2)k_f} \tag{6-24b}$$

$$R_C = \frac{(\sqrt{2} - 2e)^2}{2\pi d^2(1-2e\sqrt{2})k_s + 2(\sqrt{2} - 2e - \pi d^2(1-2e\sqrt{2}))k_f} \tag{6-24c}$$

$$R_D = \frac{2e}{e^2 k_s + (4 - e^2)k_f} \tag{6-24d}$$

where the dimensionless foam ligament radius d is given by

$$d = \sqrt{\frac{\sqrt{2}(2 - \frac{5}{8}e^3\sqrt{2} - 2\varepsilon)}{\pi(3 - 4e\sqrt{2} - e)}} \tag{6-25}$$

with the parameter $e = 0.339$. Using Equations (6-23), (6-24) and (6-25), the effective thermal conductivity k_{fe} of fluid phase can be obtained by setting $k_s = 0$, and the effective thermal conductivity k_{se} of solid phase can be obtained similarly by setting $k_f = 0$.

The thermal dispersion conductivity k_d is given by (Hunt and Tien, 1988)

$$k_d = 0.025\rho_f c_{pf} u\sqrt{K} \tag{6-26}$$

where K is the permeability of the porous media, ρ_f and c_f are the density and specific heat of fluid, respectively.

For numerical simulation, the interfacial heat transfer coefficient h_{fs} between the fluid and solid phases and the specific surface area a_{fs}, i.e. solid-fluid interfacial surface area, need to be known. The volumetric interfacial heat transfer coefficient h_{fs} in the energy equation depends on the geometric structure of metal foam and flow condition. Wakao *et al.* (1979) proposed one of the most comprehensive models for packed beds. However, no such general model exists for foamed materials. Based on the Zukauskas' (1987) correlation for staggered cylinders, a modified expression of h_{fs} (Calmidi and Mahajan, 2000) for metal foam was employed in the present study, which is expressed as

$$h_{fs} = 0.52\,\mathrm{Re}^{0.5}\,\mathrm{Pr}^{0.37}\frac{k_f}{d_l} \tag{6-27}$$

where Reynolds number $\mathrm{Re} = ud_l/\nu_f$, k_f and d_l are the thermal conductivity of fluid and ligament diameter of metal foam, respectively. The solid-fluid interfacial surface area for arrays of parallel cylinders intersecting in the three perpendicular directions is given by Arbelaez (1996) as

$$a_{fs} = \frac{3\pi d_l'}{\left(d_p'\right)^2} \tag{6-28}$$

where d_p' and d_l' are the pore and fibre diameters of the parallel cylinders arrays. Based on the three-dimensional geometric difference between the arrays of parallel cylinders and the polyhedron structure of the metal foam, Calmidi (1998) found that d_p' and d_l' of the parallel cylinders arrays can be represented by the pore diameter d_p

and ligament diameter d_l of metal foam by multiplying the equivalent factors of 0.59 and $1\text{-}e^{-((1-\varepsilon)/0.04)}$, respectively. Therefore, the interfacial surface area of metal foam can be expressed as

$$a_{fs} = \frac{3\pi\left(1-e^{\frac{1-\varepsilon}{0.04}}\right)d_l}{\left(0.59d_p\right)^2} \tag{6-29}$$

where ε, d_l and d_p are the porosity, ligament and pore diameters of metal foam, respectively.

6.1.4 Boundary Conditions

When a heat flux is directly applied to the outer surface of the metal foam, the heat is transferred to the solid and fluid phases by conduction and convection. As discussed by Amiri *et al.* (1995) and Lee and Vafai (1999), the wall heat flux boundary condition may be reviewed in two different ways. The first is to assume that each representative elementary volume at the wall surface receives a prescribed heat flux that is equal to the wall heat flux. As a result, the heat will be divided between the two phases on the basis of the physical values of their effective conductivities and their corresponding temperature gradients. The ratio of the fluid phase heat flux to the solid phase heat flux at the heated wall can be determined by the ratio of k_{fe} / k_{se} or the ratio of ε / (1 - ε). The second approach is to assume that each of the individual phases at the wall surface will receive an equal amount of heat flux. In the present study, the first method is employed in the numerical simulation. The heat fluxes obtained by the fluid and solid phases are determined by the ratio of the effective thermal conductivities of the fluid to aluminium foam (i.e. k_{fe} / k_{se}) due to the large difference in the thermal conductivity of aluminium foam and fluid (air).

Boundary conditions of the velocity adopted in the present simulation are no-slip at

the tube wall and the flow movement is assumed to cover the whole length of numerical domain. It is important to note that the boundary condition of the inlet axial velocity cannot be fixed at $x = 0$ in a full cycle due to the periodic reversal of fluid flow. Therefore, the inlet and outlet conditions of the axial velocity change at each half-cycle. At the first half-cycle, the axial velocity boundaries are

$$\text{at } x = 0, \quad u(0,y,t) = u_{in}\sin(2\pi ft)$$

$$\text{at } x = L, \quad \frac{\partial v}{\partial x}(L,y,t) = 0 \tag{6-30a}$$

where $u_{in} = x_{\max}\omega/2$ and $x_{\max}$ and ω are the maximum flow displacement and angular frequency (Zhao and Cheng, 1998b). For the second half-cycle, the axial velocity entrance shifts to $x = L$, and the boundary conditions are changed accordingly to

$$\text{at } x = 0, \quad \frac{\partial v}{\partial x}(0,y,t) = 0$$

$$\text{at } x = L, \quad u(L,y,t) = u_{in}\sin(2\pi ft) \tag{6-30b}$$

Referring to Figure 6-1, the thermal boundary conditions for the problem under consideration are

$$\text{at } x = 0, \quad T_f(0,y,t) = T_s(0,y,t) = T_{in} \tag{6-31a}$$

$$\text{at } x = L, \quad \frac{\partial T_f}{\partial x}(L,y,t) = \frac{\partial T_s}{\partial x}(L,y,t) = 0 \tag{6-31b}$$

$$\text{at } y = 0, \quad k_{fe}\frac{\partial T_f}{\partial y}(x,0,t) + k_{se}\frac{\partial T_s}{\partial y}(x,0,t) = q, \frac{q_f}{q_s} = \frac{k_{fe}}{k_{se}} \tag{6-31c}$$

$$\text{at } y = H, \quad \frac{\partial T_f}{\partial y}(x,H,t) = \frac{\partial T_s}{\partial y}(x,H,t) = 0 \tag{6-31d}$$

Equations (6-19) through (6-22) with the associated boundary and initial conditions form the model for analysing the flow and heat transfer of oscillating flow through a channel filled with porous media. The numerical computations of fluid velocity and

temperatures of the solid and fluid phases in the porous channel will be performed by the finite-volume method (FVM).

6.2 Numerical Simulation

6.2.1 General Transport Equation

For describing a two-dimensional problem in the Cartesian coordinate system, the continuity, momentum and temperature equations for steady, incompressible laminar flow can be written as:

Continuity equation

$$\frac{\partial(\rho u)}{\partial x}+\frac{\partial(\rho v)}{\partial y}=0 \tag{6-32}$$

Momentum equations in the x and y directions

$$\begin{aligned}\frac{\partial(\rho uu)}{\partial x}+\frac{\partial(\rho vu)}{\partial y}&=\frac{\partial}{\partial x}\left(\mu\frac{\partial u}{\partial x}\right)+\frac{\partial}{\partial y}\left(\mu\frac{\partial u}{\partial y}\right)-\frac{\partial P}{\partial x}+V_x+B_x+F_x\\ \frac{\partial(\rho uv)}{\partial x}+\frac{\partial(\rho vv)}{\partial y}&=\frac{\partial}{\partial x}\left(\mu\frac{\partial v}{\partial x}\right)+\frac{\partial}{\partial y}\left(\mu\frac{\partial v}{\partial y}\right)-\frac{\partial P}{\partial y}+V_y+B_y+F_y\end{aligned} \tag{6-33}$$

Temperature equation

$$\frac{\partial\left(\rho c_p uT\right)}{\partial x}+\frac{\partial\left(\rho c_p vT\right)}{\partial y}=\frac{\partial}{\partial x}\left(k\frac{\partial T}{\partial x}\right)+\frac{\partial}{\partial y}\left(k\frac{\partial T}{\partial y}\right)+S \tag{6-34}$$

where V, B and F are the additional viscous term, body force and distributed resistance, respectively. In Equation (6-34), S is the source term and T represents the temperature of the solid phase or the fluid phase. For LTE model, the temperatures of solid and fluid phases are equal, i.e. $T = T_f = T_s$, where T_f and T_s are the temperatures for fluid and solid phases, respectively.

Considering Equations (6-33) through (6-34), the above governing equations can be represented by a general transport equation as follows:

$$\frac{\partial(\rho u\Phi)}{\partial x}+\frac{\partial(\rho v\Phi)}{\partial y}=\frac{\partial}{\partial x}\left(\Gamma\frac{\partial\Phi}{\partial x}\right)+\frac{\partial}{\partial y}\left(\Gamma\frac{\partial\Phi}{\partial y}\right)+S \tag{6-35}$$

Using Cartesian tensor form, the problem for unsteady, incompressible laminar flow can be extended from Equation (6-35) as:

$$\underbrace{\frac{\partial(\rho\Phi)}{\partial t}}_{\text{Unsteady}}+\underbrace{\frac{\partial(\rho u_j\Phi)}{\partial x_j}}_{\text{Convection}}=\underbrace{\frac{\partial}{\partial x_j}(\Gamma\frac{\partial\Phi}{\partial x_j})}_{\text{Diffusion}}+\underbrace{S}_{\text{Source}} \tag{6-36}$$

where Φ can be any dependent variable such as temperature, velocity component in x and y coordinates. Γ is the diffusion coefficient and S is the source term. Equations (6-32), (6-33) and (6-34) can be obtained respectively by setting u, v and T as Φ in Equation (6-36) with suitable source term S. Based on Equation (6-36), the finite-volume method (Patankar, 1980) is employed to solve the problem discussed.

6.2.2 Numerical Scheme

6.2.2.1 Finite-Volume Method

In the finite-volume method (FVM), the conservation principles are applied to a fixed region in space known as a control volume. Sometimes this method is also referred as the control volume method. The domain is divided into a number of control volumes such that there is one control volume surrounding each grid point. As shown in Figure 6-3, a typical two-dimensional Cartesian control volume (CV) is presented and the grid point is located at the centre of a CV. The CV interface is subdivided into four plane faces, denoted by lower case letters (e, w, n and s) corresponding to their direction with respect to the central node P. The nodes are denoted by upper case letters of E, W, N and S.

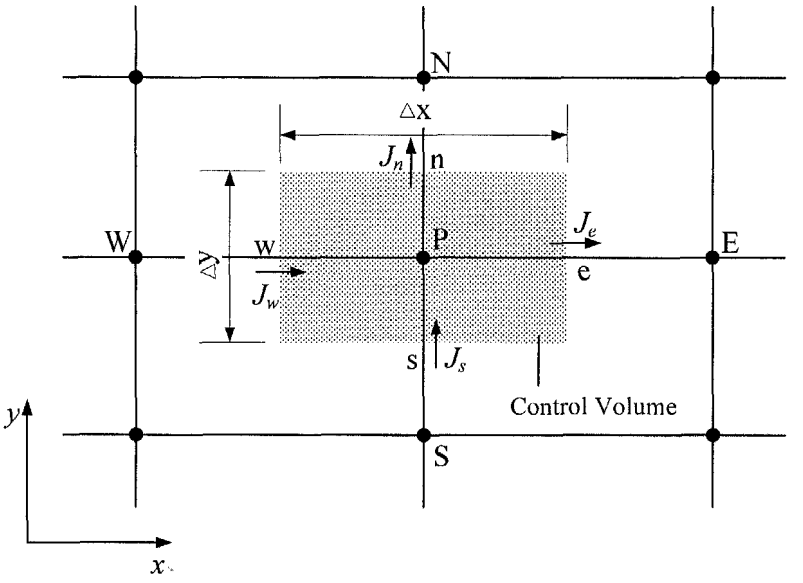

Figure 6-3 Diagram of Control Volume

The governing equation is integrated over each control volume to derive an algebraic equation containing the grid point values of Φ. The discretisation equation then expresses the conservation principle for a finite control volume just as the partial differential equation expresses it for an infinitesimal control volume. The resulting solution implies that integral conservation of quantities such as mass, momentum and energy is exactly satisfied for any group of control volumes and for the whole domain.

6.2.2.2 Discretisation

Considering the CV as shown in Figure 6-3, the total fluxes J_x and J_y (convection and diffusion) for x and y directions can be expressed as

$$J_x = \rho u\Phi - \Gamma\frac{\partial\Phi}{\partial x} \tag{6-37a}$$

$$J_y = \rho v\Phi - \Gamma\frac{\partial\Phi}{\partial y} \tag{6-37b}$$

where u and v denote the velocity components in the x and y directions. By employing J_x and J_y, the general two-dimensional transport equation (6-36) can be re-written as

$$\frac{\partial}{\partial t}(\rho\Phi)+\frac{\partial J_x}{\partial x}+\frac{\partial J_y}{\partial y}=S \tag{6-38}$$

The integration of Equation (6-38) over the CV shown in Figure 6-3 gives

$$\frac{(\rho_P\Phi_P-\rho_P'\Phi_P')\Delta x\Delta y}{\Delta t}+J_e-J_w+J_n-J_s=(S_C+S_P\Phi_P)\Delta x\Delta y \tag{6-39}$$

where ρ_P' and Φ_P' are the values at the beginning of the time step of the integration. J_e, J_w, J_n and J_s are the integrated total fluxes over the CV interfaces. It is noted that the term at the right side of Equation (6-39) is the linearised expression for source term S.

Similarly, the continuity equation of the unsteady problem can be integrated over the CV as

$$\frac{(\rho_P-\rho_P')\Delta x\Delta y}{\Delta t}+F_e-F_w+F_n-F_s=0 \tag{6-40}$$

F_e, F_w, F_n and F_s are the mass flow rates through the CV interfaces defined as

$$F_e=(\rho u)_e\Delta y \tag{6-41a}$$

$$F_w=(\rho u)_w\Delta y \tag{6-41b}$$

$$F_n=(\rho u)_n\Delta x \tag{6-41c}$$

$$F_s=(\rho u)_s\Delta x \tag{6-41d}$$

where Δx and Δy are the distances between CV interfaces. Considering Equations (6-39) and (6-40), the following equation can be obtained

$$\begin{aligned}(S_C+S_P\Phi_P)\Delta x\Delta y&=(\Phi_P-\Phi_P')\frac{\rho_P'\Delta x\Delta y}{\Delta t}\\&+(J_e-F_e\Phi_P)-(J_w-F_w\Phi_P)+(J_n-F_n\Phi_P)-(J_s-F_s\Phi_P)\end{aligned} \tag{6-42}$$

Using the power-law scheme for the CV interfaces as recommended by Patankar (1980), the terms J_e-$F_e\Phi_P$, J_w-$F_w\Phi_P$, J_n-$F_n\Phi_P$ and J_s-$F_s\Phi_P$ in Equation (6-42) can be expressed as follows:-

$$J_e - F_e\Phi_P = a_E(\Phi_P - \Phi_E) \tag{6-43a}$$

$$J_w - F_w\Phi_P = a_w(\Phi_w - \Phi_P) \tag{6-43b}$$

$$J_n - F_n\Phi_P = a_n(\Phi_p - \Phi_n) \tag{6-43c}$$

$$J_s - F_s\Phi_P = a_s(\Phi_s - \Phi_P) \tag{6-43d}$$

where the coefficients of the discretisation equation are

$$a_E = DI_eC_d(|P_e|) + \|-F_e, 0\| \tag{6-44a}$$

$$a_E = DI_wC_d(|P_w|) + \|F_w, 0\| \tag{6-44b}$$

$$a_N = DI_nC_d(|P_n|) + \|-F_n, 0\| \tag{6-44c}$$

$$a_S = DI_sC_d(|P_s|) + \|F_s, 0\| \tag{6-44d}$$

and C_d is the convection-diffusion coefficient. The diffusion rates DI_e, DI_w, DI_n, DI_s and the Peclet numbers Pe at the CV interfaces are

$$DI_e = \frac{\Gamma_e \Delta y}{(\delta x)_e}, \quad \mathrm{Pe}_e = \frac{F_e}{DI_e} = \frac{(\rho u)_e}{\frac{\Gamma_e}{\delta x_e}} \tag{6-45a}$$

$$DI_w = \frac{\Gamma_w \Delta y}{(\delta x)_w}, \quad \mathrm{Pe}_w = \frac{F_w}{DI_w} = \frac{(\rho u)_w}{\frac{\Gamma_w}{\delta x_w}} \tag{6-45b}$$

$$DI_n = \frac{\Gamma_n \Delta x}{(\delta y)_n}, \quad \mathrm{Pe}_n = \frac{F_n}{DI_n} = \frac{(\rho u)_n}{\frac{\Gamma_n}{\delta x_n}} \tag{6-45c}$$

$$DI_s = \frac{\Gamma_s \Delta x}{(\delta y)_s}, \quad \mathrm{Pe}_s = \frac{F_s}{DI_s} = \frac{(\rho u)_s}{\frac{\Gamma_s}{\delta x_s}} \tag{6-45d}$$

where δx and δy are the distances between grid points. By substituting Equation (6-45) into Equation (6-42), the two-dimensional discretisation equation can be obtained as

$$a_P\Phi_P = a_E\Phi_E + a_W\Phi_W + a_N\Phi_N + a_S\Phi_S + A \tag{6-46}$$

where

$$a_P = a_E + a_W + a_N + a_S - S_P\Delta x\Delta y \tag{6-47}$$

$$A = S_C\Delta x\Delta y \tag{6-48}$$

The power-law formulation is

$$C_d\left(|\mathrm{Pe}|\right) = \left\|0,(1-0.1|\mathrm{Pe}|)^5\right\| \tag{6-49}$$

where Pe is the Peclet number.

6.2.2.3 Programme Structure

As mentioned previously, the governing equations are solved by using the finite-volume method. This algorithm provides a remarkably successful method for simulating heat transfer in fluid flow. In the present simulation, the convection and diffusion terms are discretised by the power-law scheme and the unsteady term is handled by the forward difference scheme. The pressure-velocity coupled momentum equation is solved by SIMPLE method introduced by Patankar (1980). The velocity fields can be obtained by using an iterative method if the pressure field is estimated. The continuity equation is used to improve the estimated pressure field. In the simulation, the computation started with making an initial guess of the pressure field and solving the momentum equation to obtain the velocity field. Mass conservation is adopted at the outlet boundary to obtain the outlet velocity of oscillating flow through the porous channel in the different half-cycles. Compaq Visual Fortran (Version 6.0) is the development environment which was installed on a Pentium 4 computer with 2.8 GHz CPU and 1 GB RAM. The computation time depends mainly on the setting of the number of iteration step and time step. For different cases, the average calculation time is about eight hours.

Figure 6-4 shows the flow diagram of the computer programme which consists of MAIN and USER subprogrammes. The USER subprogramme was written by the author in FORTRAN and the MAIN subprogramme has been described in detail by Patankar (1980). The subprogrammes of MAIN and USER are actually assemblies of a number of member subroutines, whose names are shown in the appropriate boxes in Figure 6-4. These assemblies are created by using the ENTRY statement. All the required information are transferred through COMMON statements. The expediency of using subprogrammes reduces the repetition of COMMON statements, this enabling the member routines to share variables without passing them through COMMON and keeps the related physical information or mathematical operations together. The MAIN subprogramme controls the sequence of important operations by calling number of subroutines as shown Figure 6-4. In DIFLOW block, the formulation of convection diffusion $C_d(|P|)$ is calculated. The parameters of geometry and the coefficients of the discretisation equations are established in SETUP. SOLVE is the most important subroutine and prepares the numerical counterparts of the general differential equations presented previously. To obtain the numerical solution, the simultaneous algebraic equations are determined in SOLVE. The subroutines of UGRID and PRINT can be used to construct control volume faces and print out variables in a specified format, respectively.

The subprogramme USER contains six member subroutines. GRID and START are called only once during the whole simulation. GRID provides grid-related geometrical information, the number of time steps and the number of inner iterations per time step. START is used to specify the properties, initial value and useful identifier. DENSE is called at every inner iteration for all variables solved. The density ρ in Equation (6-36) is specified in DENSE. BOUND is used to calculate the boundary temperatures for

given flux which is called at every inner iteration. GAMSOR is another important member subroutine. In each iteration, it is called several times for each dependent variable. Its primary function is to specify the appropriate information about Γ and S in Equation (6-36). In addition, some boundary condition details for each Φ are given in GAMSOR. OUTPUT is called once per iteration and the required printout is specified in this part.

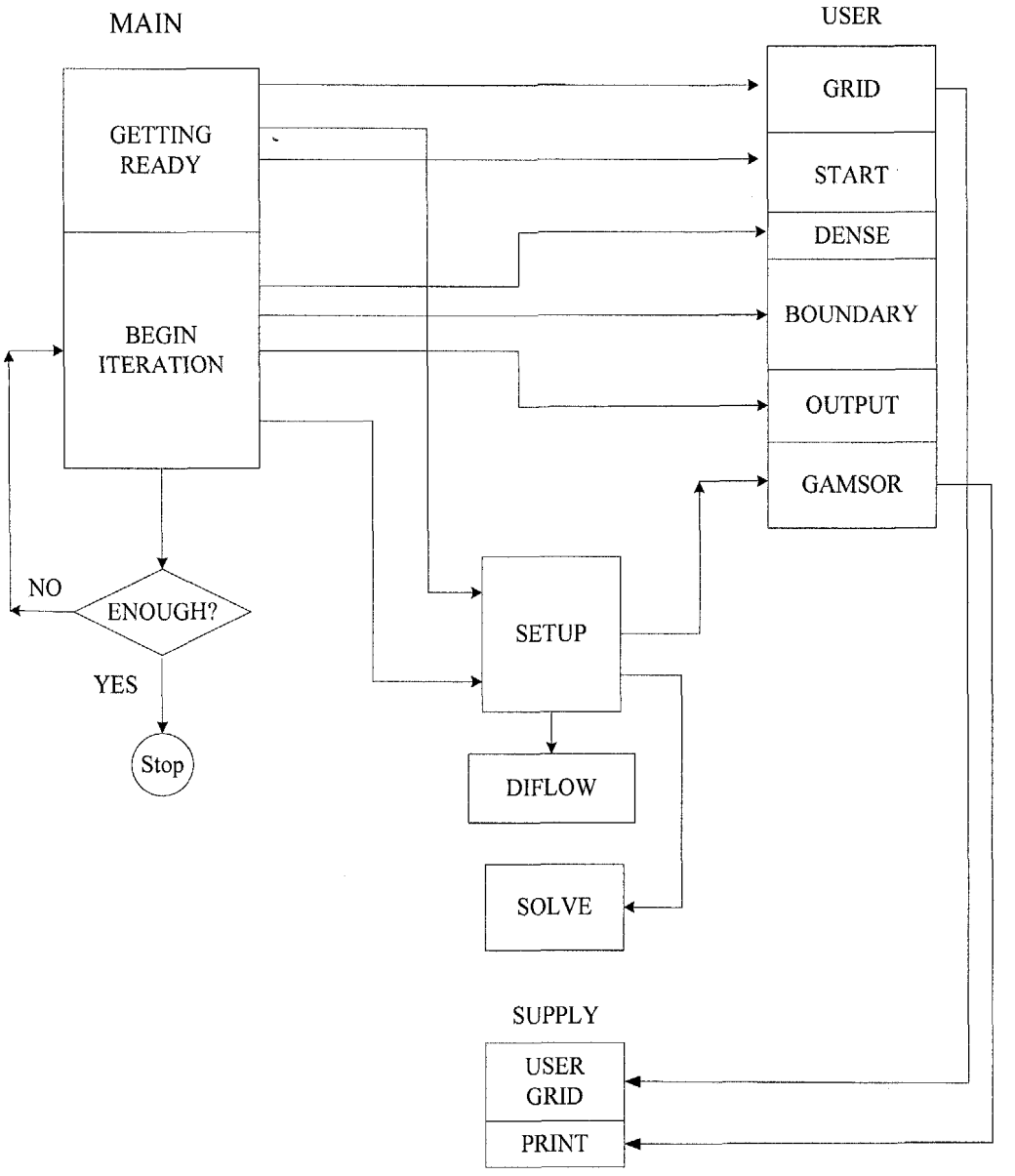

Figure 6-4 Flow chart of the computer programme

6.2.2.4 Full Domain and Boundary Conditions

Typically, the boundary can be specified based on the symmetric domain or full domain. The full domain method is employed in the present study due to the known heat flux at the bottom boundary. A grid dependent test is performed to arrive at the appropriate size of the grid which combines accuracy and efficiency. The simulation results of three types of the grids are compared. The maximum differences of the cycle-averaged Nusselt numbers between the grids of 14 × 6 and 22 × 11, and the grids 42 × 21 and 22 × 11 are less than 3 % and 2 %, respectively. Therefore, the grid of 22 × 11 was adopted to the control domain based on the tests of the different grids. In the simulation, staggered grids are used for the velocity components. The scalar variables are stored at the grid point while the velocity fluids are stored at the staggered grids which are centred on the CV interfaces. The schematic diagram of numbering system for the full domain is shown in Figure 6-5.

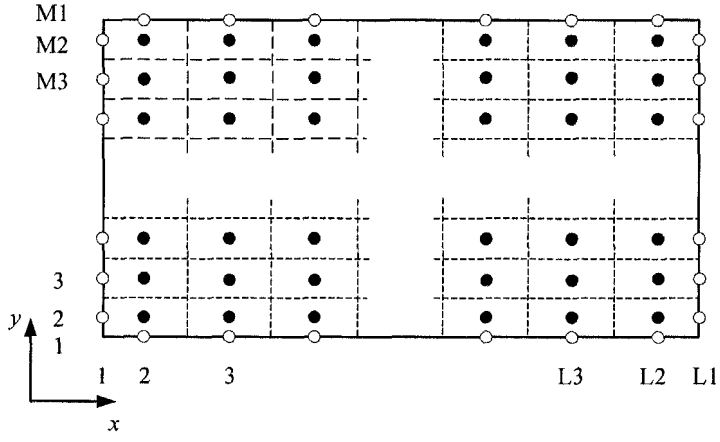

Figure 6-5 Schematic diagram of grids and nodes for numerical domain

There are three kinds of boundary conditions encountered at the boundaries of the domain, i.e. (a) boundary values are given; (b) boundary fluxes are given and (c) boundary fluxes were expressed as a combination of a reference value and boundary data. If the boundary values are given, no additional formulation is needed. For the present study, the heat flux at the bottom boundary is specified. For velocity, all the

values need to be specified at the inlet boundary. At the wall, the non-slip condition is implemented. At the outlet boundary, the velocity can be determined by satisfying the mass conservation. According the grid system shown in Figure 6-5, Equation (6-50) is used to satisfy the mass conservation at the outlet boundary.

$$u_{L1} = u_{L2} + C \tag{6-50}$$

where u_{L1} and u_{L2} are the velocity at the grid of the boundary and next to the boundary. C is a constant obtained by

$$C = \frac{M_{in} - \rho_{L1} u_{L2} A_C}{\rho_{L1} A_C} \tag{6-51}$$

where M_{in} is the inlet mass flow rate and A_C is the cross-sectional area of the metal foam.

6.2.2.5 Iteration Time-step and Convergence Criteria

To obtain good stability, appropriate values for the initial time-step in the simulation were validated. Different values of the time-step were tested for dimensionless oscillatory frequencies (i.e. the kinetic Reynolds number) ranging from 100 ~ 1090, which cover the frequency range conducted in experimental study. The appropriate values were found to be from 0.01 (for relatively low frequency) to 0.005 (for relatively high frequency) for the calculated oscillatory speeds. For values lower than 0.005, there is no difference in the final result. For values higher than 0.01, the result does not satisfy the convergence condition.

When using an iterative method to solve the linear or the nonlinear problem, it is important to know when to quit the iteration. The most common procedure is based on the difference between two successive iterations. The iteration is stopped when the difference is less than a pre-selected value. For velocity, the maximum residual can be used as convergence criterion, which is calculated by:

$$\zeta = \left| \left(\rho_w u_w - \rho_e u_e \right) \Delta y + \left(\rho_s u_s - \rho_n u_n \right) \Delta x \right|_{\max} \tag{6-52}$$

where ζ is the maximum residuals. For scalar variable, the difference between two successive iterations can be considered as a convergence criterion when

$$\left| \Phi^n - \Phi^{n-1} \right|_{\max} \le \zeta \tag{6-53}$$

The solution is deemed to have converged when the difference in values of a given variable between two successive iterations is less than a prescribed tolerance. The values for the critical parameters of the temperature and the Nusselt number are 10^{-4} and 10^{-5}, respectively.

6.3 Summary

In this chapter, two-dimensional theoretical formulations of the macroscopic momentum and energy equations based on the volume averaging method are presented. The effects of the permeability K and inertia coefficients F are included into the momentum equation. The modelling of heat transfer in open-cell metal foam is shown in detail. The main features of the energy governing equations are: (1) the local thermal non-equilibrium is taken into account; (2) the effective transport coefficients such as the effective thermal conductivity and interfacial heat transfer coefficient in the energy equations incorporate the effect of the ligament diameter of the metal foam. In addition, the specific boundary conditions for oscillating flow through the metal foam are formulated. The numerical scheme based on the finite-volume method which is used to solve the transient heat transfer in metal foam is presented. The flow chart of the computer programme written in FORTRAN is described through MAIN and USER subprograms. A grid dependence study was performed to optimise the grid number for the computational domain. The iteration time-step and convergence criteria for the problem are also discussed.

CHAPTER 7

NUMERICAL RESULTS AND DISCUSSION

7.1 Code Validation

As described previously, the aim of the present numerical study is to investigate heat transfer in metal foam channel subjected to oscillating flow. Before discussion of the numerical results, it is necessary to validate the numerical code programmed by the author. Based on the governing equations, the present code can also be used for calculating heat transfer of steady flow through metal foam by simply changing the initial and boundary conditions. In order to validate the numerical code with the results reported by other researchers, the heat transfer performance of aluminium foam 5 PPI is calculated and compared with the experimental data under steady flow condition obtained by Calmidi (1998). In his experiments, the hydraulic and thermal properties of the tested aluminium foams and the boundary values are given. The values of the physical characteristics of tested samples used in the calculation are listed in Table 7-1.

Table 7-1 Physical characteristics of the tested samples
(Source: Calmidi, 1998)

Materials	d_l (m)	K (10^7 m^2)	F	k_{se} (W/m·K)	k_{fe} (W/m·K)	ε
Al 5 PPI #1	0.0005	2.7	0.097	2.48	0.026	0.973
Al 5 PPI #2	0.0005	1.8	0.085	6.46	0.024	0.912

The values given in Table 7-1 are directly input into the numerical programme, and the boundary conditions are specified as follows:

at $x = 0$, $u = u_{in}$

$$v = 0$$

$$T_f = T_{in} \tag{7-1a}$$

at $x = L$, $\dfrac{\partial u}{\partial x} = \dfrac{\partial v}{\partial x} = 0$

$$\frac{\partial T_f}{\partial x} = \frac{\partial T_s}{\partial x} = 0 \tag{7-1b}$$

at $y = 0$, $u = v = 0$

$$k_{fe}\frac{\partial T_f}{\partial y} + k_{se}\frac{\partial T_s}{\partial y} = q \tag{7-1c}$$

at $y = H$, $u = v = 0$

$$\frac{\partial T_f}{\partial y} = \frac{\partial T_s}{\partial y} = 0 \tag{7-1d}$$

In the calculations, T_{in} is given and u_{in} can be obtained accurately from the given value of $\mathrm{Re}_K = uK^{1/2}/\nu_f$, which is the Reynolds number based on the permeability. As presented in Figure 7-1, the simulation results of the averaged Nusselt number for the tested materials increase gradually with the permeability based Reynolds number. The calculated total heat transfer rates for aluminium foam samples #1 and #2 show good agreement with the experimental data (Calmidi, 1998). The tested problem demonstrates that the present numerical method can be used to predict heat transfer in metal foam channel.

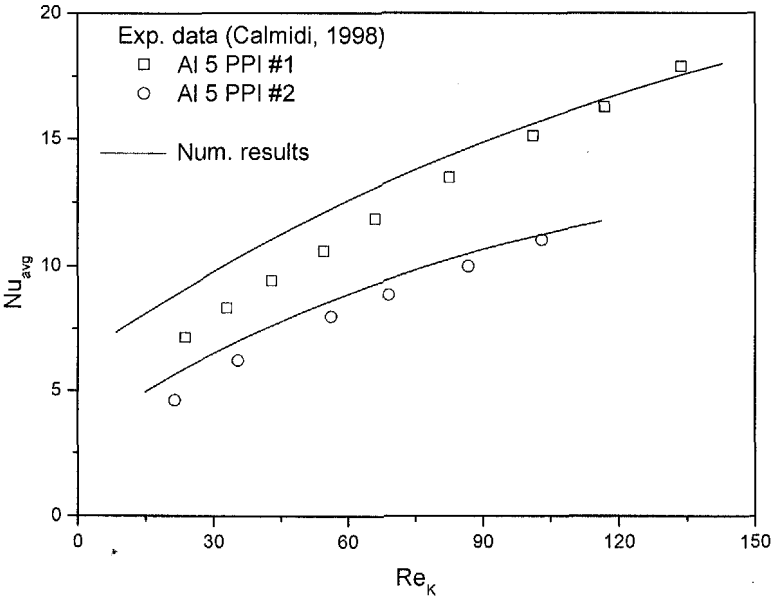

Figure 7-1 Comparison of the total heat transfer rates in aluminium foam 5 PPI samples between the numerical prediction and experimental data (Calmidi, 1998)

7.2 Numerical Results and Discussions

To study of the characteristics of heat transfer for oscillating flow through metal foam channel, the transient variations of the velocity, temperature and Nusselt number at the different locations of channel were calculated. The results discussed below are subjected to the same constant heat flux. To focus on the investigation of transient heat transfer characteristics during a complete oscillation cycle which are difficult to obtain experimentally, typical values of the porosity, permeability and ligament diameter of metal foam are chosen to be 0.9, 10^{-8} m^2 and 500 μm, respectively. Using Equations (6-23) ~ (6-29), the effective thermal conductivities of the fluid and solid phases and the interfacial surface area were calculated to be 2.8 W/m·K, 0.024 W/m·K and 760 m^2/m^3, respectively. The dimensionless parameters of Re_ω and A_0 were determined by Equations (5-29) and (5-30). In addition, the cycle-averaged values for temperature and Nusselt number along the flow direction are presented and compared

with the experimental results.

7.2.1 Variations of Instantaneous Velocity and Temperature

Typical variations of the transient temperatures of oscillating flow at different vertical locations around the centre of the channel for Re_ω = 110 at A_0 = 6 are presented in Figure 7-2 (a). The dimensionless distances of y/D_e = 0.12 and 0.3 represent the locations close to the bottom and centreline of the channel, respectively. It can be seen that the temperature profiles of the fluid at the different vertical locations decrease with the distance from the bottom to the centreline of the channel. For both locations, the transient temperature decreases first at the beginning of the cycle and increases from the quarter of the cycle. The highest temperatures for y/D_e = 0.12 and 0.3 are obtained around t = 0.5 s as the oscillatory velocity approaches zero at the end of the first half-cycle. From the next half-cycle, the fluid reverses its direction and enters channel with temperature T_{in} which is set in the boundary condition. The variation of the transient temperature in the second half-cycle shows a similar trend with that in the first half-cycle. It is also observed that the variations of the temperatures with time at y/D_e = 0.12 and 0.3 are almost synchronous during a complete cycle.

Figure 7-2 (b) presents the instantaneous axial velocity of the fluid at y/D_e = 0.12 and 0.3 calculated in the same cycle as shown in Figure 7-2 (a). It shows that the instantaneous axial velocities at y/D_e = 0.12 and 0.3 vary in phase and the difference of the velocity between these two locations is very small. This implies that the effect of the forced convection term [second term in the left side of Equation (6-21)] on the temperature variation at different vertical locations around the centre of the porous channel becomes less significant. Therefore, the transient development of temperature profiles along the vertical direction at the middle of metal foam channel depends

mainly on the diffusion mechanism. The lower transient temperature profile at y/D_e = 0.3 obtained in Figure 7-2 (a) is induced by the diffusion effect along the vertical direction of the porous channel.

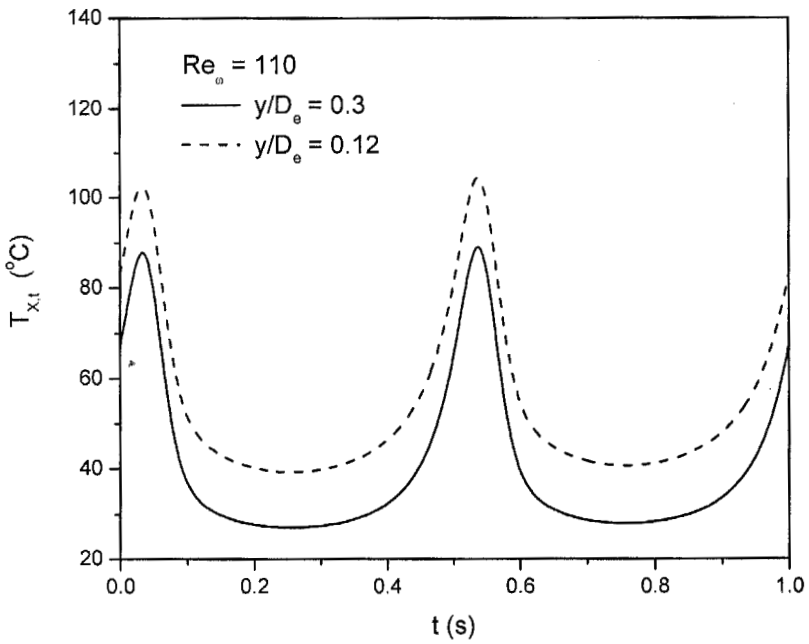

(a)

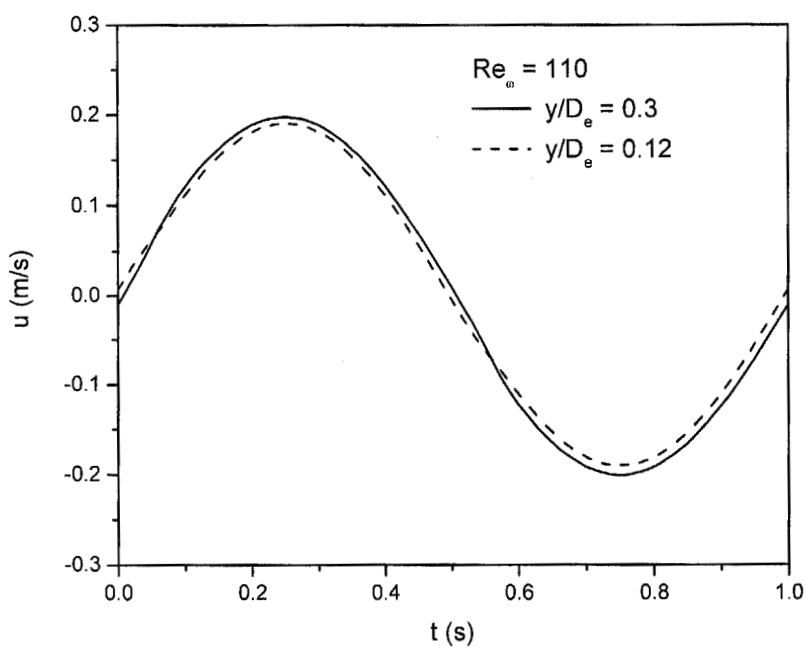

(b)

Figure 7-2 (a) Transient temperature profiles and (b) instantaneous axial velocities of fluid at y/D_e = 0.12 and 0.3 around the centre of channel for Re_ω = 110 at A_0 = 6

Figure 7-3 (a) shows the typical variations of the transient temperatures at the different axial locations of x/D_e = 0.675 and 2.333, which are symmetric at equal distance from the centre of the channel, for oscillating flow through metal foam with Re_ω = 110 at A_0 = 6. The dimensionless locations of x/D_e = 0.675 and x/D_e = 2.333 are close to the two entrances of the channel. It can be seen that the transient temperature profile for x/D_e = 0.675 is lower than that for x/D_e = 2.333 in the first half-cycle. The magnitudes of these profiles are reversed for these two locations in the second half-cycle. For both locations, the transient temperature decreases first at the beginning of the cycle and increases from the quarter of the cycle. The transient temperatures increase rapidly around t = 0.5 s because the oscillatory velocity approaches zero at the end of the first cycle.

Figure 7-3 (b) presents the instantaneous axial velocities of the fluid at x/D_e = 0.675 and 2.333 which are calculated in the same cycle as discussed in Figure 7-3 (a). It shows that the instantaneous axial velocity at x/D_e = 0.675 varies in phase with that at x/D_e = 2.333. However, it is observed the maximum instantaneous axial velocities for x/D_e = 0.675 and 2.333 are obtained in the first and the second half-cycles, respectively. In the first half-cycle, the velocity profile for the location of x/D_e = 0.675 is higher than that for the location of x/D_e = 2.333 due to the flow resistance of metal foam along the channel. In the next half-cycle, the transient velocity profile at x/D_e = 2.333 becomes higher than that at x/D_e = 0.675 because the fluid reverses its direction. Therefore, forced convection at x/D_e = 0.675 in the first half-cycle is more significant than that at x/D_e = 2.333, and the forced convection becomes stronger at x/D_e = 2.333 in the second half-cycle as compared to that at x/D_e = 0.675. This is in agreement with the findings given in Figure 7-3 (a), which shows that lower transient temperature profiles for x/D_e = 0.675 and 2.333 are obtained in different half-cycle.

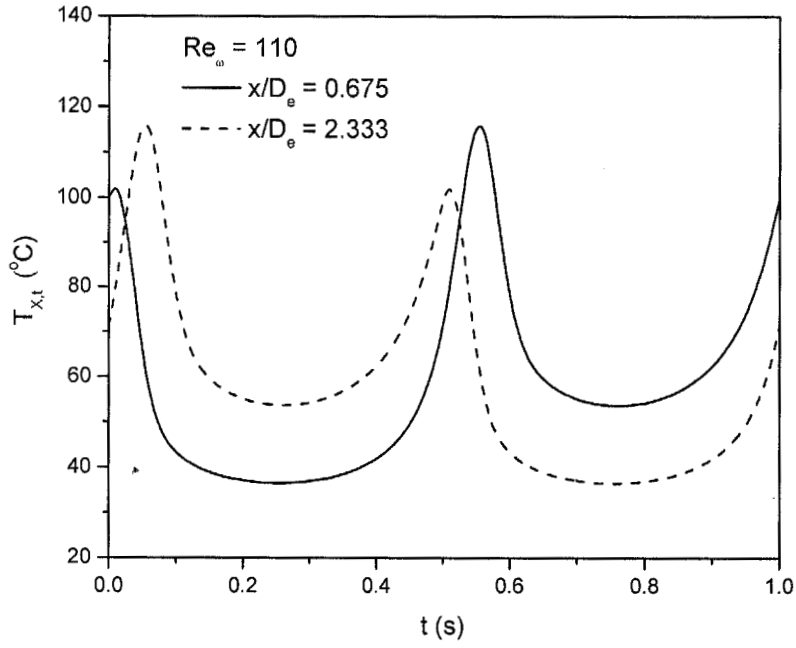

(a)

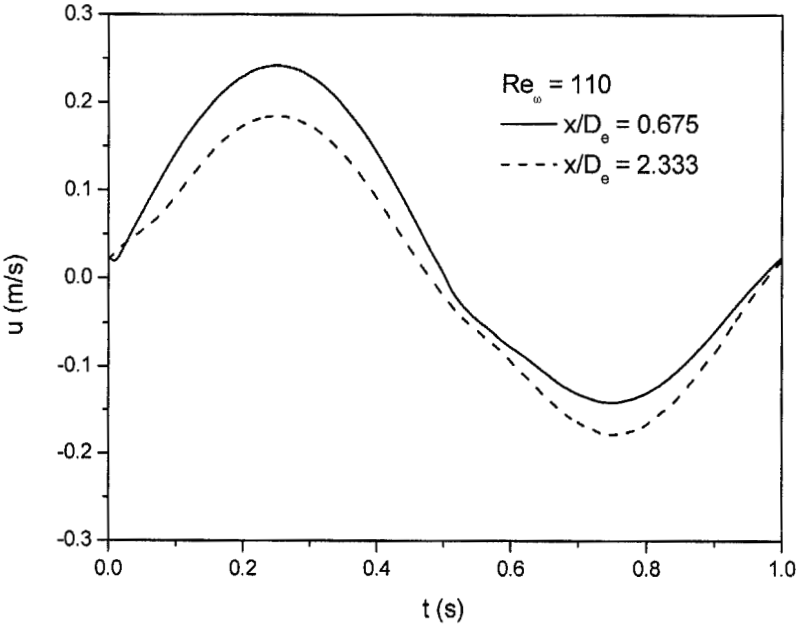

(b)

Figure 7-3 (a) Typical variations of the transient temperatures and (b) instantaneous axial velocities at x/D_e = 0.675 and 2.333 for Re_ω = 110 at A_0 = 6

7.2.2 Transient Temperature for Different Frequency and Flow Amplitude

Figure 7-4 illustrates the typical temporal variations of the fluid temperatures near the entrance and the centre of the channel for $A_0 = 6$ and $Re_\omega = 110$, i.e. $x/D_e = 0.275$ and $x/D_e = 1.433$. It is found that the transient temperature profile for the fluid near the entrance of the channel ($x/D_e = 0.275$) drops rapidly due to cooler fluid entering the metal foam channel in the first half-cycle. As the fluid moves along the metal foam channel, the warmer fluid passes through the centre of the channel which results in a high temperature at the centre of the channel. Around the end of the first half-cycle, the temperatures at both locations of $x/D_e = 0.275$ and 1.433 increase rapidly due to the sinusoidal motion of the fluid, i.e. the velocity approaches zero before reversing its direction at the end of the first half-cycle. From the next half-cycle, the temperatures at the entrance and the centre of the channels drop again due to the cooler fluid reversing its direction and entering the channel. It is noted that at different dimensionless axial locations, the temperatures at the beginning and the end of the cycles approach the same value as marked by the dashed line in Figure 7-4. This indicates that the temperature profiles obtained by the numerical simulation are under cycle-steady state for oscillating flow through metal foam channel.

Figure 7-5 presents the temporal temperature variations of oscillating flow through metal foam channel with $Re_\omega = 545$ at the same axial locations as shown in Figure 7-4. The transient temperature profiles subjected to $Re_\omega = 545$ show similar variations with those subjected to $Re_\omega = 110$. A comparison of Figures 7-4 and 7-5 shows that under the cycle-steady state condition, the local temperatures at the locations of $x/D_e = 0.275$ and 1.433 for $Re_\omega = 545$ are lower than those for $Re_\omega = 110$. This implies that the temperature of oscillating flow through metal foam channel decreases with increasing kinetic Reynolds number, i.e. oscillatory frequency.

Based on the above discussion, the effects of dimensionless flow amplitude on the instantaneous temperatures at different axial locations in a complete cycle are plotted in Figures 7-6 and 7-7. Once again, the same characteristics of transient temperature variation observed for Re_ω = 110 and 545 at A_0 = 6 can be found in Figures 7-6 and 7-7 for the same kinetic Reynolds number at A_0 = 7.2. However, comparisons between these figures show that the instantaneous temperature profiles for large dimensionless flow displacement are lower than that for small dimensionless flow displacement. For kinetic Reynolds number Re_ω = 545, the temperatures at the cycle-steady state for A_0 = 6 and 7.2 are 70.6°C and 63.2°C, respectively.

To reveal the physical phenomena behind the large dimensionless flow amplitude corresponding to low instantaneous temperature profile for oscillating flow through tested material at a fixed kinetic Reynolds number, the average axial velocity during a half-cycle versus different kinetic Reynolds number is shown in Figure 7-8. It is found that at the same kinetic Reynolds number, the mean axial velocity for large dimensionless flow amplitude is higher than that for small dimensionless flow amplitude. Large value A_0 represents the long flow movement in a half oscillation cycle. To drive the oscillating flow with different movement length through the metal foam channel in the same cycle time, the large A_0 will possess the higher axial velocity as compared to small A_0. The higher flow mean velocity for large flow amplitude directly leads to the low instantaneous temperature at different axial locations for a fixed oscillatory frequency observed in Figures 7-6 and 7-7.

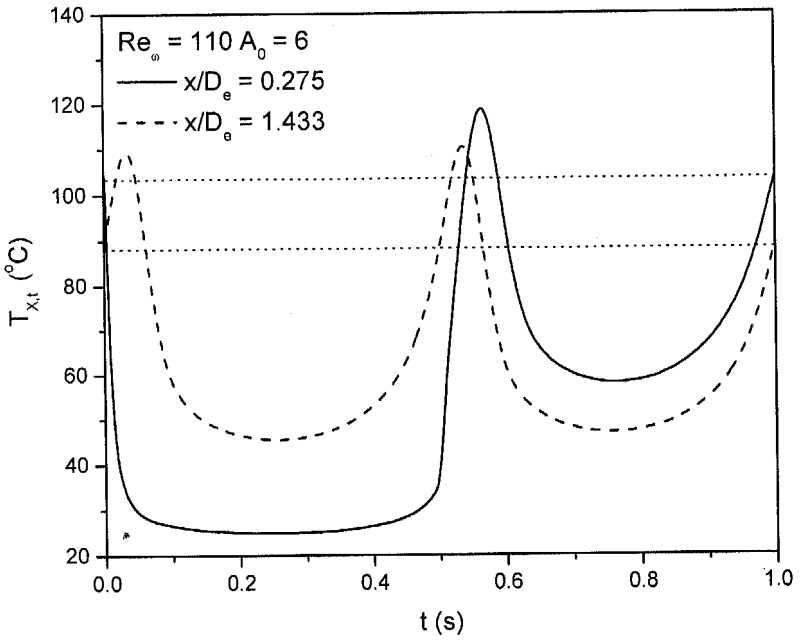

Figure 7-4 Temporal variations of the fluid temperatures near the entrance and the centre of the channel for $Re_\omega = 110$ at $A_0 = 6$

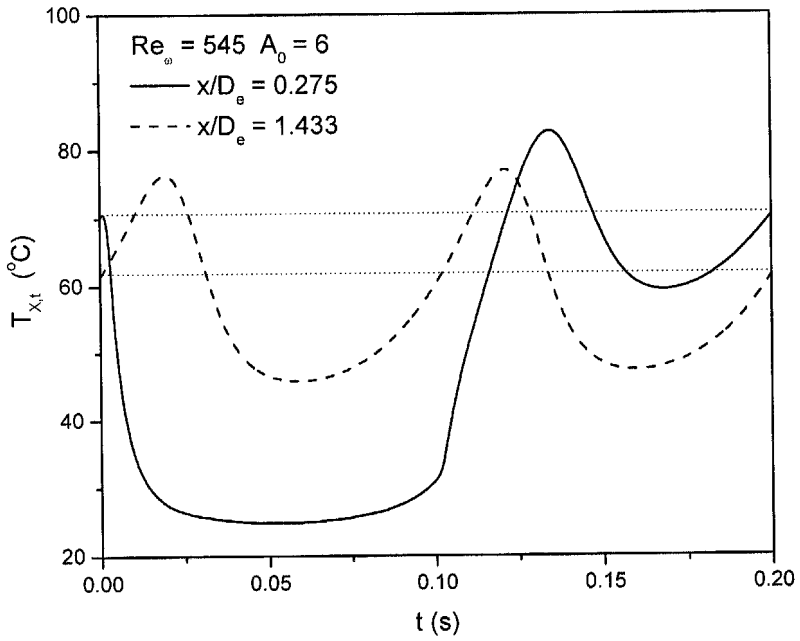

Figure 7-5 Temporal variations of the fluid temperatures near the entrance and the centre of the channel for $Re_\omega = 545$ at $A_0 = 6$

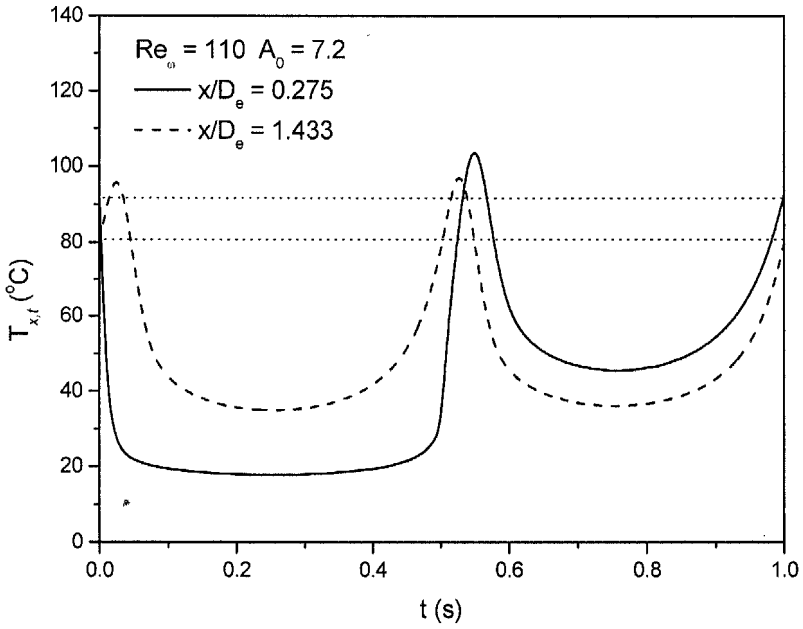

Figure 7-6 Temporal variations of the fluid temperatures near the entrance and the centre of the channel for Re_ω = 110 at A_0 = 7.2

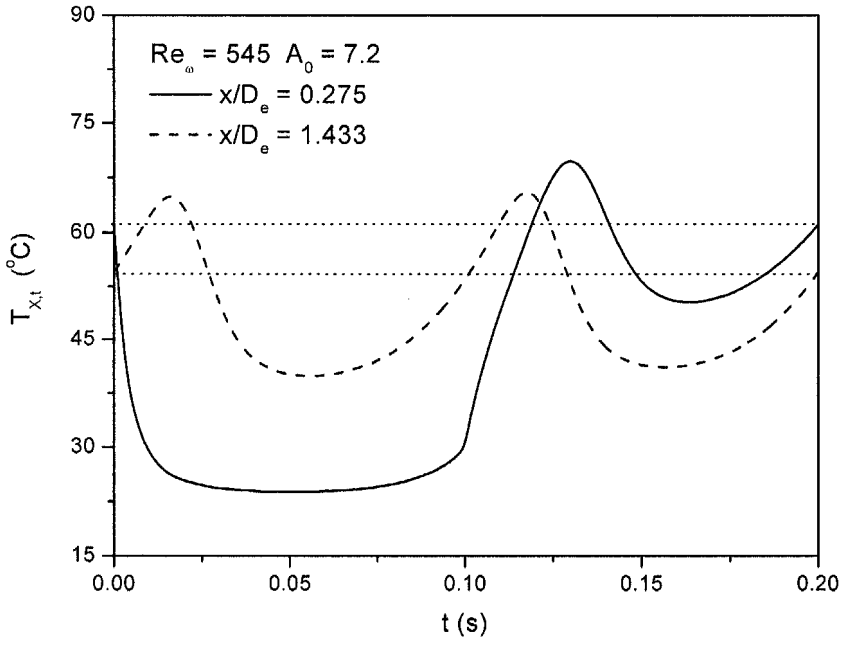

Figure 7-7 Temporal variations of the fluid temperatures near the entrance and the centre of the channel for Re_ω = 545 at A_0 = 7.2

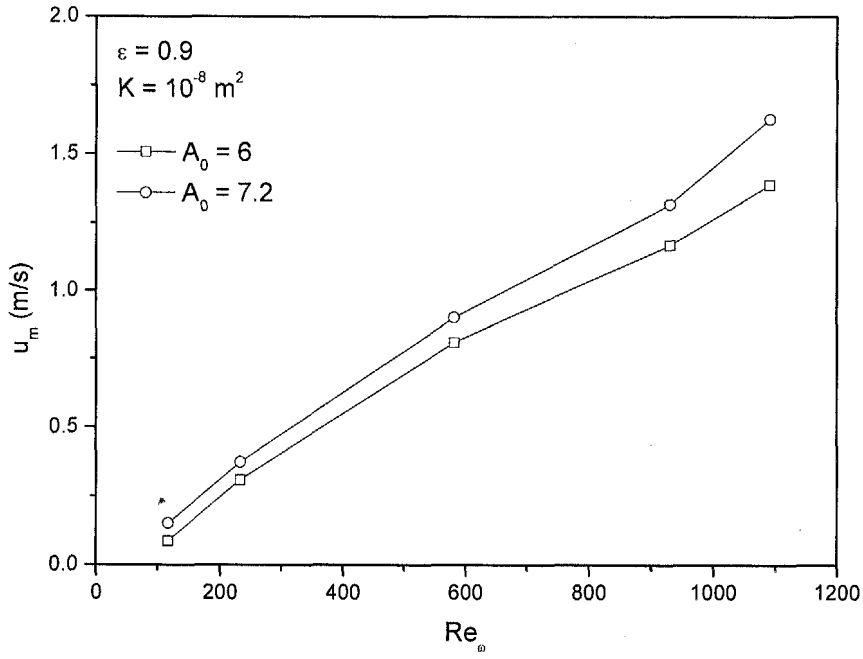

Figure 7-8 Variations of mean axial velocity during a half-cycle versus kinetic Reynolds numbers at A_0 = 6 and 7.2

7.2.3 Two-Dimensional Temperature Distributions

For electronic cooling applications, time-averaged characteristics are of practical interest in electronics thermal management. Instantaneous higher power dispersion may not damage the electronic components, but a long-lasting higher temperature will decrease their performance or even destroy them. Figures 7-9 (a), (b) and (c) show the two-dimensional (2-D) temperature distributions in the controlled domain at the cycle-steady state for oscillating flow through metal foam with Re_ω = 110, 545 and 1090 at A_0 = 6, respectively. It is observed that the 2-D temperature distributions for different kinetic Reynolds numbers are symmetric about the centre of the channel. The temperature decreases with the increase of the distance along the vertical direction of the channel for Re_ω = 110, 545 and 1090, which shows agreement with the result obtained in Figure 7-2 (a). As analysed earlier, the decreased temperature

profile at higher location is because of increased diffusion along the vertical direction of the channel. Comparing these figures, the temperature profiles in the simulated domain for small oscillatory frequency are lower than that for large oscillatory frequency. Focusing on the bottom boundary, the temperatures near the two entrance regions are lower than those near the centre of the channel. The cooler fluid enters the two inlets alternately during every half-cycle resulting in lower temperature distributions at the two entrance regions where stronger forced convection is occurring. For locations near the centre of the channel, the fluid is heated before passing through the middle locations of the channel. Therefore, the highest temperature on the substrate surface is obtained around the centre of the channel for the different kinetic Reynolds number. Figures 10 (a), (b) and (c) show the 2-D temperature distributions of the simulated domain for Re_ω = 110, 545 and 1090 at A_0 = 7.2, respectively. As analysed previously, a large flow amplitude results in a high axial mean velocity at a fixed kinetic Reynolds number for oscillating flow through metal foam channel. Therefore, the temperatures profiles in the simulated domain for different kinetic Reynolds number at A_0 = 7.2 are lower than that at A_0 = 6.

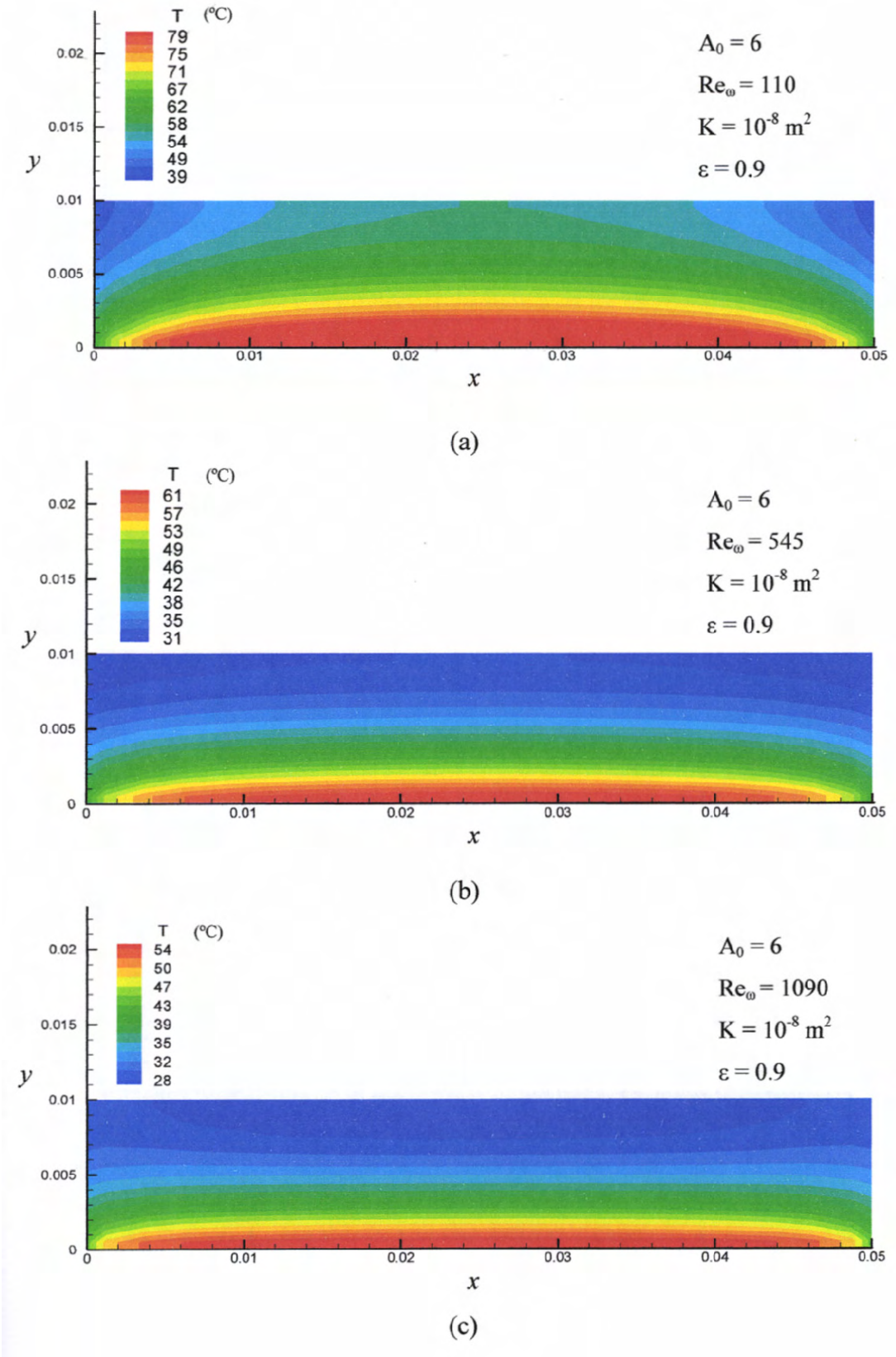

Figure 7-9 Two-dimensional temperature distribution in the numerical domain for oscillating flow through metal foam with (a) $Re_\omega = 110$, (b) $Re_\omega = 545$ and (c) $Re_\omega = 1090$ at the cycle-steady state for $A_0 = 6$

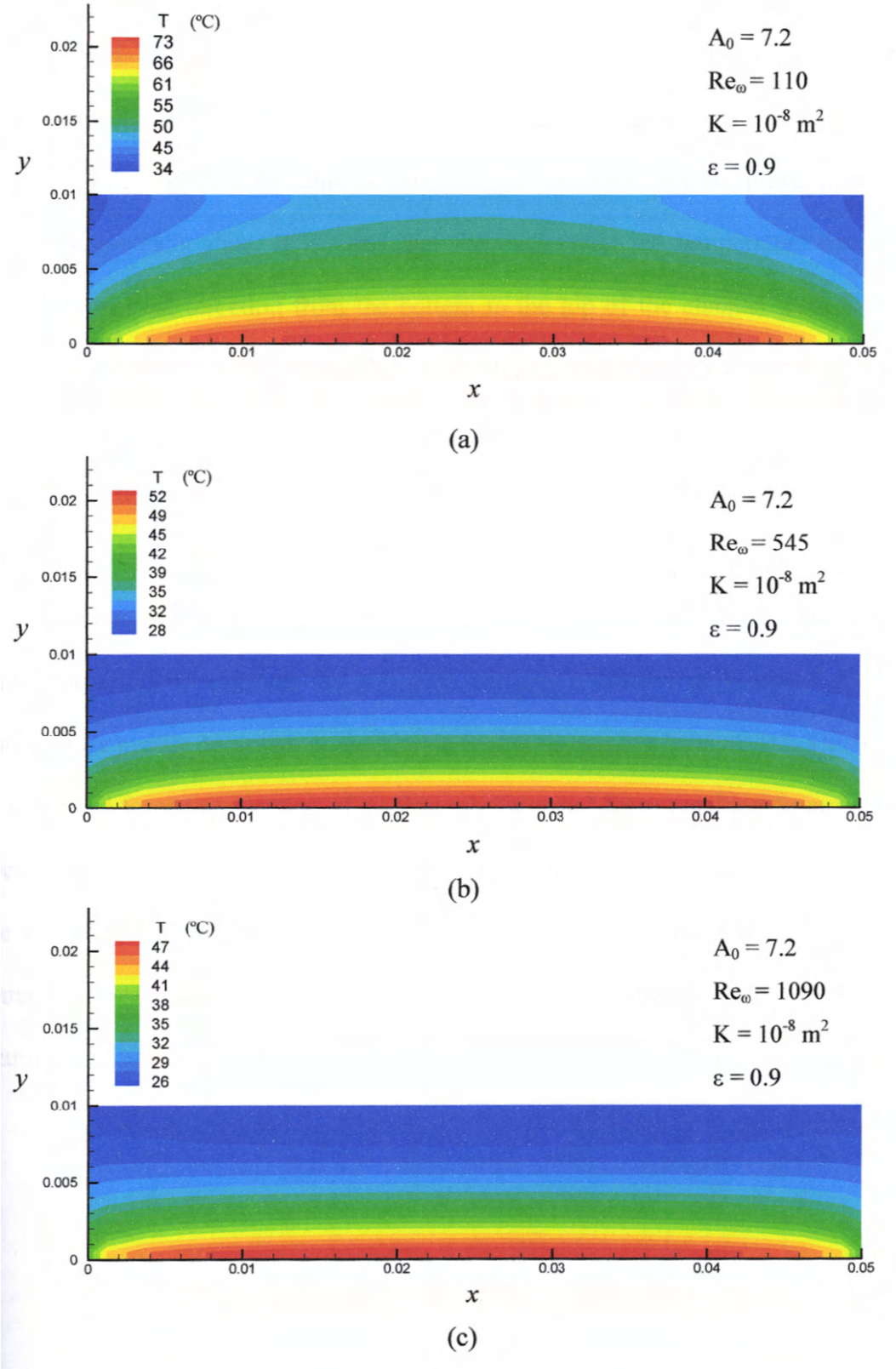

Figure 7-10 Two-dimensional temperature distribution in the numerical domain for oscillating flow through metal foam with (a) $Re_\omega = 110$, (b) $Re_\omega = 545$ and (c) $Re_\omega = 1090$ at the cycle-steady state for $A_0 = 7.2$

Figure 7-11 shows the cycle-averaged local temperature distribution at different dimensionless locations along the vertical direction for oscillating flow through metal foam channel with Re_ω = 545 at A_0 = 6. The cycle-average local temperature is the averaged value of the instantaneous temperatures obtained in a reciprocating cycles under cycle-steady state. It is clear that the cycle-averaged temperature decreases along the vertical direction from the bottom to the top of the channel. For different dimensionless locations of y/D_e, the temperature profiles are symmetric about the centre of the channel and the lowest temperatures are obtained at the two entrances. The highest temperature distribution is obtained at the location close to the bottom of the channel, i.e. $y/D_e = 0.06$.

The effect of the kinetic Reynolds number at A_0 = 6 on the cycle-averaged temperature distribution on the substrate surface is shown in Figure 7-12. The temperature profile decreases as the kinetic Reynolds number is increased. This is due to enhanced forced convection of air through the metal foam resulting from the high oscillatory speed. At each kinetic Reynolds number, the temperature increases from the entrance of the channel and then decreases after the centre of the channel. The same trend was found in the experimental study of oscillating flow through different aluminium foams at various kinetic Reynolds numbers.

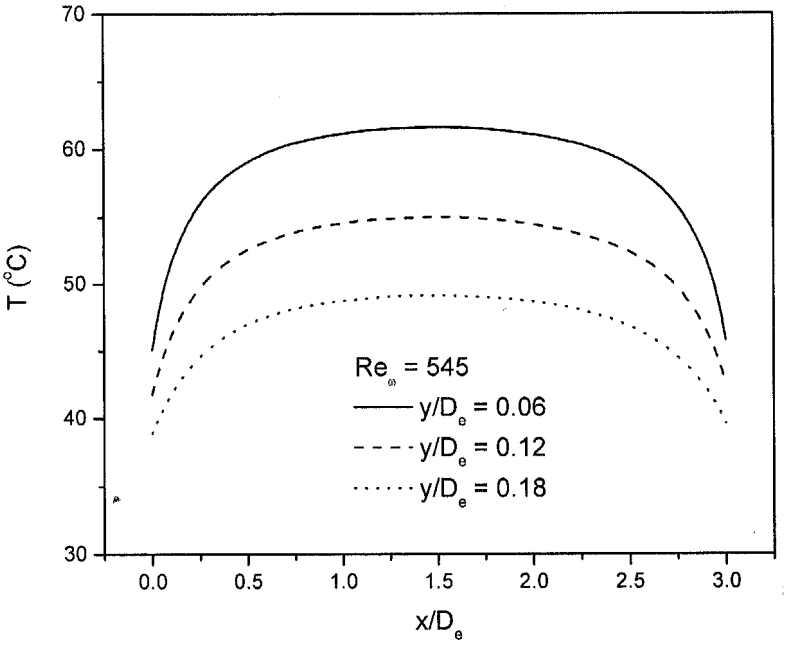

Figure 7-11 Cycle-averaged local temperature distributions at different dimensionless locations along the vertical direction at $Re_\omega = 545$

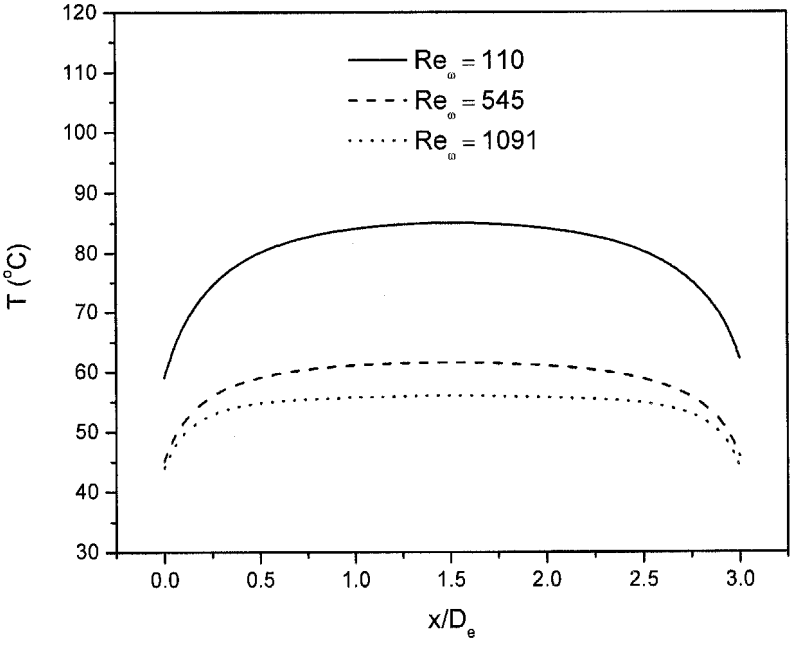

Figure 7-12 Effect of the kinetic Reynolds number on the cycle-averaged temperature distribution on the substrate surface at $A_0 = 6$

7.2.4 Heat Transfer Rates

7.2.4.1 Instantaneous Nusselt Number

The local instantaneous Nusselt number along the heated wall for unsteady flow is defined as

$$\mathrm{Nu}_{x,t} = \frac{h(x,t)D_e}{k_f} \tag{7-2}$$

where k_f is the thermal conductivity of the fluid and h is the local instantaneous heat transfer coefficient defined as

$$h(x,t) = \frac{q(x,t)}{T_w(x,t) - T_b(x,t)} \tag{7-3}$$

q is the heat flux at the bottom wall of the channel, T_w is the wall temperature and T_b is the local instantaneous bulk temperature. For uni-directional flow through a porous channel, $T_w(x,t) - T_b(x,t)$ is the thermal potential for the heat transfer, where $T_b(x,t)$ is defined as

$$T_b(x,t) = \frac{\int_0^H u(x,y,t)T(x,y,t)dy}{\int_0^H u(x,y,t)dy} \tag{7-4}$$

However, the instantaneous bulk temperature defined by Equation (7-4) loses its physical significance in oscillating flow because the cross-sectional mean velocity becomes zero twice in each cycle giving rise to an infinite value of the bulk temperature in each cycle. This will cause anomalies in evaluating the local Nusselt number and heat transfer coefficient defined by Equations (7-2) and (7-3). Therefore, the temperature difference between the heated wall and the inlet air T_w–T_i is used to evaluate the thermal potential for heat transfer from the heated wall of the porous channel to the cold fluid at the entrance and the exit of the channel. It should be noted that $\mathrm{Nu}_{x,t}$ is a function of the axial location x and time t.

The variations of the local instantaneous Nusselt number $Nu_{x,t}$ for $Re_\omega = 110$ and $A_0 = 6$ at different dimensionless axial locations on the bottom of the channel in a complete cycle are presented in Figure 7-13. The solid line represents the locations near the entrance region ($x/D_e = 0.275$) while the dash line represents the locations close to the centre of the channel ($x/D_e = 1.433$). Near the inlet position of $x/D_e = 0.275$, the instantaneous Nusselt number increases very rapidly and reaches the highest value around a quarter of the cycle. This is because the cooler fluid enters the entrance region with the maximum cross-sectional velocity obtained at a quarter of each complete cycle. Subsequently, the local instantaneous Nusselt number continues to decrease as the velocity of the entering fluid decreases to zero at the end of the first half-cycle. From the next half-cycle, the fluid reverses its direction and passes through the location $x/D_e = 0.275$ with warmer fluid due to heat exchange between the metal foam and the fluid along the channel. Consequently, the local Nusselt number at the entrance region during the second half-cycle becomes lower as compared to that during the first half-cycle. However, there is no visible difference in the instantaneous Nusselt number between the first and the second half-cycles at $x/D_e = 1.433$, i.e. the location around the centre of the channel. This is due to the flow of warmer fluid through the middle region of the channel during both the first and second half-cycles as a result of heat exchange between the cooler fluid entering from the two entrances and the inserted metal foam along the channel. A comparison of the instantaneous Nusselt numbers at $x/D_e = 0.275$ and 1.433 in a complete cycle implies that the average value of $Nu_{x,t}$ decreases as the dimensionless distance x/D_e is increased from the inlet to the middle of the channel.

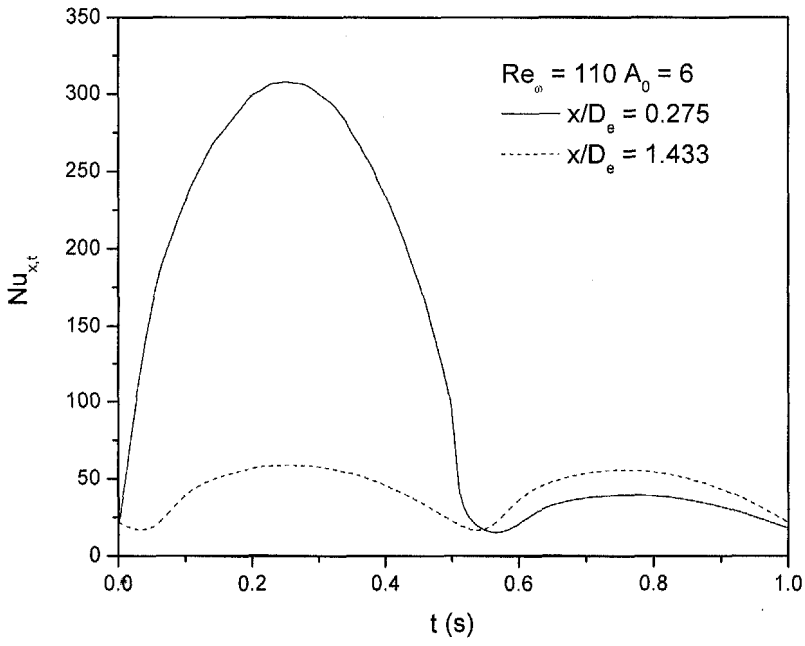

Figure 7-13 The variations of the local instantaneous Nusselt number $Nu_{x,t}$ for $Re_\omega = 110$ and $A_0 = 6$ at dimensionless axial locations of $x/D_e = 0.275$ and 1.433

The variation of the local instantaneous Nusselt number $Nu_{x,t}$ at $x/D_e = 1.508$ on the heated wall for a complete cycle of $Re_\omega = 110$ and $A_0 = 6$ is presented in Figure 7-14. It is seen that the local instantaneous Nusselt number is almost symmetric with respect to the time at the half-cycle. Compared to the instantaneous Nusselt number at $x/D_e = 1.433$ shown in Figure 7-13, the difference of the instantaneous Nusselt number variations for the locations close to the centre is not significant. As observed from Figures 7-9 and 7-10, 2-D temperature distributions for oscillating flow through metal foam channel with different kinetic Reynolds numbers are symmetric about the centre of the channel. To investigate the instantaneous Nusselt number along x direction of the channel, variations of the instantaneous Nusselt numbers at $x/D_e = 0.675$ and 2.333 with $A_0 = 6$ and 7.2 are presented in Figure 7-15. It is shown that the instantaneous Nusselt number at the same axial location for $A_0 = 7.2$ is higher than that for $A_0 = 6$. It can be observed that for both flow amplitudes, the variations of the

local instantaneous Nusselt numbers for the locations of x/D_e = 0.675 and 2.333 are almost symmetric about time t = 0.5 s, i.e. the end of the first half-cycle. This is due to the stronger forced convection which occurred at the first and the second half-cycles for the locations of x/D_e = 0.675 and x/D_e = 2.333, respectively, as the oscillating flow reverses it direction and enters the porous channel with low temperature at every half-cycle.

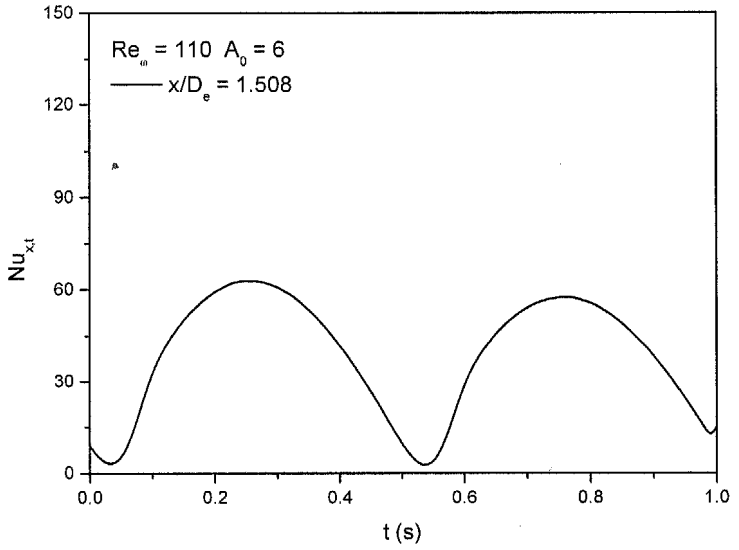

Figure 7-14 Variations of the local instantaneous Nusselt number $Nu_{x,t}$ for Re_ω = 110 and A_0 = 6 at x/D_e = 1.508

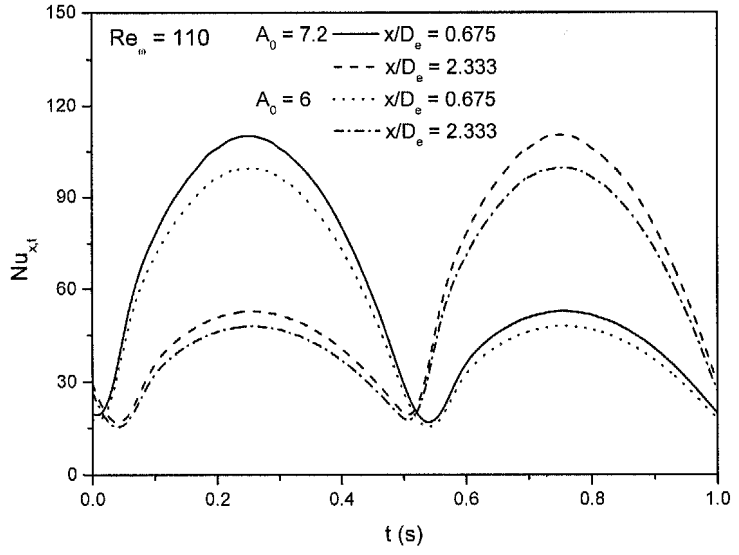

Figure 7-15 Instantaneous Nusselt number at the section of symmetry of the centre of the channel for x/D_e = 0.675 and 2.333 for A_0 = 6 and 7.2 at Re_ω = 110

7.2.4.2 Cycle- and Length-averaged Nusselt Numbers

Based on the definition of the instantaneous Nusselt number, the cycle-averaged Nusselt number can be calculated by

$$\mathrm{Nu}_x = f\int_0^{\frac{1}{f}} \mathrm{Nu}_{x,t}\,dt \tag{7-5}$$

where f is the frequency of oscillating flow. The distributions of the cycle-averaged Nusselt number on the substrate surface for oscillating flow through metal foam channel with different kinetic Reynolds numbers at $A_0 = 6$ are presented in Figure 7-16. It is seen that the cycle-averaged local Nusselt numbers are symmetrical with respect to the centre of the channel because of the symmetrical boundary conditions for both velocity and temperature in the problem under consideration. For different kinetic Reynolds number, the highest cycle-averaged Nusselt numbers are obtained at the two inlets of the channel due to good heat exchange at the two thermal entrance regions. The value of the cycle-averaged Nusselt number for different kinetic Reynolds number shows that the heat transfer rate increases with the increase of the dimensionless oscillation frequency, i.e. the kinetic Reynolds number. It can be explained in terms of the thermal boundary thickness δ_t in an oscillatory flow which can be expressed as

$$\delta_t \propto \left(\frac{1}{\mathrm{Re}_\omega}\right)^{\frac{1}{2}} \tag{7-6}$$

As the thermal boundary layer thickness decreases with the increase of kinetic Reynolds number, the heat transfer rate increases with the value of the Re_ω.

To evaluate the total heat transfer rate in a channel filled with metal foam subjected to oscillating flow, the length-averaged local Nusselt number is used to calculate the Nusselt number averaged over the whole length of the channel in a complete

oscillatory cycle which can be expressed as

$$\mathrm{Nu}_{avg} = \frac{f}{L}\int_0^{\frac{1}{f}}\int_0^{L}\mathrm{Nu}_{x,t}\,dxdt \tag{7-7}$$

where L is the length of the calculated domain. The length-averaged Nusselt numbers for oscillating flow with selected kinetic Reynolds numbers at A_0 = 6 and 7.2 through the metal foam channel are shown in Figure 7-17. The average Nusselt number along the length of channel was obtained under the cycle-averaged steady state and the kinetic Reynolds number ranges from 110 to 1090. Figure 7-17 shows that the length-averaged Nusselt number of air along the channel increases with the increase of kinetic Reynolds number and dimensionless flow amplitude. A larger cycle-averaged local Nusselt number for high kinetic Reynolds number and dimensionless flow amplitude leads to a higher length-averaged Nusselt number as compared to that for low kinetic Reynolds number and dimensionless flow amplitude.

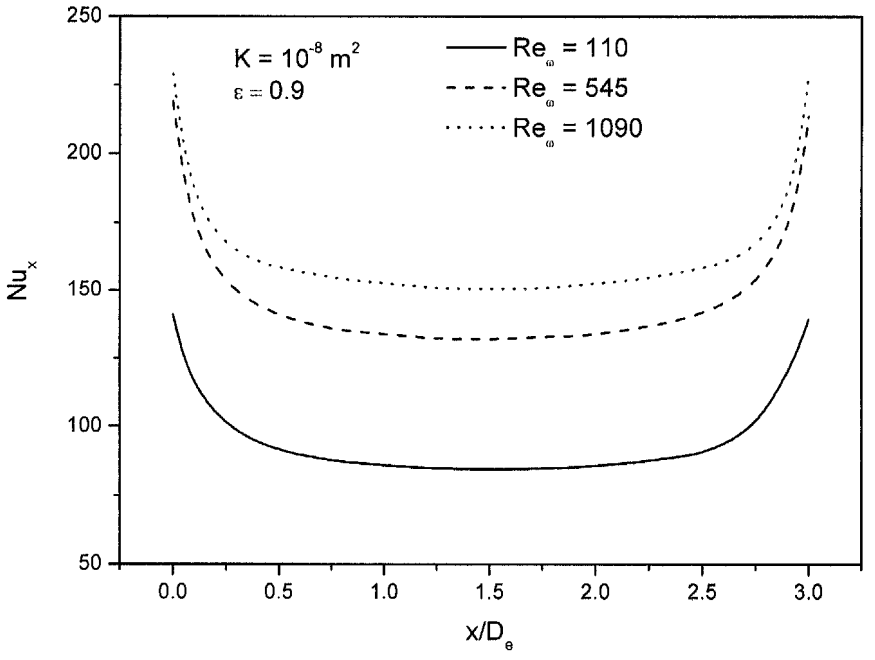

Figure 7-16 Effect of kinetic Reynolds number on the cycle-averaged Nusselt number for oscillating flow with A_0 = 6

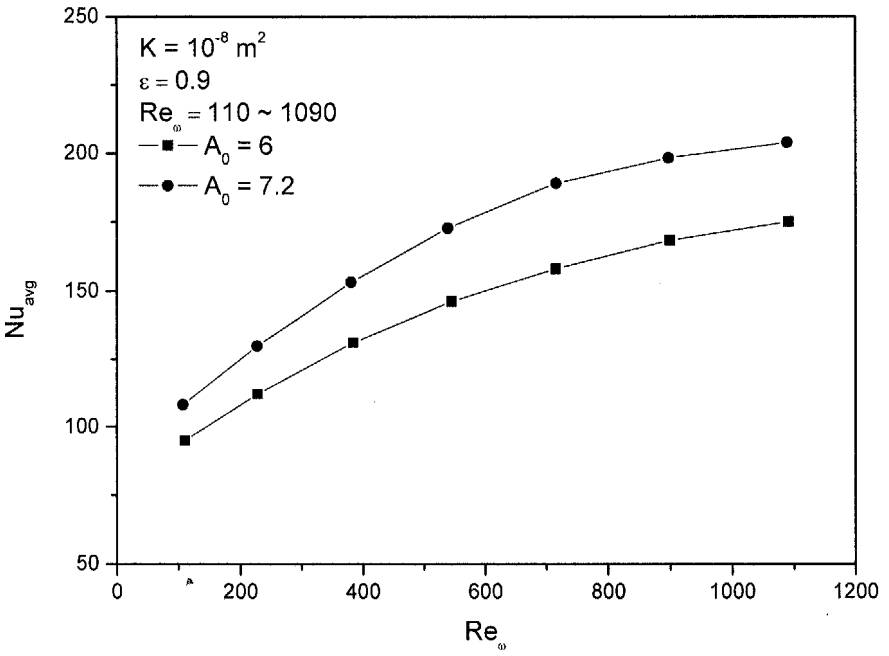

Figure 7-17 Length-averaged Nusselt number versus kinetic Reynolds number for oscillating flow through aluminium foam channel

7.3 Comparisons with Experimental Results

To compare numerical results for oscillating flow through metal foam with experimental data, flow and heat transfer in aluminium foams of 10, 20 and 40 PPI are simulated. The boundary conditions are set to be the same as those of the experiments. Thermophysical properties of the simulated materials are listed in Table 7-2.

Table 7-2 Thermophysical properties of aluminium foams

Materials	ε	k_s (W/m·K)	k_f (W/m·K)	a_{fs} (m^2/m^3)	k_{se} (W/m·K)	k_{fe} (W/m·K)
Al 10 PPI	0.91	171	0.023	800	4.1	0.025
Al 20 PPI	0.9	171	0.023	1700	5.2	0.024
Al 40 PPI	0.9	171	0.023	2650	5.9	0.026

7.3.1 Velocity Profile and Pressure Drop

The comparison of the numerical and experimental results for the mean axial cross-sectional velocity and pressure drop at the two ends of the channel for oscillating flow with flow amplitude x_{max} = 68 mm (i.e. A_0 = 4.1) and kinetic Reynolds number Re_ω = 440 are presented in Figures 7-18 and 7-19, respectively. The solid lines in these figures represent the numerically calculated results while the symbols with error bars are the experimental data obtained in this study. It can be seen that the numerical results for velocity and pressure drop vary almost in phase with the experimental data at the different kinetic Reynolds numbers in a complete cycle. The difference between the simulation and experimental results depends mainly on the assumptions employed in the numerical study and the tested conditions in the experimental investigation. For the numerical study, the calculations were based on the assumptions that the tested metal foam possesses the homogeneous and isotropic properties, and the inlet velocity strictly follows that of a sine function. However, the metal foam tested experimentally is non-homogeneous and anisotropic, and the inlet velocity of oscillating flow is influenced by the piston motion and the flow transportation through the connecting pipe. Furthermore, the air leakage and roughness of the channel may have effects on the deviation between the numerical and experimental results.

Figures 7-20 and 7-21 present the experimental and numerical results of the mean axial cross-sectional velocity and pressure drop for oscillating flow through aluminium foam 40 PPI at Re_ω = 440 and x_{max} = 68 mm. Once again, the numerical results show agreement with the experimental data. Comparing Figures 7-19 and 7-21, it is found that at approximately the same kinetic Reynolds number, i.e. oscillatory frequency, the pressure drop profile for oscillating flow through high pore density aluminium foam is higher than that through low pore density aluminium foam.

However, the difference of mean axial cross-sectional velocity profiles in Figures 7-18 and 7-20 for oscillating flow through aluminium foams 10 PPI and 40 PPI is rather small.

It is noted from Table 7-2 that the difference of porosity of the tested metal foams is very small. Thus, the porosity of open-cell aluminium foam has less effect on the pressure drop characteristics for oscillating flow through aluminium foam 10 and 40 PPI observed in Figures 7-19 and 7-21. To analyse the effect of material properties on the flow resistance in different metal foams, the momentum equation of steady flow through a porous medium was employed to simplify the problem. For fully-developed incompressible fluid flowing through a uniform porous medium, the equation is

$$0 = -\frac{1}{\rho_f}\frac{\partial P}{\partial x} + \frac{\nu_f}{\varepsilon}\frac{\partial^2 u}{\partial y^2} - \frac{\nu_f}{K}u - \frac{F}{\sqrt{K}}u^2 \tag{7-8}$$

where F and K are the inertia coefficient and permeability of porous medium, respectively. Due to the high permeability of the metal foam, the fluid viscous shear stress effect becomes negligible. The expression of the pressure gradient along the axial direction for steady fully developed flow through porous medium, i.e. the Hazen-Dupuit equation gives

$$0 = \frac{\Delta P}{\Delta x} - \frac{\mu_f}{K}u - C_f \rho_f u^2 \tag{7-9}$$

where $C_f = F/K^{1/2}$ is the form parameter of the porous medium. The last two terms of Equation (7-9) represent the lumped viscous and the lumped form effects within the permeable medium, respectively. The ratio between the form force D_C and the viscous force D_μ can be expressed as

$$\frac{D_C}{D_\mu} = \frac{\rho_f C_f u}{\frac{\mu_f}{K}} \tag{7-10}$$

Based on Equation (7-10), the ratios of form drag to viscous drag for aluminium foams 10, 20 and 40 PPI under different velocity are plotted in Figure 7-22. It can be seen that the ratio for aluminium foam 40 PPI is higher than that for aluminium foam 10 PPI due to the low permeability and high form coefficient for high pore density metal foam (Table 4-1). Therefore, for a constant porosity and fluid velocity, the flow resistance in the aluminium foams increases with increased form coefficient and decreased permeability. It is also noted from Table 7-2 that the specific surface area for high PPI metal foam is larger than that of low PPI metal foam. The increase in flow resistance of 40 PPI aluminium foam directly relates to the effective surface length as explained by Lage (1998) who related an increase in drag to the increase in specific surface area.

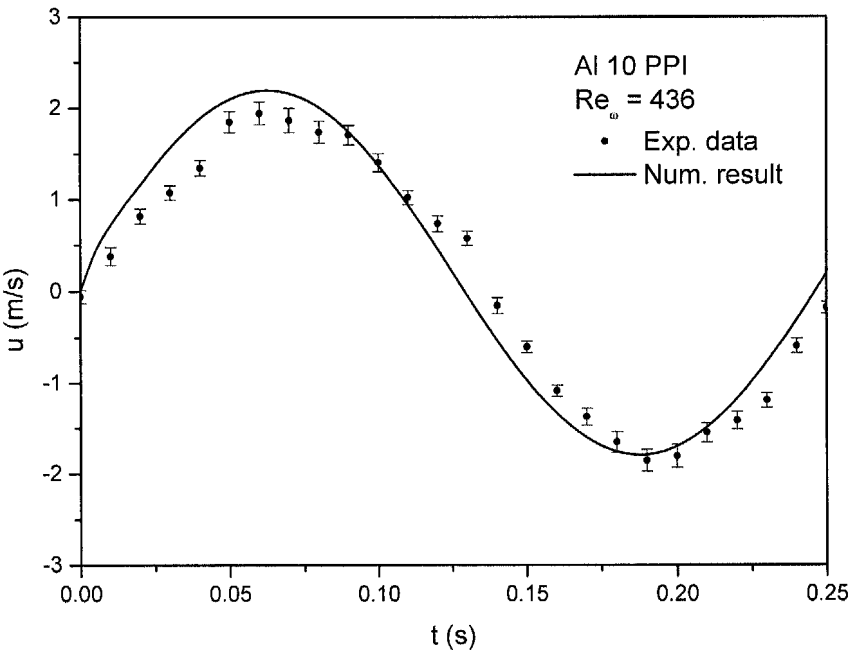

Figure 7-18 Comparison of numerical and experimental results for mean axial cross-sectional velocity for aluminium foam 10 PPI at $Re_\omega = 436$

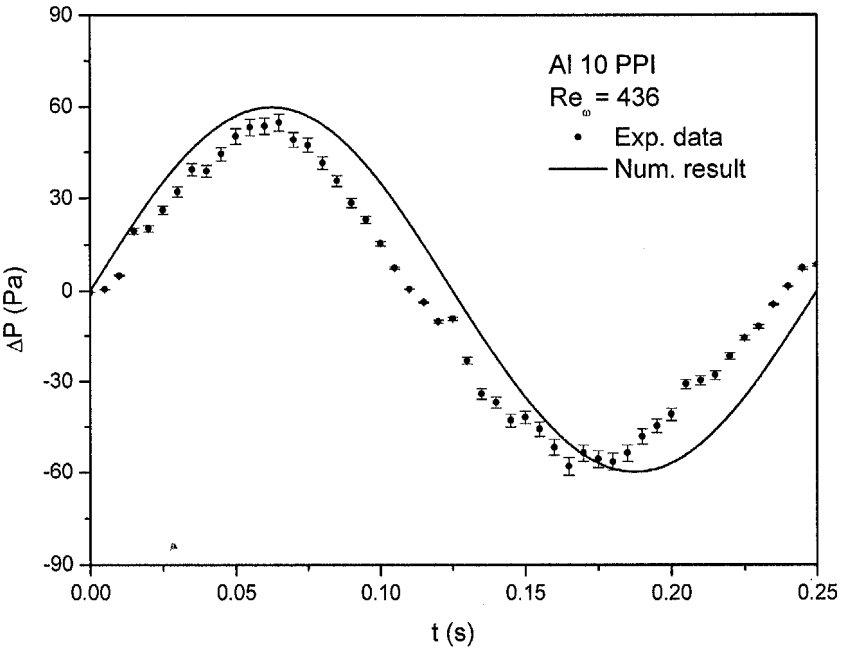

Figure 7-19 Comparison of numerical and experimental results for pressure drop across aluminium foam 10 PPI at Re_ω = 436

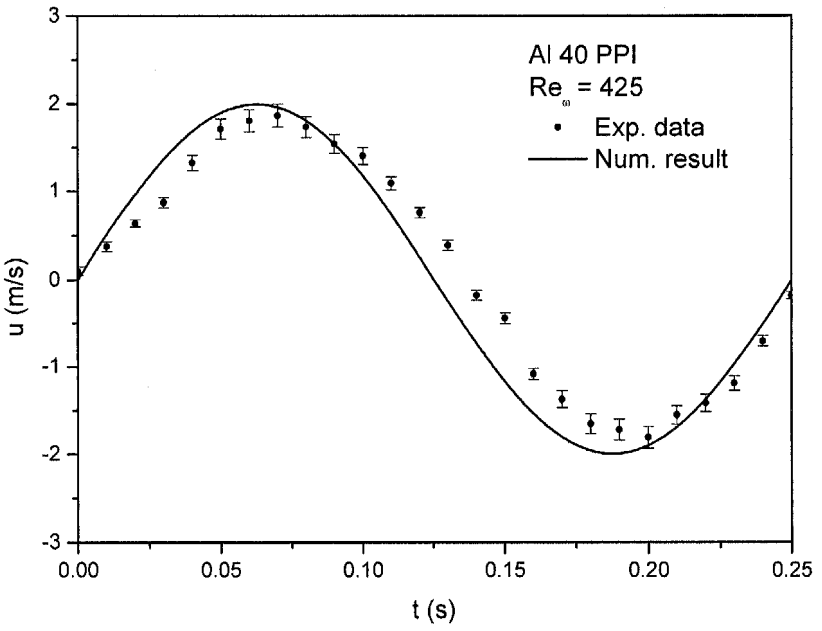

Figure 7-20 Comparison of numerical and experimental results for mean axial cross-sectional velocity in aluminium foam 40 PPI at Re_ω = 425

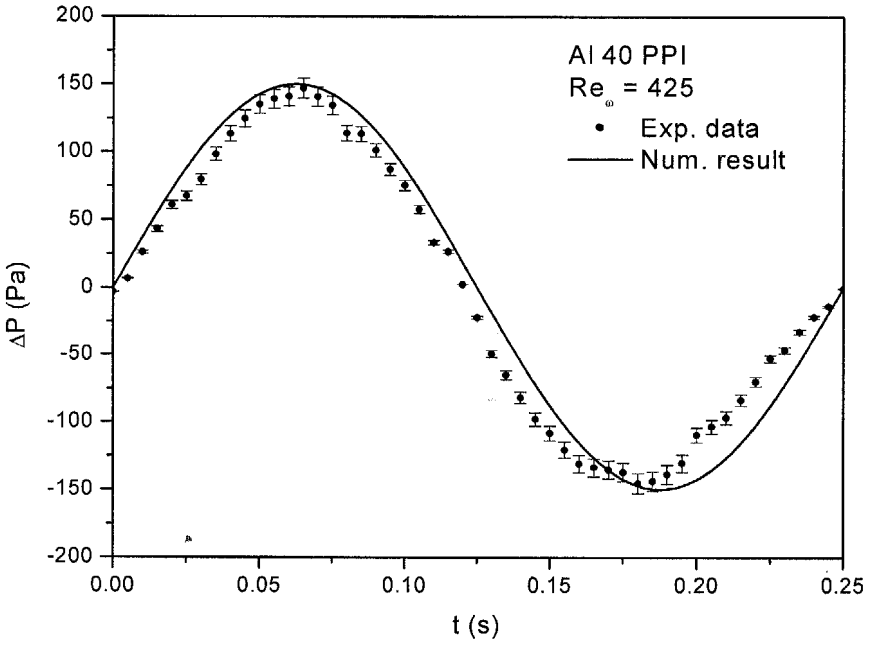

Figure 7-21 Comparison of numerical and experimental results for pressure drop across aluminium foam 40 PPI at $Re_\omega = 425$

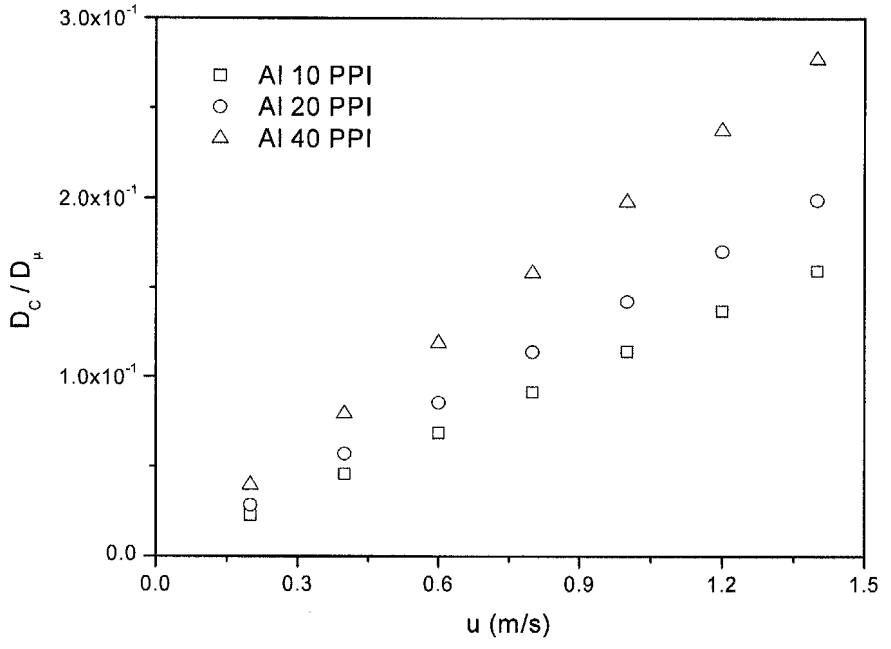

Figure 7-22 Ratio of form drag to viscous drag in 10, 20 and 40 PPI metal foams

7.3.2 Temperature Profile and Nusselt Number

Based on the LTNE model, the numerical results of the cycle-averaged temperature distributions for both solid and fluid phases of oscillating flow through aluminium 40 PPI with the experimental data at $Re_\omega = 226$ and $A_0 = 4.1$ for $Q = 40$ W are presented in Figure 7-23. The calculated solid and fluid phases temperature distributions at the bottom of the channel are of convex shape with the maximum values located at the centre of the channel. It is found that the cycle-averaged temperature for the solid phase is higher than that for fluid phase. However, the temperature difference between the solid and fluid phases at the two ends of the channel is very small. Along the axial dimensionless location and close the middle of the channel, the temperature difference becomes distinctly large. According to Equation (6-27), the larger axial velocity at the two boundaries increases the interfacial heat transfer coefficient between the fluid and solid phases, which enhances heat transfer at the two thermal entrance regions. Close to the centre of the channel, the axial velocity is reduced due to the flow resistance of metal foam and the interface heat transfer coefficient becomes small. A comparison of cycle-averaged temperature distributions obtained numerically and experimentally shows that the variation of the calculated fluid temperature is in reasonable agreement with the experimental data.

Figure 7-24 presents the numerical results of the solid and fluid phases temperature distributions on the substrate surface for oscillating flow through aluminium foam 40 PPI with the experimental data at $Re_\omega = 858$ and $A_0 = 4.1$. It can be seen that the variations of the cycle-averaged temperature of the solid and fluid phases along the axial direction are similar to those observed in Figure 7-23, which shows that the temperature for the solid phase is higher than that for the fluid phase at the different dimensionless axial locations. A very small temperature difference between the solid

and fluid phases is found at the two entrances of the channel by comparing the temperature difference between the solid and fluid phases shown in Figures 7-23 and 7-24, it is noticed that the temperature difference at the centre of channel for Re_ω = 858 is smaller than that for Re_ω = 226 due to the increased mean axial velocity at Re_ω = 858 for oscillating flow through the porous channel.

Figures 7-25 and 6-26 present the experimental data and numerical results of the cycle-averaged local Nusselt number of the fluid phase along the axial direction in 40 PPI aluminium foam for Re_ω = 226 and 858, respectively. It can be seen that the simulation results show the same trend with experimental data for the cycle-averaged Nusselt number distributions on the substrate surface of the channel. The cycle-averaged Nusselt numbers for Re_ω = 858 is higher than those for Re_ω = 226. The distribution curves of the cycle-averaged Nusselt number decrease first and increase after the centre of channel for both Re_ω = 226 and 858. The higher instantaneous local Nusselt number at the entrance region in a complete cycle shown in Figure 7-13 results in the higher cycle-averaged Nusselt number at the entrance region as compared to that at the middle of channel.

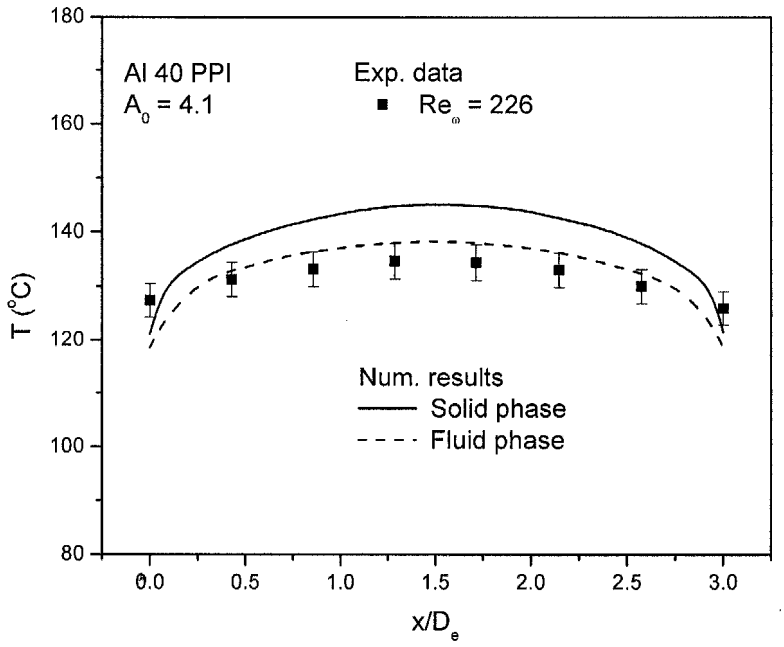

Figure 7-23 Numerical results of the cycle-averaged temperature distributions for both solid and fluid phases in aluminium 40 PPI with the experimental data at Re_ω = 226

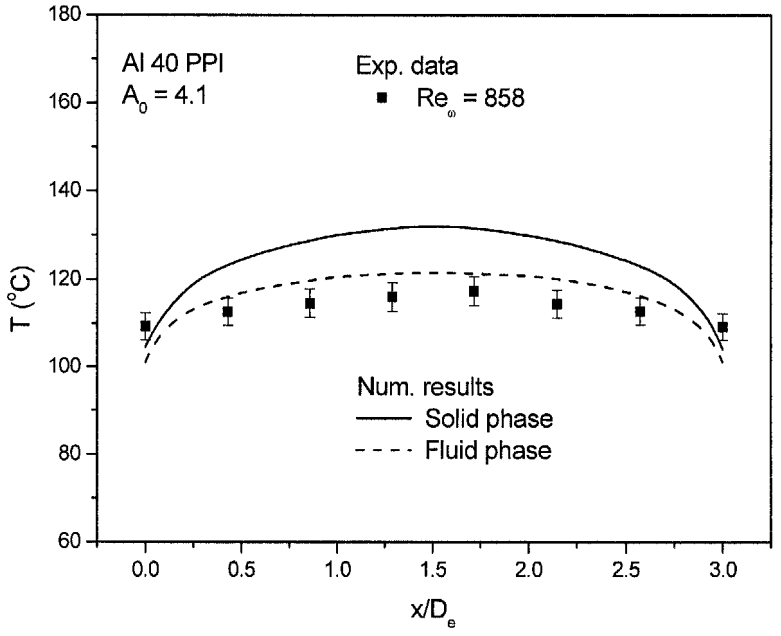

Figure 7-24 Numerical results of the cycle-averaged temperature distributions for both solid and fluid phases in aluminium 40 PPI with the experimental data at Re_ω = 858

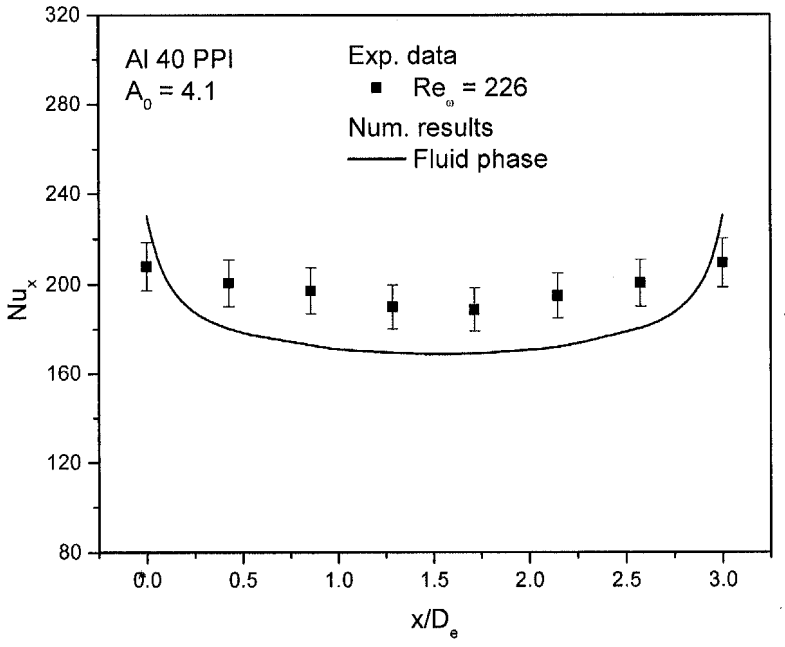

Figure 7-25 Experimental data and numerical results for the cycle-averaged Nusselt number of the fluid phase in 40 PPI aluminium foam at Re_ω = 226

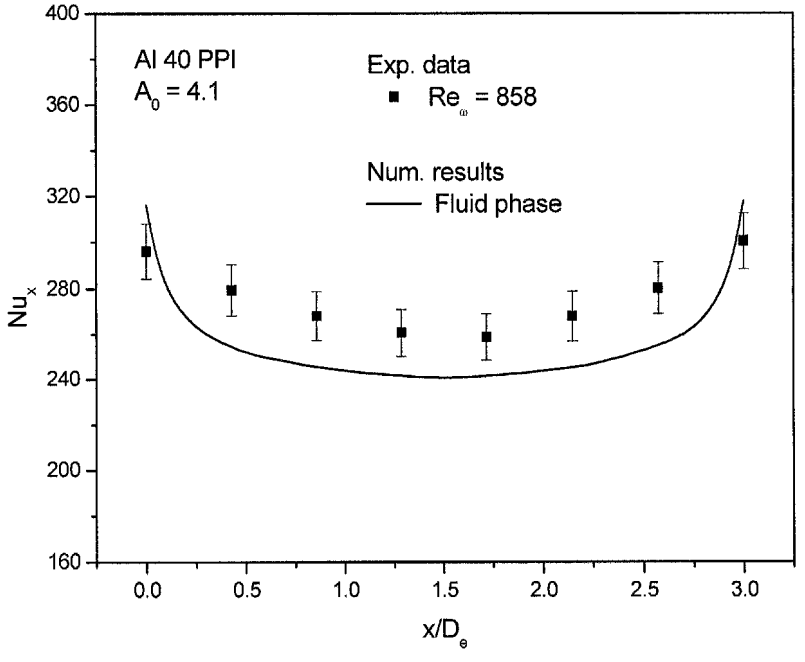

Figure 7-26 Experimental data and numerical results for the cycle-averaged Nusselt number of the fluid phase in 40 PPI aluminium foam at Re_ω = 858

The cycle-averaged temperature and local Nusselt number of oscillating flow through aluminium foam 40 PPI at Q = 40 W with various flow amplitudes are shown in Figures 7-27 and 7-28. The numerical results show that a large dimensionless flow amplitude corresponds to low temperature and large local Nusselt number distribution profiles at approximately the same kinetic Reynolds number. A similar trend can be observed from the experimental data. Physically, a higher value of the dimensionless flow amplitude means a larger amount of cooler fluid can be driven into the porous channel during each complete oscillatory cycle. According to the thermal boundary conditions at the two ends of the simulated domain, the cooler fluid with a constant value flows alternately into the channel from the two inlets during every half-cycle. Therefore, a larger flow amplitude results in a large quantity of cooler fluid flowing through the porous medium at a constant oscillatory speed and hence the heat transfer is enhanced.

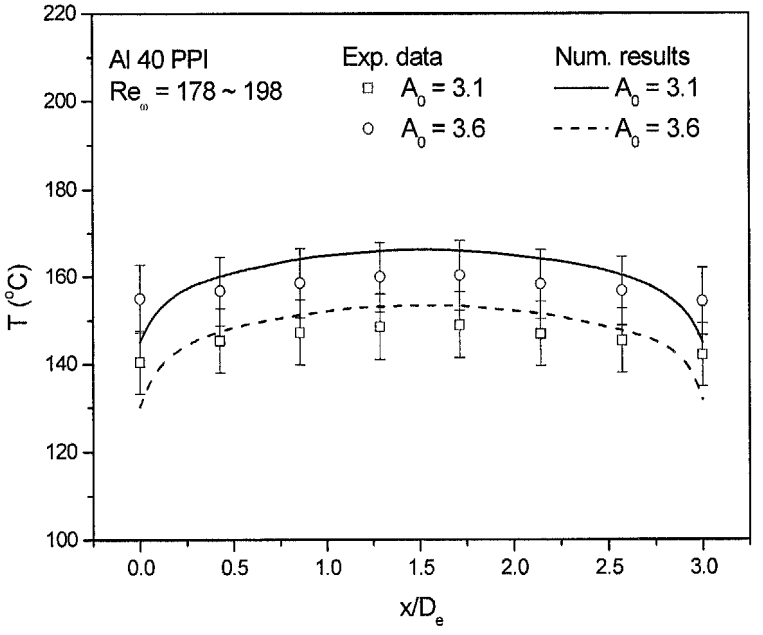

Figure 7-27 Effect of flow displacement on the cycle-averaged temperature distribution of the fluid phase in 40 PPI aluminium foam at Re_ω = 178 ~ 198

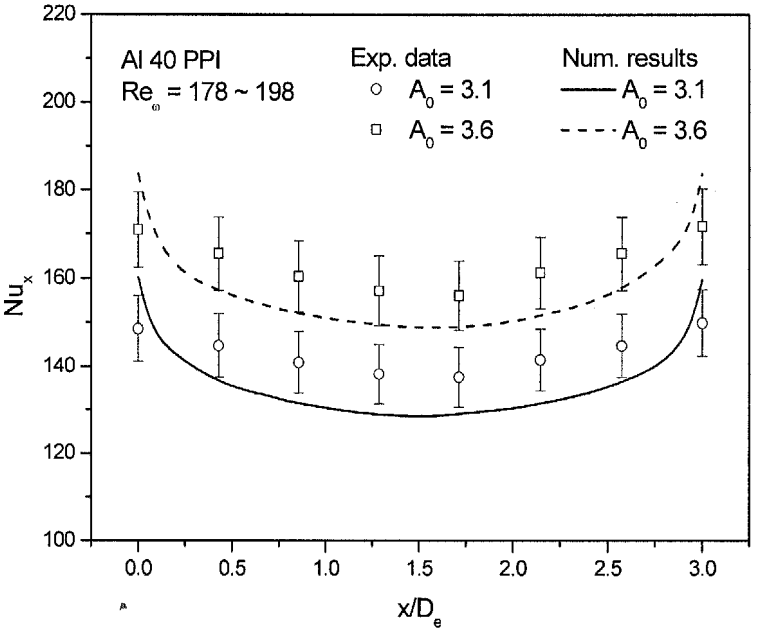

Figure 7-28 Effect of flow displacement on the cycle-averaged local Nusselt number of the fluid phase in 40 PPI aluminium foam at Re_ω = 178 ~ 198

The effects of aluminium foams with different pore densities and effective thermal conductivities on the cycle-averaged temperature and Nusselt number distributions on the bottom wall are presented in Figures 7-29 and 7-30. The solid line in Figures 7-29 and 7-30 represent the numerical result of fluid cycle-averaged temperature for aluminium foam 10 PPI at Q = 20 W, while the dash line represents that for aluminium foam 20 PPI. The symbols plotted these figures are the experimental data. From Figure 7-29, it can be seen that the simulation results of the cycle-averaged local temperatures for high pore density foam is lower than that for low pore density foam, and that they are in agreement with the trend obtained experimentally. According to Table 7-2, the effective thermal conductivity of aluminium 20 PPI is higher than that of aluminium 10 PPI, and the specific surface area of aluminium foam 20 PPI is more than two times that of aluminium foam 10 PPI. Therefore, the heat transfer performance of high pore density foam is better than that of low pore density foam under the same kinetic Reynolds number, i.e. the same oscillatory speed.

Consequently, the numerical result presented in Figure 7-30 shows that higher cycle-averaged local Nusselt number is obtained by oscillating flow through aluminium 20 PPI as compared to that through aluminium foam 10 PPI for Re_ω = 184 ~ 190. A comparison of the experimental data of oscillating flow in aluminium 10 PPI (Re_ω = 190) and in aluminium 20 PPI (Re_ω = 184) shows the same trend.

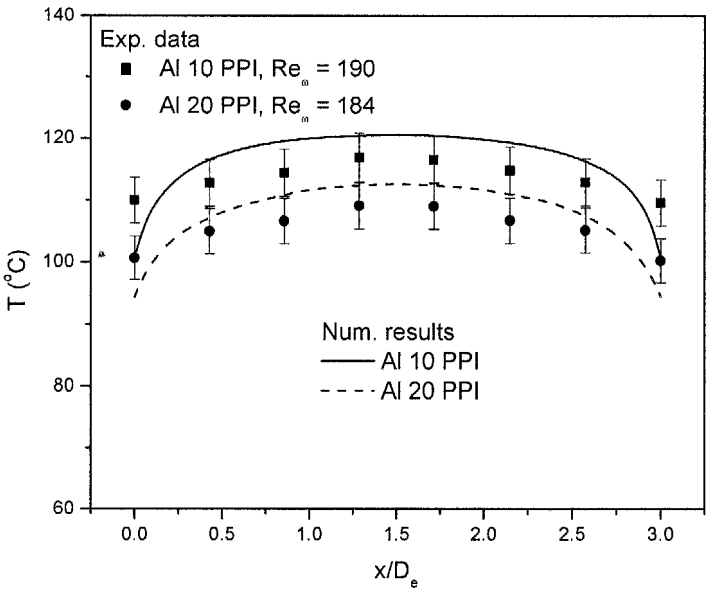

Figure 7-29 Effects of pore density on the cycle-averaged temperature distributions on the heated wall

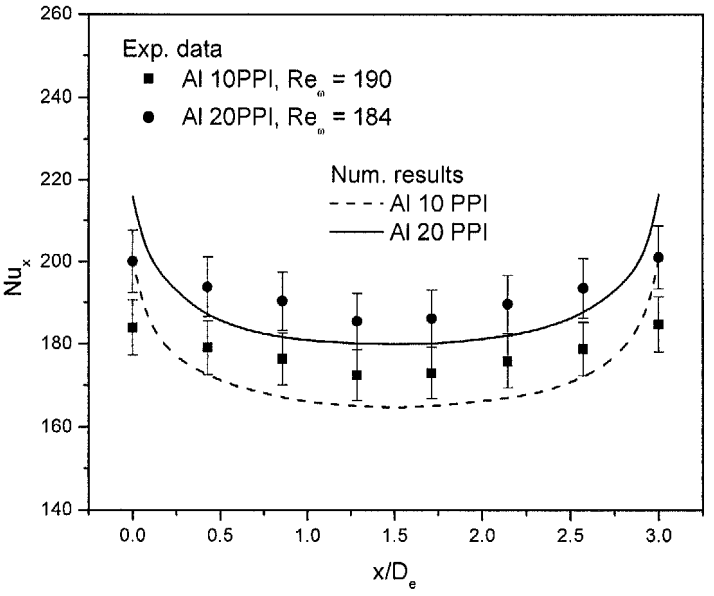

Figure 7-30 Effects of pore density on the cycle-averaged local Nusselt number distributions on the heated wall

The difference of the cycle-averaged temperature and the local Nusselt number between the experimental and numerical results presented in the above figures should take into consideration the following possible errors:

(1) The metal foams tested experimentally are non-homogeneous and anisotropic since they were manufactured by the directional solidification from a super-heated liquidus state in an environment of overpressures and high vacuum. On the other hand, the mathematical model and numerical code are based on the assumption that the metal foam is a homogeneous and isotropic porous medium.

(2) The numerical code is valid for the laminar flow regime, while the experimental data is available for the transition and turbulent flow regimes. The increased oscillation frequency leads to a transition from laminar to turbulent state in oscillating flow (Kurzweg *et al.* 1989). Therefore, as the kinetic Reynolds number increases, vortices may occur at the pore level due to the effect of the ligament and pore structure on the mixing of the flowing fluid.

(3) The numerical code does not account for conductive heat transfer in the heated wall while the experimental results are influenced by this phenomenon i.e. conjugate effect.

(4) There is also a contradiction between the inlet velocity profiles. The sinusoidal profile imposed at the two inlet boundaries in the numerical simulation would not perfectly match the actual case encountered in the experiments.

From the problems presented above, some minor issues exist between the numerical and experimental studies. For example, the numerical code does not simulate radiative heat transfer which are present in the experiments.

To examine the numerical and experimental results for the total heat transfer rates, the length-averaged Nusselt number of oscillating flow through metal foam 10 PPI

and 40 PPI obtained by the simulation and experimental investigations are compared in Figures 7-31 and 7-32, respectively. The kinetic Reynolds number at the dimensionless flow amplitude A_0 = 4.1 for numerical and experimental results ranges from 100 ~ 1090 and from 178 ~ 858, respectively. The deviation between the simulated results and the experimental data are presented. As shown in Figures 7-31 and 7-32, the length-averaged Nusselt numbers in aluminium foam 10 and 40 PPI determined experimentally and numerically show the same trend which indicates that the heat transfer rate of oscillating flow through metal foam channel increases with the kinetic Reynolds number. A comparison of the numerical result for the total heat transfer rate in Figures 7-31 and 7-32 shows that the length-averaged Nusselt number for aluminium foam 40 PPI is higher than that for aluminium foam 10 PPI, which agrees with the experimental data. The deviations of the selected points show that the difference in the length-averaged Nusselt number between the numerical and experimental data gradually increases with the kinetic Reynolds number, i.e. dimensionless oscillatory frequency. The maximum deviations between numerical and experimental results for aluminium 10 and 40 PPI are 14.8% and 18.9%, respectively. As the oscillatory speed increases, mixing of the fluid flow in the pores within the metal foam is enhanced and the fluid flow is no longer laminar. For oscillating flow through aluminium foam 40 PPI, the flow mixing at the pore level is more intense than that inside the 10 PPI aluminium foam due to the higher pore density. Therefore, the deviations between numerical and experimental results for aluminium foam 40 PPI are higher than that for aluminium foam 10 PPI.

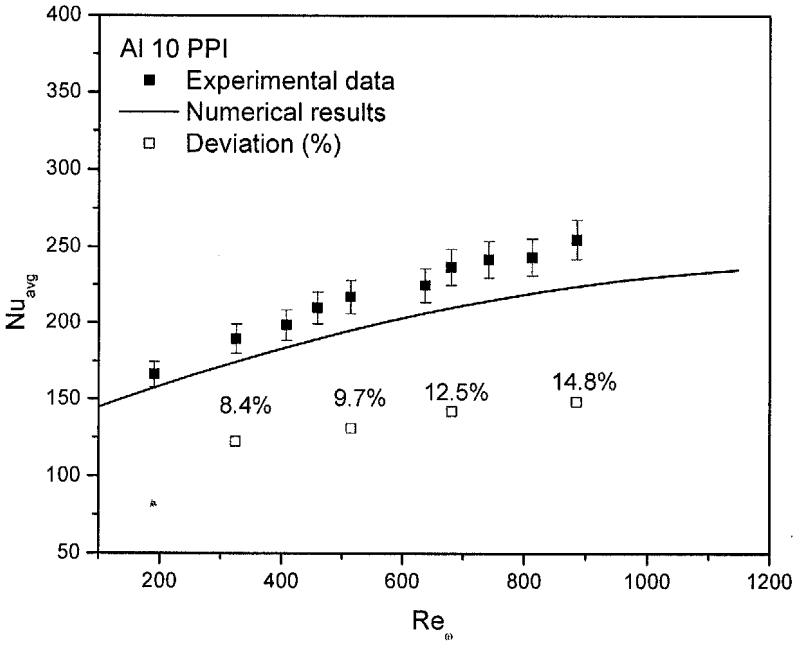

Figure 7-31 Length-averaged Nusselt number of oscillating flow through 10 PPI aluminium foam versus kinetic Reynolds number

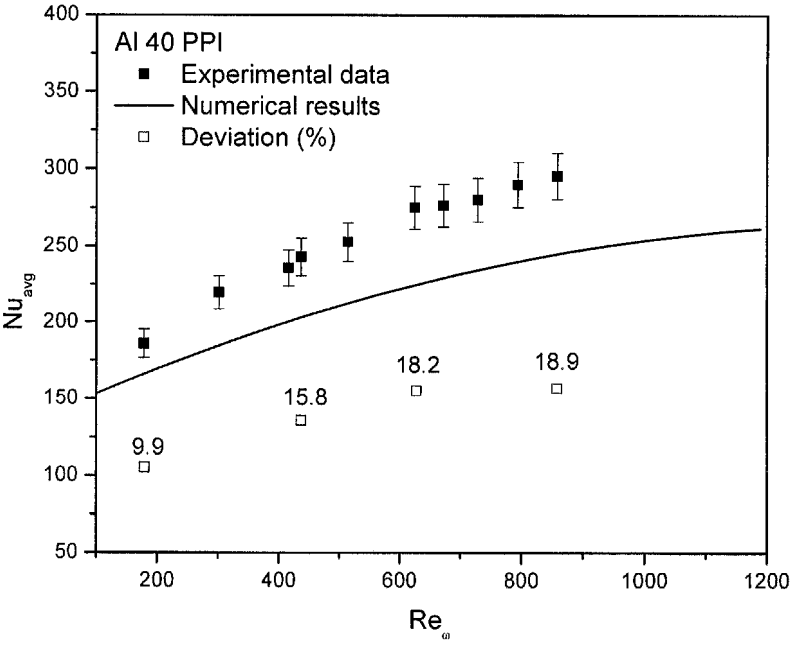

Figure 7-32 Length-averaged Nusselt number of oscillating flow through 40 PPI aluminium foam versus kinetic Reynolds number

7.4 Summary

In this chapter, the numerical results of the transient heat transfer characteristics of oscillating flow through the different locations in the metal foam channel are discussed. The instantaneous temperature decreases with the increase of the distance along the vertical direction of the channel due to the diffusion effect. The two-dimensional temperature distributions of the fluid phase in the numerical domain are symmetric about the centre of the channel under different kinetic Reynolds numbers and dimensionless flow amplitudes. It is also found from the numerical solution that the porosity of open-cell metal foam has less effect on characteristics of the transient pressure drop. According to the analysis of the ratio between the form drag and the viscous drag in aluminium foams, the flow resistance in aluminium foam channel depends mainly on form coefficient and permeability.

Based on the LTNE model, the simulation results showed that the temperature difference between the solid and fluid phases in an aluminium foam channel subjected to oscillating flow cannot be neglected. Along the axial dimensionless location close the middle of the channel, the temperature difference is significant due to the reduced interfacial heat transfer coefficient between the fluid and solid phases. The calculated cycle-averaged temperature and Nusselt number of fluid phase are compared with the results obtained by the experiments and the deviation is also analysed in detail in this chapter. The simulation results agree fairly well with the results obtained by the experiments.

CHAPTER 8

CONCLUSIONS AND RECOMMENDATIONS FOR FUTURE WORK

8.1 Conclusions

In this research, forced convection in a heated channel filled with open-cell metal foam subjected to oscillating flow has been investigated experimentally and numerically. Aluminium metal foams with 10, 20 and 40 PPI were used as the inserted materials along with air as the fluid phase. The temperature distribution on the substrate surface of the heated wall, velocity of oscillating flow through porous channel and pressure drop across the test section were measured. The effects of the different dimensionless oscillatory frequencies, flow displacements and materials' properties on the fluid behaviour and heat transfer characteristics in open-cell metal foam were analysed. In the numerical investigation, the governing equations were solved by employing by the finite-volume method with a programmed FORTRAN code. The dispersion conductivity k_d, interfacial heat transfer coefficient h_{fs}, effective thermal conductivities of solid (k_{se}) and fluid phases (k_{fe}) were modelled based on the thermophysical properties of aluminium foam and air flow with the geometric structure of open-cell metal foam. Based on the present experimental and numerical studies, the following conclusions can be drawn:

1. The experimental results show that the pressure drop and velocity of oscillating flow in an open-cell metal foam increase with the increase of the oscillatory frequency and oscillating flow amplitude, and vary almost sinusoidally due to the reversing flow direction. For oscillating flow through aluminium foams, high

pore density corresponds to high flow resistance at the same Reynolds number due to the large specific surface area of high PPI metal foam.

2. An empirical equation for the maximum friction factor of oscillating flow through aluminium foams was obtained in terms of the hydraulic ligament diameter based kinetic Reynolds number and the dimensionless flow amplitude based on an analysis of similarity parameters. For oscillating flow, the pressure drop and flow velocity increase with the increase of kinetic Reynolds number and dimensionless flow amplitude. It indicates that the characteristics of oscillating flow through metal foam channel are dominated by the oscillation frequency and maximum flow displacement.

3. The cycle-averaged temperatures were found to decrease with an increase in the kinetic Reynolds number while the cycle-averaged local Nusselt numbers exhibit the opposite trend. The empirical equation obtained by the experimental study shows that the length-averaged Nusselt number of oscillating flow through aluminium foam is governed by the kinetic Reynolds number and dimensionless flow amplitude. The total heat transfer rate of oscillating flow through metal foam channel can be 1.5 times larger than that of steady flow through metal foam channel. The average Nusselt numbers of steady and oscillating flows through metal foams are higher than those of uni-directional flow through finned heat sinks. The average temperature uniformity index of oscillating flow in aluminium foams of 10, 20 and 40 PPI is more than 6 times lower than that of steady flow.

4. For aluminium foams, the heat transfer rate increases with the increase of the pore density at a constant kinetic Reynolds number i.e. dimensionless oscillatory frequency. However, for a given pumping power, better heat transfer performance can be achieved by low pore density metal foam under the condition of oscillating flow.

In designing a novel heat sink, metal foams of low pore density can be used to enhance heat transfer with low pumping power. High pore density metal foams with their extremely large fluid-solid-contact surface areas and tortuous coolant flow paths are suitable to remove high heat fluxes in applications where pumping power is not of concern.

5. The simulation results showed that the two-dimensional temperature distributions of fluid phase in the numerical domain are symmetric about the centre of the channel for different kinetic Reynolds numbers. The temperature decreases with the increase of the distance along the vertical direction of the channel. The numerical calculation showed that the transient temperature profile for the dimensionless location x/D_e near the entrance is lower than that close to the middle of channel in a complete cycle.

6. It was found from the numerical solution that the porosity of open-cell metal foam has little effect on pressure drop characteristics. At approximately the same kinetic Reynolds number i.e. oscillatory frequency, the pressure drop profile for oscillating flow through high pore density aluminium foam is higher than that through low pore density aluminium foam. Based on the analysis of the ratio of the form drag to viscous drag in aluminium foam, the flow resistance in aluminium foam channel depends mainly on form coefficient and permeability.

7. Based on the LTNE model, the simulation results showed that the temperature difference between solid and fluid phases in aluminium foam channel subjected to oscillating flow cannot be neglected. The calculated cycle-averaged temperature distribution for solid phase is higher than that for fluid phase. However, the temperature difference of the solid and fluid phases at the two ends of the channel is very small. Along the axial dimensionless location close to the middle of the

channel, the temperature difference is significant due to the reduced interfacial heat transfer coefficient between the fluid and solid phases. The calculated cycle-averaged temperature and Nusselt number of fluid phase agree fairly well with the results obtained by the experiments.

8.2 Recommendations for Future Work

Based on the achievements of the present experimental and numerical investigations, some possible extended studies are recommended as future research. It should be noted that the suggestions are restricted to the issues discussed in this thesis due to the variety of transport phenomena in metal foam that can be studied. Suggested future investigations are as follows:

1. In order to gain a better physical insight into fluid flow and pressure drop in metal foams, experiments can be conducted by constructing a transparent artificial medium with the structure as shown in Figure 3-14. Thus, some advanced measuring technique can be applied to measure flow movement into the pore level of metal foam, such LDA (Laser Doppler Anemometer) and PIV (Particle Image Velocimetry). Furthermore, CFD analysis can be performed with similar geometries and compared with experimental data measured by LDA or PIV.

2. The coolant in the present work is air. For normal temperature air, the thermal conductivity and Prandtl number is about 0.026 W/m·K and 0.707, respectively. To achieve better heat transfer, some studies can be conducted using coolant of higher thermal conductivity. For example, FC-72 as shown in Table 8-1 has thermal conductivity and Prandtl number of 0.09 W/m·K and 0.13, respectively. The thermal conductivity for FC-72 is 3.6 times that of air. To apply the metal foam subjected to oscillating flow in various thermal management applications, the use of

high thermal conductivity coolant is an effective method to improve the heat transfer performance.

Table 8-1 Properties of coolants at atmospheric pressure

Coolants	T (K)	ρ (kg/m^3)	c_p (kJ/kg·K)	μ × 10^5 (kg/m·s)	k (W/m·K)	Pr
Air	300	1.16	1.007	1.85	0.025	0.707
FC-72	300	1930	1.15	1002	0.09	0.13

3. As presented earlier, the numerical simulation was based on the assumptions of uniform and isotropic properties of metal foam. However, the actual metal foam is non-uniform and anisotropic. To predict accurately the fluid flow and heat transfer in metal foam subjected to oscillating flow, non-homogeneous and anisotropic modelling of the metal foam should be adopted. A feasible method is to build an un-structured grid system according to the assumption that the pores are distributed randomly in the numerical domain. In addition, three-dimensional numerical modelling can be used to study fluid flow and heat transfer in metal foam.

4. High pore density metal foam (i.e. low permeability) with their extremely large fluid-solid-contact surface areas and tortuous coolant flow paths is suitable to remove extraordinarily high heat fluxes (up to 100 W/cm^2 in densely packed circuit board) in applications where pumping power is not of concern. For these cases, the volume of the cooling system is not a major problem. A direct application was performed by Lage *et al.* (2004) which used synthetic oil through a large metal foam heat exchanger with low permeability to cool phased-array radar system. However, for the purpose of using oscillating flow to achieve high heat transfer rates and uniform temperature distribution in electronic cooling, a miniature cooling system is

needed for the purpose of application. The design of a simplified micro oscillation producer is a significant work for practical application.

REFERENCES

Afrid, M. and Zebib, A., Natural convection air cooling of heated components mounted on a vertical wall, *Numerical Heat Transfer*, Vol. 15, pp. 243-260 (1989)

Afrid, M. and Zebib, A., Three-dimensional laminar and turbulent natural convection cooling of heated blocks, *Numerical Heat Transfer*, Vol. 19, pp. 405-424 (1991)

Amer, Y. O., Chikh, S., Bouhadef, K. and Lauriat, G., Forced convection cooling enhancement by use of porous materials, *International Journal of Heat and Mass Transfer*, Vol. 19, pp. 215-258 (1998)

Amiri, A. and Vafai, K., Analysis of dispersion effects and non-thermal equilibrium, non-Darcian, variable porosity incompressible flow through porous media, *International Journal of Heat and Mass Transfer*, Vol. 37, pp. 939-954 (1994)

Amiri, A., Vafai, K. and Kuzay, T. M., Effects of boundary conditions on non-Darcian heat transfer through porous media and experimental comparisons, *Numerical Heat Transfer* Vol. 27, pp. 651-664 (1995)

Anderson, A. M. and Moffat, R. J., Direct air cooling of electronic components: reducing component temperatures by controlled thermal mixing, *Symposium on Fundamentals of Forced Convection Heat Transfer,* ASME HTD Vol. 101, pp. 9-16 (1988)

Antohe, B. V. and Lage, J. L., A general two-equation turbulence model for incompressible flow in porous media, *International Journal of Heat and Mass Transfer*, Vol. 40, pp. 3013-3024 (1997)

Arbelaez, F., *An experimental investigation of the pool boiling characteristics of saturated FC-72 over an aluminium foam heat sink*, MS Thesis, University of Colorado, USA (1996)

Azar, K. and Morabito, J., Managing power requirements in the electronics industry, *Electronics Cooling*, Vol.6, No.4, pp. 12-25 (2000)

Azar, K., The history of power dissipation, *Electronics Cooling*, Vol. 6, No.4, pp. 42-50 (2000)

Banhart, J., Manufacture, characterisation and application of cellular metals and metal foams, *Progress in Materials Science*, Vol. 46, pp. 559-632 (2001)

Becker, H. and Gartner, C., Polymer microfabrication methods for microfluidic analytical applications, *Electrophoresis*, Vol. 21, pp. 12-26 (2000)

Bhattacharya, A., Calmidi, V. V. and Mahajan, R. L., Thermophysical properties of high porosity metal foams, *International Journal of Heat and Mass Transfer*, Vol. 44, pp. 827-836 (2001)

Bhattacharya, A. and Mahajan, R. L., Finned metal foam heat sinks for electronics cooling in forced convection, *ASME Journal of Electronic Packaging*, Vol. 124, pp. 155-163 (2002)

Boomsma, K. and Poulikakos, D., On the effective thermal conductivity of a three-dimensionally structured fluid-saturated metal foam, *International Journal of Heat and Mass Transfer*, Vol. 44, pp. 827-836 (2001)

Boomsma, K. and Poulikakos, D., The effects of compression and pore size variations on the liquid flow characteristics in metal foams, *ASME Journal of Fluids Engineering*, Vol. 124, pp. 263-272 (2002)

Boomsma, K., Poulikakos, D. and Ventikos, Y., Simulations of flow through open cell metal foams using an idealized periodic cell structure, *International Journal of Heat and Fluid Flow*, Vol. 24, pp. 825-834 (2003a)

Boomsma, K., Poulikakos, D. and Zwick, F., Metal foams as compact high performance heat exchangers, *Mechanics of Materials*, Vol. 35, pp. 1161-1176 (2003b)

Brinkman, H. C., A calculation of viscous force exerted by a flowing fluid on a dense swarm of particles, *Applied Scientific Research,* Vol. 1, pp. 27-34 (1947)

Burd, T., CPU info and system performance summary, Internet website, *http://bwrc.eecs.berkeley.edu/CIC/summary* (2004), accessed on 12 July. 2004

Calmidi, V. V., *Transport Phenomena in High Porosity Fibrous Metal Foam*, PhD Thesis, University of Colorado, USA, (1998)

Calmidi, V. V. and Mahajan, R. L., The effective thermal conductivity of high porosity fibrous metal foams, *ASME Journal of Heat Transfer*, Vol. 121, pp. 466-471 (1999)

Calmidi, V. V. and Mahajan, R. L., Forced convection in high porosity metal foams, *ASME Journal of Heat Transfer*, Vol. 122, pp. 557-565 (2000)

Chatwin, P. C., On the longitudinal dispersion of passive contaminant in oscillatory flow in tubes, *Journal of Fluid Mechanic*, Vol. 71, pp. 513-526 (1975)

Cheng, P., Wall effects on fluid flow and heat transfer in porous media, *Proceedings of 2nd ASME/JSME Thermal Engineering Joint Conference*, Vol. 2, pp. 297-303 (1987)

Cheng, P., Hsu, C. T. and Choudhury, A., Forced convection in the entrance region on a packed channel with asymmetric heating, *ASME Journal of Heat Transfer*, Vol. 110, pp. 946-954 (1988)

Cheng, P. and Zhu, H., Effects of radial thermal dispersion on fully-developed forced convection in cylindrical packed tubes, *ASME Journal of Heat Transfer*, Vol. 30, pp. 2373-2383 (1987)

Chikh, S., Boumedien, A., Bouhadef, K. and Lauriat, G., Analytical solution of non-Darican forced convection in an annular duct partially filled with a porous medium, *International Journal of Heat and Mass Transfer,* Vol. 38, pp. 1543-1551 (1995a)

Chikh, S., Boumedien, A., Bouhadef, K. and Lauriat, G., Non-Darican forced convection in an annular duct partially filled with a porous medium, *Numerical Heat Transfer A*, Vol. 28, pp. 707-722 (1995b)

Choi, C. Y. and Kulacki, F. A., Numerical study of free and mixed convection in horizontal porous layers with multiple heat sources, *AIAA Journal of Thermophysics and Heat Transfer*, Vol. 4, No. 2, pp. 221-227 (1990)

Chrysler, G. M. and Simons, R. E., An experimental investigation of the forced convection heat transfer characteristics of fluorocarbon liquid flowing through a packed-bed for immersion cooling of microelectronic heat sources, *IAA/ASME Thermophysics and Heat Transfer Conference*, ASME HTD Vol. 131, pp. 21-27 (1990)

Cooper, W. L., Nee, V. M. and Yang K. T., An experimental investigation of convective heat transfer from the heated floor of a rectangular duct to a low frequency, large tidal displacement oscillating flow, *International Journal of Heat and Mass Transfer,* Vol. 37, pp. 581-592 (1994)

David, E., Lauriat, G. and Cheng, P., A numerical solution of variable porosity effects on natural convection in a packed-sphere cavity, *ASME Journal of Heat Transfer*, Vol. 113, pp. 391-399 (1991)

Davalath, J. and Bayazitoglu, Y. Forced convection cooling across rectangular blocks, *Journal of Heat Transfer*, Vol. 109, pp. 321-328 (1987)

Dybbs, A. and Edwards, R. V., A new look at porous media fluid mechanics - Darcy to turbulent, *Fundamentals of Transport Phenomena in Porous Media*, Martinus Nishoff Publishers, pp. 199–256 (1984)

ERG Materials and Aerospace Corporation, Oakland, CA, USA, *DUOCEL aluminium foam data sheet*, (2002)

Fedorov, A.G. and Viskanta, R., A Numerical simulation of conjugate heat transfer in an electronic package formed by embedded discrete sources in contact with a porous heat sink, *ASME Journal of Electronic Packaging.*, Vol. 119, pp. 8-16 (1997)

Fu, H. L., *Heat Transfer of a Channel Filled with Porous Media Subjected to Oscillating Flow*, Internal report, School of Mechanical and Production Engineering, Nanyang Technological University (2000a)

Fu, H.L., Leong, K.C., Huang, X.Y. and Liu, C.Y., A novel method of cooling electronic packages using a porous channel subjected to oscillating flow, *Proceedings of ITherm 2000, the 7th Intersociety Conference on Thermal and Thermomechanical Phenomena in Electronic Systems*, Las Vegas, USA, 23 - 26 May. 2000b

Fu, H. L., Leong, K. C., Huang, X. Y. and Liu, C. Y., An experimental study of heat transfer of a porous channel subjected to oscillating flow, *ASME Journal of Heat Transfer*, Vol. 123, pp. 162-170 (2001)

Gedeon, D., Mean-parameter modelling of oscillating flow, *ASME Journal of Heat Transfer*, Vol. 107, pp. 513-518 (1986)

Givler R. C. and Altobelli, S. A., A determination of the effective viscosity for the Brinkman-Forchheimer flow model, *Journal of Fluid Mechanics*, Vol. 258, pp. 355-370 (1994)

Goldstein, M. E. and Siegel, R., Analysis of heat transfer for compressible flow in two-dimensional porous media, *International Journal of Heat and Mass Transfer*, Vol. 14, pp. 1677-1699 (1971)

Gratton, L., Travkin, V. S. and Catton, I., Numerical solution of turbulent heat and mass transfer in a stratified geostatistical porous layer for high permeability media, *ASME Proceedings*, HTD Vol. 41, pp. 1-14 (1994)

Gunther, S. H., Binns, F., Carmean, D. M. and Hall, J. C., Managing the impact of increasing microprocessor power consumption, *Intel Technology Journal*, Vol. 1, pp. 1-9 (2001)

Guo, Z. X., Kim S. Y. and Sung, H. J., Pulsating flow and heat transfer in a pipe partially filled with a porous medium, *International Journal of Heat and Mass Transfer*, Vol. 40, No. 17, pp. 4209-4218 (1997)

Haritonov, V. V., Kiceleva, U. N., Atamanov, V. V., Jeigarnik, U.A. and Ivanov, F.P., Generalization of the results on heat transfer intensification in channels with porous insertion, *High Temperature*, Vol. 32 No. 3 pp. 433-440 (1994)

Holman, J., *Heat Transfer*, 7th Edition, McGraw-Hill, New York (1990)

Hsieh, W. H., Wu, J. Y., Shih, W. H. and Chiu, W. C. Experimental investigation of heat transfer characteristics of aluminium-foam heat sinks, *International Journal of Heat and Mass Transfer*, Vol. 47, pp. 5149-5157 (2004)

Hsu, C. T. and Cheng, P., Thermal dispersion in a porous medium, *International Journal of Heat and Mass Transfer*, Vol. 33, pp. 1587-1597 (1990)

Huang, P. C. and Vafai, K., Analysis of forced convection enhancement in a channel using porous blocks, *AIAA Journal of Thermophysics & Heat Transfer*, Vol. 8, pp. 563-573 (1994)

Hunt, M. L. and Tien, C. L., Effects of thermal dispersion on forced convection in fibrous media, *International Journal of Heat and Mass Transfer,* Vol. 31 pp. 301-309 (1988)

Hwang, G. and Chao, C., Heat transfer measurement and analysis for sintered porous channels, *ASME Journal of Heat Transfer*, Vol. 116, pp. 456-464 (1994)

Hwang, G., Wu. C. C. and Chao, C., Investigation of non-Darcian forced convection in an asymmetrically heated sintered porous channel, *ASME Journal of Heat Transfer*, 117, pp. 725-732 (1995)

Incropera, F. P. and DeWitt, D. P., *Fundamentals of Heat and Mass Transfer*, 5th Edition, Wiley, New York, (2002)

Jeigarnik, U. A., Ivanov, F. P. and Ikranikov, N. P., Experimental data on heat transfer and hydraulic resistance in unregulated porous structures, *Teploenergetika*, Vol. 21, pp. 33-38 (1991)

Jiang, P. X., Fan, M. H. Si, G. S. and Ren, Z. P., Thermal-hydraulic performance of small scale micro-channel and porous-media heat-exchangers, *International Journal of Heat and Mass Transfer*, Vol. 44, pp. 1039-1051 (2001)

Jiang, P. X. and Ren, Z. P., Numerical simulation of forced convection heat transfer in porous plate channels using thermal equilibrium or non-thermal equilibrium models, *Numerical Heat Transfer*, Vol.35, No.1, pp. 99-113 (1999)

Jiang, P. X., Ren, Z. P., Wang, B. X. and Wang, Z., Forced convective heat transfer in a plate channel filled with solid particles, *Journal of Thermal Science*, Vol. 5, No.1, pp. 43-53 (1996)

Jiang, P. X. and Ren, Z. P., Numerical investigation of forced convection heat transfer in porous media using a thermal non-equilibrium model, *International Journal of Heat and Fluid Flow*, Vol. 22, pp. 102-110 (2001)

Ju, Y. L. and Zhou, Y, Experimental study of the oscillating flow characteristics for a regenerator in a pulse tube cryocooler, *Cryogenics*, Vol. 38, pp. 649–656 (1998)

Jue, T. C., Analysis of oscillatory flow with thermal convection in a rectangular cavity filled with porous medium, *International Communications in Heat and Mass Transfer*, Vol. 27, No. 7, pp. 985-994 (2000)

Kaviany, M., Laminar flow through a porous channel bounded by isothermal parallel plates, *International Journal of Heat and Mass Transfer*, Vol. 28, pp. 815-858 (1985)

Khodadadi, J. M., Oscillatory fluid flow through a porous medium channel bounded by two impermeable parallel plates, *ASME Journal of Fluids Engineering*, Vol. 113, pp. 509-511 (1991)

Kidder, R. E., Unsteady flow of gas through a semi-infinite porous medium, *ASME Journal of Applied Mechanics*, Vol. 24, pp. 329-332 (1957)

Kim, S. Y., Kang, B. H. and Hyuan, J. M., Heat transfer from pulsating flow in a channel filled with porous media, *International Journal of Heat and Mass Transfer*, Vol. 37, pp. 2025-2033 (1994)

Kim, S. Y., Paek, J. W. and Kang, B. H., Flow and heat transfer correlations for porous fin in a plate-fin heat exchanger, *ASME Journal of Heat Transfer*, Vol. 122, pp. 572-578 (2000)

Kim, S. Y., Kang, B. H. and Kim, J. H., Forced convection from aluminium foam materials in an asymmetrically heated channel, *International Journal of Heat and Mass Transfer*, Vol. 44, pp. 1451-1454 (2001)

Knupp, P. and Lage, J. L., Generalization of the Forchheimer-extended Darcy flow model to the tensor permeability case via a variational principle, *Journal of Fluid Mechanics*, Vol. 299, pp. 97-104 (1995)

Ko, K. H. and Anand, N. K., Use of porous baffles to enhance heat transfer in a rectangular channel, *International Journal of Heat and Mass Transfer*, Vol. 46, pp. 4191-4199 (2003)

Koh, J. C. Y. and Colony, R., Analysis of cooling effectiveness for porous materials in a coolant passage, *ASME Journal of Heat Transfer*, Vol. 96, pp. 324-330 (1974)

Koh, J. C. Y. and Stevens, R. L., Enhancement of cooling effectiveness by porous materials in coolant passage, *ASME Journal of Heat Transfer*, Vol. 97, pp. 309-311 (1975)

Kuo, S. M. and Tien, C. L., Heat transfer augmentation in a foam material filled duct with discrete heat sources, *Intersociety Conference on Thermal Phenomena in the Fabrication and Operation of Electronic Components, IEEE*, New York, pp. 87-91 (1988)

Kurzweg, U. H., Enhanced heat conduction in oscillating viscous flows within parallel-plate channels, *Journal of Fluid Mechanics*, Vol. 156, pp. 291-300 (1985)

Kurzweg, U. H., Lindgren, E. R. and Lothrop, B., Onset of turbulence in oscillating flow at low Womersley number, *Physics of Fluids* A, Vol. 12, pp. 1972-1975 (1989)

Kuznetsov, A. V., Analytical study of fluid flow and heat transfer during forced convection in a composite channel partly filled with a Brinkman-Forchheimer porous medium, *Flow, Turbulence and combustion*, Vol. 60, pp. 173-192 (1998)

Lage, J. L., Antohe, B. V. and Nield, D. A., Two types of drag variation in transition to turbulent incompressible flow through a porous medium, *ASME Journal of Fluids Engineering*, Vol. 119, pp. 3013-3024 (1997)

Lage, J. L., The fundamental theory of flow through permeable media from Darcy to turbulence, in *Transport Phenomena in Porous Media* - Vol. 1 (Eds. D. B. Ingham and I. Pop), Pergamon, Oxford, pp. 1-30 (1998)

Lage, J. L., Narasimhan, A., Porneala, D.C. and Price, D.C., Experimental study of forced convection through microporous enhanced heat sinks: enhanced heat sinks for cooling airborne microwave phased-array radar antennas, *Emerging Technologies and Techniques in Porous Media*, vol. 28, pp. 433-452 (2004)

Lau, K. S. and Mahajan, R. L., Effects of tip clearance and fin density on the performance of heat sinks for VLSI packages, *IEEE Transactions on Components Hybrids and Manufacturing Technology*, Vol. 12, pp. 757-765 (1989)

Lauriat, G. and Prasad, V., Non-Darcian effects on natural convection in a vertical porous enclosure, *International Journal of Heat and Mass Transfer*, Vol. 32, pp. 2135-2148 (1989)

Lee, D. Y. and Vafai, K., Analytical characterization and conceptual assessment of solid and fluid temperature differentials in porous media, *International Journal of Heat and Mass Transfer*, Vol. 122, pp. 303-326 (1999)

Lee, K. and Howell, J. R., Forced convective and radiative transfer within a highly porous layer exposed to a turbulent external flow field, *Proceedings of the 2nd ASME/JSME Thermal Engineering Joint Conference,* Vol. 2, pp. 337-386 (1987)

Leong, K. C., Forced convection heat transfer in a porous channel subjected to oscillating flow, *Proceedings of the 6th ASME-JSME Thermal Engineering Joint Conference*, Hawaii Island, Hawaii, USA, 16-20 March. 2003

Ling, J. X. and Dybbs, A., The effect of variable viscosity on forced convection over a flat plate submersed in a porous medium, *ASME Journal of Heat Transfer*, Vol. 114, pp. 1063-1065 (1992).

Liu, B. M., Xin, R. C. and Tao, W. Q., Experimental and numerical investigations on flow resistance in porous medium composed of randomly packed spheres, *Transport Phenomena in Thermal Engineering*, Vol. 1, pp. 213-236 (1993)

Lu, T. J., Heat transfer efficiency of metal honeycombs, *International Journal of Heat and Mass Transfer*, Vol. 42, pp. 2031-2040 (1999)

Lu, T. J., Stone, H. A. and Ashby, M. F., Heat transfer in open-cell metal foams, *Acta Mater*, Vol. 46, pp. 3619-3635 (1998)

MacDonald, R. W., Griffiths, R. F. and Cheah, S. C., Field experiments of dispersion through regular arrays of cubic structures, *Atmospheric Environment*, Vol. 31, pp. 783-795 (1997)

Mahajan, R. L., Nair, R., Wakharkar, V., Swan, J., Tang, J. and Vandentop, G., Emerging directions for packaging technologies, *Intel Technology Journal*, Vol. 6, pp. 62-75 (2002)

Mahalingam, M. and Berg, H., Thermal trends in component level packaging, *International Journal of Hybrid Microelectronics*, Vol. 7, pp. 1-9 (1984)

Marafie, A. and Vafai, K., Analysis of non-darcian effects on temperature differentials in porous media, *International Journal of Heat and Mass Transfer*, Vol. 44, pp. 4401-4411 (2001)

Moffat, R. J. and Anderson, A. M., Applying heat transfer coefficient data to electronics cooling, *Symposium on Fundamentals of Forced Convection Heat Transfer*, ASME HTD Vol. 101, pp. 33-43 (1988)

Moffat, R. J. and Ortega, A., Buoyancy induced forced convection, *Heat Transfer in Electronic Equipment*, ASME HTD Vol. 57, pp. 135-144 (1986)

Moore, G. E., Cramming more components onto integrated circuits, *Electronics*, Vol. 38, No. 8, pp. 1-4 (1965)

Morrison, F. A., Transient gas flow in a porous column, *Journal of Engineering Chemical Fundamentals*, Vol. 11, No. 2, pp. 191-197 (1972)

Nasr, K., Ramadhyani, S. and Viskanta, R., An experimental investigation on forced convection heat transfer from a cylinder embedded in a packed bed, *ASME Journal of Heat Transfer*, Vol. 116, pp. 73-80 (1994)

Nield, D. A. and Lage, J. L., The role of longitudinal diffusion in fully developed forced convective slug flow in a channel, *International Journal of Heat and Mass Transfer*, Vol. 41, pp. 4375-4377 (1998)

Nield D. A., Porneala, D. C. and Lage, J. L., A theoretical study with experimental Verification of the temperature-dependent viscosity effect on the forced convection through a porous medium channel, *ASME Journal of Heat Transfer*, Vol. 121, pp. 500-503 (1999)

Nozad, R. G., Carbonell, R. G. and Whitaker, S., Heat conduction in multiphase systems: I. Theory and experiment for two-phase systems, *Chemical Engineering Science*, Vol. 40, pp. 843-855 (1985)

Ortega, A. and Moffat, R. J., Heat transfer from an array of simulated electronic components: experimental results for free convection with and without a shrouding wall, *Heat Transfer in Electronic Equipment*, ASME HTD Vol. 48, pp. 5-15 (1985)

Paek, J. W., Kang, B. H. and Hyun, J. M., Transient cool-down of a porous medium in pulsating flow, *International Journal of Heat and Mass Transfer*, Vol. 42, pp. 3523-3527 (1999)

Patankar, S. V., *Numerical Heat Transfer and Fluid Flow*, Taylor & Francis, (1980)

Peterson, G. P. and Ortega, A., Thermal control of electronic equipment and devices, *Advances in Heat Transfer*, Vol. 20, pp. 181-314 (1990)

Poulikakos, D. and Kazmierczak, M., Transient double diffusion in a fluid layer extending over a permeable substrate, *ASME Journal of Heat Transfer*, Vol. 113, pp. 148-157 (1987)

Prescott, P. J. and Incropera, F. P., The effect of turbulence on solidification of a binary metal alloy with electromagnetic stirring, *ASME Journal of Heat Transfer*, Vol. 117, pp. 716-724 (1995)

Quintard, M. and Whitaker, S., Transport in chemically and mechanically heterogeneous porous media IV: Large-scale mass equilibrium for solute transport with adsorption, *Advances in Water Resources*, Vol. 22, No. 1, pp. 33-57 (1998)

Quintard, M. and Whitaker, S., Transport in ordered disordered porous media: Volume-averaged equations, closure problems, comparison with experiment, *Chemical Engineering Science*, Vol. 48, pp. 2537-2564 (1993)

Quintard, M., Modelling local non-equilibrium heat transfer in porous media. In: Heat Transfer 1998, *Proceedings of the 11th International Heat Transfer Conference*, Vol. 1, pp. 279-285 (1998)

Rachedi, R. and Chikh, S., Enhancement of electronic cooling by insertion of foam materials, *Heat and Mass Transfer*, Vol. 37, pp. 371-378 (2001)

Rix, D. H., *An Enquiry into Gas Process Asymmetry in Stirling Cycle Machines*, PhD Thesis, University of Cambridge (1984)

Roach, P. D. and Bell, K. J. Analysis of pressure drop and heat transfer data from the reversing flow test facility, Report no. ANL/MCT-88-1, Argonne National Laboratory, Argonne, Illinois (1988)

Rudraiah, N., Siddheshwar, G. and Masuoka, T., Turbulent convection in a high porosity porous medium with convective acceleration, *Journal of Mathematical and Physical Sciences*, Vol. 19, pp. 93-117 (1985)

Rudraiah, N., Turbulent convection in porous media with non-Darcy effects, *ASME Proceedings*, HTD 96, pp. 747-754 (1988)

Schreck, S. and Kleis, S. J., Modification of grid-generated turbulence by solid particles, *Journal of Fluid Mechanics*, Vol. 249, pp. 665-688 (1993)

Sherman, A. J., Williams, B. E., Delarosa, M. J. and Laferla, R., Characterization of porous cellular materials fabricated by CVD, In *Proceedings of MRS Fall Meeting*, Boston, 26-30 November 1990.

Siegel, R., Influence of oscillation-induced diffusion on heat transfer in a uniformly heated channel, *ASME Journal of Heat Transfer,* Vol. 109, pp. 244-247 (1987)

Simons, R., Thermal management of electronic packages, *Solid State Technology*, Vol. 26, pp. 131-137 (1983)

Slattery, J. C., Flow of viscoelastic fluids through porous media, *AIChE Journal*, Vol. 13, pp. 1066-1071 (1967)

Sozen, M. and Vafai, K., Analysis of oscillating flow compressible flow through a packed bed, *International Journal of Heat and Fluid Flow*, Vol. 12, No. 2, pp. 130-136 (1990)

Spiga, M. and Morini, G. L., Laminar heat transfer between parallel plates as the limiting solution for the rectangular duct, *International Communications in Heat and Mass Transfer*, Vol. 23, No. 4, pp. 555-562 (1996)

Stanek, V. and Szekely, Y., Three-dimensional flow of fluids through nonuniform packed beds, *AIChE Journal*, Vol. 20, pp. 974-980 (1974)

Subbojin, V. I. and Haritonov, V. V., Thermophysics of cooled laser, *Thermal Science*, Vol. 5 No. 1, pp. 43-53 (1996)

Sung, H. J., Kim, S. Y. and Hyun, J. M., Forced convection from an isolated heat source in a channel with porous medium, *International Journal of Heat and Fluid Flow*, Vol.16, pp. 527-535 (1995)

Tanaka, M., Yamashita, I. and Chisaka, F., Flow and heat transfer characteristics of the Stirling engine regenerator in an oscillating flow, *JSME International Journal Series II*, Vol. 33, pp. 283-289 (1990)

Taylor, J. R., *An Introduction to Error Analysis*, 2th Edition, University Science Books, California (1997)

Teng, H. and Zhao, T. S., An extension of Darcy's law to non-Stokes flow in porous media, *Chemical Engineering Science*, Vol. 55, pp. 2727-2735 (2000)

Tien, C. L. and Hunt, M. L., Boundary-layer flow and heat transfer in porous beds, *Chemical Engineering and Processing*, Vol. 21 pp. 53-63 (1987)

Tong, A. Y. and Sirignano, W. A., Vaporization response of fuel droplet in oscillatory field, *Proceedings of the 24th National Heat Transfer Conference and Exhibition*, Pittsburgh, USA., 9-12 August. 1987

Tong, A. Y. and Sirignano, W. A., Oscillatory vaporization of fuel droplets in an unstable combustor, *Journal of Propulsion and Power*, Vol. 5, pp. 257-261 (1989)

Tong, L. S. and London, A. L., Heat-transfer and flow friction characteristics of woven-screen and crossed-rod matrixes, *Trans. ASME*, Vol. 12, pp. 1558-1570 (1957)

Tong, T. W., Sharatchandra, M. C. and Gdoura, Z., Using porous inserts to enhance heat transfer in laminar fully-developed flows, *International Communications in Heat Mass Transfer*, Vol. 20, pp. 761-770 (1993)

Travkin, V. and Catton, I., A two-temperature model for turbulent flow and heat transfer in a porous layer, *ASME Journal of Fluids Engineering*, Vol. 117, pp. 181-188 (1995)

Tsuji, Y., Morikawa, Y. and Shiomi, H. H., LDV measurements of an air-solid two-phase flow in a vertical pipe, *Journal of Fluid Mechanics*, Vol. 139, pp. 417-442 (1984)

Tuckerman, D. B. and Pease, R. F. W., High-performance heat transfer sinking for VLSI, *IEEE Transactions on Electron Device Letters*, Vol. 2, pp. 126-129 (1981)

Uchida, S., The pulsating viscous flow superimposed on the steady laminar motion of incompressible fluid in a circular pipe, *Zeitschrift Angewangte Mathematik Physik*, Vol. 7, pp. 403-421 (1956)

Vafai, K., Analysis of the channelling effect in variable porosity media, *ASME Journal of Energy Resource Technology.*, Vol. 108, pp. 131-139 (1986)

Vafai, K. and Kim, S. J., Forced convection in a channel filled with a porous medium: an exact solution, *ASME Journal of Heat Transfer*, Vol. 111, pp. 1103-1106 (1989)

Vafai, K. and Sozen, M., Analysis of energy and momentum transport for fluid flow through a porous bed, *ASME Journal of Heat Transfer*, Vol. 112, pp. 690-699 (1990a)

Vafai, K. and Sozen, M., An investigation of a latent heat storage packed bed and condensing flow through it, *ASME Journal of Heat Transfer*, Vol. 112, pp. 1014-1022 (1990b)

Vafai, K. and Thiyagaraja, R., Analysis of flow and heat transfer at the interface region of a porous medium, *International Journal of Heat and Mass Transfer*, Vol. 30, pp. 1391-1405 (1987).

Vafai, K. and Tien, C. L., Boundary and inertia effects on flow and heat transfer in porous media, *International Journal of Heat and Mass Transfer*, Vol. 24, pp. 195-203 (1981)

Vafai, K. and Tien, C. L., Boundary and inertia effects on convective mass transfer in porous media, *International Journal of Heat and Mass Transfer*, Vol. 25, pp. 1183-1190 (1982)

Viswanath, R., Wakharkar, V., Watwe, A. and Lebonheur, V., Thermal performance challenges from silicon to systems, *Intel Technology Journal*, Vol. 3, pp. 1-16 (2000)

Vortmeyer, D. and Schuster, J., Evaluation of steady flow profiles in rectangular and circular packed beds by a variational method, *Chemical Engineering Science*, Vol. 38, pp. 1691-1699 (1988)

Wakao, N., Kaguei, S. and Funazkri, T., Effect of fluid dispersion coefficients on particle-to-fluid heat transfer coefficients in packed beds, *Chemical Engineering Science*, Vol. 34, pp. 325-336 (1979)

Walsh, T. E., Yang, K. T., Nee, V. W. and Liao, Q. D., Forced convection cooling in microelectronic cabinets via oscillatory flow techniques, In *Experimental Heat Transfer, Fluid Mechanics and Thermodynamics*, Vol. 2, pp. 1846 - 1853 (1993)

Wakeland, R. S. and Keolian, R. M., Measurements of resistance of individual square-mesh screens to oscillating flow at low and intermediate Reynolds numbers, *ASME Journal of Fluids Engineering*, Vol. 125, pp. 851-863 (2003)

Wang, H. and Takle, E. S., Boundary-layer flow and turbulence neat porous obstacles, *Boundary Layer Meteorology*, Vol. 74, pp. 73-88 (1995)

Whitaker, S., Diffusion and dispersion in porous media, *AIChE Journal*, Vol. 13, pp. 420-427 (1967)

Whitaker, S., Flow in porous media II, The governing equations for immiscible two-phase flow, *Transport in Porous Media*, Vol. 1, pp. 105-113 (1986)

Womersley, J. R., Method for the calculation of velocity, rate of flow and viscous drag in arteries when the pressure gradient is known, *Journal of Physiology*, Vol. 127, pp. 553-563 (1955)

Xu, J. and Wirtz, A., In-plane effective thermal conductivity of plain-weave screen laminates, *IEEE Transactions on Components and Packaging Technologies*, Vol. 25, pp. 615-620 (2002)

Yang, Y. T. and Hwang, C. Z., Calculation of turbulent flow and heat transfer in a porous-baffled channel, *International Journal of Heat and Mass Transfer*, Vol. 46, pp. 771-780 (2003)

Yuan, Z. S. and Dybbs, A., Oscillating flow and heat transfer in a Stirling engine regenerator, *Fundamentals of Heat Transfer in Porous Media*, ASME HTD, Vol. 193, (1992)

Zebib, A. and Wo, Y., A two-dimensional conjugate heat transfer model for forced air cooling of an electronic devices, *ASME Journal of Electronic Packaging*, Vol. 111, pp. 41-45 (1989)

Zhao, C. Y., Lu, T. J., Hodson, H. P. and Jackson, J. D., The temperature dependence of effective thermal conductivity of open-celled steel alloy foams, *Materials Science and Engineering A*, Vol. 367, pp. 123-131 (2004)

Zhao C. Y., Lu, T. J. and Hodson, H. P., Thermal radiation in ultralight metal foams with open cells, *International Journal of Heat and Mass Transfer*, Vol. 47, pp. 2927-2939 (2004)

Zhao, T. S. and Cheng P., Numerical solution to laminar forced convection in a heated pipe subjected to periodically flow, *International Journal of Heat and Mass Transfer*, Vol. 38, pp. 3011-2022 (1995)

Zhao, T. S. and Cheng, P., The friction coefficient of a fully developed laminar reciprocating flow in a circular pipe, *International Journal of Heat and Fluid Flow*, Vol. 17, pp. 167-172 (1996a)

Zhao, T. S. and Cheng, P., Oscillatory pressure drop through a woven-screen packed column subjected to a cyclic flow, *Cryogenics*, Vol. 36, pp. 333-341 (1996b)

Zhao, T. S. and Cheng, P., Experimental studies on the onset of turbulence and frictional losses in an oscillatory turbulent pipe flow, *International Journal of Heat and Fluid Flow*, Vol. 17, pp. 356-362 (1996c)

Zhao, T. S. and Cheng, P., A numerical study of laminar reciprocating flow in a pipe of finite length, *Applied Scientific Research*, Vol. 59, pp. 11-25 (1998a)

Zhao, T. S. and Cheng, P., Heat transfer in oscillatory flows, in: *Annual Review of Heat Transfer*, Ed: Tien, C. L., Vol. 9 (1998b)

Zhao, T. S. and Liao, Q., On capillary-driven flow and phase-change heat transfer in a porous structure heated by a finned surface: measurements and modelling, *International Journal of Heat and Mass Transfer*, Vol. 43, pp. 1141-1155 (2000)

Zukauskas, A. A., Convective heat transfer in cross-flow, *Handbook of Single-Phase Heat Transfer*, Wiley, New York (1987)

APPENDIX A

Specifications of Measuring Equipment

1. Sine Wave Carrier Demodulator CD15

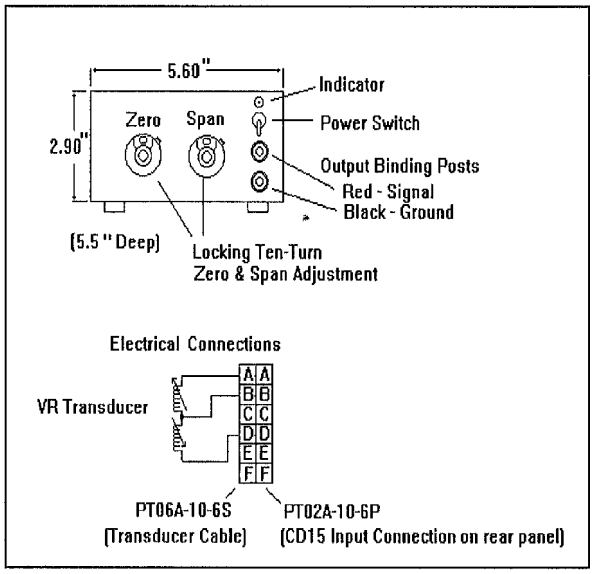

The CD15 Sine Wave Carrier Demodulator operates with variable reluctance transducers to provide a DC output signal for dynamics as well as steady state measurements. The DC output is obtained from an active filter circuit and gives a uniform response from steady state to 1000 Hz. The low impedance sine wave excitation allows operation with the transducer located over 305 m from the CD15. The specifications of sine wave carrier demodulator CD15 are:

Input Sensitivity	15mV/V minimum input for 10 VDC FS output
Transducer Excitation	5V rms, 5 kHz sine wave
Voltage	-10 VDC at 10 mA. Short circuit proof.
Output Impedance	10 ohms, nominal
Frequency Response	DC to 1000 Hz flat –10%
Stability	-0.1% / 30 days
Ripple	Less than 10 mV peak-to-peak
Zero Shift	-0.005% / °C average
Temperature Range	-18 – 85°C
Power Requirements	105 – 125 VAC, 50 – 400 Hz, 5 W, nominal
Weight	1.58 kg
Connector	mating connector, PT06A-10-6S (SR) Bendix or equal

2. DP15 Differential Pressure Transducer

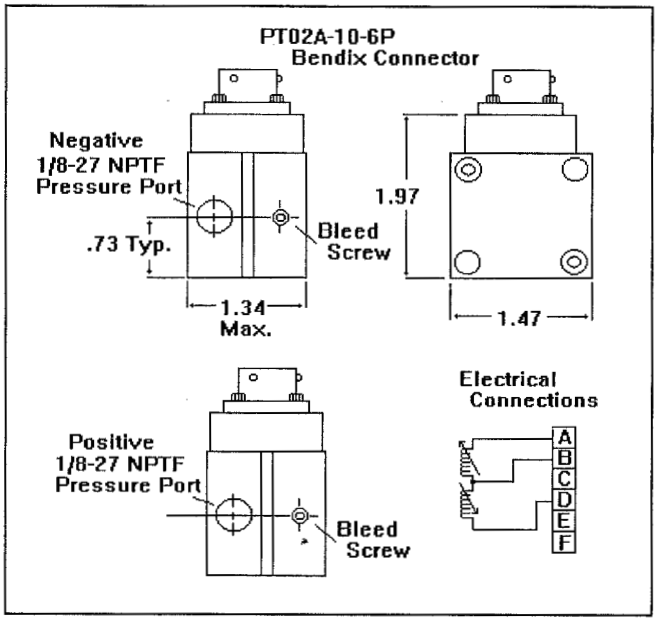

A pressure-sensing diaphragm maximises the system's functionality by making pressure measurements from ±2.22" H_2O to ±3200 psi in one compact unit. Rugged and reliable, the DP15 provides superior accuracy for measuring low-pressure liquids and gasses, while it withstands the abuse of field and laboratory testing. The DP15 works with Carrier Demodulator CD15. Features including easy calibration, compact size, bright LED readout display or portability make these carrier demodulators ideal for any type of pressure measurement. The specifications of DP15 differential pressure transducer are:

Standard Ranges	±0.06 kPa FS to 2176 kPa FS
Accuracy	±0.25% FS
Overpressure	2176 kPa operating
Output	±35 mV/V full-scale, nominal
Inductance	20 mh nominal, each coil
Zero Balance	Within 5 mV/V
Pressure Media	Corrosive liquids and gases both sides, compatible with 410 SS and Inconel
Temperature	Operating: -54°C to 121°C
Pressure Cavity Volume	1.2×10^{-2} cm^3
Volumetric Displacement	6×10^{-4} cm^3
Pressure connection	NPTF
Electrical Connection	PTO2A-10-6P, Amphenol (formerly Bendix) or equivalent.
Weight	0.34 kg

3. IFA100 Constant Temperature Anemometer

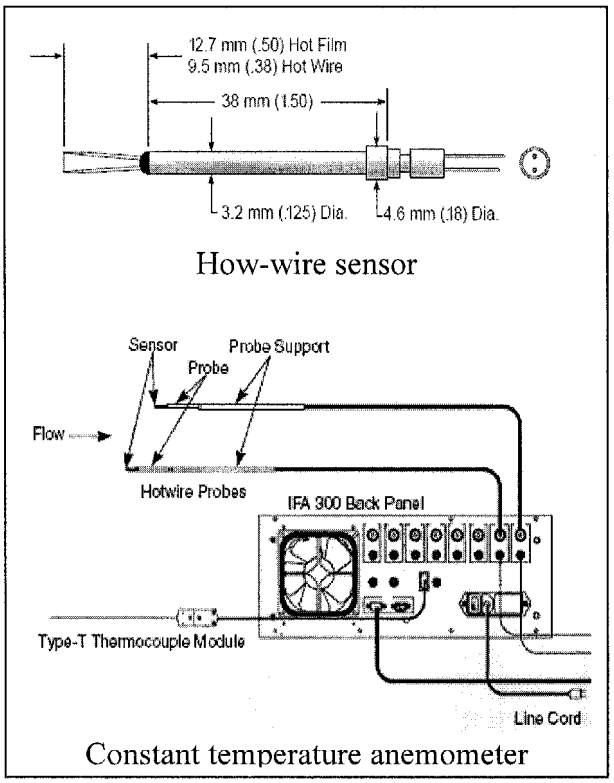

TSI 1213-60W hot-wire permits measurement of up to three mean velocity components with a single sensor by rotating the probe about its axis. TSI IFA 100 is a high-performance, low-noise, constant-temperature anemometer. It can be used for all hot-wire in liquids or gases where application dictates ease of operation, high-frequency response, high accuracy. The specifications of IFA100 constant temperature anemometer are:

Typical input voltage	1:1 bridge position: 1.85 μV/Hz standard and Hi Pwr bridge position: 2.5 μV/Hz
Equivalent input drift:	
5:1 bridge	0.35 μV/°C
1:1 bridge	0.6 μV/°C
Output impendance	50 ohm
Output voltage range	0 – 12 V
Maximum bridge current	1.2 A
Amplifier gain	$> 1 \times 10^6$
Operating temperature	0 – 50°C

4. Hot-wire Calibrator Model 1126

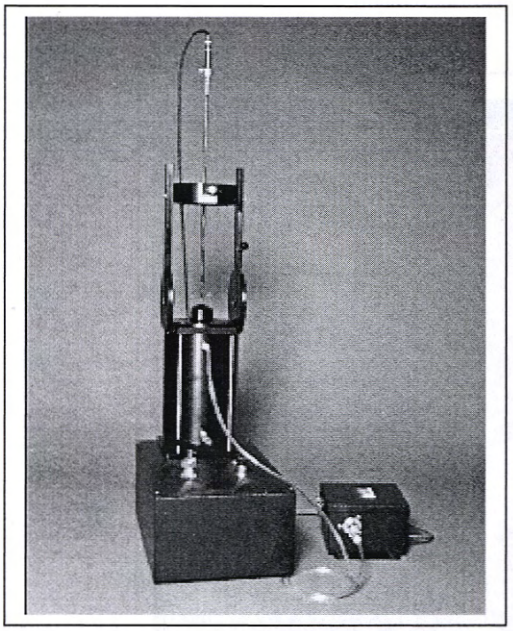

TSI's Model 1126 monitors the velocity through the output of a built-in pressure transducer, acquires sensor data, adjusts the flow rate to a new velocity, and repeats the process, until the entire velocity range is covered. The data is automatically integrated into the software calibration section. Its exclusive flow nozzle design exhibits a flat velocity profile over a broad dynamic range. The specifications of the hot-wire calibrator 1126 are:

Turbulence intensity	0.3% typical
Velocity accuracy	0.5% typical
Fluid temperature range	Ambient
Nozzle sizes	10 mm and 14 mm
Weight	10.2 kg for calibrator; 5.8 kg for air filter system
Dimensions	0.43 m (W) × 0.25 m (D) × 0.79 m (H)
Air requirements	0.025 m^3/s at 0.5 to 0.7 MPa
Pressure transducers Accuracy	0.15% of reading (includes effects of nonlinearity, hysteresis, and repeatability)
Resolution	0.01% full scale
Temperature sensitivity	Zero: 0.005% of full scale/°C
Span: 0.02% of reading/°C	0.02% of reading/°C

5. Photograph of Experimental Setup

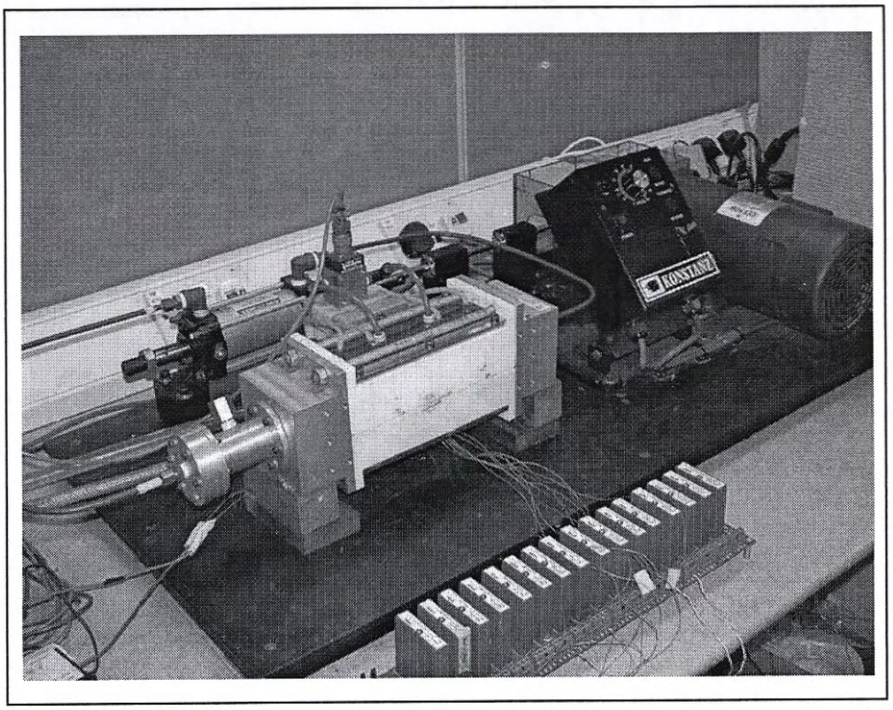

Figure A-1 Overall view of experimental facility

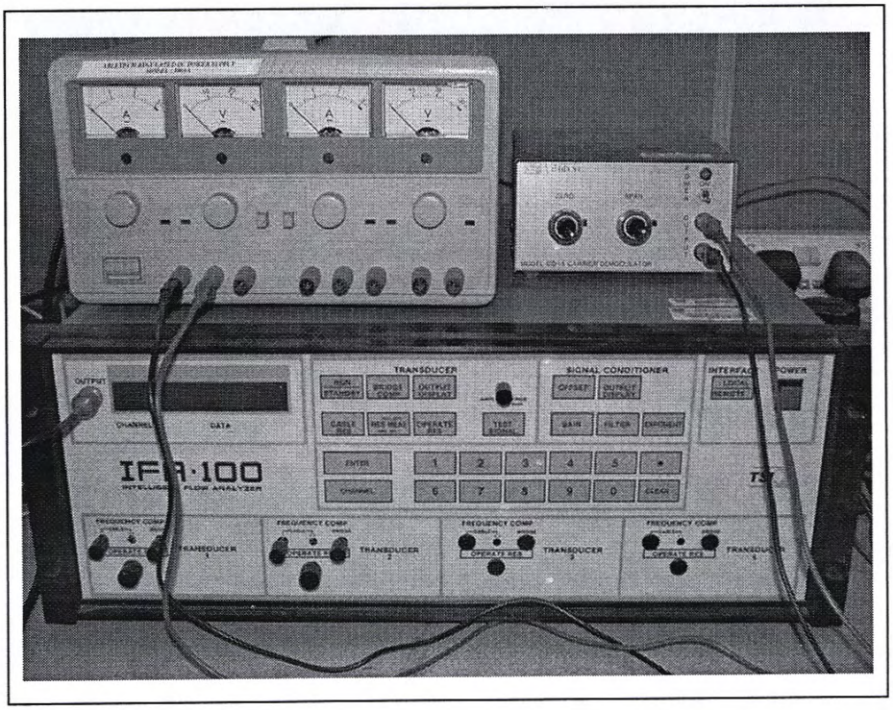

Figure A-2 Measuring system

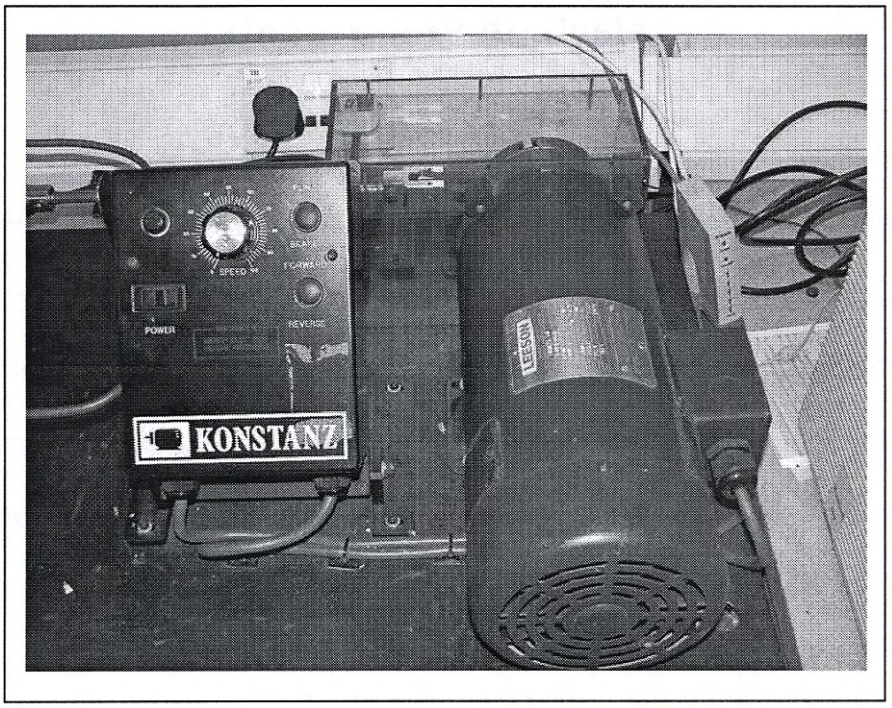

Figure A-3 Oscillating flow generator

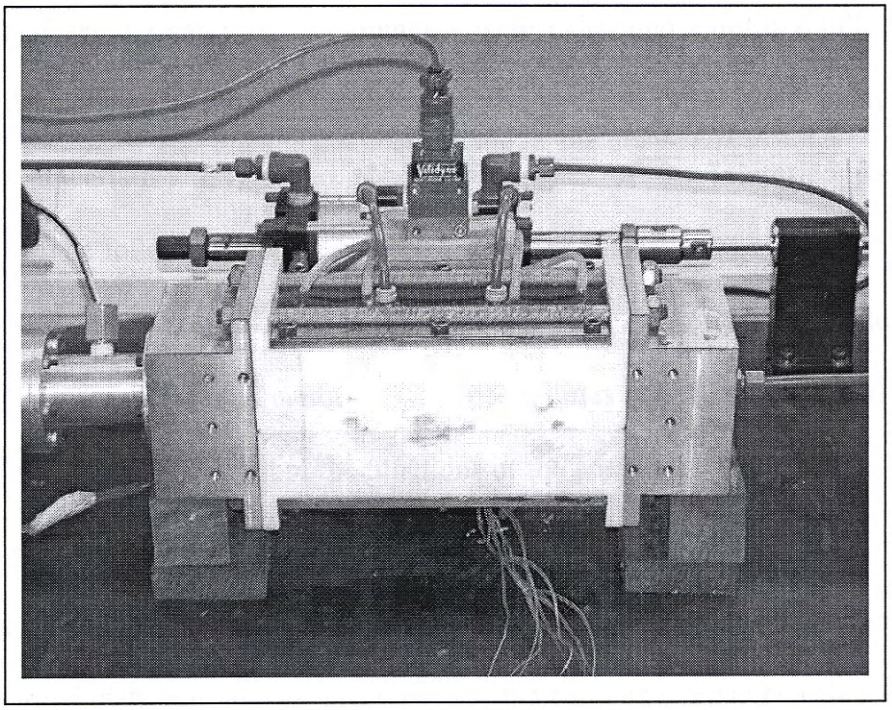

Figure A-4 Test section

APPENDIX B

Uncertainty Analysis

Measurement uncertainty generally occurs during data acquisition and reduction. Uncertainty in data acquisition usually results from improper performance of instruments, limitation in probe sensitivity and frequency response, and inaccuracy of instruments. The uncertainty can be classified into systematic uncertainty and random uncertainty. The systematic uncertainty is mainly due to the wrong operation of instruments and other human errors. With careful operations and regular calibrations, systematic uncertainty can be minimised. In the present experiments, the test equipments of hot-wire, pressure transducer and thermocouple were selected carefully to guarantee the sufficient accuracy and response frequency. As described in the experimental setup section, the equipments were calibrated carefully following the strict calibration procedures. Therefore, in the present uncertainty analyses, the systematic uncertainty is ignored. The uncertainties of the interested parameters calcualted in the following test means the random uncertainty.

The present uncertainty analysis is based on the method described by Taylor (1997). If $v, \ldots y, \ldots z$ are measured quantities with uncertainties $\delta v, \ldots \delta y, \ldots \delta z$, and the measured values of $v,\ldots y,\ldots z$ are the functions of the parameter q as

$$q = f(v,...y,...z) \tag{B-1}$$

Assuming the uncertainties of the measured quantities are independent and with random normal distributions, the uncertainty of the parameter q can be calculated by

$$\frac{\delta q}{|q|} = \sqrt{\left(\frac{\delta v}{v}\right)^2 + \cdots + \left(\frac{\delta y}{y}\right)^2 + \cdots + \left(\frac{\delta z}{z}\right)^2} \tag{B-2}$$

Form the above equation, it can be seen that the uncertainty of calculated parameter depends on the uncertainties of the independent quantities $v,...y,...z$. For N measurements, the standard deviation of the mean is used to describe the uncertainty. For example, the standard deviation of the quantities v in N measurements can be obtained by

$$\sigma_v = \sqrt{\frac{1}{N}\sum_{i=1}^{N}(v_i - \bar{v})^2} \tag{B-3}$$

where v_i and $\bar{v} = \frac{\sum v_i}{N}$ are the measured value and averaged value for quantity v, respectively. Therefore, the uncertainty of v can be given by the standard deviation σ_v divided by $\sqrt{N}$ i.e.

$$\delta_v = \frac{\sigma_v}{\sqrt{N}} \tag{B-4}$$

Equation (B-4) indicates that the uncertainty of quantity v due to data reduction results mainly form the use of finite data in calculating a statistical mean. This type of uncertainty depends on the reduction scheme. To minimize the reduction uncertainty, data with 100 cycle length was collected for oscillating flow experiments. Therefore, after time-averaging, the uncertainty of the measured quantities can be reduced. For the velocity, pressure drop and temperature value are the standard deviation of the value obtained by cycle-averaging. Using the method described above, the uncertainties of the interested parameters are listed in Table B-1.

Table B-1 Uncertainties of the measured and calculated parameters

Parameter	Uncertainty %
ρ_f	0.5
ν_f	0.5
μ_f	0.5
u	2.0
P	2.0
T	3.0
d_l	1.0
D_e	1.5
D_h	2.5
L	1.0
Q	2.0
x_{max}	1.0
A_{Dh}	3.5
A_0	1.0
ε	1.0
K	3.5
F	4.0
Re_ω	3.9
$Re_{\omega(Dh)}$	4.9
$Re_{max(Dh)}$	6.5
Nu_x	5.7
Nu_{avg}	8.9
f_{max}	9.7

APPENDIX C

DUOCEL Aluminium Foam

OVERVIEW

Duocel Aluminium Foam is available in a density range of 3-12% uncompressed and can be compressed up to 60% dense relative to the solid base metal. Available standard pore sizes include 5, 10, 20 and 40 pores per linear inch (PPI) and can be adjusted independently or by varying the relative density. Duocel Foam is produced through a proprietary process developed by ERG in which the resulting foam has the identical chemical composition of the base alloy used. Duocel is presently available in aluminium alloys of 6101 and A356 with other alloys available on special order. Foam properties can be tailored for a specific application and material response by adjusting the foam density, pore size, alloy, and ligament structure. The high specific surface area, low density and open-celled nature of Duocel provide a combination of properties ideally suited for high-tech applications where conventional materials and products are not adequate. Physical characteristics of DUOCEL aluminium foam are listed below.

Compression Strength	2.170 MPa
Tensile Strength	1.240 MPa
Shear Strength	1.31 MPa
Modulus of Elasticity (Compression)	93.1 MPa
Modulus of Elasticity (Tension)	75.8 MPa
Shear Modulus	200 MPa
Vickers Hardness	35
Specific Heat	895 J/kg·K
Coefficient of Thermal Expansion (0-100°C)	2.35×10^{-7}·m·m^{-1}·°C^{-1}
Bulk Resistivity	7.1×10^{-7} ohm·m
Melting Point	660°C

COMMON APPLICATIONS

Compact Heat Exchangers

As with fluid flow control devices, the high surface area to volume ratio allows for a more compact design than other materials can provide. The ligament structure of Duocel foam promotes complete mixing and efficient scrubbing of the heat exchange surfaces. All aluminium brazed joints provide continuous, highly conductive heat paths and superior overall thermal conductivity, all at less than 10% the weight of solid aluminium.

Fluid Flow Control Devices

Gas Diffusers and Mixers: The large surface area of Duocel Aluminium foam promotes uniform gas distribution regardless of flow asymmetry even in low pressure flow regions. A controlled pressure drop and tortuous path through the foam provides the essential micro-turbulent blending for thorough mixing. Several materials are available that can be tailored to the specific system for longer life and reduced maintenance. Aluminium foam used in etching showerheads delivers uniform gas flow and grounds the assembly to prevent plasma arcing. A large surface area to volume ratio allows for a more compact design and improved system efficiency.

Liquid/Gas Separators: The three-dimensional continuous ligament structure of Duocel foam promotes complete removal of entrained liquids. Aluminium foam alone or with standard surface treatments ensures long life and low maintenance. With up to 97% void volume, extremely small pressure drops can be achieved. The continuously connected aluminium structure prevents particle generation from within the liquid/gas separator.

Energy/Impact Absorption

The stress-strain response of Duocel foam can be tailored for a number of specific application requirements by varying the density and alloy of the foam, while its isotropic properties provide identical response without regard to impact angle. A high strength-to-weight ratio results in superior performance and greater shear strength than honeycomb of the same density. The constant stress portion of the stress-strain curve extends to more than 50% strain, and the foam can be pre-crushed to change the yield point and response as needed.

Orthopaedic Devices

Cellular materials are common in nature, with just a few examples being wood, cork, coral and bone. The open-celled, interconnected structure of Duocel foam mimics (Figure C-1) that of the cancellous bone (Figure C-2) material found in our own bodies, especially when made in the same 8-10% density. In the past, our foam has been used for its bio-mimicing structure in orthopaedic applications and the only real limit to future uses is the users imagination.

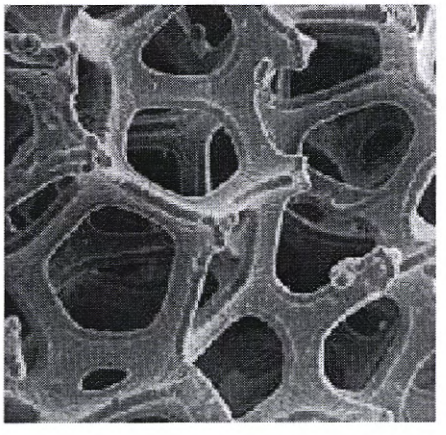

Figure C-1 Generic metal foam

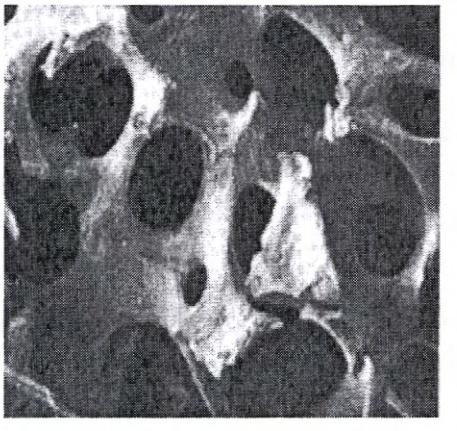

Figure C-2 Human cancellous bone

APPENDIX D

Derivation of Energy Equation

For forced convection in porous medium, the microscopic energy equations for the fluid and solid phases are

$$\rho_f c_{pf} \frac{\partial T_f}{\partial t} + \rho_f c_{pf} \nabla \cdot \left(\mathbf{u}_f T_f \right) = \nabla \cdot \left(k_f \nabla T_f \right) \tag{D-1}$$

$$\rho_s c_{ps} \frac{\partial T_s}{\partial t} = \nabla \cdot \left(k_s \nabla T_s \right) \tag{D-2}$$

where k_f and k_s are the thermal conductivities of the fluid and solid phases, respectively. According to Figure 6-2, the interface conditions between the fluid and solid phases at A_{fs} are

$$T_f = T_s \tag{D-3}$$

$$\mathbf{n}_{fs} \cdot k_f \nabla T_f = \mathbf{n}_{fs} \cdot k_s \nabla T_s \tag{D-4}$$

where T_f and T_s are the temperatures of the fluid and solid phases, respectively. $\mathbf{n}$ is the outward unit vector of a surface. To derive the macroscopic equations from the microscopic equations, the following averaging theorems relating the volume average of a spatial derivative to the spatial derivative of the volume average are needed:

$$\frac{1}{V} \int_V \langle \nabla \Phi \rangle dV = \nabla \left(\frac{1}{V} \int_V \langle \Phi \rangle dV \right) + \frac{1}{V} \int_{A_{fs}} \Phi d\mathbf{A} \tag{D-5a}$$

$$\frac{1}{V} \int_V \langle \nabla \cdot \Phi \rangle dV = \nabla \cdot \left(\frac{1}{V} \int_V \langle \Phi \rangle dV \right) + \frac{1}{V} \int_{A_{fs}} \Phi \cdot d\mathbf{A} \tag{D-5b}$$

where Φ is any quantity being averaged and the symbol $< >$ refers to the volume average quantity. With the aid of Equation (D-5), volume averaging of Equations (D-

1) and (D-2) gives

$$\frac{\partial}{\partial t}\left(\varepsilon\rho_f c_{Pf}\overline{T}_f + \rho_f c_{pf}\nabla\cdot\left(\varepsilon\left\langle\overline{\mathbf{u}_f T_f}\right\rangle\right)\right)$$
$$= \nabla\cdot\left(k_f\nabla\left(\varepsilon\left\langle\overline{T}_f\right\rangle\right)\right) + \nabla\cdot\left(\frac{1}{V}\int_{A_{fs}} k_f\left\langle T_f\right\rangle dA\right) + \frac{1}{V}\int_{A_{fs}} k_f\nabla T_f\cdot dA \tag{D-6}$$

$$\frac{\partial}{\partial t}\left((1-\varepsilon)\rho_s c_{Ps}\overline{T}_s\right) = \nabla\cdot\left(k_s\nabla(1-\varepsilon)\left\langle\overline{T}_s\right\rangle\right)$$
$$-\nabla\cdot\left(\frac{1}{V}\int_{A_{fs}} k_s\left\langle T_s\right\rangle dA\right) - \frac{1}{V}\int_{A_{fs}} k_s\nabla T_s\cdot dA \tag{D-7}$$

where $\overline{T}_f$ and $\overline{T}_s$ are the intrinsic temperatures of the fluid and solid phases given by

$$\overline{T}_f = \frac{1}{V_f}\int_{V_f} T_f dV \tag{D-8a}$$

$$\overline{T}_s = \frac{1}{V_s}\int_{V_s} T_s dV \tag{D-8b}$$

The quantity $\overline{\mathbf{u}_f T_f}$ in Equation (D-6) is defined as

$$\overline{\mathbf{u}_f T_f} = \frac{1}{V_f}\int_{V_f}\mathbf{u}_f T_f dV \tag{D-9}$$

Combining Equations (D-6) and (D-7) with the aid of Equations (D-3) and (D-4) provides

$$\varepsilon\rho_f c_{Pf}\frac{\partial\left\langle\overline{T}_f\right\rangle}{\partial t} + \rho_f c_{pf}\nabla\cdot\left(\varepsilon\left\langle\overline{\mathbf{u}_f T_f}\right\rangle\right) + (1-\varepsilon)\rho_s c_{Ps}\frac{\partial\left\langle\overline{T}_s\right\rangle}{\partial t} =$$
$$\nabla\cdot\left(k_f\nabla\left(\varepsilon\left\langle\overline{T}_f\right\rangle\right)\right) + \nabla\cdot\left((1-\varepsilon)k_s\nabla\left\langle\overline{T}_s\right\rangle\right) + \nabla\cdot\left(\frac{1}{V}\int_{A_{fs}}\left(k_f\left\langle T_f\right\rangle - k_s\left\langle T_s\right\rangle\right)dA\right) \tag{D-10}$$

In Equation (D-10), T_f and T_s can be decomposed as

$$T_f = \overline{T}_f + \Delta T_f \tag{D-11a}$$

$$T_s = \overline{T}_s + \Delta T_s \tag{D-11b}$$

where ΔT_f and ΔT_s are the fluctuation value to the intrinsic temperatures of the fluid and solid phases, respectively. Substituting Equation (D-11) into Equation (D-10), the energy equation can be rewritten as

$$\varepsilon\rho_f c_{Pf}\frac{\partial\overline{T}}{\partial t}+\rho_f c_{pf}\nabla\left(\varepsilon\left\langle\overline{\mathbf{u}}_f\right\rangle\left\langle\overline{T}\right\rangle+\varepsilon\left\langle\overline{\Delta\mathbf{u}_f\Delta T_f}\right\rangle\right)+(1-\varepsilon)\rho_s c_{Ps}\frac{\partial\overline{T}}{\partial t}=$$
$$\nabla^2\left(\varepsilon k_f+(1-\varepsilon)k_s\right)\left\langle\overline{T}\right\rangle+\nabla\cdot\left(\frac{1}{V}\int_{A_{fs}}\left(k_f\left\langle\Delta T_f\right\rangle-k_s\left\langle\Delta T_s\right\rangle\right)dA\right) \tag{D-12}$$

where

$$\overline{T}_f=\overline{T}_s=\overline{T} \tag{D-13}$$

$$\overline{\Delta\mathbf{u}_f\Delta T_f}=\frac{1}{V_f}\int_{V_f}\Delta\mathbf{u}_f\Delta T_f dV \tag{D-14}$$

Equation (D-14) represents the thermal dispersion effect. Nozad *et al.* (1985) showed that the terms on the right-hand of Equation (D-12) can be expressed as

$$\nabla^2\left(\varepsilon k_f+(1-\varepsilon)k_s\right)\left\langle\overline{T}\right\rangle$$
$$+\nabla\cdot\left(\frac{1}{V}\int_{A_{fs}}\left(k_f\left\langle\Delta T_f\right\rangle-k_s\left\langle\Delta T_s\right\rangle\right)dA\right)=\nabla\left(k_{sd}\nabla\left\langle\overline{T}\right\rangle\right) \tag{D-15}$$

Submitting Equation (D-15) into Equation (D-12), the macroscopic energy conservation equation for convection in a porous medium can be expressed as

$$\frac{\partial}{\partial t}\left(\varepsilon\rho_f c_{pf}+(1-\varepsilon)\rho_s c_{ps}\right)\left\langle\overline{T}\right\rangle$$
$$+\rho_f c_{pf}\nabla\cdot\left(\varepsilon\left\langle\overline{\mathbf{u}}_f\right\rangle\left\langle\overline{T}\right\rangle+\varepsilon\left\langle\overline{\Delta\mathbf{u}_f\Delta T_f}\right\rangle\right)=\nabla\cdot\left(k_{sd}\nabla\left\langle\overline{T}\right\rangle\right) \tag{D-16}$$

where k_{sd} is the stagnant thermal conductivity of the saturated porous medium.